

Electron Transfer and Protein Engineering Studies of the
Soluble Methane Monooxygenase from *Methylococcus capsulatus* (Bath)

by
Jessica L. Blazyk
B.S. Chemistry
Ohio University, 1996

SUBMITTED TO THE DEPARTMENT OF CHEMISTRY IN PARTIAL
FULFILLMENT OF THE REQUIREMENTS FOR THE DEGREE OF

DOCTOR OF PHILOSOPHY IN CHEMISTRY
AT THE
MASSACHUSETTS INSTITUTE OF TECHNOLOGY

September 2003

© Massachusetts Institute of Technology, 2003
All rights reserved

Signature of Author: _____

Department of Chemistry
June 16, 2003

Certified by: _____

Stephen J. Lippard
Thesis Supervisor

Accepted by: _____

Robert W. Field
Chairman, Departmental Committee on Graduate Students

This doctoral thesis has been examined by a Committee of the Department of Chemistry as follows:

John M. Essigmann
William R. and Betsy P. Leitch Professor of Chemistry and Toxicology
Committee Chairman

Stephen J. Lippard
Arthur Amos Noyes Professor of Chemistry
Thesis Supervisor

Catherine L. Drennan
Cecil and Ida Green Career Development Assistant Professor of Chemistry

JoAnne Stubbe
Novartis Professor of Chemistry and Professor of Biology

Electron Transfer and Protein Engineering Studies of the
Soluble Methane Monooxygenase from *Methylococcus capsulatus* (Bath)

by

Jessica L. Blazyk

Submitted to the Department of Chemistry on June 16, 2003, in partial fulfillment of the requirements for the Degree of Doctor of Philosophy

Abstract

Chapter 1. Introduction: Electron Transfer in Biological Systems

In many biological processes, including oxidative phosphorylation and photosynthesis, electron transfer reactions play vital roles. Electrons must be transported at catalytically relevant rates and with specificity to prevent indiscriminate electron transfer that would quickly bring cells to equilibrium. To meet these requirements, biological systems employ a panoply of organic and inorganic redox centers, most of which are sequestered within proteins. In addition to protecting a cofactor from undesirable reactions, the surrounding protein environment tunes its redox properties and mediates specific contacts with other molecules. This brief overview describes the types of redox centers used in biology, the application of electron transfer theory to physiological systems, the kinetic complexity introduced by interprotein interactions, and general mechanisms for regulating biological electron transfer.

Chapter 2. Expression and Site-Directed Mutagenesis of the Reductase Component of Soluble Methane Monooxygenase from *Methylococcus capsulatus* (Bath)

The soluble methane monooxygenase (sMMO) system comprises three components, a hydroxylase (MMOH), a reductase (MMOR), and a regulatory protein (MMOB), all of which are required for conversion of methane to methanol by this system in methanotrophic bacteria. The reductase protein employs flavin adenine dinucleotide (FAD) and [2Fe-2S] cofactors to facilitate electron transfer from NADH to MMOH. MMOR from *Methylococcus capsulatus* (Bath) was overexpressed in *Escherichia coli*, affording high yields of pure reductase after a two-step purification procedure. Recombinant MMOR was indistinguishable from native MMOR isolated from *M. capsulatus* (Bath) in every respect examined, including mass, amino acid composition, cofactor content, activity, and spectroscopic (optical and EPR) properties. Seven site-directed MMOR mutants, D26A, R43A, E72A, E73A, E74A, E75A, and E76A, were prepared in order to investigate MMOH-MMOR binding interactions. Iron depletion in the mutant reductases was largely overcome by slightly modifying the purification protocol, but MMOR(R43A) could not be obtained with full [2Fe-2S] complementation.

Steady-state sMMO activity assays indicated reduced MMOH–MMOR binding affinity and/or frequency for the E73A, E75A, and D26A mutants. In single-turnover reactions with NADH, the electron transfer steps in all six reductase mutants proceeded at rates similar to those observed for wild-type MMOR (MMOR-wt). MMOR(E73A), which displayed the same distribution of electrons after reduction with NADH as MMOR-wt, was selected for further study. A K_d of $\sim 50 \mu\text{M}$ was determined for the MMOH–MMOR(E73A) interaction at pH 7.0 and 25 °C by isothermal titration calorimetry. Roles for the mutated reductase residues in complex formation with MMOH are discussed, and an evaluation of the MMOH–MMOR docking model used for mutant selection is presented.

Chapter 3. Expression and Characterization of Ferredoxin and Flavin Adenine Dinucleotide-Binding Domains of the Reductase Component of Soluble Methane Monooxygenase from *Methylococcus capsulatus* (Bath)

Soluble methane monooxygenase (sMMO) from *Methylococcus capsulatus* (Bath) catalyzes the selective oxidation of methane to methanol, the first step in the primary catabolic pathway of methanotrophic bacteria. A reductase (MMOR) mediates electron transfer from NADH through its FAD and [2Fe-2S] cofactors to the dinuclear non-heme iron sites housed in a hydroxylase (MMOH). The structurally distinct [2Fe-2S], FAD, and NADH binding domains of MMOR facilitated division of the protein into its functional ferredoxin (MMOR-Fd) and FAD/NADH (MMOR-FAD) component domains. The 10.9-kDa MMOR-Fd (MMOR residues 1-98) and 27.6-kDa MMOR-FAD (MMOR residues 99-348) were expressed and purified from recombinant *Escherichia coli* systems. The Fd and FAD domains have optical features identical to those of the [2Fe-2S] and flavin components, respectively, of MMOR. Redox potentials, determined by reductive titrations including indicator dyes, for the [2Fe-2S] and FAD cofactors in the domains are $[2\text{Fe-2S}]_{\text{ox/red}}$ $-205 \pm 1 \text{ mV}$; $\text{FAD}_{\text{ox/sq}}$ $-172 \pm 2 \text{ mV}$; and $\text{FAD}_{\text{sq/hq}}$ $-266 \pm 4 \text{ mV}$. Kinetic and spectral properties of intermediates observed in the reaction of oxidized MMOR-FAD (FAD_{ox}) with NADH at 4 °C were established with stopped-flow UV-visible spectroscopy. Analysis of the influence of pH on MMOR-FAD optical spectra, redox potentials, and NADH reaction kinetics afforded $\text{p}K_a$ values for the semiquinone (FAD_{sq}) and hydroquinone (FAD_{hq}) MMOR-FAD species and two protonatable groups near the flavin cofactor. Electron transfer from MMOR-FAD_{hq} to oxidized MMOR-Fd is extremely slow ($k = 1500 \text{ M}^{-1} \text{ s}^{-1}$ at 25 °C, compared to 90 s^{-1} at 4 °C for internal electron transfer between cofactors in MMOR), indicating that cofactor proximity is essential for efficient interdomain electron transfer.

Chapter 4. Intermolecular Electron Transfer Reactions in Soluble Methane Monooxygenase from *Methylococcus capsulatus* (Bath): A Role for Hysteresis in Protein Function

Electron transfer from NADH to the hydroxylase component (MMOH) of soluble methane monooxygenase (sMMO) primes its non-heme diiron centers for reaction with dioxygen to generate high-valent iron intermediates that convert

methane to methanol. This intermolecular electron transfer step is facilitated by a reductase (MMOR), which contains [2Fe-2S] and flavin adenine dinucleotide (FAD) prosthetic groups. In order to investigate interprotein electron transfer, chemically reduced MMOR was mixed rapidly with oxidized MMOH in a stopped-flow apparatus, and optical changes associated with reductase oxidation were recorded. The reaction proceeds via four discrete kinetic phases corresponding to the transfer of four electrons into the two dinuclear iron sites of MMOH. Pre-equilibrating the hydroxylase with sMMO auxiliary proteins MMOB or MMOD severely diminishes electron transfer throughput from MMOR, primarily by shifting the bulk of electron transfer to the slowest pathway. The biphasic reactions for electron transfer to MMOH from several MMOR ferredoxin analogs are also inhibited by MMOB. These results contrast sharply with the previous finding that MMOB enhances interprotein electron transfer when pre-formed MMOR–MMOH–MMOB complexes are reacted with NADH. To account for the extremely slow electron transfer rates observed for the ternary pre-complex in this work, a model in which conformational changes imparted to the hydroxylase by MMOR are retained throughout the catalytic cycle is proposed. Several electron transfer schemes are discussed with emphasis on those that invoke multiple interconverting MMOH populations. Applying electron transfer theory expressions to the temperature dependence of electron transfer rate constants provides an estimate of 11 Å for the distance between the reductase [2Fe-2S] and hydroxylase diiron centers in the MMOH–MMOR complex.

Chapter 5. Domain Engineering of the Reductase Component of Soluble Methane Monooxygenase from *Methylococcus capsulatus* (Bath)

Upon separation of the soluble methane monooxygenase reductase (MMOR) ferredoxin (MMOR-Fd, MMOR residues 1-98) and FAD/NADH (MMOR-FAD, MMOR residues 99-348) domains, nearly all biochemical properties of full-length MMOR are retained, except for interdomain electron transfer rates. In order to investigate the extent to which rapid electron transfer between domains might be restored and further to explore the modularity of MMOR, the MMOR-Fd and MMOR-FAD proteins were connected in a non-native fashion. Four different linker sequences were employed to create reversed-domains MMOR (MMOR-RD) constructs, MMOR(99-342)–linker–MMOR(2-98), with a domain connectivity observed in other homologous oxidoreductases. The optical, redox, and electron transfer properties of the four MMOR-RD proteins were characterized and compared to those of wild-type MMOR. The linker sequence plays a key role in controlling solvent accessibility to the FAD cofactor, as evidenced by perturbed flavin optical spectra, decreased FAD_{ox}/FAD_{sq} redox potentials, and increased steady-state oxidase activities in three of the constructs. Stopped-flow optical spectroscopy revealed slow interdomain electron transfer ($k < 0.04 \text{ s}^{-1}$ at 4 °C, compared to 90 s^{-1} for wild-type MMOR) for all three MMOR-RD proteins with 7-residue linkers. A long (14-residue), flexible linker afforded much faster electron transfer between the FAD and [2Fe-2S] cofactors ($k = 0.9 \text{ s}^{-1}$ at 4 °C).

Chapter 6. Expression in *Escherichia coli* of the Hydroxylase Component of Soluble Methane Monooxygenase from *Methylococcus capsulatus* (Bath)

Soluble methane monooxygenase from *Methylococcus capsulatus* (Bath) is a three-component enzyme system that catalyzes the selective conversion of methane to methanol. Reductive activation of dioxygen and substrate oxidation occur at non-heme diiron sites in MMOH, a 251-kDa $\alpha_2\beta_2\gamma$ hydroxylase. Site-directed mutagenesis affords the opportunity to probe specifically the contributions of individual amino acid residues to catalysis or binding, but to employ this method, the protein of interest must be expressed from controllable genes. Several strategies, including stringent regulation of expression, placing all six sMMO genes on the expression vector, and constructing artificial *mmo* operons, were undertaken to facilitate production of active recombinant *M. capsulatus* (Bath) MMOH in *Escherichia coli*. For the first time, all three hydroxylase subunits were expressed in the soluble fraction of *E. coli* hosts, but the subunits did not assemble to produce the native $\alpha_2\beta_2\gamma$ configuration. A second series of expression plasmids yielded a very small quantity of properly folded recombinant MMOH (rMMOH), which was detected by native PAGE Western blot analysis of soluble cell extracts. Attempts to purify this material were hampered by contamination from native MMOH at some stage in the purification procedure. Despite varying many expression conditions, the amounts of soluble, folded rMMOH produced by the *E. coli* systems were not increased substantially. In an effort to find factors required for MMOH folding and assembly, genes flanking the *mmo* operon of *M. capsulatus* (Bath) were identified by examining open reading frames for homology with other known proteins. Of particular note is a GroEL homolog located immediately downstream of the *mmo* operon. Suggestions for developing high-yield heterologous MMOH expression systems are presented.

Thesis Supervisor: Stephen J. Lippard

Title: Arthur Amos Noyes Professor of Chemistry

For my mother,
who taught me to care,
even about the little things.

And for my father,
who pointed me
in the right direction.

Acknowledgments

I must first acknowledge my thesis advisor, Steve Lippard, who provided me a place to hang my hat throughout the years. His enthusiasm for science, dedication to excellence, and attention to detail have served as valuable models. I thank Steve especially for the great scientific freedom he gave me to pursue not just individual experiments but entire projects that I found interesting.

When preparing to write this section, I discovered that I have overlapped with no fewer than seventy-four people in the Lippard lab during my tenure at MIT – not including undergrads. More remarkable than the length of this list is the high caliber of scientific talent and genuine kindness of the group; I could not have asked for better coworkers. In particular, George Gassner taught me many biochemical and analytical techniques, answered my endless questions, and offered a constant source of encouragement. From Dave Coufal, in whose footsteps I followed, I learned the tricks of the cloning trade. The other past and present members of the MMO subgroup have offered camaraderie both inside and outside the lab. Included in this group are fellow graduate students Ann Valentine, Doug Whittington, Dan Kopp, Matt Sazinsky, Joey Bautista, Lisa Chatwood, and Leslie Murray and postdocs Hans Brandstetter, Shannon Stahl, Maarten Merckx, Jens Müller, Edna Ambundo, Elisabeth Cadieux, and Laurance Beauvais.

In my early days, platinum subgroup members Deborah Zamble, Karen Sandman, Uta-Maria Ohndorf, and Qing He offered lots of helpful advice, and undergraduates Carisa Leise and Christina Eng provided good company in the bio bay. In addition to the folks listed above, I have enjoyed the friendship of Dirk Burdinski, Krista Kneip, Min Wei, Amanda Yarnell, Dong Wang, and, last but not least, Yongwon Jung. I apologize for leaving so many people unnamed and so many deeds uncited; there is simply not enough room here for a complete enumeration. Suffice it to say that the collective group made the lab an interesting and fun place to work.

Before I came to MIT, Carol Beale at Athens High School provided my first formal instruction in chemistry and advocated high standards that have served me well ever since. I made my first foray into bioinorganic chemistry during two summers in Jim Penner-Hahn's lab at the University of Michigan. Jim's unwavering support and enthusiastic recommendation encouraged me to aim high and opened many doors for me in the following years. I also thank the members of the Penner-Hahn lab who showed me the ropes of academic science and made my time there so enjoyable.

Finally, I am grateful to my family for all of their support (and for putting up with me) throughout the years. My parents, in particular, deserve credit for expecting excellence, encouraging me to work hard, and helping me achieve my goals. To my sister Laura, yes, I did manage to graduate before 2010! And to my little sister Katie, thanks for all the fish!

Table of Contents

Abstract.....	3
Dedication.....	7
Acknowledgments.....	8
Table of Contents.....	9
List of Tables.....	16
List of Schemes.....	17
List of Figures.....	18
Chapter 1. Introduction: Electron Transfer in Biological Systems.....	22
Introduction.....	23
Electron Transfer Components.....	23
Redox Centers in Biology.....	23
Classes of Electron Transfer Proteins.....	25
Biological Electron Transfer.....	28
ET Theory.....	28
Kinetic Complexity of Interprotein ET Reactions.....	30
Regulation of Electron Transfer.....	32
Thesis Overview.....	34
References.....	35
Chapter 2. Expression and Site-Directed Mutagenesis of the Reductase Component of Soluble Methane Monooxygenase from <i>Methylococcus capsulatus</i> (Bath).....	42
Introduction.....	43
Materials and Methods.....	45
MMOH Purification.....	45
Native MMOR Purification.....	47
MMOB Expression and Purification.....	48
Construction of MMOR Expression Vectors.....	49
Expression and Purification of Recombinant MMOR.....	51

General Characterization.....	52
Mass Spectrometric Analysis	53
Total Amino Acid Analysis.....	53
EPR Spectroscopy	53
Steady-State sMMO Activity Assays.....	54
Construction of Site-Directed MMOR Mutants.....	54
Expression and Purification of MMOR Mutants.....	55
Stopped-Flow Studies of MMOR Mutant Reaction with NADH	56
Isothermal Titration Calorimetry.....	56
Results.....	57
Correction of <i>mmoC</i> Sequence in Expression Plasmids	57
Characterization of Recombinant MMOR	58
Preparation of MMOR Mutants.....	58
Steady-State sMMO Activity for MMOR Mutants.....	59
Kinetics of MMOR Mutant Reduction by NADH.....	60
Measurement of the MMOH–MMOR(E73A) Binding Constant	61
Discussion.....	62
Recombinant MMOR.....	62
Activity of MMOR Mutants	64
Involvement of Glu73 in MMOH–MMOR Interaction	66
Insights from NMR Spectroscopy.....	67
Evaluation of MMOH–MMOR Docking Model.....	68
Conclusions	69
Acknowledgment.....	70
References.....	71

Chapter 3. Expression and Characterization of Ferredoxin and Flavin Adenine

Dinucleotide-Binding Domains of the Reductase Component of Soluble

Methane Monooxygenase from *Methylococcus capsulatus* (Bath).....

Introduction.....	89
Materials and Methods.....	91
General Methods.....	91

MMOR Domain Selection.....	91
MMOR Domain Cloning	91
Expression and Purification of MMOR-Fd	92
Expression and Purification of MMOR-FAD.....	94
Expression and Purification of MMOR.....	94
Mass Spectrometric Analysis	95
EXAFS Spectroscopy.....	95
EPR Spectroscopy.....	96
Determination of FAD _{sq} Optical Spectrum by Evolving Factor Analysis	98
pH Effects on MMOR Domains Optical Spectra	99
Redox Potential Determinations	100
Isothermal Titration Calorimetry.....	103
MMOR-FAD Reaction with NADH	104
Interdomain Electron Transfer Reactions	105
Results.....	105
General Characterization of MMOR Domains	105
Evolving Factor Analysis for MMOR-FAD Component Spectra.....	106
Effect of pH on MMOR Domains Optical Spectra	107
Redox Potentials of MMOR-Fd and MMOR-FAD	107
Measurement of the MMOR-FAD _{ox} -NAD ⁺ Binding Constant	110
Kinetics of MMOR-FAD Reduction by NADH.....	110
Effect of pH on the Reaction of MMOR-FAD with NADH.....	112
Interdomain Electron Transfer Reactions	113
Discussion.....	114
Recombinant MMOR Domains.....	114
Redox Potentials of MMOR-Fd and MMOR-FAD	115
Reaction of MMOR-FAD with NADH.....	115
Influence of pH on MMOR-FAD Spectral, Redox, and Kinetic Properties.....	117
Interdomain Electron Transfer.....	121
Conclusions.....	122
Acknowledgment.....	123
References.....	124

Chapter 4. Intermolecular Electron Transfer Reactions in Soluble Methane

Methane Monooxygenase from <i>Methylococcus capsulatus</i> (Bath): A Role for Hysteresis in Protein Function	143
Introduction.....	144
Materials and Methods.....	147
Protein Purification.....	147
Construction and Purification of MMOR-Fd(1-120+tail) Fragment.....	148
Isothermal Titration Calorimetry.....	148
Kinetic Measurements of Intermolecular Electron Transfer	149
Results.....	150
MMOR Domain Separation.....	150
Measurement of MMOH–MMOR-Fd(1-98) Binding Affinity	151
Protein Concentration Dependence of Intermolecular Electron Transfer.....	151
Intermolecular ET from Ferredoxin Analogs to MMOH.....	152
Effect of MMOB on Intermolecular ET from Ferredoxins	153
Intermolecular ET from MMOR _{3e-} to MMOH	155
Effects of MMOB and MMOD on ET from MMOR _{3e-} to MMOH	156
Discussion.....	157
MMOH–MMOR-Fd and MMOH–MMOR Binding Interactions	157
Formation of Electron Transfer Complexes.....	159
Modeling Intermolecular ET in the sMMO System	160
Interconversion of Rapid and Slow Electron Transfer Pathways.....	162
Hysteresis in Intermolecular ET Reactions	167
MMOR Ferredoxins as Models for Intermolecular ET	169
Application of ET Theory to Intermolecular ET in sMMO.....	170
Concluding Remarks	172
Acknowledgment.....	173
References.....	174
Chapter 5. Domain Engineering of the Reductase Component of Soluble Methane Monooxygenase from <i>Methylococcus capsulatus</i> (Bath)	202
Introduction.....	203

Materials and Methods.....	205
MMOR Reversed-Domains Construct Design.....	205
Cloning of MMOR-RD Expression Plasmids.....	206
pTrc-Fd1 and pTrc-Fd2 Construction.....	206
Construction of pTrc-RD1m, pTrc-RD2m, pTrc-RD3m, and pTrc-RD4	207
Site-Directed Mutagenesis to Yield pTrc-RD1, pTrc-RD2, and pTrc-RD3.....	209
Construction of pRED-RD1, pRED-RD2, pRED-RD3, and pRED-RD4	209
Expression Trials for MMOR-RD Proteins.....	210
Expression and Purification of MMOR-RD Proteins	211
Purification of MMOH, MMOB, and MMOR.....	212
Basic Characterization of MMOR-RD Constructs	212
Optical Spectra of MMOR-RD Proteins	213
Relative Redox Potential Determinations	213
Absolute Redox Potential Determinations.....	214
Steady-State Dye Reduction Activity Assays	215
Steady-State sMMO Activity Assays.....	216
MMOR-RD Reactions with NADH	216
Results.....	217
Expression of MMOR-RD Constructs	217
Initial Characterization of MMOR-RD Constructs.....	218
MMOR-RD Optical Spectra.....	218
Redox Potentials of MMOR-RD Proteins.....	219
Steady-State Diaphorase Activity	219
Steady-State sMMO Activity.....	220
Kinetics of MMOR-RD Reduction with NADH	220
Discussion.....	221
MMOR-RD Constructs	221
MMOR-RD Redox Potentials	222
Steady-State MMOR-RD Activity	223
Reaction of MMOR-RD Constructs with NADH	224
Conclusions.....	227
Acknowledgment.....	227

References.....	228
Chapter 6. Expression in <i>Escherichia coli</i> of the Hydroxylase Component of Soluble Methane Monooxygenase from <i>Methylococcus capsulatus</i> (Bath)	248
Introduction.....	249
Materials and Methods.....	252
sMMO Purification and Characterization.....	252
Plasmid Construction	253
pJLB001 for DNA Sequencing.....	253
Site-Directed Mutagenesis of pJLB001 to “Correct” <i>mmoZ</i> Sequence.....	253
Series I Vectors for MMOH Expression.....	254
Series II Vectors for MMOH Expression	255
DNA Sequencing of the <i>mmo</i> Operon	259
Protein Characterization.....	259
MMOH Expression in <i>E. coli</i> Hosts: Series I Plasmids.....	260
MMOH Expression in <i>E. coli</i> Hosts: Series II Plasmids.....	262
Expression from pJLB400.....	263
Coexpression with pRED.....	264
Expression from pJLB300.....	265
Purification of Recombinant MMOH.....	266
MMOH from JM105/pJLB201.....	266
MMOH from BL21(DE3)/pJLB300	266
Assays for Recombinant MMOH Activity.....	268
Search for Open Reading Frames Surrounding the <i>mmo</i> Operon	270
Results.....	271
Corrections to the <i>M. capsulatus</i> (Bath) sMMO Gene Sequences	271
Series I Expression Vectors.....	272
Expression of sMMO Proteins in <i>E. coli</i>	272
Purification of rMMOH from JM105/pJLB201	274
Assays for rMMOH Activity	275
Series II Expression Vectors	276
Expression of sMMO Proteins in <i>E. coli</i>	276

Purification of rMMOH from BL21(DE3)/pJLB300	277
Gas Chromatographic Assays for rMMOH Activity.....	278
Mock Purification of rMMOH from BL21(DE3)/pMMB277	278
Identification of Genes Flanking the <i>mmo</i> Operon of <i>M. capsulatus</i> (Bath)	279
Discussion.....	280
Corrections to the <i>M. capsulatus</i> (Bath) sMMO Gene Sequences.....	280
MMOH Expression in Heterologous Hosts	281
Homologous Expression of MMOH in <i>M. trichosporium</i> OB3b.....	283
Future Directions.....	284
Acknowledgment.....	285
References.....	286
Biographical Note	311
Curriculum Vitae	312

List of Tables

Table 2.1	Primers for Site-Directed Mutagenesis of MMOR.....	75
Table 2.2	Properties of Native and Recombinant MMOR.....	76
Table 2.3	sMMO Steady-State Propylene Reaction Parameters for MMOR Mutants.....	77
Table 2.4	Thermodynamic Parameters for MMOH–MMOR(E73A) Binding.....	78
Table 3.1	Properties of MMOR-Fd, MMOR-FAD, and MMOR.....	128
Table 4.1	Thermodynamic Parameters for MMOH–MMOR-Fd and MMOH–MMOR Interactions	178
Table 4.2	Intermolecular Electron Transfer Rate Constants for MMOR-Fd and MMOR.....	179
Table 4.3	Activation Energies for Intermolecular Electron Transfer.....	180
Table 4.4	Electron Transfer Parameters Determined from the Temperature Dependence of ET Rate Constants	181
Table 4.5	Effect of MMOB on Intermolecular Electron Transfer from MMOR Ferredoxin Analogs to MMOH	182
Table 4.6	Distribution of Electrons in Intermolecular Electron Transfer Intermediates	183
Table 5.1	Primary Sequences for Reversed-Domains MMOR Constructs.....	231
Table 5.2	Primers for Site-Directed Mutagenesis of MMOR-RD Sequences	232
Table 5.3	Properties of MMOR and MMOR-RD Constructs.....	233
Table 5.4	Relative Redox Potentials for MMOR-RD Constructs.....	234
Table 5.5	Absolute Redox Potentials for MMOR-RD Constructs.....	235
Table 5.6	Steady-State Activities for MMOR-RD Proteins.....	236
Table 5.7	Rate Constants for MMOR-RD Reaction with NADH.....	237
Table 6.1	Descriptions of Plasmids Used for Constructing sMMO Expression Vectors	291
Table 6.2	Open Reading Frames Located Near the <i>M. capsulatus</i> (Bath) <i>mmo</i> Operon	292

List of Schemes

Scheme 2.1	Simplified View of the sMMO Catalytic Cycle	79
Scheme 2.2	MMOR Reaction with NADH	80
Scheme 3.1	FAD Oxidation and Protonation Equilibria.....	129
Scheme 3.2	MMOR-FAD Reaction with NADH	130
Scheme 4.1	Simplified View of the sMMO Catalytic Cycle	184
Scheme 4.2	Possible Mechanisms for Intermolecular Electron Transfer from Reduced MMOR Ferredoxins to Oxidized MMOH.....	185
Scheme 4.3	Possible Mechanisms for Intermolecular Electron Transfer from Three-Electron Reduced MMOR to Oxidized MMOH.....	186
Scheme 4.4	Intermolecular Electron Transfer in the sMMO System: Multiple Populations of MMOH.....	187
Scheme 4.5	Midpoint Potentials for Equilibrated Complexes of sMMO Protein Components	188
Scheme 5.1	Expression Plasmid Construction for MMOR-RD Proteins.....	238
Scheme 5.2	MMOR-RD Reaction with NADH.....	239

List of Figures

Figure 1.1	Quinoprotein cofactors.....	38
Figure 1.2	Redox states of pyridine nucleotides, flavins, and ubiquinone.....	39
Figure 1.3	Active-site structures of iron-sulfur proteins and plastocyanin.....	40
Figure 1.4	Structures of hemes <i>a</i> , <i>b</i> , and <i>c</i>	41
Figure 2.1	Schematic view of the four sMMO protein components.....	81
Figure 2.2	MMOH–MMOR docking model developed by analyzing packing contacts in MMOH crystals.....	82
Figure 2.3	pRED plasmid for recombinant MMOR expression.....	83
Figure 2.4	Mutated MMOR residues mapped onto the MMOR-Fd structure	84
Figure 2.5	MMOR concentration dependence for NADH consumption in steady-state sMMO propylene assays.....	85
Figure 2.6	Comparison of kinetic traces monitored at 625 nm for the reaction of MMOR site-directed mutants with NADH at 4 °C	86
Figure 2.7	Determination of MMOH–MMOR(E73A) binding constants by isothermal titration calorimetry.....	87
Figure 3.1	Examples of alternative connectivities between the one-electron carrier and flavin/NAD(P) binding domains of flavoprotein electron transferases	131
Figure 3.2	Microwave progressive power saturation data for MMOR-FAD _{sq,max} and MMOR _{sq,max} at 100 K.....	132
Figure 3.3	Optical spectra at pH 7.0 of MMOR-Fd and MMOR-FAD in the fully oxidized and fully reduced oxidation states	133
Figure 3.4	Determination of the FAD _{sq} optical spectrum at pH 7.0 by evolving factor analysis of reductive titration data.....	134
Figure 3.5	Effect of pH on the optical spectra of MMOR-FAD in the oxidized, semiquinone, and hydroquinone oxidation states.....	135
Figure 3.6	Difference spectra for the reductive titration of a mixture of MMOR-FAD and phenosafranine by dithionite at pH 7.0.....	136
Figure 3.7	pH dependence of the relative redox potentials of MMOR-FAD	137
Figure 3.8	Determination of the MMOR-FAD _{ox} –NAD ⁺ binding constant by	

	isothermal titration calorimetry.....	138
Figure 3.9	Kinetics of MMOR-FAD reduction with NADH at 4 °C. (A) Raw diode array stopped-flow spectra; (B) Intermediate spectra derived from global analysis of diode array data; (C) Single-wavelength stopped-flow traces recorded at 625 and 725 nm.....	139
Figure 3.10	Dependence of the CT1 formation rate constant on NADH concentration for the reaction of MMOR-FAD with NADH at 4 °C	140
Figure 3.11	Influence of pH on the reaction of MMOR-FAD with NADH at 4 °C. (A) Variation of rate constants with pH; (B) Variation of CT2 intermediate spectrum with pH; (C) Determination of the pK_a value for CT2 optical changes	141
Figure 3.12	Electron transfer from fully reduced MMOR-FAD to (A) oxidized MMOR-Fd at 25 °C or (B) oxidized MMOR-FAD at 4 °C.....	142
Figure 4.1	(A) Examples of alternative connectivities between the one-electron carrier and flavin/NAD(P) binding domains of flavoprotein electron transferases; (B) MMOR proteins examined in Chapter 4.....	189
Figure 4.2	Component spectra determined for the MMOR domain proteins.....	190
Figure 4.3	Determination of the MMOH–MMOR-Fd(1-98) binding constant by isothermal titration calorimetry	191
Figure 4.4	Effect of MMOR-Fd concentration on electron transfer from chemically reduced MMOR-Fd(1-98) to oxidized MMOH at 4 °C.....	192
Figure 4.5	Effect of temperature on intermolecular electron transfer from reduced MMOR-Fd(1-98) to oxidized MMOH	193
Figure 4.6	Spectra of intermediates for the reaction of chemically reduced MMOR-Fd(1-98) with oxidized MMOH in the absence and presence of MMOB	194
Figure 4.7	Time courses for MMOH reduction by MMOR ferredoxin analogs and MMOR at 4 °C: effects of MMOB and MMOD	195
Figure 4.8	Effect of MMOB on electron transfer from reduced MMOR-Fd(1-98) to oxidized MMOH at 4 °C	196
Figure 4.9	(A) Spectra of intermediates for the reaction of $MMOR_{3e^-}$ with oxidized MMOH at 4 °C; (B) Intermediate species compositions	197

Figure 4.10	Effect of temperature on intermolecular electron transfer from MMOR _{3e-} to oxidized MMOH	198
Figure 4.11	(A) Spectra of intermediates for the reaction of MMOR _{3e-} with a pre-equilibrated mixture of oxidized MMOH and two equivalents of MMOB; (B) Intermediate species compositions.....	199
Figure 4.12	(A) Spectra of intermediates for the reaction of MMOR _{3e-} with a pre-equilibrated mixture of oxidized MMOH and two equivalents of MMOD; (B) Intermediate species compositions.....	200
Figure 4.13	Effect of MMOB on electron transfer from MMOR _{3e-} to oxidized MMOH at 4 °C	201
Figure 5.1	Reductase domain arrangement derived from the MMOR gene sequence and homology to members of the flavoprotein electron transferase family	240
Figure 5.2	Component spectra determined for the MMOR domain proteins.....	241
Figure 5.3	Optical spectrum of pure MMOR-RD2 fit with a linear combination of Fd _{ox} and FAD _{ox} component spectra.....	242
Figure 5.4	Calculated MMOR-RD flavin component spectra in the fully oxidized and fully reduced oxidation states	243
Figure 5.5	Difference spectra for the reductive titration of a mixture of MMOR-RD2 and anthraquinone-2-sulfonate by dithionite.....	244
Figure 5.6	MMOR-RD concentration dependence of NADH consumption in steady-state sMMO propylene assays.....	245
Figure 5.7	Kinetics of MMOR-RD reduction with NADH at 4 °C: diode array stopped-flow studies	246
Figure 5.8	Kinetics of MMOR-RD reduction with NADH at 4 °C: single wavelength stopped-flow studies	247
Figure 6.1	Schematic of the <i>mmo</i> operon of <i>M. capsulatus</i> (Bath).....	293
Figure 6.2	Plasmid map for the pJLB001 sequencing vector.....	294
Figure 6.3	Series I expression vectors: pJLB100, pJLB200, pJLB201, and pJLB207.....	295
Figure 6.4	Construction of pJLB300 via pTXY and pTXYZ.....	296
Figure 6.5	Construction of pJLB400 via pTX-Z and pTX-C.....	297

Figure 6.6	SDS-PAGE analysis of protein expression from JM105/pJLB100 for samples collected at regular intervals after induction.....	298
Figure 6.7	Western blot analysis of MMOH produced by three series I expression plasmids: pJLB100, pJLB200, and pJLB201	299
Figure 6.8	SDS-PAGE and native PAGE Western blot analyses of MMOH expressed from pJLB201 with 0.05 mM IPTG.....	300
Figure 6.9	Western blot analysis of MMOH in fractions of JM105/pJLB201 proteins resolved on a Q-Sepharose Fast Flow column	301
Figure 6.10	SDS-PAGE analysis of proteins produced in JM105/pJLB300 and JM105/pJLB400 cells over a period of 5 h.....	302
Figure 6.11	SDS-PAGE and native PAGE Western blot analyses of MMOH expressed from pJLB300 with 0.05 mM IPTG.....	303
Figure 6.12	SDS-PAGE and native PAGE Western blots of BL21(DE3)/pJLB300 proteins resolved on a Sepharose CL-6B column.....	304
Figure 6.13	SDS-PAGE and native PAGE gels and Western blots of crude recombinant MMOH from BL21(DE3)/pJLB300 resolved on a Superdex 200 size-exclusion column.....	305
Figure 6.14	Gas chromatographic traces for detection of propylene oxide in steady-state sMMO propylene assays.....	306
Figure 6.15	Open reading frames located downstream of the <i>M. capsulatus</i> (Bath) <i>mmo</i> operon	307
Figure 6.16	Sequence alignment of GroEL homologs from <i>M. capsulatus</i> (Bath) and <i>M. trichosporium</i> OB3b.....	308
Figure 6.17	Sequence alignment of chaperone proteins from <i>M. capsulatus</i> (Bath) and <i>E. coli</i> K12.	309
Figure 6.18	Comparison of α -subunit protein sequences with the <i>M. capsulatus</i> (Bath) MMOH X-ray crystal structure electron density	310

Chapter 1

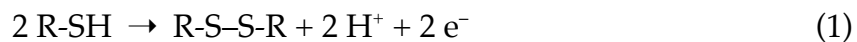
Introduction: Electron Transfer in Biological Systems

Introduction

Electron transfer (ET) reactions are fundamental steps in many biological processes, including respiration, photosynthesis, nitrogen fixation, neurotransmitter metabolism, and the immune response.^{1,2} Aerobic respiration and photosynthesis produce most of the energy required to support life and largely maintain the global carbon, hydrogen, and oxygen cycles. This chapter describes the various redox centers employed for ET in biology, the application of ET theory to physiological electron transfer reactions, and several regulatory mechanisms for achieving rapid and specific biological electron transfer.

Redox Centers in Biology

Oxidation-reduction (redox) centers employed by biological systems fall into three broad categories: protein side chains, small molecules, and inorganic cofactors. Although the redox-active properties of amino acids in proteins have sometimes been overlooked, this class comprises many unique prosthetic groups that effect a wide range of chemical transformations. Cysteine sulfhydryl functionalities are readily oxidized to form a dimer, cystine (eq 1), where R-SH represents the cysteine side chain.



Interconversion between the cysteine and cystine oxidation states occurs in several redox enzymes, including xanthine oxidase, thioredoxin, and mercuric ion reductase.² Electron paramagnetic resonance (EPR) spectroscopy of proteins with specific isotopic labels has identified amino acid radicals localized on tyrosine (class I ribonucleotide reductase (RNR) and photosystem II),^{3,4} tryptophan (cytochrome *c* peroxidase),⁵ cysteine (class II RNR),⁶ and glycine (class III RNR and pyruvate formate lyase)^{7,8} residues. Formation of these transient radical species, which subsequently interact

directly with substrates, usually requires metal cofactors.⁹ Modified tyrosine and tryptophan amino acids, including topaquinone (TPQ), lysine tyrosylquinone (LTQ), tryptophan tryptophylquinone (TTQ), and cysteine tryptophylquinone (CTQ) (Figure 1.1), represent a still-expanding class of biological redox centers.^{10,11} After oxidation of primary amine substrates, electrons are transferred from the reduced quinone cofactor to dioxygen or other exogenous acceptors to complete the catalytic cycle.

Three types of small organic molecules, pyridine nucleotides, flavins, and quinones, function as carriers of reducing equivalents in cells. Nicotinamide adenine dinucleotide (NAD⁺, Figure 1.2A) and flavin adenine dinucleotide (FAD, Figure 1.2B) transmit electrons derived from the oxidation of fuel molecules to the terminal electron acceptor in energy-generating processes. In reductive biosynthesis, the reduced form of nicotinamide adenine dinucleotide phosphate (NADPH) is the major electron donor. The most common quinone, coenzyme Q or ubiquinone (Figure 1.2C), has a long isoprenoid tail that allows it to diffuse through membranes; this quinone cofactor exists in both free and protein-bound forms.² Flavins and pyrroloquinoline quinone (PQQ, Figure 1.1), which is functionally similar to TPQ, LTQ, TTQ, and CTQ,¹⁰ are usually attached noncovalently to proteins. Whereas the pyridine nucleotides are two-electron carriers, flavins and quinones can be reduced by either one or two electrons. Therefore, these cofactors can facilitate ET between two-electron redox reagents and one-electron carriers (e.g. many metal centers).

The biological functions of metalloproteins include electron transfer, the binding and activation of substrates, and atom- and group-transfer chemistry.¹² Electron-carrying metalloproteins typically employ iron or copper, metals that can be tuned by the surrounding protein environment to access a wide range of biologically relevant redox potentials. For inorganic redox centers, one-electron transfer is generally

avored. Upon electron transfer, metal-ligand bonds are retained in order to minimize structural reorganization. Some complex metalloenzymes such as cytochrome *c* oxidase and nitrogenase contain redox cofactors that shuttle electrons between other metal sites in the same protein.

Classes of Electron Transferases

Electron transfer proteins, or electron transferases, possess several common characteristics.¹³ They must, of course, contain a suitable cofactor for accepting electrons. For intermolecular electron transfer at biologically useful rates, the cofactor must be positioned relatively close to the protein surface. A hydrophobic cavity adjacent to, but not necessarily completely surrounding, the cofactor is a typical feature. Electron transfer is accompanied by only small structural changes at the redox center. Finally, a flexible architecture that permits slight expansion or contraction upon electron transfer is employed. A key feature of electron transferases is their ability to modulate cofactor redox potentials by hydrogen bonding, electrostatic, and other interactions between the polypeptide and the redox center.

There are four classes of electron transferases, which are defined by their redox cofactors: flavoproteins, iron-sulfur proteins, blue copper proteins, and cytochromes.² As their name implies, flavoproteins contain an FAD or flavin mononucleotide (FMN) cofactor (Figure 1.2B), which is bound, in most cases noncovalently, to the protein. Examples include the flavodoxins of bacteria and algae¹⁴ and ferredoxin:NADP⁺ reductase, which produces NADPH during photosynthesis.¹⁵ For free flavins, the formal reduction potential of the second redox couple is higher than the first, such that only the oxidized and two-electron reduced (hydroquinone) species are thermodynamically accessible. In flavoproteins, however, both flavin potentials are

substantially altered by the protein environment, thereby stabilizing the one-electron reduced (semiquinone) oxidation state. Thus, flavoproteins can interact with both one- and two-electron carriers.

Virtually all living organisms utilize iron-sulfur proteins as electron carriers in processes such as oxidative phosphorylation, photosynthesis, and nitrogen fixation.^{2,12} Iron-sulfur clusters comprising varying numbers of iron and sulfide ions are ligated to these proteins via cysteine side chains (Figure 1.3A). The simplest iron-sulfur protein, rubredoxin, has a single iron atom tetrahedrally coordinated by four cysteines. This cofactor cycles between the Fe^{3+} and Fe^{2+} oxidation states with a redox potential between -50 and $+50$ mV. The [2Fe-2S] ferredoxins have $[\text{Fe}_2\text{S}_2(\text{S-Cys})_4]^{2-}$ clusters in which the tetrahedrally coordinated iron atoms are bridged by two sulfide ligands. The biologically relevant redox couple interconverts the $[\text{Fe}_2\text{S}_2]^{2+}$ (two Fe^{3+} ions) and $[\text{Fe}_2\text{S}_2]^+$ (formally one Fe^{2+} ion and one Fe^{3+} ion) forms and exhibits a reduction potential between -280 and -490 mV. In [3Fe-4S] ferredoxins, the three iron and four sulfide ions are arranged at seven corners of a distorted cube with a cysteine ligated to each iron atom. One-electron reduction of the $[\text{Fe}_3\text{S}_4]^+$ cluster occurs with a midpoint potential of ca. -120 mV. The fourth type of iron-sulfur proteins, which contain [4Fe-4S] clusters, is the most common in biological systems. The core cluster contains four iron ions and four sulfides at alternate corners of a distorted cube. Four cysteine thiolates coordinate the iron atoms, anchoring the cube to the protein. Each [4Fe-4S] cofactor uses a single redox couple, but two classes of ferredoxins access different oxidation states. Thus, redox potentials for proteins that use the $[\text{Fe}_4\text{S}_4]^{2+}/[\text{Fe}_4\text{S}_4]^+$ couple range from -650 to -280 mV, whereas ferredoxins operating between the $[\text{Fe}_4\text{S}_4]^{3+}$ and $[\text{Fe}_4\text{S}_4]^{2+}$ states have potentials near $+350$ mV. Taken as a whole, the most

striking feature of iron-sulfur proteins is the wide range of redox potentials (ca. 850 mV) achieved primarily by rearranging iron, sulfide, and cysteine building blocks.

Blue copper proteins are characterized by intense thiolate-to-copper charge-transfer bands near 600 nm. These sites are found in relatively small proteins like azurin (from bacteria) and plastocyanin (from plants), which have a single copper ion, as well as multicopper oxidases that contain four or more copper ions arranged in multiple, distinguishable centers.^{16,17} The copper ion in plastocyanin is coordinated in a distorted tetrahedron by one cysteine, two histidines, and one methionine. The copper site exhibits a quite short Cu-S(Cys) bond (2.1 Å) and a very long Cu-S(Met) bond (2.9 Å), as shown in Figure 1.3B. The structure of azurin from *Alcaligenes denitrificans* is quite similar to that of plastocyanin, but the copper is five-coordinate, with the cysteine and two histidine ligands arranged in a trigonal plane. Long axial bonds to the copper ion (ca. 3 Å) are formed between a methionine sulfur and a backbone amide oxygen.^{18,19} The five-coordinate copper site of azurin gives rise to a significantly lower redox potential (+230 to +280 mV) than that determined for plastocyanin (+360 mV).¹⁹

Cytochromes contain one or more heme cofactors, three types of which are depicted in Figure 1.4. Heme *a*, which has a long phytol tail, is found in cytochrome *c* oxidase, *b*-type cytochromes and globins possess heme *b*, and heme *c* is covalently attached via two thioether linkages to *c*-type cytochromes.² The prosthetic groups are coordinated to cytochromes by one histidine and one methionine or by two histidines. Different cofactor environments yield a very wide range of redox potentials (–350 to +350 mV) for cytochromes. Chlorophylls, the principal photoreceptors in photosynthetic light-harvesting complexes, have Mg²⁺ ions coordinated by cyclic tetrapyrroles similar to those of hemes. In photosynthetic organisms, these cofactors

absorb photons and participate in electron transport chains that generate proton gradients used to generate chemical energy.

Biological Electron Transfer: ET Theory

With the repertoire of biological redox centers outlined above, electron transport over long distances, often $> 10 \text{ \AA}$, can be achieved by arranging redox cofactors in pathways such that ET is thermodynamically favorable. Individual steps may be endergonic, as long as the flux through the pathway is maintained by other exergonic processes.²⁰ Two important conditions must be fulfilled for functional electron transfer in biological systems. First, ET reactions must occur at rates that are metabolically useful. Second, in order to prevent rapid cellular equilibration (and death), electrons must be transferred between specific redox partners. Sequestering redox cofactors within proteins solves the problem of short circuits and affords specificity via molecular recognition in protein–protein complexes.²¹ The dynamics of protein complex formation should yield a complex with a lifetime long enough to allow the electron transfer reaction but not so long that steady-state turnover rates are substantially compromised.

A key distinction between adiabatic chemical reactions which involve making and breaking bonds and nonadiabatic electron transfer reactions is the probability of forming products when the activation energy is reached.¹ For adiabatic processes, this probability is approximately unity, allowing analysis by classical transition state theory. On the other hand, the probability of nonadiabatic reactions occurring when the reactants reach the transition state is much less than unity. Therefore, a modified form of transition state theory is required to describe these reactions (eqs 2 and 3),¹

$$k_{ET} = \frac{4\lambda^2 H_{AB}^2}{h\sqrt{4\pi\lambda RT}} e^{-[\Delta G^\circ + \lambda]^2 / 4\lambda RT} \quad (2)$$

$$k_{ET} = k_0 e^{-\lambda(r-r_0)} e^{-[\Delta G^\circ + \lambda]^2 / 4\lambda RT} \quad (3)$$

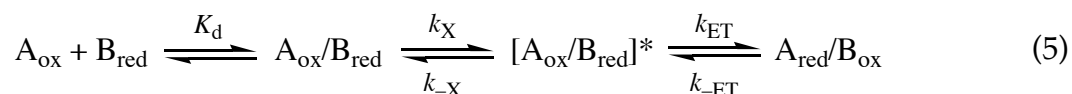
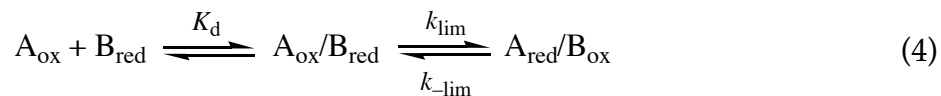
where h is Planck's constant, R is the universal gas constant, and k_0 is the characteristic frequency of the nuclei, generally taken as 10^{13} s^{-1} . At a given temperature (T), the rate of electron transfer between two redox centers (k_{ET}) is controlled primarily by donor-acceptor distance (r), driving force (ΔG°), and reorganizational energy (λ). The activation free energy is given by $(\Delta G^\circ + \lambda)^2 / 4\lambda$, where ΔG° is determined from the difference in redox potentials between the donor and acceptor molecules. The reorganizational energy is defined as the energy required for deforming the nuclear configuration of the reactants to that of the product as well as inducing charge-dependent changes in the surrounding medium. For biological electron transfer, this term includes not only solvent repolarization, but also repolarization of the protein surrounding the redox centers and perhaps even the protein-protein interface.²¹ The degree of nonadiabaticity is described by H_{AB} , the electronic coupling matrix element. Reactions with very little wave function overlap between donor and acceptor sites have small values of H_{AB} ; adiabatic reactions have large H_{AB} values ($> 80 \text{ cm}^{-1}$) and are better treated by transition state theory.²² In eq 3, this probability term is expressed instead in terms of the distance between redox centers ($r - r_0$), where r_0 is the close contact distance (3.0 Å), and λ , which is related to the nature of the intervening medium. For proteins, λ values ranging from 0.7 to 1.4 Å⁻¹ are typically used.^{23,24}

A systematic investigation of optimal intramolecular electron transfer rates suggested that proteins exhibit a nearly uniform electronic barrier to electron tunneling that is well described by a λ value of $1.4 \pm 0.2 \text{ Å}^{-1}$.²³ This value is intermediate between

that determined for electron tunneling through covalent bonds in synthetic systems ($\beta = 0.9 \text{ \AA}^{-1}$)²⁵ and through a vacuum ($\beta = 2.8 \text{ \AA}^{-1}$).²³ Because the interiors of proteins are chemically heterogeneous, it is remarkable that these varied protein matrices present similar environments for electron transfer. One possibility is that the large size of biological redox centers affords multiple competing electron transfer pathways, thereby producing uniform β values.²³ Theoretical approaches that define specific pathways by assigning different β values to electron transfer through covalent bonds, hydrogen bonds, and through-space jumps have also been proposed.^{26,27} This so-called pathways model has been used successfully to describe electron transfer in chemically modified cytochrome *c*.^{28,29} Expansion of the model to group multiple similar pathways into a tube or central path for electron transfer has yielded more accurate descriptions of systems for which the original single pathway model was insufficient.³⁰

Kinetic Complexity of Interprotein Electron Transfer Reactions

Electron transfer between proteins is facilitated by formation of a specific protein–protein complex prior to electron transfer. For a simple kinetic model of intermolecular electron transfer (eq 4), the observed first-order rate constant for



electron transfer is given by k_{lim} . Interprotein redox reactions often include additional adiabatic steps such as conformational rearrangements or proton transfers before electron transfer occurs, necessitating a more complex kinetic model (eq 5). These

preceding steps may influence the observed rate constant for electron transfer, k_{obs} , so this value must be interpreted carefully.

For interprotein electron transfer events that are preceded by a reversible prerequisite non-electron transfer process, three situations are possible.^{24,31} True electron transfer is observed when k_{ET} is the slowest step in the redox reaction, such that $k_{\text{obs}} = k_{\text{ET}}$. Reasonable values for Δ , H_{AB} , and r may be determined when electron transfer is rate-limiting. When the adiabatic step preceding electron transfer is fast but very unfavorable ($K_{\text{x}} = k_{\text{x}}/k_{-\text{x}} \ll 1$), the observed rate constant for electron transfer will be influenced by the equilibrium constant for the non-ET step ($k_{\text{obs}} = k_{\text{ET}}K_{\text{x}}$), resulting in coupled electron transfer. For this type of reaction, Δ will contain contributions for both the preceding adiabatic step and the electron transfer event; H_{AB} may also be an apparent value. Gated electron transfer occurs when the reaction step prior to electron transfer is rate-limiting ($k_{\text{obs}} = k_{\text{x}}$). Analysis by ET theory will yield unreasonably large Δ and H_{AB} values that are unrelated to the electron transfer event and, in some cases, negative values for the donor–acceptor distance.

Applying ET theory to biological electron transfer reactions has been performed primarily by measuring the dependence of reaction rates on ΔG° . Modulation of ΔG° values can be accomplished by covalently attaching ruthenium complexes with varying redox potentials to the surface of a protein of interest and monitoring intramolecular electron transfer between the ruthenium and the native redox center.²² Another methodology involves changing the metal or organic prosthetic groups of redox cofactors to achieve different redox potentials.^{21,23} Finally, site-directed mutagenesis of amino acids near a redox center has been employed to alter ΔG° .^{32,33} The approach of varying ΔG° is not always possible or convenient for interprotein electron transfer systems. If the redox center or the surrounding protein matrix is perturbed by the

modifications to ΔG° , parameters determined by analysis with ET theory will not be valid. Moreover, in many biological electron transfer reactions $-\Delta G^\circ$ is much smaller than λ , so that producing sufficiently large $-\Delta G^\circ$ values may not be feasible.

An alternative experimental approach involves analyzing the temperature dependence of electron transfer rates by ET theory.^{24,31} There are several important caveats for applying this method to interprotein electron transfer. First, ΔG° may vary with temperature. Determining the redox potentials of the proteins at varying temperatures can verify the assumption that ΔG° is constant. Even if ΔG° changes with temperature (or is not precisely known), the effect on most biological electron transfer reactions, in which $-\Delta G^\circ$ is small compared to λ is often not important for determining accurate electron transfer parameters.³¹ A change in the rate-limiting step with temperature could complicate analysis by ET theory. In ideal cases, it might be possible to obtain electron transfer parameters for the ET event and activation parameters for the preceding adiabatic step. Temperature-dependent changes in protein conformation may alter H_{AB} or λ . This effect is minimized by the requirement for performing experiments within a relatively narrow range of temperatures within which the proteins are stable. This method has yielded accurate values for the donor–acceptor distance in several proteins for which structures are known.³⁴⁻³⁶ In addition, the characteristic H_{AB} , λ , and r values obtained when analyzing gated electron transfer reactions by ET theory are useful for proper classification.

Regulation of Biological Electron Transfer

Several mechanisms exist for regulating the rates of electron transfer in biological systems. First, variation of the ΔG° , λ , λ_{reorg} , and r parameters affords control of electron transfer rates over many orders of magnitude. Robust electron transfer in

proteins is maintained by positioning redox cofactors within 14 Å of each other.²⁰ By employing limited donor–acceptor distances, optimal electron transfer rates are far faster than typical catalytic rates. Therefore, ΔG° , κ , and λ can be varied substantially before electron transfer becomes the rate-limiting step in a reaction. Beyond the 14-Å limit, rates of electron transfer are much more susceptible to changes in other ET parameters; therefore, natural selection appears to favor shorter distances between redox centers.

By placing redox cofactors in separate proteins, an exquisite level of control over electron transfer rates can be achieved via complex protein–protein interactions. For example, many monooxygenase and dioxygenase enzyme systems employ separate reductase components.³⁷ Protein conformational changes or rearrangement of proteins within an ET complex may occur prior to electron transfer in order to optimize the positions and geometries of the redox centers.³⁸ In this manner, electron transfer can be closely coupled with enzyme turnover, a feat that would be more difficult if both functions resided in the same protein. In addition, the timing of electron transfer with respect to other steps in the catalytic cycle is controlled by carefully orchestrated changes in properties such as affinity or redox potentials.

In several biological electron transfer systems, a chemical activation step is employed to transform a slow, unfavorable process into a much faster, favorable reaction.³⁹ Chemical gating may represent a common metabolic strategy that allows control of electron transfer rates by the concentration of specific metabolites, effector molecules, or pH. The flux of electrons through such a system may be regulated effectively provided that the ET rates for the unactivated and activated forms are sufficiently different. Thus, this regulatory mechanism can prevent metabolically unnecessary electron transfer when, for instance, a suitable electron acceptor is

unavailable or the reaction products are already present in sufficient concentrations. Further studies will reveal whether chemically gated electron transfer plays an important role in metabolic regulation.

Thesis Overview: ET Reactions in sMMO

Much of this thesis details the exploration of electron transfer reactions involving the reductase component (MMOR) of soluble methane monooxygenase (sMMO) from *Methylococcus capsulatus* (Bath). Site-directed mutagenesis was employed to probe the contributions of surface MMOR residues in binding the sMMO hydroxylase component (MMOH), its physiological redox partner (Chapter 2). Characterization of the individual [2Fe-2S] and FAD/NADH domains of MMOR demonstrated the modular nature of the reductase and facilitated experiments not possible for the full-length protein (Chapter 3). Examination of intermolecular ET reactions between MMOR and MMOH revealed a complex system regulated by protein–protein binding interactions (Chapter 4). Finally, Chapter 5 documents the effect on interdomain ET rates when the MMOR domains are attached in a non-native configuration.

REFERENCES

- (1) Marcus, R. A.; Sutin, N. *Biochim. Biophys. Acta* **1985**, *811*, 265-322.
- (2) Gray, H. B.; Ellis, W. R., Jr. In *Bioinorganic Chemistry*; Bertini, I., Gray, H. B., Lippard, S. J., Valentine, J. S., Eds.; University Science Books: Mill Valley, CA, 1994, pp 315-363.
- (3) Karthein, R.; Dietz, R.; Nastainczyk, W.; Ruf, H. H. *Eur. J. Biochem.* **1988**, *171*, 313-320.
- (4) Barry, B. A.; El-Deeb, M. K.; Sandusky, P. O.; Babcock, G. T. *J. Biol. Chem.* **1990**, *265*, 20139-20143.
- (5) Huyett, J. E.; Doan, P. E.; Gurbiel, R.; Houseman, A. L. P.; Sivaraja, M.; Goodin, D. B.; Hoffman, B. M. *J. Am. Chem. Soc.* **1995**, *117*, 9033-9041.
- (6) Licht, S.; Gerfen, G. J.; Stubbe, J. *Science* **1996**, *271*, 477-481.
- (7) Mulliez, E.; Fontecave, M.; Gaillard, J.; Reichard, P. *J. Biol. Chem.* **1993**, *268*, 2296-2299.
- (8) Unkrig, V.; Neugebauer, F. A.; Knappe, J. *Eur. J. Biochem.* **1989**, *184*, 723-728.
- (9) Stubbe, J.; van der Donk, W. A. *Chem. Rev.* **1998**, *98*, 705-762; 2661.
- (10) Anthony, C. *Biochem. J.* **1996**, *320*, 697-711.
- (11) Klinman, J. P. *Proc. Nat. Acad. Sci. USA* **2001**, *98*, 14766-14768.
- (12) Lippard, S. J.; Berg, J. M. *Principles of Bioinorganic Chemistry*; University Science Books: Mill Valley, CA, 1994.
- (13) Adman, E. T. *Biochim. Biophys. Acta* **1979**, *549*, 107-144.
- (14) Ludwig, M. L.; Luschinsky, C. L. In *Chemistry and Biochemistry of Flavoenzymes*; Müller, F., Ed.; CRC Press: Boca Raton, FL, 1992; Vol. 3, pp 427-466.
- (15) Karplus, P. A.; Bruns, C. M. *J. Bioenerg. Biomembr.* **1994**, *26*, 89-99.

- (16) Chapman, S. K. In *Perspectives in Bioinorganic Chemistry*; Hay, R. W., Dilworth, J. R., Nolan, K. B., Eds.; JAI Press: London, 1991; Vol. 1, pp 95-140.
- (17) Sykes, A. G. *Struct. and Bond.* **1991**, 75, 175-224.
- (18) Norris, G. E.; Anderson, B. F.; Baker, E. N. *J. Am. Chem. Soc.* **1986**, 108, 2784-2785.
- (19) Ainscough, E. W.; Bingham, A. G.; Brodie, A. M.; Ellis, W. R.; Gray, H. B.; Loehr, T. M.; Plowman, J. E.; Norris, G. E.; Baker, E. N. *Biochemistry* **1987**, 26, 71-82.
- (20) Page, C. C.; Moser, C. C.; Chen, X.; Dutton, P. L. *Nature* **1999**, 402, 47-52.
- (21) McLendon, G.; Hake, R. *Chem. Rev.* **1992**, 92, 481-490.
- (22) Winkler, J. R.; Gray, H. B. *Chem. Rev.* **1992**, 92, 369-379.
- (23) Moser, C. C.; Keske, J. M.; Warncke, K.; Farid, R. S.; Dutton, P. L. *Nature* **1992**, 355, 796-802.
- (24) Davidson, V. L. *Acc. Chem. Res.* **2000**, 33, 87-93.
- (25) Smalley, J. F.; Feldberg, S. W.; Chidsey, C. E. D.; Linford, M. R.; Newton, M. D.; Liu, Y.-P. *J. Phys. Chem.* **1995**, 99, 13141-13149.
- (26) Beratan, D. N.; Betts, J. N.; Onuchic, J. N. *Science* **1991**, 252, 1285-1288.
- (27) Onuchic, J. N.; Beratan, D. N.; Winkler, J. R.; Gray, H. B. *Annu. Rev. Biophys. Biomol. Struct.* **1992**, 21, 349-377.
- (28) Wuttke, D. S.; Bjerrum, M. J.; Winkler, J. R.; Gray, H. B. *Science* **1992**, 256, 1007-1009.
- (29) Beratan, D. N.; Onuchic, J. N.; Winkler, J. R.; Gray, H. B. *Science* **1992**, 258, 1740-1741.
- (30) Regan, J. J.; Onuchic, J. N. In *Electron Transfer: From Isolated Molecules to Biomolecules, Part Two*; Jortner, J., Bixon, M., Eds.; John Wiley & Sons, Inc.: New York, 1999; Vol. 107, pp 497-553.
- (31) Davidson, V. L. *Biochemistry* **1996**, 35, 14035-14039.

- (32) Ortega, J. M.; Mathis, P.; Williams, J. C.; Allen, J. P. *Biochemistry* **1996**, *35*, 3354-3361.
- (33) Arlt, T.; Bibikova, M.; Penzkofer, H.; Oesterhelt, D.; Zinth, W. J. *Phys. Chem.* **1996**, *100*, 12060-12065.
- (34) Chen, L.; Durley, R. C. E.; Mathews, F. S.; Davidson, V. L. *Science* **1994**, *264*, 86-90.
- (35) Chiu, H.-J.; Peters, J. W.; Lanzilotta, W. N.; Ryle, M. J.; Seefeldt, L. C.; Howard, J. B.; Rees, D. C. *Biochemistry* **2001**, *40*, 641-650.
- (36) Chabrière, E.; Charon, M.-H.; Volbeda, A.; Pieulle, L.; Hatchikian, E. C.; Fontecilla-Camps, J.-C. *Nat. Struct. Biol.* **1999**, *6*, 182-190.
- (37) Batie, C. J.; Ballou, D. P.; Correll, C. C. In *Chemistry and Biochemistry of Flavoenzymes*; Müller, F., Ed.; CRC Press: Boca Raton, FL, 1992; Vol. III, pp 543-556.
- (38) Hoffman, B. M.; Ratner, M. A. *J. Am. Chem. Soc.* **1987**, *109*, 6237-6243.
- (39) Davidson, V. L. *Biochemistry* **2002**, *41*, 14633-14636.

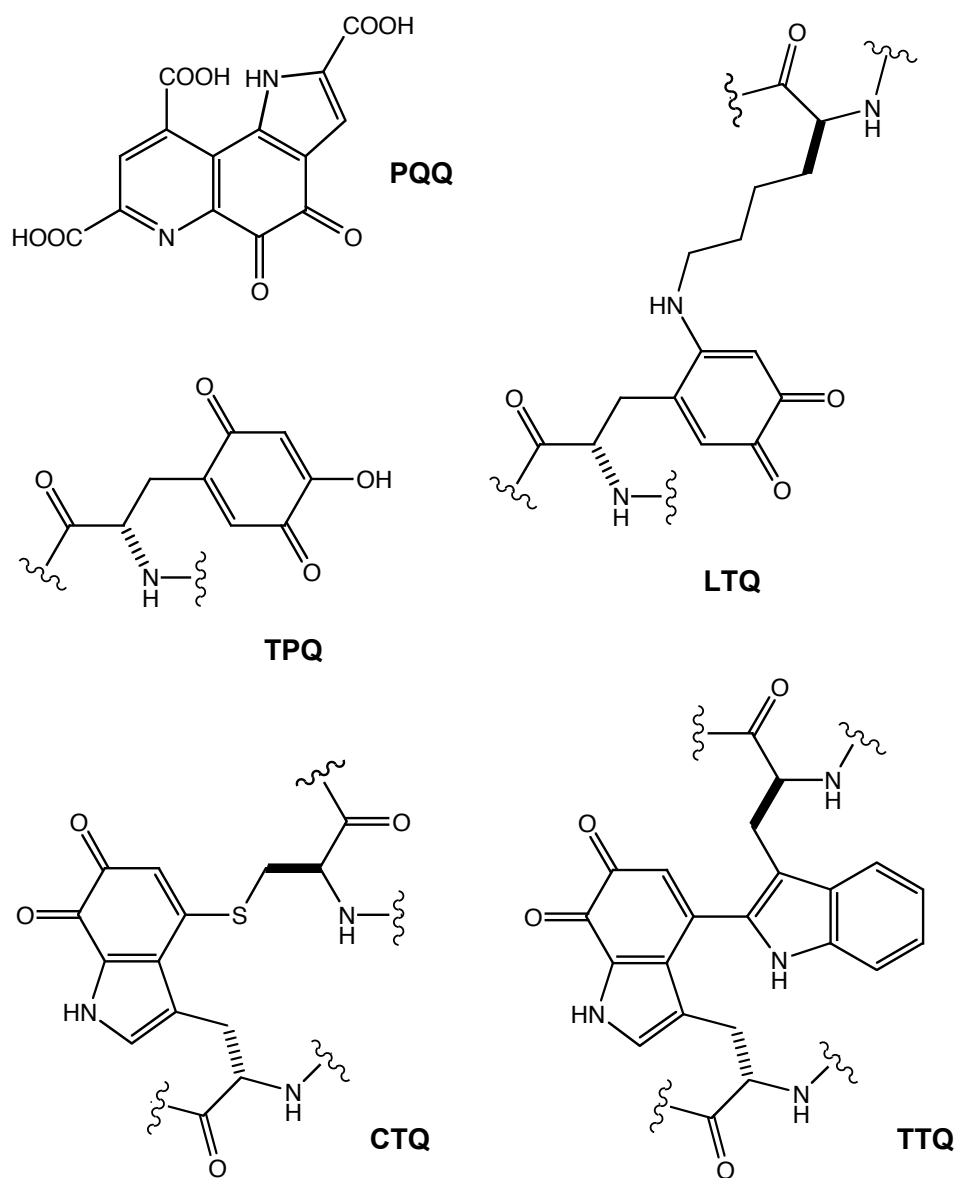


Figure 1.1. Quinoprotein cofactors. PQQ, pyrroloquinoline quinone; TPQ, topaquinone; LTQ, lysine tyrosylquinone; CTQ, cysteine tryptophylquinone; TTQ, tryptophan tryptophylquinone.

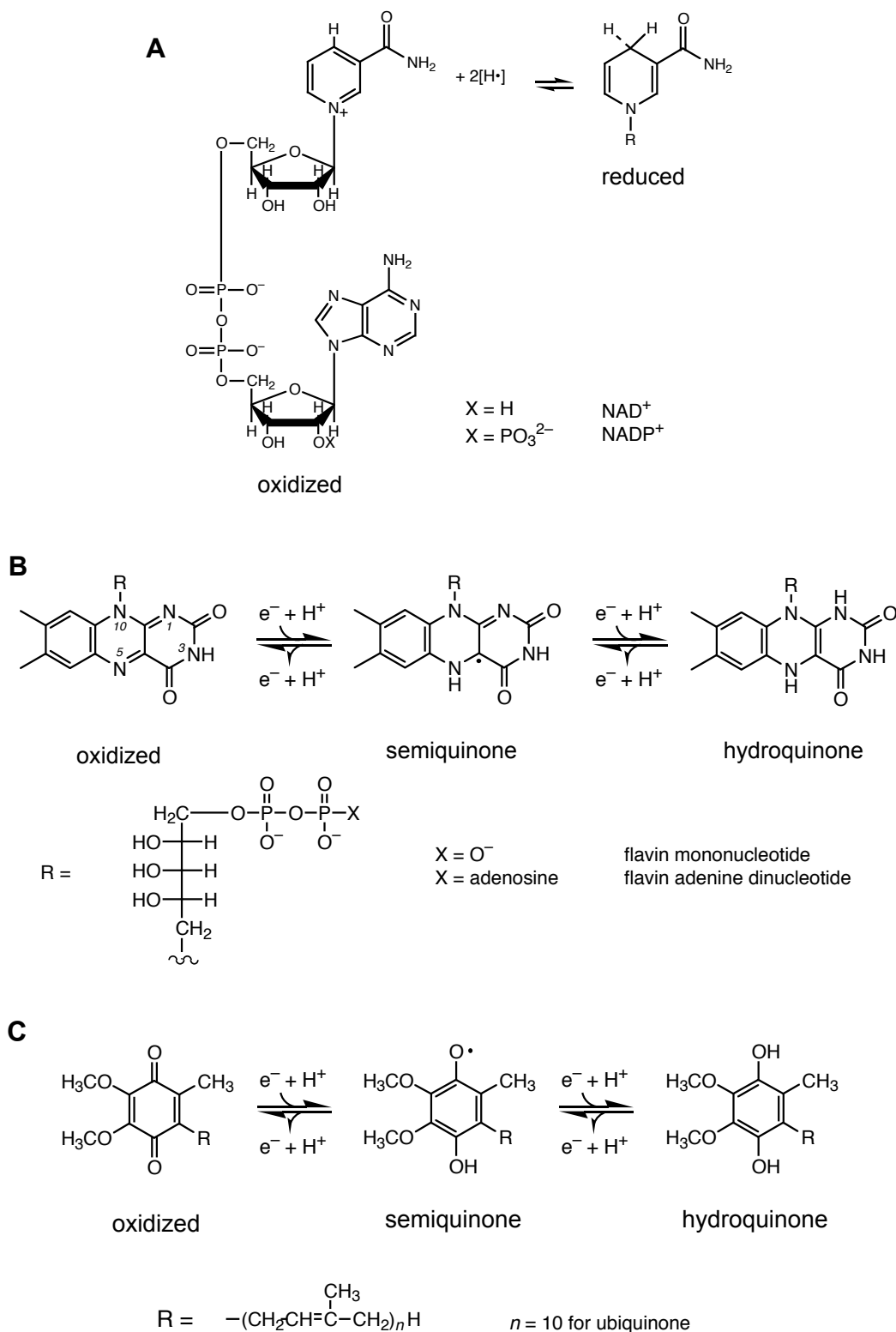


Figure 1.2. Redox states of (A) pyridine nucleotides, (B) flavins, and (C) ubiquinone.

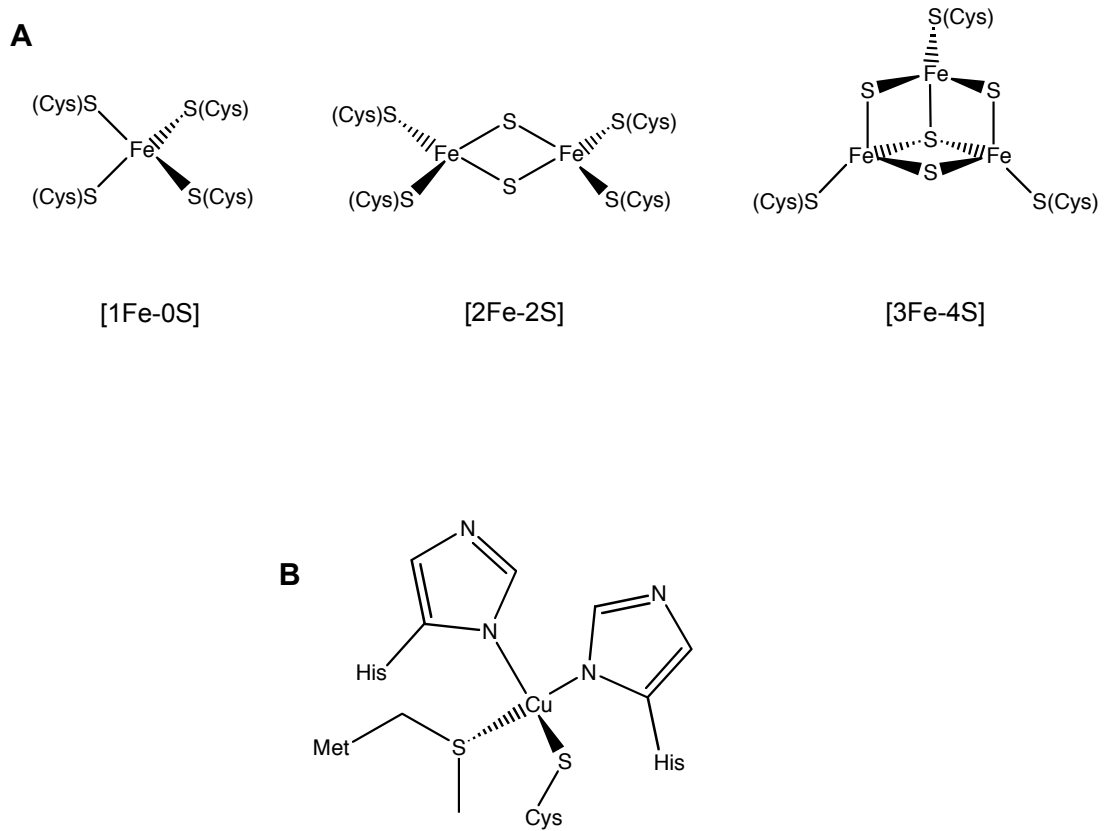


Figure 1.3. Active site structures for (A) iron-sulfur proteins and (B) plastocyanin, a blue copper protein.

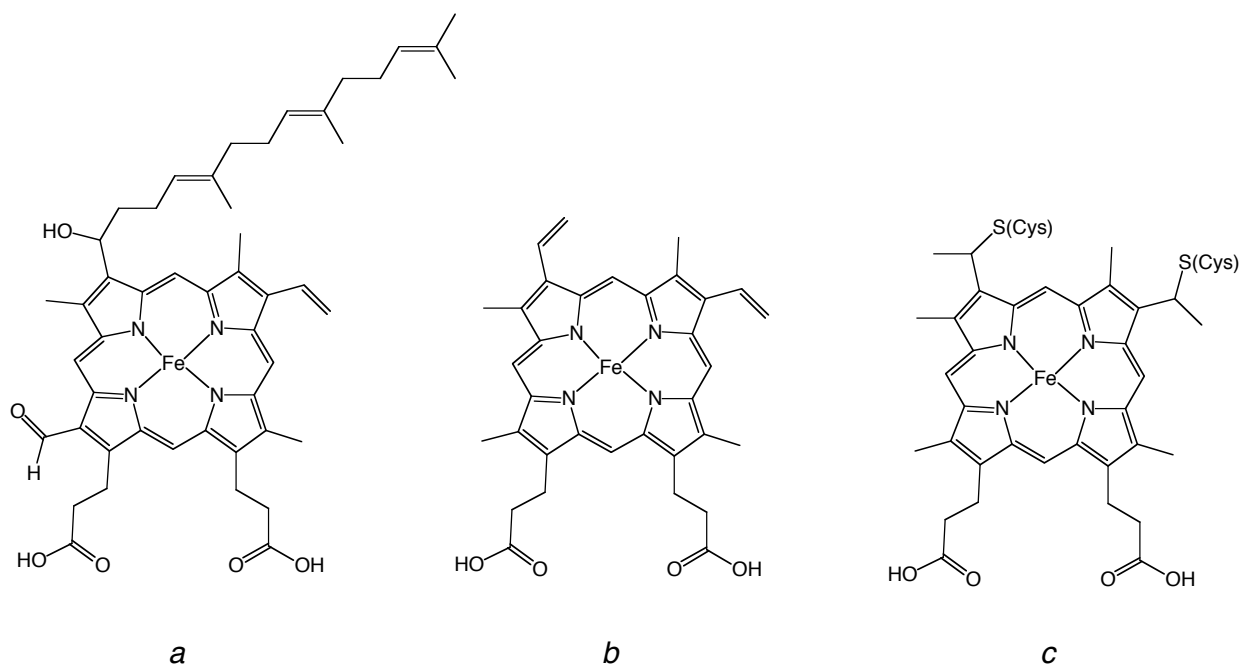


Figure 1.4. Structures of hemes *a*, *b*, and *c*.

Chapter 2

Expression and Site-Directed Mutagenesis of the Reductase Component of Soluble Methane Monooxygenase from *Methylococcus capsulatus* (Bath)*

INTRODUCTION

The first step in the primary catabolic pathway of methanotrophic bacteria is the selective oxidation of methane to methanol by methane monooxygenases (MMOs) (eq 1).^{1,2} After this remarkable chemical transformation, methanol dehydrogenase oxidizes



the methanol product to formaldehyde, which is assimilated into cellular biomass or further oxidized to generate reducing equivalents necessary for biosynthesis.³ These organisms play an important role in regulating atmospheric levels of methane, a potent greenhouse gas,⁴ and in environmental bioremediation applications.^{5,6}

Virtually all methanotrophs can produce a membrane-bound, particulate MMO (pMMO),⁷ which contains 4-5 copper atoms associated with two types of active sites.^{8,9} Due largely to difficulties in purification and instability of pMMO, the soluble form of MMO (sMMO), expressed under low copper-to-biomass conditions in a few methanotrophic bacteria,¹⁰ has received considerable attention. The sMMO enzyme systems from *Methylococcus capsulatus* (Bath) and *Methylosinus trichosporium* OB3b have been characterized extensively by a wide range of biochemical and spectroscopic methods.¹¹⁻¹⁶ Both systems comprise three components: a dimeric ($(\alpha\beta)_2$) hydroxylase (MMOH, 251 kDa) containing carboxylate-bridged diiron centers where dioxygen activation and methane hydroxylation occur, a [2Fe-2S]- and FAD-containing reductase (MMOR, 38.5 kDa), and a regulatory protein (MMOB, 15.9 kDa), all of which are required for catalysis (Figure 2.1).^{17,18} In addition, a fourth protein (MMOD, 11.9 kDa) was identified recently in the sMMO from *M. capsulatus* (Bath), although its function has not yet been determined.¹⁹

The sMMO catalytic cycle is illustrated in Scheme 2.1. To prime MMOH for dioxygen activation, two electrons are transferred from NADH through the FAD and

[2Fe-2S] cofactors of MMOR to the hydroxylase active sites housed in the α subunit, yielding the reduced diiron(II) state. In the presence of MMOB, reduced MMOH reacts with O_2 to generate a series of transient intermediate species.²⁰⁻²³ Upon substrate hydroxylation, the MMOH active sites return to the resting diiron(III) oxidation state. Until recently,^{18,24,25} the intra- and intermolecular electron transfer reactions required for catalysis received little attention relative to the dioxygen and methane activation steps of the sMMO reaction.

MMOR has been assigned to a class of modular flavoprotein electron transferases on the basis of function and sequence homology.²⁶⁻²⁸ Members of this protein family include ferredoxin (Fd), ferredoxin:NADP⁺ oxidoreductase (FNR), phthalate dioxygenase reductase (PDR), cytidine diphosphate-6-deoxy- $\Delta^{3,4}$ -glucoseen reductase (E_3), nitrate reductase, cytochrome *b5* reductase, and cytochrome P450 reductase. In addition, other bacterial mono- and dioxygenases, including phenol hydroxylase and alkene monooxygenase, employ similar reductase systems.²⁹⁻³² All of these proteins use flavins to facilitate electron transfer between NAD(P)H, a two-electron redox reagent, and metal centers, which often function as single-electron conduits.

Despite the detailed biochemical characterization of interactions between the sMMO component proteins,^{18,33-36} there is little structural information available about the complexes. By covalently cross-linking *M. trichosporium* OB3b sMMO proteins, the polypeptides involved in component binding were identified.³⁷ At the time the work presented here was begun, the only existing high-resolution structural description of inter-protein interactions was an MMOH–MMOR docking model generated by analyzing packing contacts in MMOH crystals.³⁸ In this model, the [2Fe-2S] domain of MMOR was postulated to bind to a domain of the MMOH α subunit that does not

contain the catalytic diiron core (Figure 2.2). A low-resolution model for the ternary MMOH–MMOB–MMOR complex, in which MMOH undergoes a large structural rearrangement, has also been proposed based on small-angle X-ray scattering studies.³⁹

In recent years, several methods have been employed to investigate complexes of the sMMO proteins. NMR titrations of MMOB and the ferredoxin domain of MMOR (MMOR-Fd)²⁵ revealed specific residues that interact with MMOH.⁴⁰⁻⁴² The binding faces of MMOB and MMOR were clearly delineated in these NMR experiments. A mass spectrometric study of MMOR-Fd covalently cross-linked to MMOH identified two specific cross-links between residues on the non-binding face of MMOR-Fd with the N-terminus of the MMOH α subunit.⁴³ Modifying positively charged surface residues of MMOH inhibited MMOB binding and electron transfer from MMOR.⁴⁴

In the absence of crystal structures of the MMOH–MMOB or MMOH–MMOR complexes, site-directed mutagenesis provides a means of probing the inter-protein contacts necessary for complex formation and catalysis. Here we report a high-yield *Escherichia coli* expression system for MMOR, which was required for making site-specific mutations. This strategy was pursued to investigate the roles of several MMOR residues in promoting MMOH–MMOR interactions. In addition, we evaluate the docking model³⁸ used to select MMOR mutants. This work provides a framework for learning how individual MMOR residues might facilitate the binding and transfer of electrons to the hydroxylase.

MATERIALS AND METHODS

Purification of MMOH from *M. capsulatus* (Bath). The sMMO hydroxylase protein was purified from *M. capsulatus* (Bath) cells by following a published protocol

with minor modifications.¹⁸ Frozen *M. capsulatus* (Bath) cell paste (70-100 g) was thawed on ice in a large stainless steel beaker and suspended in about 125 mL of cold cracking buffer [25 mM 3-[*N*-morpholino]-propanesulfonic acid (MOPS; pH 7.0), 200 μ M Fe(NH₄)₂(SO₄)₂·6H₂O, 8 mM sodium thioglycolate (NaTG), 2 mM cysteine, and 5 mM MgCl₂] containing DNase (1.5 units/mL) and Pefabloc SC (Roche Molecular Biochemicals, Indianapolis, IN). The cell suspension was sonicated on ice at 40% maximum output (Branson Sonifier Model 450 equipped with a 3/4-inch horn) with three 5-min pulses, which were separated by 5 min to prevent overheating. To prevent proteolysis during sonication, additional Pefabloc SC (ca. 10 mg) was added after the second pulse. The lysed cells were centrifuged at 98,000g for 30 min in order to separate the soluble and insoluble materials. The supernatant was transferred to clean ultracentrifuge tubes, which were spun again for 30 min. The soluble portion was decanted immediately and filtered through 0.45 μ m membranes then through 0.2 μ m membranes.

The soluble cell extract (ca. 150 mL) was loaded onto a DEAE Sepharose Fast Flow (Amersham Pharmacia Biotech, Piscataway, NJ) column (5.0 cm \times 30 cm) equilibrated with buffer A [25 mM MOPS (pH 7.0), 200 μ M Fe(NH₄)₂(SO₄)₂·6H₂O, 8 mM NaTG, and 2 mM cysteine]. Proteins were eluted with a 4.3-L linear gradient from buffer A to buffer B [buffer A plus 400 mM NaCl]. Under these conditions, MMOH and MMOR eluted around 130 and 350 mM NaCl, respectively. MMOH fractions were identified by sodium dodecyl sulfate-polyacrylamide gel electrophoresis (SDS-PAGE), pooled in two batches, and concentrated by ultrafiltration. To obtain pure MMOH, small quantities (35-60 mg) of this crude MMOH solution were resolved with a Superdex 200 (Amersham Pharmacia) size-exclusion column (2.6 cm \times 80 cm) equilibrated in 25 mM MOPS (pH 7.0), 120 mM NaCl, 1 mM 1,4-dithiothreitol (DTT),

and 5% glycerol. Alternatively, crude MMOH (500-800 mg) was purified further with a Sephacryl S300 (Amersham Pharmacia) size-exclusion column (5.0 cm \times 95 cm). Fractions containing MMOH were pooled based on purity as determined by SDS-PAGE then drop-frozen in liquid nitrogen and stored at -80 °C. The iron content of pure hydroxylase was determined with a standard ferrozine iron assay.^{45,46} Typical preparations yielded 10-12 mg of pure MMOH ($\epsilon_{280} = 665,000 \text{ M}^{-1} \text{ cm}^{-1}$) per gram of *M. capsulatus* (Bath) cell paste. The pure hydroxylase contained 3.9-4.0 mol Fe per mol protein; specific activity for the conversion of propylene to propylene oxide at 45 °C was 250-300 nmol min⁻¹ mg⁻¹ MMOH.

Purification of MMOR from *M. capsulatus* (Bath). The MMOR fractions from the DEAE Fast Flow column were identified by SDS-PAGE and 2,6-dichlorophenolindophenol (DCPIP; Sigma, St. Louis, MO) activity assays and then pooled and concentrated by ultrafiltration. To reduce the salt concentration, the crude MMOR solution was diluted 8-fold with 25 mM MOPS (pH 7.0), 8 mM NaTG before loading onto a DEAE Sepharose CL-6B (Amersham Pharmacia) column (2.6 cm \times 15 cm) equilibrated with buffer A [20 mM Tris (pH 7.0), 8 mM NaTG, and 50 mM NaCl]. Proteins were resolved with a 630-mL linear gradient from 85% buffer A (117 mM NaCl solution) to buffer B [20 mM Tris (pH 7.0), 8 mM NaTG, and 500 mM NaCl]. Fractions containing MMOR were pooled based on their optical spectra in the 320-650 nm region, concentrated to 10 mL, and diluted to 80 mL with NaCl-free buffer to reduce the salt concentration. This solution was loaded onto a Sepharose 5'-AMP (Sigma) column (2.6 cm \times 10 cm) equilibrated with buffer A. The column was washed with 20 mM Tris (pH 7.0), 8 mM NaTG containing 95 mM NaCl (55 mL), 410 mM NaCl (40 mL), and then 50 mM NaCl (120 mL) to remove protein contaminants. The reductase was eluted with buffer B containing 1 mM NADH. Fractions were pooled

according to their A_{280} values, concentrated to ca. 2 mL by ultrafiltration over a YM3 membrane, and exchanged into 20 mM Tris (pH 7.0), 8 mM NaTG with a Biogel P6 desalting column (Bio-Rad, Hercules, CA). The concentration and yield were determined from A_{458} measurements ($\epsilon_{458} = 20,800 \text{ M}^{-1} \text{ cm}^{-1}$), and the protein was drop-frozen in liquid nitrogen. By SDS-PAGE analysis of the pure MMOR, a high-molecular weight contaminant was identified. To remove this protein, the reductase was run over a Superdex 200 size-exclusion column, as described above for MMOH. Iron content of the pure MMOR protein was analyzed with a ferrozine assay.

Expression and Purification of MMOB. A 50-mL Luria-Bertani medium (LB)-ampicillin (Ap, 100 $\mu\text{g}/\text{mL}$) solution was inoculated with *Escherichia coli* JM105/pWWB \square cells from a frozen stock.⁴⁷ The flask was transferred to a 37 °C incubator set to rotate at 200 rpm for overnight growth. Six 1-L quantities of LB-Ap (100 $\mu\text{g}/\text{mL}$) medium were inoculated with 5-mL aliquots of the saturated JM105/pWWB \square culture and transferred to a 37 °C incubator (200 rpm). When the OD_{600} of the cultures reached ca. 0.7, MMOB expression was induced by adding isopropyl \square -D-thiogalactopyranoside (IPTG) to a final concentration of 1.0 mM. Two hours after induction was started, cells from the JM105 cultures were collected by centrifugation for 10 min at 2700g. The cell pellets were drained briefly then transferred to ice and suspended in 100 mL of cracking buffer [25 mM MOPS (pH 7.0), 8 mM NaTG, and 5 mM MgCl_2] containing DNase (1.5 units/mL), 1 mM Pefabloc SC, and 1 mM phenylmethylsulfonyl fluoride (PMSF). The cells were sonicated on ice with three 2-min pulses at 40% maximum output (Branson Sonifier Model 450 equipped with a 3/4-inch horn), allowing for adequate sample cooling between pulses. The soluble cell extract was separated from insoluble material by centrifugation for 40 min at 98,000g, then filtered through 0.2 μm membranes.

The filtered cell extract was loaded onto a Q-Sepharose (Amersham Pharmacia) column (2.6 cm \times 12 cm) equilibrated with buffer A [25 mM MOPS (pH 7.0), 1 mM DTT, and 150 mM NaCl]. A 2-L gradient from buffer A to buffer B [25 mM MOPS (pH 7.0), 1 mM DTT, and 350 mM NaCl] was performed. Fractions containing MMOB were identified by SDS-PAGE analysis, pooled, and concentrated by ultrafiltration over a YM3 membrane. The concentrated protein was drop-frozen in liquid nitrogen and stored as crude MMOB. A Sephadex G-50 (Amersham Pharmacia) size-exclusion column (2.6 cm \times 85 cm) was equilibrated with buffer A. About half of the crude MMOB solution was thawed and applied to the column with a superloop. Proteins were eluted by washing with buffer A' [buffer A plus 1 mM ethylenediaminetetraacetic acid (EDTA)]. MMOB-containing fractions were identified by SDS-PAGE and pooled; the concentration was determined by UV-visible absorbance measurements ($\epsilon_{280} = 19,300 \text{ M}^{-1} \text{ cm}^{-1}$), and the protein was drop-frozen in liquid nitrogen.

DNA Primer Synthesis and Purification. All of the primers used for cloning and DNA sequencing were designed manually and synthesized on an Applied Biosystems Model 392 DNA/RNA synthesizer. Each primer was purified by polyacrylamide gel electrophoresis on a 12% denaturing polyacrylamide gel, extracted from the gel slices by using a crush and soak method, then precipitated to remove most of the salt added during extraction. The DNA pellets were suspended in appropriate quantities of deionized distilled water and stored at $-20 \text{ }^{\circ}\text{C}$.

Construction of Expression Vectors for MMOR Expression. The *mmoC* gene, which codes for the MMO reductase protein, was amplified from pCH4 by polymerase chain reaction (PCR) using the primers RFE10 (5'-CGGAATTCAACATTAAGGAGGT-AAATTTATGCAGCGAG) and RRH10 (5'-TCACAGTACTTAAGCTTTTCAGGCCGC-CCCGGAC). RFE10 and RRH10 introduced the restriction sites *EcoRI* and *HindIII*,

respectively, into the ends of the resulting 1093-bp amplified gene (boldface font). PCR was performed with *Taq* DNA polymerase (Gibco BRL, Gaithersburg, MD) with the following thermal cycler conditions: 2 min at 96 °C; 1 min at 96 °C, 1 min at 60 °C, and 2 min at 72 °C for 22 cycles, followed by extension for 10 min at 72 °C. The resulting PCR product was digested with the restriction enzymes *Eco*RI and *Hind*III (New England Biolabs, Inc., Beverly, MA) by following the provided instructions. pKK223-3, a relatively high-copy-number expression plasmid with a *tac* promoter (Amersham Pharmacia), was digested with the same enzymes to remove the *Eco*RI–*Hind*III multiple cloning site fragment. The restriction enzymes in both the PCR product and plasmid digests were inactivated by incubation at 65 °C for 20 min. The pKK223-3 digest was treated with alkaline phosphatase (AP; Boehringer Mannheim, Indianapolis, IN) to prevent recircularization in the subsequent ligation reaction. After inactivating the AP by adding 20 mM ethylene glycol-bis[β -aminoethyl ether]-*N,N,N',N'*-tetraacetic acid (EGTA) and heating at 65 °C for 10 min, the DNA was extracted with an equal volume of phenol:chloroform:isoamyl alcohol (25:24:1) and precipitated with ethanol. The AP-treated pKK223-3 digest and *mmoC* PCR digest were ligated by using T4 DNA ligase (New England Biolabs), and the ligation products were transformed into *E. coli* XL1-Blue cells for selection on LB-Ap (94 μ g/mL) plates. By restriction digest analysis of plasmid DNA isolated from minipreps, five positive clones (Figure 2.3A) were identified.

DNA sequencing (MIT Biopolymers Laboratory) of two positive clones, pRED(AP5) and pRED(AP14), revealed point mutations in *mmoC*, which would result in T123I and T6A mutations, respectively, in the expressed MMOR. Site-directed mutagenesis using the QuikChange kit (Stratagene, La Jolla, CA) was performed on pRED(AP14) with the primers 5'-GCAGCGAGTTCACACTATCACGGCGGTG and 5'-

CACCGCCGTGATAGTGTGAACTCGCTGC. Isolation and sequencing of the resulting plasmid, pRED-K2, revealed that it contained the native *mmoC* sequence.

Redesign of *mmoC* Ribosome Binding Site. The sequence AAGGA is one of the most common *E. coli* ribosome binding sites, although much variation exists, and the selection of a Shine-Dalgarno sequence for maximum expression is still not fully understood.⁴⁸⁻⁵⁰ The native *mmoC* gene has a rather unconventional ribosome binding site (RBS), CAGGTA, and a short 5-nucleotide translational spacer between the RBS and start codon of the gene.⁵¹ Although this sequence may function well in the native *M. capsulatus* (Bath), it was altered to the longer Shine-Dalgarno sequence UAAGGAGG, which affords at least threefold better translation in *E. coli* than the consensus sequence AAGGA,⁵² to ensure translational recognition in the foreign host. In addition, the translational spacer (TS) was lengthened to 7 nucleotides, since efficient translation occurs when $5 < \text{TS} < 13$.⁵² Figure 2.3B depicts the changes introduced in this region by the PCR primer RFE10.

Expression and Purification of Recombinant MMOR. The pRED-K2 expression plasmid was transformed into *E. coli* JM105 cells. A 100-mL Terrific Broth (TB)-Ap (100 $\mu\text{g}/\text{mL}$) culture was inoculated with cells from a single colony of JM105/pRED-K2 and grown overnight at 37 °C with 200 rpm shaking. To each of six 1-L quantities of TB-Ap (100 $\mu\text{g}/\text{mL}$) medium were added 10 mL of freshly prepared filter-sterilized 10 mM $\text{Fe}(\text{NH}_4)_2(\text{SO}_4)_2 \cdot 6\text{H}_2\text{O}$ in 100 mM sodium citrate (pH 7.0) and 10 mL of the unsaturated JM105/pRED-K2 starter culture. When the OD_{660} reached 0.6, the cultures were supplemented with 80 μM Fe^{2+} , added as 2 mL of a 40 mM $\text{FeSO}_4 \cdot 7\text{H}_2\text{O}$ solution in 12.5 mM H_2SO_4 per liter of cell culture, and induction of MMOR expression was started by adding IPTG to a final concentration of 1.0 mM. After 3.5 h, the cells were collected by centrifugation and then suspended in 100 mL of

cracking buffer [20 mM Tris (pH 7.0), 8 mM NaTG, 5 mM MgCl₂, and 200 μM Fe(NH₄)₂(SO₄)₂·6H₂O] containing DNase (1.5 units/mL) and 1 mM Pefabloc SC. The cells were sonicated on ice with three well-separated 2-min pulses at 40% maximum output (Branson Sonifier model 450 equipped with a 3/4-inch horn). The soluble cell extract was isolated by centrifugation for 40 min at 98,000g and then filtered through 0.2 μm membranes.

This solution was loaded onto a DEAE Sepharose CL-6B column (2.6 cm × 15 cm) equilibrated with buffer A [20 mM Tris (pH 7.0), 8 mM NaTG, and 50 mM NaCl]. After a 120-mL wash with buffer A, proteins were eluted with a 740-mL linear gradient from buffer A to buffer B [20 mM Tris (pH 7.0), 8 mM NaTG, and 500 mM NaCl]. Under these conditions, MMOR eluted at approximately 350 mM NaCl. Fractions were pooled as crude MMOR based on SDS-PAGE analysis and UV-visible absorbance spectra. The crude protein was concentrated by ultrafiltration over a YM10 membrane and then diluted to a NaCl concentration of ca. 50 mM with 20 mM Tris (pH 7.0), 8 mM NaTG. This material was applied to a Sepharose 5'-AMP column (2.6 cm × 18 cm) equilibrated in buffer A. The column was washed with 20 mM Tris (pH 7.0), 8 mM NaTG containing 95 mM NaCl (70 mL), 410 mM NaCl (50 mL), and then 50 mM NaCl (175 mL) to remove protein contaminants. Elution with buffer B containing 1 mM NADH afforded >95% pure MMOR, as judged by SDS-PAGE. Pure protein was concentrated over a YM10 membrane, exchanged into 20 mM Tris (pH 7.0), 8 mM NaTG with a Biogel P6 desalting column, drop-frozen in liquid nitrogen, and stored at -80 °C.

General Characterization of Recombinant MMOR. UV-visible spectra were obtained with an HP 8452A diode array spectrophotometer. The ferrozine method was used to determine the iron content of recombinant MMOR. FAD determinations were

performed by boiling a sample of MMOR for 3 min, centrifuging for 5 min at 10,000g to pellet the denatured protein, and quantifying FAD in the supernatant ($\epsilon_{450} = 11,300 \text{ M}^{-1} \text{ cm}^{-1}$).

Mass Spectrometric Analysis of Native and Recombinant MMOR. Native and recombinant MMOR were exchanged into distilled deionized water with Quick Spin Sephadex G-50 columns (Boehringer Mannheim). Methanol and acetic acid were added to the desalted MMOR solutions to yield 15 pmol/ μL protein in 50% methanol, 0.1% acetic acid, and the samples were submitted to the MIT Biopolymers Laboratory for analysis by electrospray ionization mass spectrometry (ESI-MS). To remove cofactors that had separated from the reductase peptides during sample preparation, high performance liquid chromatography (HPLC) purification was necessary. The protein components were analyzed with a Sciex model API 365 triple stage mass spectrometer.

Total Amino Acid Analysis of Native and Recombinant MMOR. Samples of native and recombinant MMOR were exchanged into 10 mM potassium phosphate buffer (pH 7.0) with a Biogel P6 desalting column. A sample of each protein (50 μg) and a buffer blank were submitted to the Harvard Medical School Biopolymers Laboratory (Boston, MA) for total amino acid analysis. Each sample was examined in triplicate.

EPR Spectroscopy. Recombinant MMOR in 25 mM potassium phosphate buffer (pH 7.0) was made anaerobic by vacuum gas exchange with O_2 -free N_2 . In an anaerobic chamber, protein, anaerobic buffer, and sodium dithionite were combined to yield a 258 μM MMOR solution containing 1.5 mM dithionite. After equilibration for several minutes, an aliquot of the fully reduced protein, MMOR_{3e-} , was transferred to an EPR tube and frozen in liquid nitrogen. EPR spectra of the MMOR_{3e-} sample were

recorded with a Bruker EMX X-band spectrometer fitted with an Oxford ESR 900 liquid helium cryostat set to 10 K. The power saturation behavior of the sample was examined, and a high-quality spectrum was collected at a power at which the signal was not saturated.

Steady-State sMMO Activity Assays. Reductase concentration-dependence studies were performed for steady-state sMMO propylene assays in order to characterize the binding and electron transfer abilities of recombinant MMOR. In a 1-mL masked cuvette, 1.0 μM MMOH, 1.0 μM MMOB, 0.8 mM propylene, and buffer [25 mM MOPS (pH 7.0) and 1 mM DTT] were mixed. The MMOR concentration was varied from 0 to 3.2 μM ; 13 different concentrations were assayed in duplicate. NADH (0.16 mM) was added to initiate the propylene epoxidation reaction. The contents were mixed thoroughly, and NADH consumption was monitored at 340 nm ($\epsilon_{340} = 6220 \text{ M}^{-1} \text{ cm}^{-1}$) for 110 s. The temperature was held constant at 25 °C with a circulating water bath. The kinetic traces were fit with lines in KaleidaGraph v. 3.0 (Synergy Software, Reading, PA). Plots of activity vs [MMOR] were constructed and fit with a hyperbolic function describing hydroxylase activity added to a line representing MMOR oxidase activity. From the fit parameters, $V_{\text{max,app}}$ and pseudo K_M values were determined and compared to those of native MMOR.

Construction of MMOR Site-Directed Mutants. Seven amino acids, Asp26, Arg43, Glu72, Glu73, Glu74, Glu75, and Glu76, which are all located in the ferredoxin domain of MMOR (Figure 2.4), were selected for mutagenesis based on a proposed MMOH–MMOR docking model (Figure 2.2) and homology to similar ferredoxins and reductases. Site-directed mutagenesis was performed to introduce mutations into the pRED-K2 plasmid by using a QuikChange kit. The primers in Table 2.2 were designed and purified for use in the *Pfu* DNA polymerase-catalyzed PCR mutagenesis reactions.

Subsequent isolation and sequencing (MIT Biopolymers Laboratory) of pRED(D26A), pRED(E74A), and pRED(E75A) showed all three had sequence errors. Upon observing that cells containing the pRED plasmid with an intact *mmoC* gene (no frame-shift deletions) grow rather poorly, clones were selected for this quality before plasmid purification. By using this approach, the mutant plasmids pRED(D26A), pRED(R43A), pRED(E72A), pRED(E73A), pRED(E74A), pRED(E75A), and pRED(E76A) were isolated; DNA sequencing verified the gene sequences contained only the desired mutations.

Expression and Purification of MMOR Mutants. The MMOR mutant proteins were expressed and purified by following the same protocol for wild-type MMOR (MMOR-wt) outlined above. The D26A and R43A mutants purified in this manner were significantly iron-depleted, as determined spectroscopically and by performing iron assays. To avoid cofactor depletion, a shallower gradient was used on the CL-6B column, and CL-6B column fractions were analyzed more rigorously before pooling. Based on spectroscopic observations, iron-depleted MMOR elutes slightly earlier from the CL-6B column than fully complemented reductase. Thus, each MMOR fraction was characterized spectrophotometrically, and plots of relevant absorbance values (A_{332} , A_{458} , and A_{550}/A_{458}) were produced to determine quantitatively appropriate pooling cutoffs. The [2Fe-2S] cluster of MMOR contributes significantly to absorbances at 332 and 550 nm, whereas the peak at 458 nm is due to both the [2Fe-2S] and FAD cofactors. Fractions with low A_{550}/A_{458} or A_{332} values were discarded. Because the D26A mutant was expressed only in low quantities, larger expression volumes (10-12 L) were required to yield adequate amounts of this protein.

Characterization of MMOR Mutants. The iron content of each MMOR mutant was determined with the standard ferrozine assay. Steady-state sMMO assays

(described above) were performed to evaluate the effect of the mutations on sMMO activity, MMOH–MMOR binding, and MMOR oxidase activity. In each set of steady-state assays, wild-type MMOR was included as a control.

Stopped-Flow Analysis of MMOR Mutant Reduction with NADH. To examine whether the MMOR mutations altered intramolecular electron transfer rates in the reductase, a stopped-flow experiment was performed. A Hi-Tech Scientific SF-61 DX2 double-mixing stopped-flow spectrophotometer was configured in single wavelength photomultiplier tube mode. Prior to use, the stopped-flow apparatus was made anaerobic by scrubbing with glucose/glucose oxidase and then washed with anaerobic buffer. Each MMOR sample was exchanged into 25 mM MOPS (pH 7.0), 1 mM DTT and made anaerobic by 12 cycles of vacuum gas exchange with O₂-free N₂. An anaerobic solution of NADH in 25 mM MOPS (pH 7.0), 1 mM DTT was prepared by bubbling nitrogen through the solution. Concentrations of MMOR and NADH were 20 μ M and 200 μ M, respectively, after mixing. The MMOR–NADH reaction was monitored at 458, 625, and 725 nm, and data points (512) were collected in 2-s or 200-s shots on a log time scale. The temperature was maintained at 4 °C with a constant temperature circulating water bath. Five or more shots were collected per wavelength. The experiment was repeated for MMOR-wt, MMOR(D26A), MMOR(E72A), MMOR(E73A), MMOR(E74A), MMOR(E75A), and MMOR(E76A). KinetAsyst 2, v. 2.0 was used to fit each kinetic trace with sums of four or five exponentials.

Isothermal Titration Calorimetry. A VP-ITC isothermal titration calorimeter (MicroCal, Inc., Northampton, MA) was used to measure the binding affinity of the MMOH–MMOR(E73A) complex. All titrations were performed at 25 °C in 25 mM MOPS (pH 7.0), 1 mM DTT. Titrant (371 μ M MMOR(E73A)) was injected in 10- μ L aliquots from a 250- μ L stirred titration syringe into the 1.430-mL sample cell containing

9.76 μM MMOH. Stirring was maintained at 310 rpm throughout the titration. To measure the heat of dilution for MMOR(E73A), the experiment was repeated with buffer in the sample cell. For comparison, data were collected for wild-type MMOR (150-400 μM in the titrating syringe) binding to MMOH (9.5-10.0 μM). Data were integrated and fit with the MicroCal Origin version 5.0 software package.

RESULTS

DNA Sequencing and Correction of *mmoC* in pRED Plasmids. DNA sequencing of *mmoC* in pCH4 revealed a two-base inversion (CAC \rightarrow ACC) in the original published sequence,⁵¹ resulting in a change from V²⁵²WHEP to V²⁵²WTEP in MMOR. A native reductase mass of 38,545.6 Da was obtained by ESI-MS, which is consistent with the sequence change. With the N-terminal methionine intact and the H254T sequence correction, the expected mass is 38,542.6, less than a 0.01% difference from the observed value and within the accuracy range of the mass spectrometer. On the other hand, the published sequence would yield a mass of 38,578.7 Da, a difference of 33 Da (0.09%), which is well outside the expected accuracy of the instrument.

Two of the pRED plasmids constructed by insertion of a *Taq* DNA polymerase-generated *mmoC* gene into pKK223-3 had single point mutations in the coding region. Several attempts at site-directed mutagenesis were required before a pRED expression plasmid with the native *mmoC* sequence was prepared. In order to isolate pRED without base deletions, it was routinely necessary to select colonies that did not grow to saturation in overnight cultures. Thus, there must be a low level of read-through transcription and MMOR production, which appears to interfere with normal *E. coli* growth. Colony selection based on the poor-growth criterion proved highly successful for obtaining *mmoC* sequences without deletions.

Characterization of Recombinant MMOR. MMOR was prepared in good yield from a recombinant expression system. A purification protocol, which includes the DEAE Sepharose CL-6B and Sepharose 5'-AMP columns used in the purification of native MMOR, was developed for recombinant MMOR. The expression conditions were later altered slightly by substituting LB medium for TB medium, which is more expensive and time-consuming to prepare. In addition, 25 mM MOPS (pH 7.0), 1 mM DTT was frequently used in place of 20 mM Tris (pH 7.0), 8 mM NaTG throughout the chromatographic steps. A typical preparation yielded ca. 15 mg of pure MMOR per liter of *E. coli* culture.

Cofactor analysis indicated that recombinant MMOR contained 1.99 ± 0.05 mol Fe and 1.0 ± 0.1 mol FAD per mol of protein, in agreement with literature values (Table 2.2).⁵³ The optical spectra of the native and recombinant proteins were indistinguishable. The EPR spectrum of fully reduced MMOR exhibits a rhombic signal characteristic of a mixed-valent $[2\text{Fe-2S}]^+$ center with g values very similar to those reported for native MMOR.⁵⁴ Molecular weights within experimental error of the calculated values for the apoproteins (N-terminal Met intact and the H254T alteration to the published sequence⁵¹) were obtained by mass spectrometry. Total amino acid analysis of native and recombinant MMOR demonstrated that the proteins contained essentially the same ratio of component amino acids. Substituting recombinant MMOR for native MMOR in sMMO activity assays afforded identical results.

Expression and Purification of MMOR Site-Directed Mutants. Isolating MMOR mutants with full iron content proved somewhat difficult. Purification of MMOR(D26A) and MMOR(E74A) by following the protocol used successfully for wild-type MMOR resulted in protein that was significantly iron-depleted. The DEAE Sepharose CL-6B column was able to resolve to some extent iron-depleted MMOR

from fully complemented reductase, so careful analysis and pooling of the CL-6B fractions afforded MMOR(E73A), MMOR(E74A), and MMOR(E75A) proteins with 2.0 Fe/protein. The MMOR(E72A) and MMOR(E76A) mutants were purified with 1.8 and 1.7 Fe/protein, respectively. The JM105/MMOR(D26A) expression system produced large amounts of inclusion bodies; the yield from the initial 4-L expression was only 5 mg of iron-depleted reductase. In subsequent expressions, larger culture volumes, a shallower NaCl gradient on the CL-6B column, and rigorous CL-6B fraction pooling yielded 24 mg of MMOR(D26A) with full iron content. Despite multiple purification attempts, MMOR(R43A) was obtained with only 1.2-1.4 Fe/protein. Arg43 is located immediately next to one of the cysteine ligands of the [2Fe-2S] cluster; the cofactor may be inherently unstable in this mutant. Therefore, this mutant was not included in any of the subsequent studies.

Steady-State sMMO Activity Assays for MMOR Mutants. Reductase concentration dependence for the steady-state sMMO propylene reaction was investigated for the MMOR-wt, MMOR(D26A), MMOR(E72A), MMOR(E73A), MMOR(E74A), MMOR(E75A), and MMOR(E76A) proteins. Plots of NADH consumption rate vs MMOR concentration obtained from one experiment are shown in Figure 2.5. By treating MMOR as a substrate of MMOH, the data were fit with a function (eq 2) representing both sMMO activity (hyperbola) and MMOR oxidase

$$v = \frac{V_{\max} [R]}{K_M + [R]} + k_{\text{oxidase}} [R] \quad (2)$$

activity (line), yielding $V_{\max, \text{app}}$ and pseudo K_M values for MMOR and the mutant proteins (Table 2.3). The $V_{\max, \text{app}}/K_M$ value, a measurement of specificity, was markedly lower for three of the mutants (mutant, % of wild-type): MMOR(E73A), 31%;

MMOR(D26A), 42%; and MMOR(E75A), 49%. The D26A, E73A, and E75A mutations caused significant increases in the K_M value, which correspond to decreases in either the binding affinity or binding frequency of the hydroxylase and reductase. The oxidase activities of four mutants, E73A, E74A, E75A, and E76A, were slightly lower than that of the wild-type reductase.

Kinetics of MMOR Mutant Reduction with NADH. The reactions of oxidized MMOR mutants with NADH at 4 °C were monitored at 458, 625, and 725 nm in a stopped-flow experiment. The kinetic steps for the reduction of wild-type MMOR with NADH have been determined previously^{18,24,25} and are depicted in Scheme 2.2. Upon NADH binding to MMOR, intermediate CT1, which is characterized by a charge transfer interaction between the NADH nicotinamide ring and flavin isoalloxazine group ($\lambda_{\text{max}} \approx 575$ nm), is formed. Hydride transfer from NADH to the oxidized FAD produces intermediate CT2, which exhibits a lower-energy charge transfer band ($\lambda_{\text{max}} \approx 740$ nm) between the NAD^+ and reduced flavin (FAD_{hq}) groups. Release of NAD^+ occurs simultaneously with intramolecular electron transfer between the MMOR cofactors, forming intermediate SQ1 with $\text{FAD}_{\text{sq/hq}}$ and $[\text{2Fe-2S}]_{\text{red/ox}}$ cofactors. Additional electron transfer (35% of total) from FAD_{hq} to $[\text{2Fe-2S}]_{\text{ox}}$ yields the final species, SQ2.

The most obvious difference between wild-type MMOR and the mutants was the varying shapes of the kinetic traces at 625 nm, corresponding to formation of charge transfer complexes and flavin semiquinone (Figure 2.6A). Each kinetic trace was fit with sums of four or five exponentials. Nearly every data set could be fit well by fixing the rate constants at 400 s^{-1} , 180 s^{-1} , 106 s^{-1} , 30 s^{-1} , and 1 s^{-1} .^{24,55} By starting with all of the rates fixed and then allowing some or all of the rates to vary in subsequent fitting iterations, rate constants were obtained for the NADH reduction of for

MMOR-wt, MMOR(D26A), MMOR(E72A), MMOR(E73A), MMOR(E74A), MMOR(E75A), and MMOR(E76A). There were not enough data to establish any statistical differences between the rate constants for the reductases. The multiple rates, which are not very different from one another, made the fitting process difficult; many sets of rate constants could be used to fit the data adequately.

Comparison of the 625-nm traces (Figure 2.6A) leads to a few generalizations. The D26A, E72A, E74A, E75A, and E76A mutants formed only about 60% as much FAD semiquinone, as judged by the total increase in absorbance at 625 nm, as the wild-type protein. The E73A mutant forms approximately the same amount of semiquinone as wild-type reductase, but the corresponding 625-nm traces do not have the same shape (Figure 2.6B). Thus, the kinetics for intramolecular electron transfer are slightly perturbed in the mutant. Comparing traces of mutants which performed poorly in the steady-state assays (D26A, E73A, and E75A; Figure 2.6C) with traces of mutants which exhibited unaltered steady-state kinetic parameters (E72A, E74A, and E76A; Figure 2.6D) does not allow any correlation to be made between pre-steady-state intramolecular and steady-state intermolecular electron transfer results.

Measurement of the MMOR(E73A)–MMOH Binding Constant. MMOR(E73A), which exhibited a significantly increased K_M value in steady-state sMMO assays but relatively unaltered pre-steady-state intramolecular electron transfer, was selected for further analysis. The binding affinity of the E73A mutant for MMOH was examined by isothermal titration calorimetry. Figure 2.7A shows the power required to compensate for the exothermic binding reaction after each addition of titrant to the sample cell. Data for wild-type MMOR binding to MMOH are also displayed for comparison. The incremental heat change for each injection was calculated by integrating the heat pulses with respect to time. A plot of these data as a

function of the MMOR/MMOH molar ratio is presented in Figure 2.7B. The data could be fit with either the two-site (noninteracting sites) or sequential (interacting sites) binding model resident in the Origin software. Sequential fitting was performed with both uncorrected and corrected MMOH concentrations, as described for sMMO component interactions in ref 18. Because the heat pulses for the MMOH–MMOR(E73A) binding interaction were very small and the binding affinity fairly weak, the calorimetry data could be fit reasonably well with several different models. Thermodynamic parameters obtained from two fits to a sequential binding model (uncorrected and corrected [MMOH]), as well as values for the MMOH–MMOR interaction determined previously,¹⁸ are included in Table 2.4. Depending on the fitting model employed, the E73A mutation decreases MMOH–MMOR binding affinity by a factor of 20-120 (average of 50-fold) at 25 °C.

In this study, the MMOH–MMOR binding reaction was complete after only a few additions (Figure 2.7A), but approximate K_d values of 1 μ M were determined. Furthermore, the heat changes observed for MMOH–MMOR binding in 25 mM MOPS (pH 7.0), 1 mM DTT have a smaller absolute value than for the same interaction measured in 20 mM Tris (pH 7.0), 1 mM DTT.¹⁸ Although the buffer composition appears to affect the ΔH and ΔS parameters for MMOH–MMOR binding, the K_d values are relatively unchanged.

DISCUSSION

Recombinant MMOR. The first high-yield recombinant system for MMOR expression was developed, affording good yields of pure reductase with a full complement of [2Fe-2S] and FAD cofactors. In *Methylosinus trichosporium* OB3b cells, MMOR is present at only ~10% of the MMOH level.⁵⁶ Therefore, only small quantities

of reductase can be isolated from sMMO-expressing methanotrophs; for instance, 100 g of *M. capsulatus* (Bath) cell paste yields only 5-10 mg of pure MMOR in a typical preparation. A previous account of *M. capsulatus* (Bath) MMOR expression in *E. coli* demonstrated MMOR activity in cell extracts, but expression levels were similar to those in the native organism and purification was not reported.⁵⁷ With the recombinant system reported here, however, the 100-mg quantities of MMOR required for extensive characterization are easily obtained.

In every respect that has been examined, purified recombinant MMOR is identical to native MMOR isolated from *M. capsulatus* (Bath) (Table 2.2). As judged by optical and EPR spectroscopy, the reductase cofactors and surrounding protein environments are the same. Total amino acid and mass spectrometric analysis establish the identity of the recombinant and native apoproteins. Steady-state sMMO activity and pre-steady-state reduction with NADH are unchanged. Finally, the redox potentials of recombinant MMOR²⁴ are nearly identical to those reported previously for the native reductase.⁵⁴ We conclude that the recombinant and native MMOR proteins are fully interchangeable.

Selection of MMOR Residues for Site-Directed Mutagenesis. The expression system described here not only produces sufficient reductase for detailed biochemical studies of the wild-type protein,^{18,24} but also enables preparation of site-directed MMOR mutants. At the time this work was undertaken, no structural information was available for MMOR or the MMOH–MMOR complex. A novel, semi-empirical analysis of packing contacts in MMOH crystals had just been employed to locate potential binding sites for MMOB or MMOR on MMOH.³⁸ Assuming that MMOH–MMOH crystal contacts mimic MMOH–MMOB or MMOH–MMOR interactions, sequences involved in helix-helix contacts between two MMOH molecules were examined for

homology with MMOB and MMOR. From this analysis, an 11-residue peptide of MMOR (D²⁴EDVITAALRQ³⁴) was identified with a putative binding site on the second domain of the MMOH α subunit. Superimposing a homologous [2Fe-2S] ferredoxin (PDB entry 1FRD) onto the peptide generated a docking model for MMOR with MMOH which appeared to feature compatible binding interactions (Figure 2.2). By using this docking model, several MMOR residues were identified as potentially involved in MMOH–MMOR binding interactions: Asp26, Arg43, Glu72, Glu73, Glu74, Glu75, and Glu76.⁵⁸ Criteria for selection included residency in the ferredoxin domain, location near the protein-protein interface (with minor adjustments for the glutamate loop), and conservation between the *M. capsulatus* (Bath) and *M. trichosporium* OB3b MMOR proteins. The docking model predicted no hydrophobic contacts for the MMOH–MMOR interface.

Activity of MMOR Mutants. All seven MMOR mutants were obtained by site-directed mutagenesis of the pRED-K2 expression plasmid. Except for R43A, which could not be prepared with full [2Fe-2S] complementation, difficulties with iron depletion in the mutant reductases were largely overcome by slightly modifying the purification protocol. To evaluate the effects of these site-specific mutations on MMOH–MMOR interactions, steady-state sMMO propylene activity assays were performed with the D26A, E72A, E73A, E74A, E75A, and E76A mutants. All of these MMOR mutants are capable of transferring electrons to MMOH, which suggests that the mutations did not cause gross changes in the wild-type reductase structure or redox potentials. The $V_{\max,app}$ parameter for hydroxylase activity (propylene epoxidation) is relatively unaffected for the MMOR mutants compared to MMOR-wt (Table 2.3), in accord with the notion that the electron transfer step is not rate-limiting in the sMMO reaction.¹⁸ In the E73A, D26A, E75A, and, to a much lesser extent, E76A

mutants, K_M a measure of MMOH–MMOR binding affinity and/or frequency is significantly increased. Because the MMOR binding and electron transfer reactions are quite fast with respect to substrate oxidation at the MMOH active site, a single reductase molecule can service many hydroxylase molecules during one turnover.¹⁸ Therefore, the differences in pseudo K_M values determined in this study probably underestimate the actual changes in MMOH–MMOR binding constants by a factor of at least 10.

Stopped-flow studies of the reduction of MMOR mutants with NADH were undertaken to investigate electron transfer in the reductive half reaction. For all of the mutants, the absorbance traces could be fit with the same kinetic model and rate constants determined for wild-type MMOR (Scheme 2.2), demonstrating that the intramolecular electron transfer steps are not severely perturbed by mutagenesis of amino acids in the ferredoxin domain. Of the six MMOR mutants examined, only E73A formed the same amount of FAD_{sq} as MMOR-wt, judging by the total absorbance increase at 625 nm (Figure 2.6). Flavin semiquinone generation in the D26A, E72A, E74A, E75A, and E76A mutants appeared to be only ca. 60% that of the wild-type reductase. Traces similar to those observed for these five mutants have been noted for iron-depleted MMOR-wt,⁵⁵ which leads to the obvious suggestion that these proteins were not fully complemented with iron. It is curious that all five generated essentially equivalent amounts of semiquinone, regardless of somewhat varying iron contents after purification. Other explanations for decreased semiquinone formation in the reaction with NADH include altered redox potentials of the [2Fe-2S] centers, decreased extinction coefficients of the $[2Fe-2S]_{red}$ or FAD_{sq} species, diminished stability of the reduced protein, or even a large structural perturbation. Without further experiments, we cannot distinguish between these possibilities with a high degree of confidence.

Considering the difficulty encountered in isolating MMOR mutants with full [2Fe-2S] complementation, however, iron depletion probably occurs.

The E72A and E74A mutants, which show decreased FAD_{sq} formation in the single-turnover reaction with NADH, have sMMO steady-state kinetic parameters that are nearly the same as those measured for wild-type MMOR (Table 2.3). Therefore, diminished semiquinone production under pre-steady-state conditions does not preclude normal steady-state intermolecular electron transfer. By extension of this argument, the increased K_{M} values observed for E73A, D26A, and E75A in steady-state assays are probably due at least in part to reduced binding affinity and/or frequency between MMOH and MMOR, rather than solely to altered [2Fe-2S] potentials.

Involvement of Glu73 in MMOH–MMOR Interaction. Intrinsic differences in the mutants, such as altered redox potentials or protein structure, make it difficult to make valid comparisons to MMOR-wt regarding MMOH–MMOR binding interactions. Therefore, the MMOR(E73A) protein, which has an increased K_{M} (300% of wild-type value) in steady-state sMMO reactions with propylene but also forms wild-type levels of FAD_{sq} when reduced with NADH, was selected for further study. Isothermal titration calorimetry yielded a K_{d} of $\sim 50 \mu\text{M}$ for the interaction of MMOR(E73A) with MMOH at pH 7.0 and 25 °C. By comparing the relative binding constants determined in this study, it is apparent that the full effect of decreased MMOH–MMOR affinity (20- to 120-fold difference for the E73A mutant compared to wild-type MMOR¹⁸) is masked in the steady-state sMMO propylene assays (3-fold difference), in which intermolecular electron transfer is not the rate-limiting step.

A recent parallel mutagenesis study on the *M. trichosporium* OB3b MMOR protein complements the results reported here.⁵⁹ Five MMOR mutants, D10A/E12A, K48A, D69A/E70A, E71A, and R80A, were prepared and examined in steady-state

sMMO assays at a single MMOR concentration. Only MMOR(D69A/E70A) exhibited significantly reduced hydroxylase activity with nitrobenzene (5-fold decrease compared to wild-type MMOR; [MMOR] not described). The E72A and E73A mutants of *M. capsulatus* (Bath) MMOR, which correspond directly with the *M. trichosporium* OB3b D69A and E70A mutations, were studied separately in this work. In steady-state activity assays and calorimetry experiments, MMOR(E73A) but not MMOR(E72A) displayed decreased affinity to MMOH. Therefore, the diminished activity observed for the *M. trichosporium* MMOR double mutant is likely due to the E70A rather than the D69A mutation, although synergistic effects cannot be ruled out.

Insights from NMR Spectroscopy. Subsequent to this work, the ferredoxin domain of MMOR was expressed as a separate protein,²⁵ and its NMR solution structure was solved.⁴² Figure 2.4 displays the amino acid residues mutated in this study mapped onto the MMOR-Fd structure. All are located on the protein surface except for Glu74, which is somewhat buried. The E74A reductase mutant displayed essentially unaltered kinetic parameters in sMMO steady-state assays, a result that correlates well with its buried position. Of the glutamate helix (α 3, Glu72-Glu76) surface residues, only Glu73 and Glu75 are strongly implicated in binding MMOH in this mutagenesis study. It is interesting to note that Glu73, Glu74, and Glu75 are absolutely conserved in all sMMO reductases, while some have aspartate rather than glutamate at positions 72 and 76. The inability to isolate MMOR(R43A) with full cofactor complementation suggests a structural role for this residue. In the ten lowest energy MMOR-Fd structures, the location of the Arg43 side chain varies greatly. This amino acid is within the paramagnetic region of the $[2\text{Fe-2S}]^+$ cofactor, however, so proper constraints could not be determined. Therefore, it is possible that Arg43 makes

a specific contact with another structural element, perhaps helix α 1, that is vital for stability of the [2Fe-2S] cluster.

Amino acids involved in intermolecular contacts between MMOR-Fd and MMOH were also identified in the NMR spectroscopic study.⁴² With this method, the binding interface was determined to comprise mostly hydrophobic but also uncharged polar and charged residues. The MMOR-Fd surface residues most affected by the addition of MMOH include Thr29 (helix α 1), Met39 (loop), Lys51 (beta strand β 3), Gln67 (β 2), Ala68 (β 2), Leu69 (β 2), and Glu73 (β 3). This result confirms the involvement of Glu73 in binding MMOH first identified by site-directed mutagenesis. In addition, Asp26 is located on the MMOR-Fd binding face and immediately precedes helix α 1, which was implicated in binding MMOH.⁴² This information, coupled with the increased K_M for MMOR(D26A) in steady-state sMMO reactions, may indicate a role for this residue in the MMOH–MMOR binding interaction.

Evaluation of MMOH–MMOR Docking Model. The MMOH–MMOR docking model³⁸ used to select MMOR residues for mutagenesis can be evaluated, at least in part, by comparison with the NMR solution structure of MMOR-Fd and associated MMOH binding experiments.⁴² In terms of the MMOR binding interface, the docking prediction is quite accurate, identifying the correct binding face of the MMOR ferredoxin domain as well as specific α helices, Asp24–Gln34 and Glu72–Glu76, involved in the MMOH–MMOR interface. The NMR structure verifies that the Val27–Gln34 sequence forms an α helix and that the first half of the helix is close to the binding interface with MMOH. The Asp26 and Arg43 residues mutated in this study are indeed located close to the MMOR-Fd contact surface. Although the docking model failed to identify an α helix deemed absolutely necessary for binding to MMOH (β 2, Val66–Leu69),⁴² the possibility of deviations from the template structure were

noted specifically for the P⁷⁰PEEEEEEG⁷⁷ helix and the V⁶⁶QAL insertion immediately preceding this structural element.⁵⁸ The prediction that hydrophobic contacts are absent from the MMOH–MMOR interface is incorrect; the NMR titration experiments show clearly that the interface comprises both electrostatic and hydrophobic interactions.

According to the MMOH–MMOR docking model, MMOR contacts Lys385 of the MMOH α subunit, which would position the [2Fe-2S] and non-heme diiron cofactors 40 Å from each other. For MMOR to transfer electrons efficiently to MMOH, the cofactors are likely to be separated by 10-15 Å,⁶⁰ ruling out this proposed MMOH binding site in the absence of a large structural change upon MMOH–MMOR complex formation or a special long-range electron transfer system. A recent mass spectrometric analysis of MMOR-Fd cross-linking to MMOH found specific cross-links between both Glu56 and Glu91 of MMOR-Fd and the N-terminus of the MMOH α subunit.⁴³ Because these Glu residues are located on the side of the Fd domain farthest from the [2Fe-2S] center and least affected by MMOH binding,⁴² it is unclear whether these cross-links represent physiologically important binding interactions. In contrast to these results, MMOR from *M. trichosporium* OB3b cross-links to the MMOH α subunit.³⁷ It is possible that MMOR binds near the α/α interface in both systems, and the disparate cross-linking behavior simply reflects different positioning of reactive residues on the protein surfaces. Definitive identification of the MMOH binding site awaits determination of the MMOH–MMOR complex structure.

Conclusions. The MMOR mutagenesis studies reported here, coupled with the MMOR-Fd NMR solution structure,⁴² provide the groundwork for probing the contacts in the MMOH–MMOR binding interface. The identification of the same reductase residues involved in binding MMOH (Glu73 and Asp26) by site-directed mutagenesis

of MMOR and NMR titrations of MMOR-Fd demonstrates that full-length MMOR and the Fd domain contact MMOH with similar geometry. By using the MMOR-Fd structure to guide future MMOR mutagenesis experiments, the roles of specific reductase residues in the MMOH binding and intermolecular electron transfer steps may be delineated.

ACKNOWLEDGMENT

This work was supported by National Institutes of Health Research Grant GM32134 (S.J.L.). J.L.B. was a Howard Hughes Medical Institute predoctoral fellow. We thank Dr. Hans Brandstetter for providing the initial impetus for MMOR mutagenesis, Dr. George Gassner for many helpful discussions, and Dr. Jens Müller for generating Figure 2.4 and assisting with structural analysis. We also acknowledge the Multiuser Facility for the Study of Complex Macromolecular Systems (NSF-0070319) for access to an isothermal titration calorimeter.

REFERENCES

- (*) Portions of this work have been published in altered form in references (24) and (47).
- (1) Higgins, I. J.; Best, D. J.; Hammond, R. C.; Scott, D. *Microbiol. Rev.* **1981**, *45*, 556-590.
- (2) Hanson, R. S.; Hanson, T. E. *Microbiol. Rev.* **1996**, *60*, 439-471.
- (3) Anthony, C. *Adv. Microbiol. Physiol.* **1986**, *27*, 113-210.
- (4) Higgins, I. J.; Best, D. J.; Hammond, R. C. *Nature* **1980**, *286*, 561-564.
- (5) Fox, B. G.; Borneman, J. G.; Wackett, L. P.; Lipscomb, J. D. *Biochemistry* **1990**, *29*, 6419-6427.
- (6) Bragg, J. R.; Prince, R. C.; Harner, E. J.; Atlas, R. M. *Nature* **1994**, *368*, 413-418.
- (7) Murrell, J. C. *Biodegradation* **1994**, *5*, 145-159.
- (8) Nguyen, H.-H. T.; Elliott, S. J.; Yip, J. H.-K.; Chan, S. I. *J. Biol. Chem.* **1998**, *273*, 7957-7966.
- (9) Lieberman, R. L.; Shrestha, D. B.; Doan, P. E.; Hoffman, B. M.; Stemmler, T. L.; Rosenzweig, A. C. *Proc. Nat. Acad. Sci. USA* **2003**, *100*, 3820-3825.
- (10) Prior, S. D.; Dalton, H. J. *Gen. Microbiol.* **1985**, *131*, 155-163.
- (11) Woodland, M. P.; Dalton, H. J. *Biol. Chem.* **1984**, *259*, 53-59.
- (12) Green, J.; Dalton, H. J. *Biol. Chem.* **1985**, *260*, 15795-15801.
- (13) Liu, K. E.; Lippard, S. J. In *Adv. Inorg. Chem.*; Sykes, A. G., Ed.; Academic Press: San Diego, 1995; Vol. 42, pp 263-289.
- (14) Feig, A. L.; Lippard, S. J. *Chem. Rev.* **1994**, *94*, 759-805.
- (15) Wallar, B. J.; Lipscomb, J. D. *Chem. Rev.* **1996**, *96*, 2625-2657.
- (16) Merckx, M.; Kopp, D. A.; Sazinsky, M. H.; Blazyk, J. L.; Müller, J.; Lippard, S. J. *Angew. Chem. Int. Ed.* **2001**, *40*, 2782-2807.

- (17) Colby, J.; Dalton, H. *Biochem. J.* **1978**, *171*, 461-468.
- (18) Gassner, G. T.; Lippard, S. J. *Biochemistry* **1999**, *38*, 12768-12785.
- (19) Merkx, M.; Lippard, S. J. *J. Biol. Chem.* **2002**, *277*, 5858-5865.
- (20) Lee, S.-K.; Nesheim, J. C.; Lipscomb, J. D. *J. Biol. Chem.* **1993**, *268*, 21569-21577.
- (21) Liu, K. E.; Valentine, A. M.; Wang, D.; Huynh, B. H.; Edmondson, D. E.; Salifoglou, A.; Lippard, S. J. *J. Am. Chem. Soc.* **1995**, *117*, 10175-10185.
- (22) Shu, L.; Nesheim, J. C.; Kauffmann, K.; Münck, E.; Lipscomb, J. D.; Que, L., Jr. *Science* **1997**, *275*, 515-518.
- (23) Valentine, A. M.; Stahl, S. S.; Lippard, S. J. *J. Am. Chem. Soc.* **1999**, *121*, 3876-3887.
- (24) Kopp, D. A.; Gassner, G. T.; Blazyk, J. L.; Lippard, S. J. *Biochemistry* **2001**, *40*, 14932-14941.
- (25) Blazyk, J. L.; Lippard, S. J. *Biochemistry* **2002**, *41*, 15780-15794.
- (26) Andrews, S. C.; Shipley, D.; Keen, J. N.; Findlay, J. B. C.; Harrison, P. M.; Guest, J. R. *FEBS Lett.* **1992**, *302*, 247-252.
- (27) Karplus, P. A.; Daniels, M. J.; Herriott, J. R. *Science* **1991**, *251*, 60-66.
- (28) Correll, C. C.; Batie, C. J.; Ballou, D. P.; Ludwig, M. L. *Science* **1992**, *258*, 1604-1610.
- (29) Zhou, N.-Y.; Jenkins, A.; Chan Kwo Chion, C. K. N.; Leak, D. J. *FEBS Lett.* **1998**, *430*, 181-185.
- (30) Nordlund, I.; Powlowski, J.; Shingler, V. J. *Bacteriol.* **1990**, *172*, 6826-6833.
- (31) Mason, J. R.; Cammack, R. *Annu. Rev. Microbiol.* **1992**, *46*, 277-305.
- (32) Butler, C. S.; Mason, J. R. *Adv. Microbiol. Physiol.* **1997**, *38*, 47-84.
- (33) Lund, J.; Woodland, M. P.; Dalton, H. *Eur. J. Biochem.* **1985**, *147*, 297-305.
- (34) Froland, W. A.; Andersson, K. K.; Lee, S.-K.; Liu, Y.; Lipscomb, J. D. *J. Biol. Chem.* **1992**, *267*, 17588-17597.

- (35) Liu, Y.; Nesheim, J. C.; Lee, S.-K.; Lipscomb, J. D. *J. Biol. Chem.* **1995**, *270*, 24662-24665.
- (36) Liu, Y.; Nesheim, J. C.; Paulsen, K. E.; Stankovich, M. T.; Lipscomb, J. D. *Biochemistry* **1997**, *36*, 5223-5233.
- (37) Fox, B. G.; Liu, Y.; Dege, J. E.; Lipscomb, J. D. *J. Biol. Chem.* **1991**, *266*, 540-550.
- (38) Rosenzweig, A. C.; Brandstetter, H.; Whittington, D. A.; Nordlund, P.; Lippard, S. J.; Frederick, C. A. *Proteins* **1997**, *29*, 141-152.
- (39) Gallagher, S. C.; Callaghan, A. J.; Zhao, J.; Dalton, H.; Trehwella, J. *Biochemistry* **1999**, *38*, 6752-6760.
- (40) Walters, K. J.; Gassner, G. T.; Lippard, S. J.; Wagner, G. *Proc. Natl. Acad. Sci. USA* **1999**, *96*, 7877-7882.
- (41) Chang, S. L.; Wallar, B. J.; Lipscomb, J. D.; Mayo, K. H. *Biochemistry* **2001**, *40*, 9539-9551.
- (42) Müller, J.; Lugovskoy, A. A.; Wagner, G.; Lippard, S. J. *Biochemistry* **2002**, *41*, 42-51.
- (43) Kopp, D. A.; Berg, E. A.; Costello, C. E.; Lippard, S. J. *J. Biol. Chem.* **2003**, *278*, 20939-20945.
- (44) Balendra, S.; Lesieur, C.; Smith, T. J.; Dalton, H. *Biochemistry* **2002**, *41*, 2571-2579.
- (45) Massey, V. *J. Biol. Chem.* **1957**, *229*, 763-770.
- (46) Stookey, L. L. *Anal. Chem.* **1970**, *42*, 779-781.
- (47) Coufal, D. E.; Blazyk, J. L.; Whittington, D. A.; Wu, W. W.; Rosenzweig, A. C.; Lippard, S. J. *Eur. J. Biochem.* **2000**, *267*, 2174-2185.
- (48) Roberts, I.; Hylemon, P. B.; Holmes, W. M. *Prot. Expr. Purif.* **1991**, *2*, 117-121.
- (49) Singer, B. W.; Gold, L.; Shinedling, S. T.; Colkitt, M.; Hunter, L. R.; Pribnow, D.; Nelson, M. A. *J. Mol. Biol.* **1981**, *149*, 405-432.

- (50) Shinedling, S.; Gayle, M.; Pribnow, D.; Gold, L. *Mol. Gen. Genet.* **1987**, *207*, 224-232.
- (51) Stainthorpe, A. C.; Lees, V.; Salmond, G. P. C.; Dalton, H.; Murrell, J. C. *Gene* **1990**, *91*, 27-34.
- (52) Gold, L. *Annu. Rev. Biochem.* **1988**, *57*, 199-233.
- (53) Colby, J.; Dalton, H. *Biochem J.* **1979**, *177*, 903-908.
- (54) Lund, J.; Dalton, H. *Eur. J. Biochem.* **1985**, *147*, 291-296.
- (55) Kopp, D. A.; Lippard, S. J., unpublished results.
- (56) Fox, B. G.; Froland, W. A.; Dege, J. E.; Lipscomb, J. D. *J. Biol. Chem.* **1989**, *264*, 10023-10033.
- (57) West, C. A.; Salmond, G. P. C.; Dalton, H.; Murrell, J. C. *J. Gen. Microbiol.* **1992**, *138*, 1301-1307.
- (58) Brandstetter, H.; Lippard, S. J., unpublished results.
- (59) Broadwater, J. A.; Lipscomb, J. D., presented at the 6th European Conference on Bioinorganic Chemistry (EUROBIC-6), Lund, Sweden, July 29-August 3, 2002, as reported by Dr. Jens Müller.
- (60) Page, C. C.; Moser, C. C.; Chen, X. X.; Dutton, P. L. *Nature* **1999**, *402*, 47-52.

Table 2.1: Primers for Site-Directed Mutagenesis of MMOR

Mutant	Forward Primer ^a
D26A	5'-CCGTTCCGGACGAGG <u>CC</u> GCATCACC
R43A	5'-ATGTCGTCCTGC <u>G</u> CGGAGGGCGGCTG
E72A	5'-TGCCGCCGG <u>C</u> AGAGGAGGAGGAAG
E73A	5'-TGCCGCCGGAAG <u>C</u> GGAGGAGGAAG
E74A	5'-GCCGGAAGAGG <u>C</u> GGAGGAAGGGTTG
E75A	5'-CGGAAGAGGAGG <u>C</u> GGAAGGGTTGGTG
E76A	5'-CGGAAGAGGAGG <u>C</u> AGGGTTGGTG

^a Forward primers are depicted; reverse primers are the reverse complements. The altered codon is shown in bold with the changed base(s) underlined.

Table 2.2: Properties of Recombinant and Native MMOR

	Recombinant MMOR	Native MMOR
MW measured ^a (Da)	38,546.9 ± 3.9	38,545.6 ± 3.9
Fe content (mol/mol protein)	1.99 ± 0.05	1.92 ^b
FAD content (mol/mol protein)	1.0 ± 0.1	1.00 ^b
□ _{max} (nm), pH 7.0, 25 °C	334, 394, 458	334, 394, 458
g values (fully reduced)	2.047, 1.958, 1.871 ^c	2.047, 1.960, 1.864 ^b
FAD _{ox/sq} (mV), pH 7.0, 25 °C	-176 ± 7 ^d	-150 ± 20 ^e
[2Fe-2S] _{ox/red} (mV), pH 7.0, 25 °C	-209 ± 14 ^d	-220 ± 20 ^e
FAD _{sq/hq} (mV), pH 7.0, 25 °C	-266 ± 15 ^d	-260 ± 5 ^e

^a Expected 38,542.6 Da for apoprotein with H254T sequence correction and N-terminal methionine intact. ^b As reported in ref 53. ^c EPR recorded at 10 K, 500 μW at 9.478 GHz, 10.0-G modulation amplitude. ^d As reported in ref 24. ^e As reported in ref 54.

Table 2.3: sMMO Steady-State Propylene Reaction Parameters for MMOR Mutants

Mutant	$V_{\max,app}$ (% of wt) ^a	K_M (% of wt)	V_{\max}/K_M (% of wt)	$k_{oxidase}$ (% of wt)
D26A	85	202	42	107
E72A	92	107	86	100
E73A	92	301	31	77
E74A	97	114	86	89
E75A	94	191	49	90
E76A	100	139	72	90

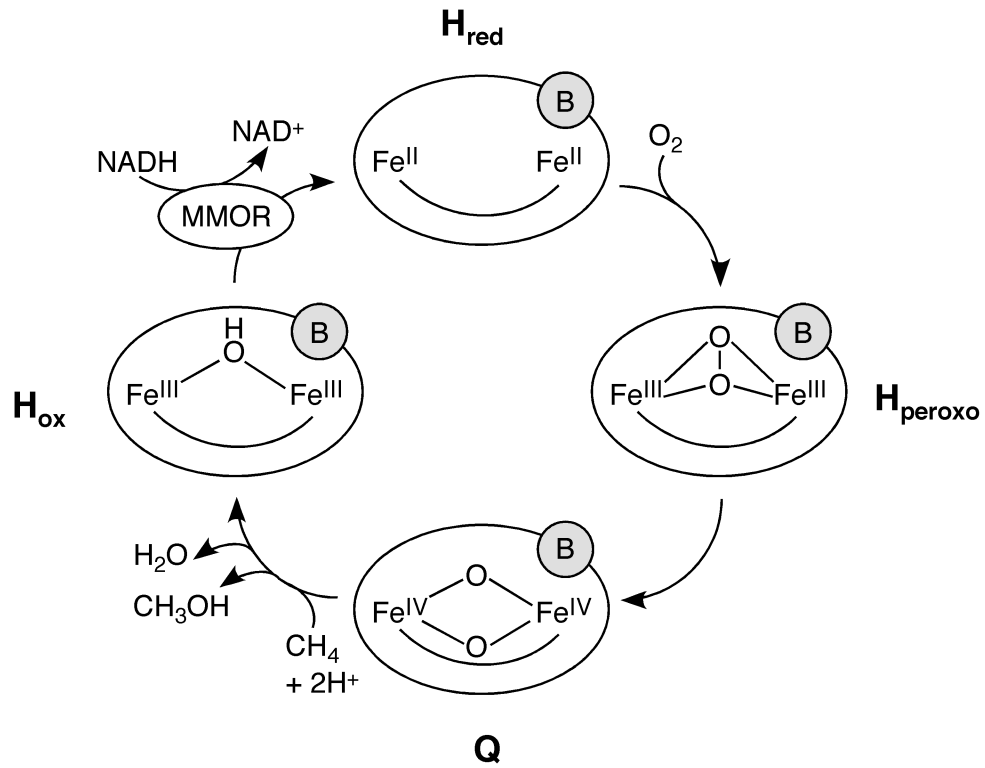
^a Kinetic parameters reported as percentage of wild-type MMOR parameters. Bold values deviate significantly from those of MMOR-wt.

Table 2.4: Thermodynamic Parameters for MMOH–MMOR Binding at 25 °C

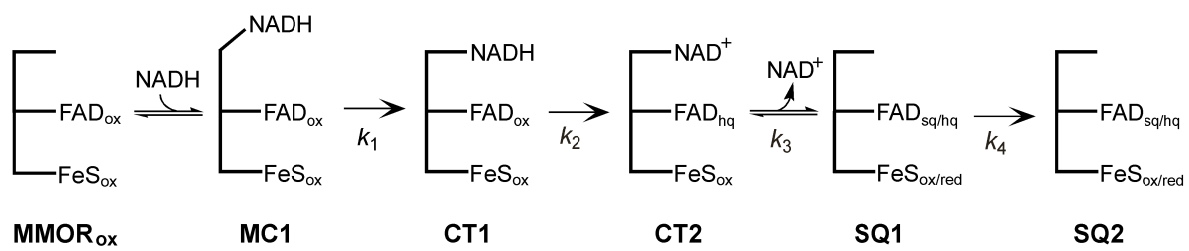
MMOR	K_{d1} (μM)	ΔG_1 (kcal mol^{-1})	ΔH_1 (kcal mol^{-1})	$T\Delta S_1$ (kcal mol^{-1})	K_{d2} (μM)	ΔG_2 (kcal mol^{-1})	ΔH_2 (kcal mol^{-1})	$T\Delta S_2$ (kcal mol^{-1})
E73A ^a	22	-6.4	-3.9	2.5	65	-5.7	-20.8	-15.1
E73A ^b	56	-5.8	-13.5	-7.7	52	-5.8	-23.8	-18.0
wt ^c	0.9	-8.3	8.1	16.4	2.6	-7.6	6.5	14.1

^a Sequential fitting model. ^b Sequential fitting model with [MMOH] correction; see ref 18 for details.

^cFrom ref 18.



Scheme 2.1



Scheme 2.2

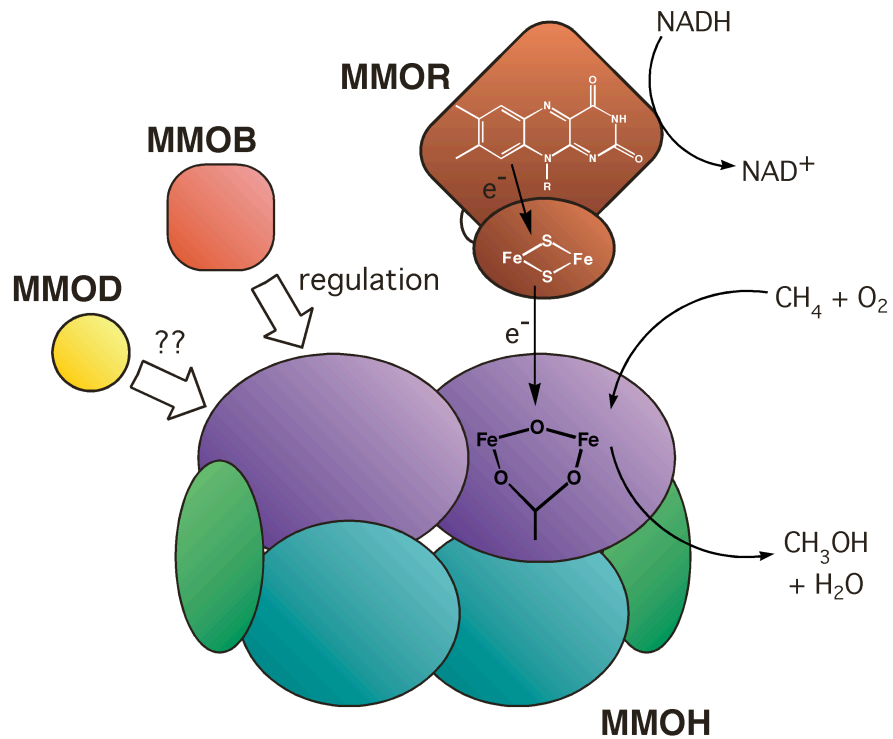


Figure 2.1. Schematic view of the four protein components that comprise the soluble methane monooxygenase enzyme system. The role of each protein in catalysis is indicated, except for MMOD, for which a function is currently unknown. Only one of the two non-heme diiron centers in the MMOH dimer is depicted.

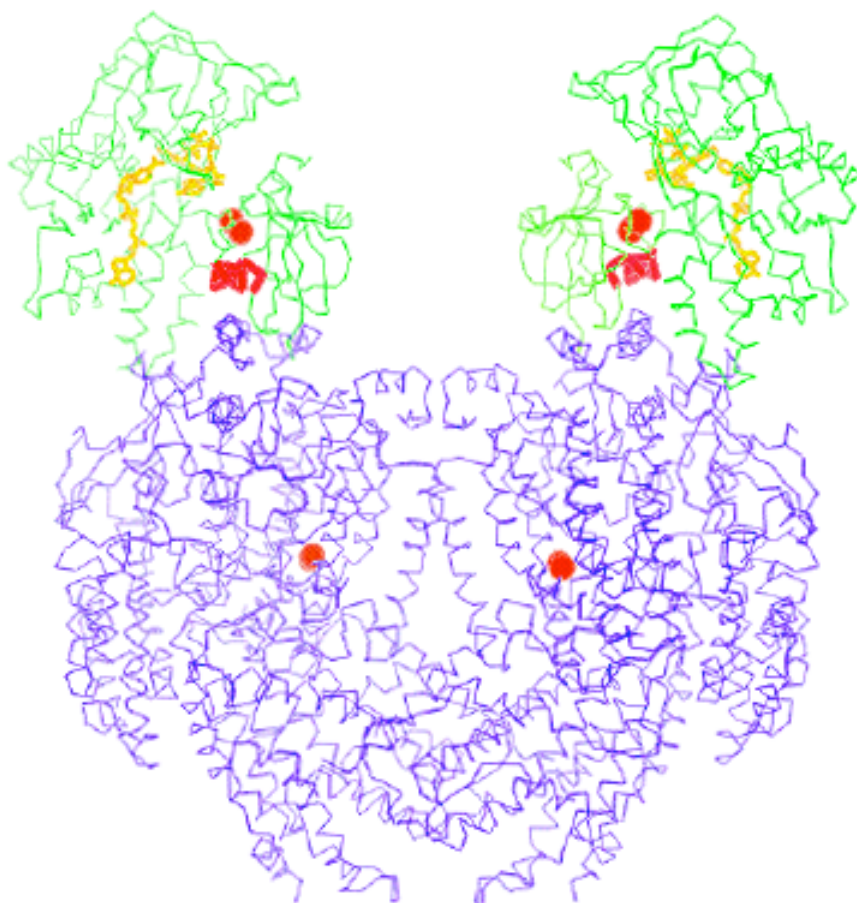


Figure 2.2. MMOH–MMOR docking model developed by analyzing packing contacts in MMOH crystals (ref 38). The MMOH backbone is shown in blue, and the putative MMOR binding helix, D²⁴EDVITAALRQ³⁴, is highlighted in red. The MMOR model (green backbone) was generated by aligning a homologous ferredoxin protein (PDB entry 1FRD) with the MMOR contact helix. The FAD/NADH portion of MMOR was added by mapping the corresponding portion of PDR (PDB entry 2PIA) onto the docked ferredoxin protein. The irons in the MMOH active sites and MMOR [2Fe-2S] sites are depicted as red spheres, and the organic cofactors of MMOR are outlined in yellow.

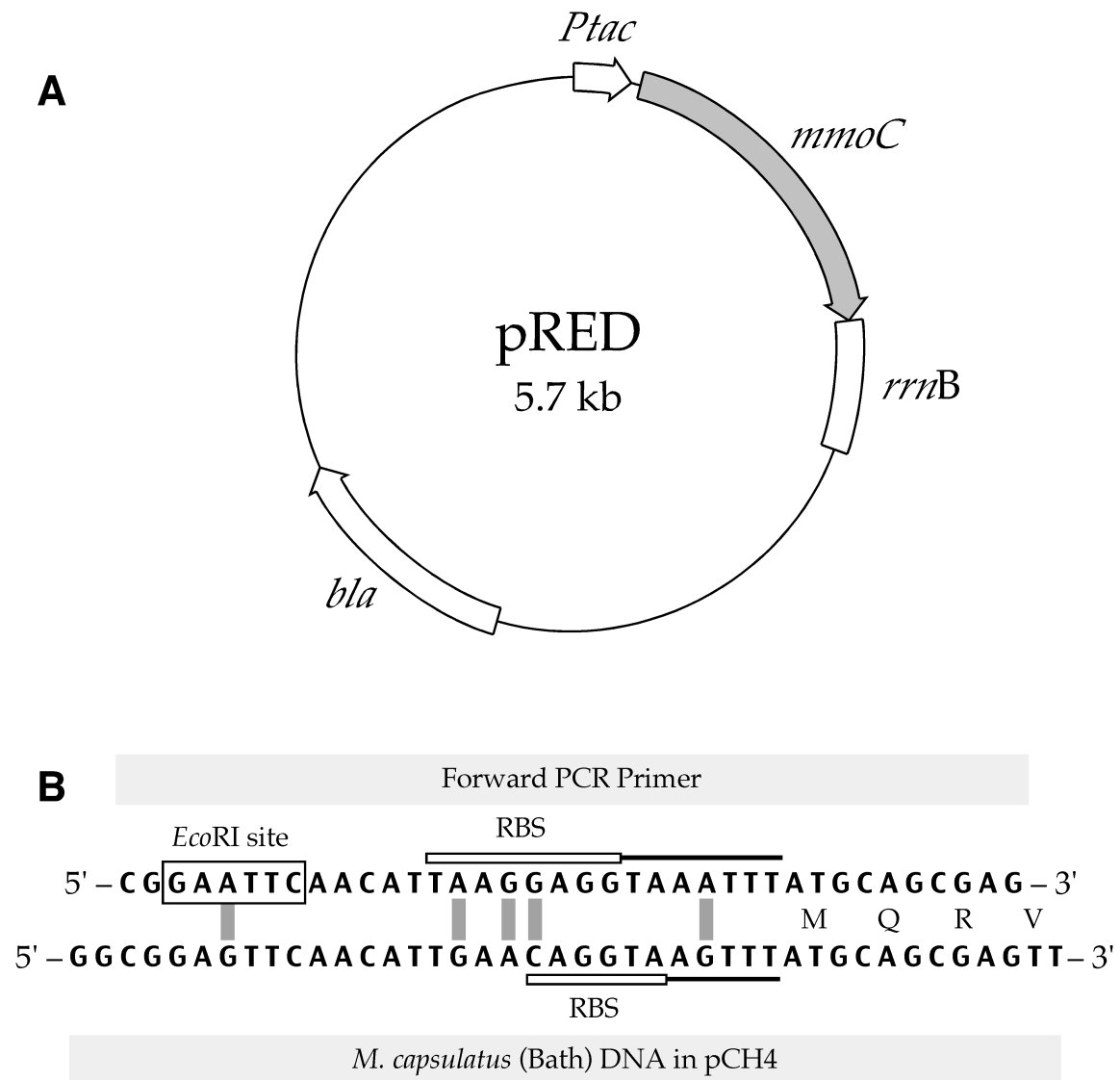


Figure 2.3. pRED plasmid for recombinant MMOR expression. (A) Plasmid map for pRED, showing *mmoC* inserted into the multiple cloning site of the pKK223-3 expression vector. (B) Redesign of the *mmoC* ribosome binding site by altering the DNA sequence of the forward primer used to amplify the gene from pCH4.

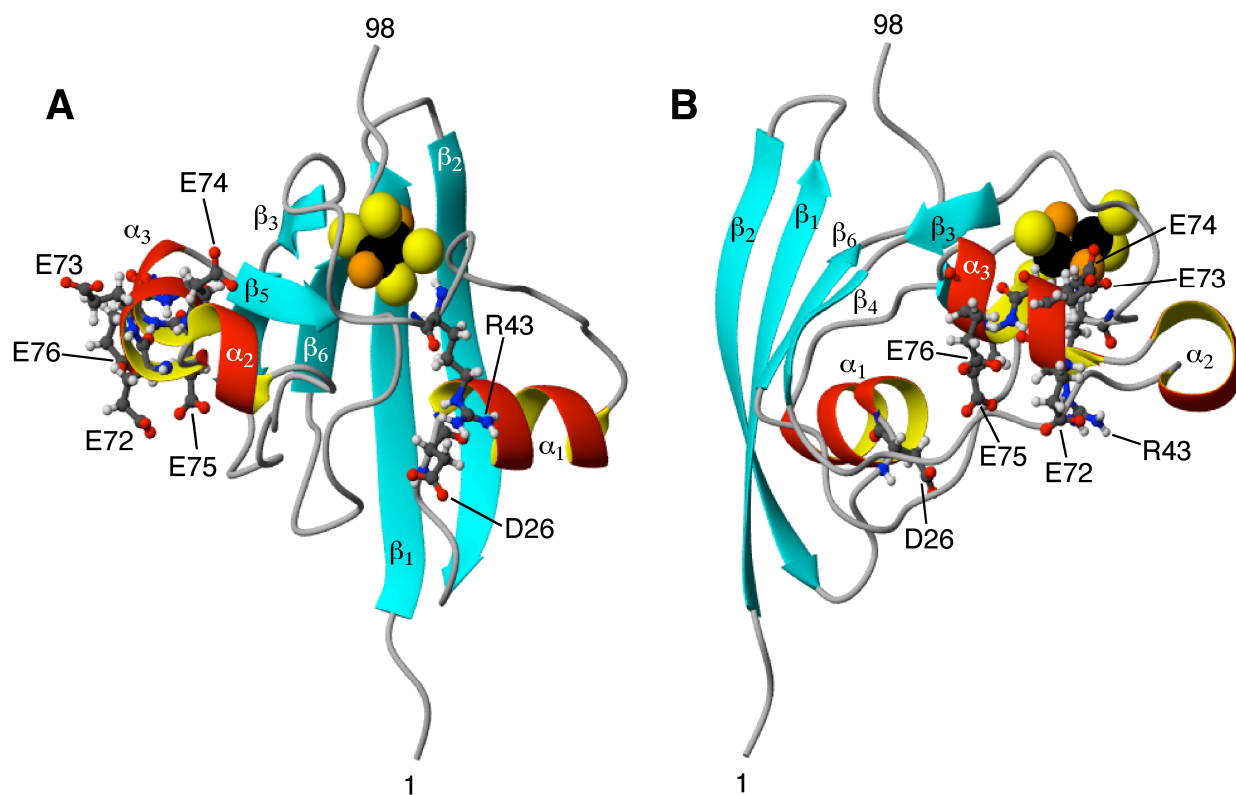


Figure 2.4. Mutated MMOR residues mapped onto the MMOR-Fd structure (PDB code 1JQ4). \square strands and \square helices are colored blue and red, respectively. Residues Asp26, Arg43, Glu72, Glu73, Glu74, Glu75, and Glu76 are shown as balls and sticks and the [2Fe-2S] cluster as black (iron), yellow (cysteine sulfur), and orange (inorganic sulfur) spheres. (A) Direct view of the MMOR-Fd face that binds MMOH, as determined by NMR titration experiments. (B) View A rotated by 90° about the vertical axis.

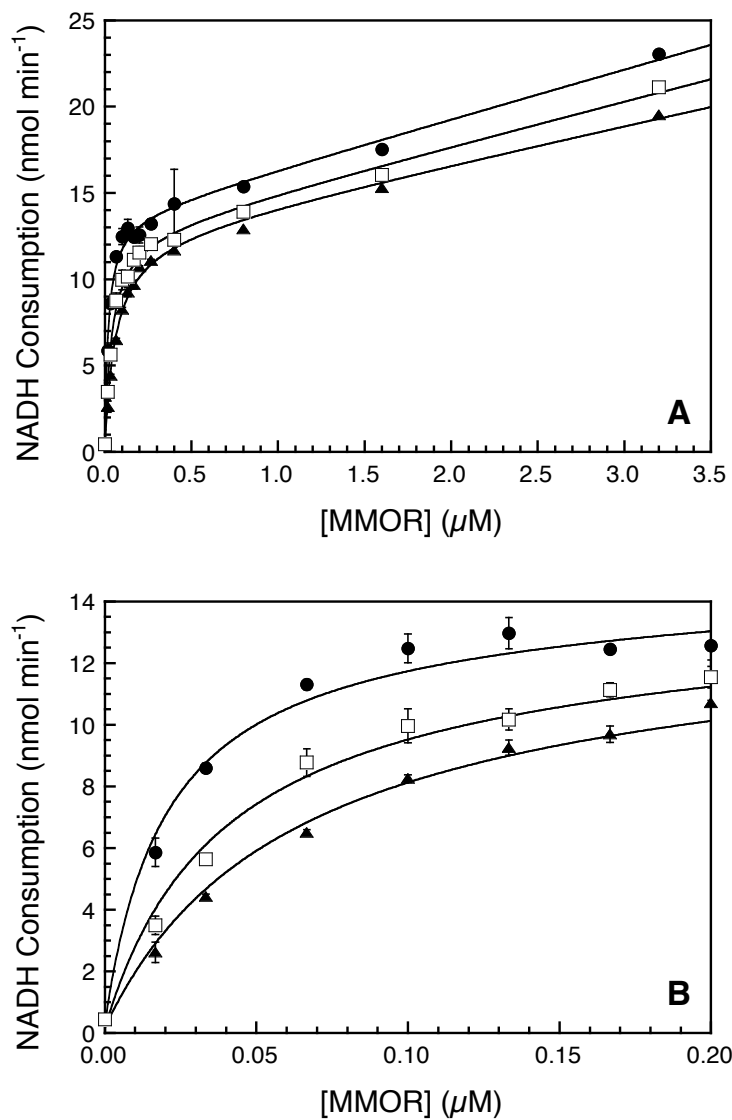


Figure 2.5. MMOR concentration dependence for NADH consumption in steady-state sMMO propylene assays. (A) Curves for MMOR-wt (circles), MMOR(E73A) (triangles), and MMOR(E75A) (squares) fit with an expression representing hydroxylase and MMOR oxidase activity (eq 2; solid lines). (B) Expanded region of (A) for MMOR concentrations between 0 and 0.2 μM . Error bars show one standard deviation.

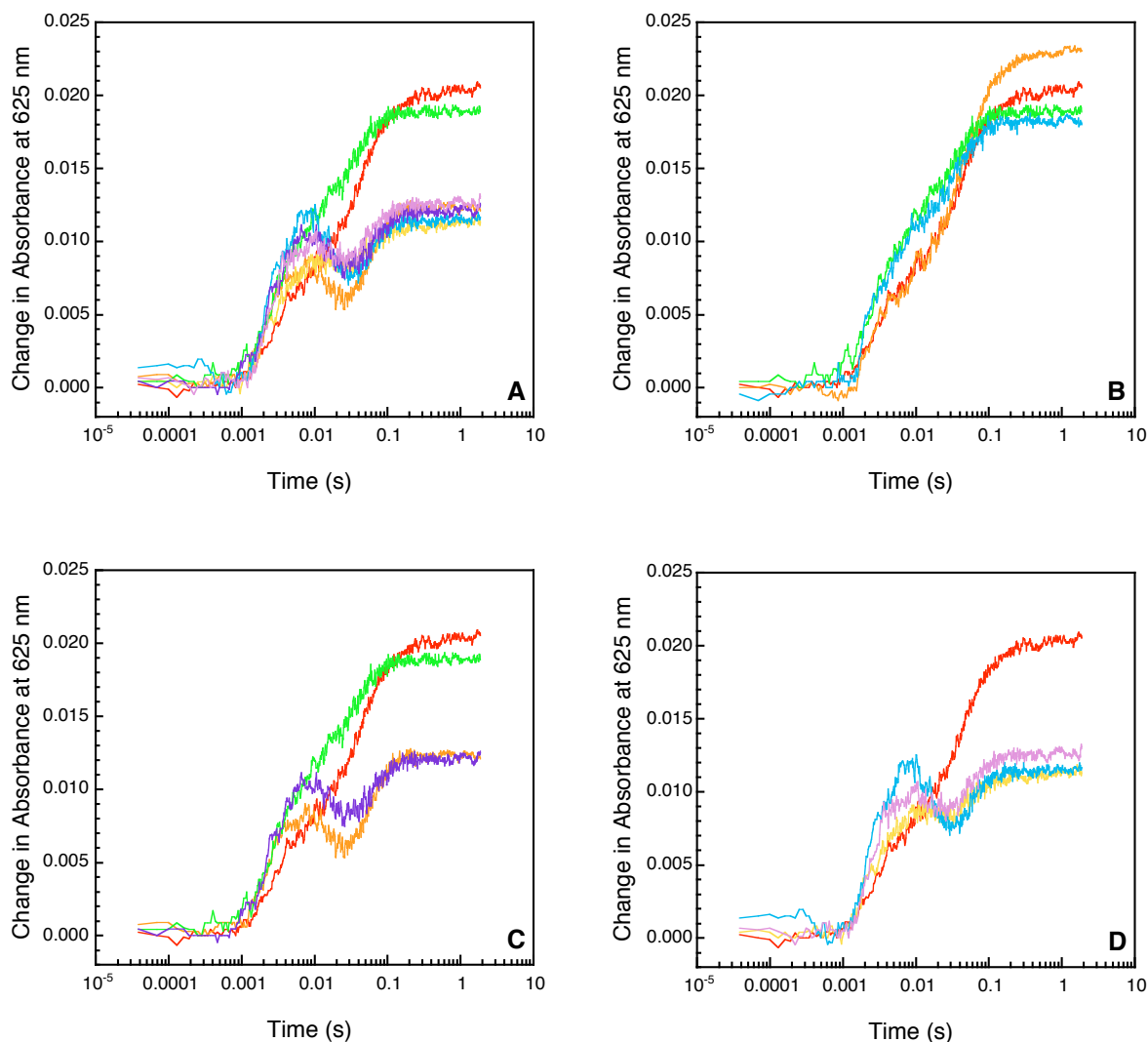


Figure 2.6. (A) Comparison of the kinetic traces monitored at 625 nm for the reaction of MMOR site-directed mutants with NADH at 4 °C. (B) Traces for duplicate samples of MMOR-wt (red and orange) and MMOR(E73A) (green and blue). (C) Overlay of stopped-flow data for the MMOR mutants that performed poorly in steady-state sMMO assays (D26A, E73A, and E75A). (D) Kinetic traces for MMOR mutants that showed relatively unaltered kinetic parameters in steady-state assays (E72A, E74A, and E76A). For panels A, C, and D, the coloring scheme is: MMOR-wt, red; D26A, orange; E72A, gold; E73A, green; E74A, blue; E75A, violet; E76A, pink.

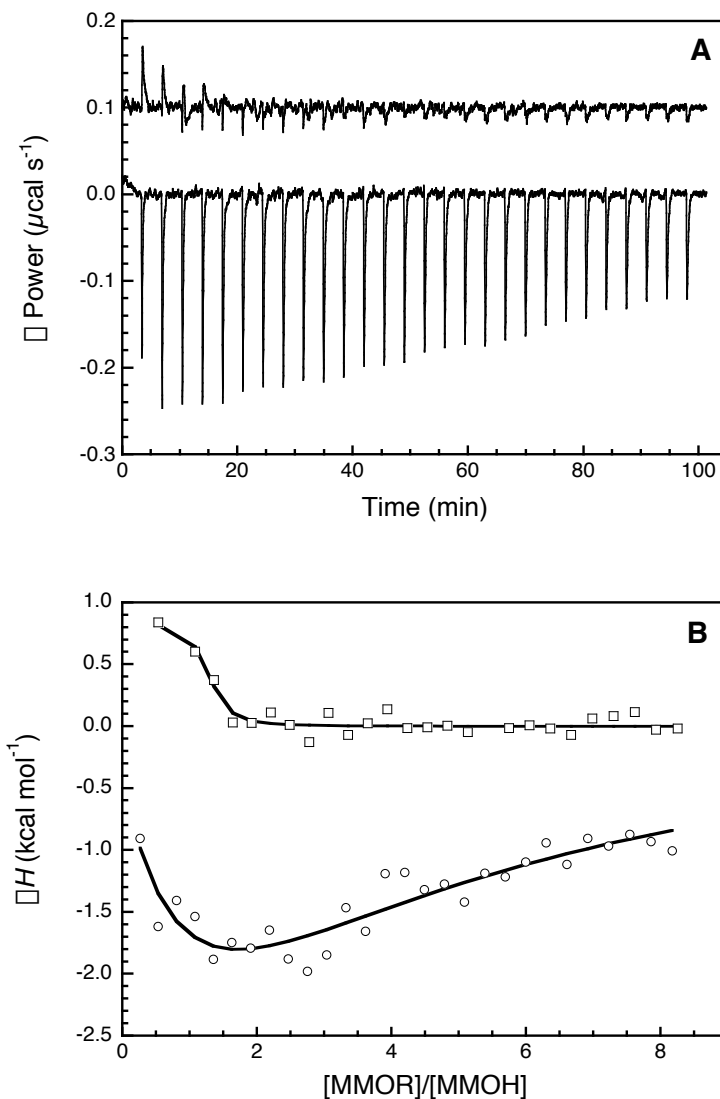


Figure 2.7. Determination of MMOH–MMOR(E73A) binding constants by isothermal titration calorimetry. (A) Data recorded for the formation of the complex between MMOR-wt (upper trace, offset by 0.1 $\mu\text{cal s}^{-1}$ for clarity) or MMOR(E73A) (lower trace) and MMOH at 25 °C. (B) Integrated enthalpy data for the MMOH–MMOR (squares) and MMOH–MMOR(E73A) (circles) binding interactions fit with sequential binding models (solid lines).

Chapter 3

**Expression and Characterization of Ferredoxin and Flavin Adenine
Dinucleotide-Binding Domains of the Reductase Component of Soluble Methane
Monooxygenase from *Methylococcus capsulatus* (Bath)***

INTRODUCTION

Methanotrophic bacteria serve an important role in the carbon cycle by consuming methane produced in anaerobic sediments and thereby limiting the flux of this greenhouse gas into the atmosphere.¹ The first step of the process, which is catalyzed by the enzyme methane monooxygenase (MMO), involves the conversion of methane to methanol (eq 1). All methanotrophs express a membrane-bound



particulate MMO (pMMO), which contains copper.² In the few species of methanotrophic bacteria capable of producing a second, soluble form of MMO (sMMO), differential expression of the two enzyme systems is regulated by the availability of copper ions. When the copper-to-biomass ratio is low, sMMO activity is observed, whereas pMMO is expressed at high copper-to-biomass ratios.³

The sMMO complex from *Methylococcus capsulatus* (Bath) has been characterized extensively by a wide range of reactivity, spectroscopic, crystallographic, and kinetic methods.⁴⁻⁹ It comprises three proteins, a hydroxylase (MMOH, 251 kDa), a reductase (MMOR, 38.5 kDa), and a regulatory protein (MMOB, 15.9 kDa), all of which are required for catalytic function.^{10,11} Recent work demonstrates that a fourth protein, MMOD, is also involved in the sMMO system.¹² The hydroxylase, a dimer of three subunits⁴ in an $\alpha_2\beta_2$ configuration, contains two dinuclear carboxylate-bridged iron centers where dioxygen activation and methane hydroxylation occur. MMOR is an iron-sulfur flavoprotein that shuttles electrons from NADH to the hydroxylase to prime the enzyme system for reaction with dioxygen.^{13,14} The MMOR [2Fe-2S] center is located in the N-terminal portion of the protein and exhibits significant homology with ferredoxins of plants, cyanobacteria, and archaeobacteria.¹⁵ The C-terminal domain binds a single flavin adenine dinucleotide (FAD) molecule, which accepts two electrons

from NADH. Electrons are then delivered one at a time to the [2Fe-2S] center for transfer to the hydroxylase diiron site.^{11,14,16}

MMOR belongs to a class of modular flavoprotein electron transferases (Figure 3.1), also called the ferredoxin:NADP⁺ oxidoreductase (FNR) family. These proteins contain a flavin domain capable of accepting two electrons from a nicotinamide dinucleotide and a one-electron carrier domain, which may be linked or dissociable.¹⁷⁻¹⁹ The ability to attach the electron carrier domain to either the N- or C-terminal end of the core flavin/NAD(P) protein implies that this domain is an independent modular unit. In accord with this notion, the crystal structure of *Burkholderia cepacia* phthalate dioxygenase reductase (PDR), a member of the FNR family, reveals distinct flavin mononucleotide (FMN), NADH binding, and [2Fe-2S] domains.¹⁹ Removal of the PDR [2Fe-2S] domain by fortuitous proteolytic cleavage produces a stable, truncated form amenable to biochemical characterization.²⁰

The highly modular nature of FNR family proteins suggested that dividing MMOR into its component ferredoxin (MMOR-Fd) and flavin/pyridine nucleotide (MMOR-FAD) domains should be feasible. The separate domain proteins were predicted to serve as useful models for studying the intra- and intermolecular electron transfer reactions of MMOR. In this paper, we report recombinant *Escherichia coli* systems for the high-yield expression of the individual MMOR domains. For both MMOR-Fd and MMOR-FAD, spectroscopic properties and redox potentials are examined and compared to those of MMOR. The kinetics of MMOR-FAD reduction with NADH and interdomain electron transfer reactions are described. An examination of the influence of pH on MMOR-FAD optical spectra, redox potentials, and NADH reaction kinetics is also presented. Ultimately, characterization of the individual electron transfer steps in the sMMO system, combined with the structures of

MMOR and MMOH, will provide the means for tracing the electron transfer pathway from NADH through the flavin and [2Fe-2S] cofactors of MMOR into the carboxylate-bridged diiron active sites of MMOH.

MATERIALS AND METHODS

General Methods. The ferrozine method^{21,22} was used to determine the iron content of MMOR-Fd; FAD determinations were performed as described in ref 16. UV-visible spectra were obtained with an HP 8453 diode array spectrophotometer. Fluorescence excitation and emission scans were recorded with a Hitachi F-3010 fluorescence spectrophotometer.

MMOR Domain Selection. To define the Fd and FAD/NADH domain boundaries of *M. capsulatus* (Bath) MMOR, sections of MMOR were aligned with the full-length *B. cepacia* PDR protein sequence (PDB code 2PIA) by using ClustalW.²³ In addition, the approximate MMOR domain sequences (residues 1-114, Fd domain; residues 89-348, FAD/NADH domain) were compared to and aligned with other protein sequences in the non-redundant National Center for Biotechnology Information protein databases with the PSI-BLAST program. The C-terminal end of the MMOR-Fd domain was selected as residue 98, and the MMOR-FAD domain was designed to start at residue 99 after an obligatory methionine residue.

MMOR Domain Cloning. The Fd portion of the *mmoC* gene, which codes for MMOR,¹⁵ was amplified with *Pfu* DNA polymerase (Stratagene, La Jolla, CA) from pCH4,²⁴ obtained from J. C. Murrell (University of Warwick, UK), by using the following primers: 5'-CGGAATTCAACATTAAGGAGGTAAATTTATGCAGCGAG and 5'-CCTCTCCAAAGCTTATGCGTCAATGGGTATAG. The primers, 5'-CGAAGACCACCTGGAATTCTAAGGAGGTTATAATATGTGCCGCATCAGTTTTGGTGAG

and 5'-TCACAGTACTTAAGCTTTTCAGGCCGCCCCGGAC, were used to amplify the region of *mmoC* corresponding to the MMOR-FAD domain. The resulting 344-bp (Fd) and 809-bp (FAD) fragments were flanked by *EcoRI* and *HindIII* sites (boldface font), which were introduced by the forward and reverse primers, respectively. The amplified DNA was purified from the PCR reactions by using the QIAquick PCR purification kit (Qiagen Inc., Valencia, CA). Both PCR products were digested with the restriction enzymes *EcoRI* and *HindIII* (New England Biolabs, Beverly, MA) by following the provided instructions. The high-copy-number plasmid pKK223-3 (Amersham Pharmacia Biotech, Piscataway, NJ) was digested with the same restriction enzymes, and then treated with alkaline phosphatase (AP; Boehringer Mannheim, Indianapolis, IN) to prevent recircularization in the subsequent ligation reaction. After inactivating the AP by adding 20 mM ethylene glycol-bis[β -aminoethyl ether]-*N,N,N',N'*-tetraacetic acid (EGTA) and heating at 65 °C for 10 min, the DNA was isolated with the QIAquick PCR purification kit. The AP-treated pKK223-3 digest and *mmoC*-Fd or *mmoC*-FAD digest were ligated with T4 DNA ligase (New England Biolabs); the resulting plasmid solutions were transformed into *E. coli* XL1-Blue cells and plated on Luria-Bertani (LB)-ampicillin (Ap; 100 μ g/mL) agar plates. Colonies with ampicillin resistance were analyzed further by restriction mapping of DNA obtained from plasmid minipreps. DNA sequencing (MIT Biopolymers Laboratory) of positive pRED-Fd and pRED-FAD clones confirmed that the inserted genes contained no errors.

Expression and Purification of MMOR-Fd. The pRED-Fd(2) expression plasmid was transformed into *E. coli* JM105 cells. Cells were grown to saturation in 100 mL of LB-Ap (100 μ g/mL) medium at 37 °C with 200 rpm shaking. To each of six 1-L quantities of LB-Ap (100 μ g/mL) medium were added 10 mL of freshly prepared filter-

sterilized 10 mM $\text{Fe}(\text{NH}_4)_2(\text{SO}_4)_2 \cdot 6\text{H}_2\text{O}$ in 100 mM sodium citrate (pH 7.0) and 10 mL of the saturated JM105/pRED-Fd(2) starter culture. When the OD_{660} values reached 0.6, the cultures were supplemented with 80 μM Fe^{2+} , added as 2 mL of 40 mM $\text{FeSO}_4 \cdot 7\text{H}_2\text{O}$ in 12.5 mM H_2SO_4 per L of cell culture, and induction was started by adding isopropyl thio- β -D-galactopyranoside (IPTG) to a final concentration of 1.0 mM. After 3.5 h, the cells were collected by centrifugation, then suspended in 100 mL of cold cracking buffer [25 mM 3-(*N*-morpholino)propanesulfonic acid (MOPS; pH 7.0), 1 mM 1,4-dithiothreitol (DTT), 5 mM MgCl_2 , and 200 μM $\text{Fe}(\text{NH}_4)_2(\text{SO}_4)_2 \cdot 6\text{H}_2\text{O}$] containing DNase (1.5 units/mL) and 1 mM Pefabloc SC. The cells were sonicated on ice with three 2-min pulses at 40% output (Branson Sonifier Model 450 equipped with a 3/4-inch horn) and then centrifuged for 40 min at 98,000g to separate the soluble and insoluble materials. The soluble cell extract was filtered through a 0.2 μm membrane and loaded onto a DEAE Sepharose CL-6B (Amersham Pharmacia) column (2.6 \times 15 cm) equilibrated with buffer A [25 mM MOPS (pH 7.0), 1 mM DTT, and 50 mM NaCl]. After a 120-mL wash with buffer A, proteins were eluted with a 740-mL linear gradient from buffer A to buffer B [25 mM MOPS (pH 7.0), 1 mM DTT, and 500 mM NaCl]. MMOR-Fd eluted at approximately 370 mM NaCl. Fractions containing MMOR-Fd were identified by optical spectroscopy and SDS-PAGE, then pooled and concentrated by ultrafiltration. This crude Fd protein solution was filtered through a 0.2 μm membrane and applied to a Superdex 75 (Amersham Pharmacia) size-exclusion column (2.6 \times 60 cm) equilibrated with 25 mM MOPS (pH 7.0) containing 1 mM DTT and 150 mM NaCl. Fractions were pooled based on color and SDS-PAGE analysis. Typical preparations yielded 12-14 mg of >98% pure MMOR-Fd (98 residues, MW 10,931) per L of *E. coli* expression culture.

Expression and Purification of MMOR-FAD. A 100-mL JM105/pRED-FAD(1) culture in LB-Ap (100 $\mu\text{g}/\text{mL}$) was grown to saturation at 37 °C with shaking at 200 rpm. Each of six 1-L quantities of LB-Ap (100 $\mu\text{g}/\text{mL}$) medium was inoculated with 10 mL of the saturated starter culture and transferred to a 37 °C incubator set to rotate at 200 rpm. When the OD_{660} reached ca. 0.6, expression of the MMOR-FAD domain was induced with 1.0 mM IPTG. After 3.5 h, the cells were collected by centrifugation, suspended in 100 mL of cracking buffer, and sonicated as described above. The soluble cell extract was obtained by centrifugation for 40 min at 98,000g followed by filtration through a 0.2 μm membrane. The first chromatographic step, resolution on a DEAE Sepharose CL-6B anion-exchange column, was performed exactly as described for MMOR-Fd. Fractions containing the FAD domain, which eluted at approximately 240 mM NaCl, were identified by SDS-PAGE and pooled. Half of this crude material was loaded onto a 5'-AMP Sepharose (Sigma, St. Louis, MO) column (2.6 \times 18 cm) equilibrated with buffer A. The column was washed with 25 mM MOPS (pH 7.0), 1 mM DTT containing 95 mM NaCl (70 mL), 410 mM NaCl (50 mL), and then 50 mM NaCl (175 mL) to remove protein contaminants. The FAD domain was eluted with buffer B containing 1 mM NADH. All of the fractions collected in the NADH wash were combined as pure MMOR-FAD domain and concentrated over a YM10 Amicon membrane. The FAD domain was exchanged into 25 mM MOPS (pH 7.0), 2 mM DTT with a Biogel P6 desalting column (Bio-Rad, Hercules, CA). This procedure typically afforded 25 mg of >95% pure MMOR-FAD (250 residues, MW 27,629) per L of expression culture.

Expression and Purification of MMOR. Full-length MMOR was prepared from a recombinant *E. coli* expression system exactly as published,¹⁶ except that iron was added to the media as described for MMOR-Fd domain expression.

Mass Spectrometric Analysis. Pure MMOR-Fd and MMOR-FAD proteins in 25 mM MOPS (pH 7.0) were submitted to the MIT Biopolymers Laboratory for analysis by electrospray ionization mass spectrometry (ESI-MS). To remove cofactors which separated from the proteins upon treatment with ammonium acetate, formic acid, and acetonitrile, HPLC purification was necessary. The protein component was analyzed with a Sciex Model API 365 triple stage mass spectrometer.

EXAFS Spectroscopy. MMOR-Fd and MMOR in 25 mM MOPS (pH 7.0), 1 mM DTT were made anaerobic by vacuum gas exchange with O₂-free N₂. To reduce the proteins completely, protein, anaerobic buffer, and excess sodium dithionite were mixed in an anaerobic chamber to produce 1.75 mM MMOR-Fd and 0.92 mM MMOR solutions in 25 mM MOPS (pH 7.0), 1 mM DTT, 10 mM Na₂S₂O₄, and 39% (v/v) glycerol. After the samples had equilibrated for ca. 20 min, 100- μ L aliquots were loaded into lucite EXAFS cells (1 mm thick) with Kapton tape windows, the cells were capped, and the samples were immediately frozen in liquid nitrogen.

The X-ray absorption spectra for MMOR-Fd and MMOR were measured at the Stanford Synchrotron Radiation Laboratory (SSRL) on unfocussed 8-pole wiggler beam line 7-3, with the ring operating at 3 GeV and 50-100 mA. A Si(220) monochromator was utilized for energy selection at the Fe K-edge. To minimize higher harmonic components in the X-ray beam, the monochromator was detuned 50% at 7987 eV. The sample was maintained at 10 K during data collection by using a continuous flow liquid helium cryostat (Oxford Instruments model CF1208). Data were measured to $k = 17 \text{ \AA}^{-1}$ in fluorescence mode with a Canberra Ge 30-element array detector. Internal energy calibration was performed by simultaneous measurement of the absorption of a Fe foil placed between two ionization chambers located after the sample. The first inflection point of the foil was assigned to 7111.2 eV.

No evidence of photoreduction was observed for either MMOR-Fd or MMOR. The final averages included 20 and 25 scans for MMOR-Fd and MMOR, respectively. The averaged data were processed by fitting a second-order polynomial to the post-edge region and subtracting this background from the entire spectrum. A three-segment spline (polynomial curves of orders 2, 3, and 3) was used to model the smooth background above the edge. Normalization of the data was achieved by subtracting the spline and setting the edge jump to 1.0 at 7150 eV. To enhance the impact of high- k data, the resultant EXAFS data were k^3 -weighted, where the photoelectron wave vector $k = [2m_e(E - E_0)/(h/2\pi)^2]^{1/2}$, E is energy, E_0 is the energy of onset of the EXAFS, and m_e is the mass of an electron. Because of the signal-to-noise level, the EXAFS data were truncated at $k = 15 \text{ \AA}^{-1}$ during the analysis. Simulated EXAFS spectra were calculated with FEFF 6.0^{25,26} using phase and amplitude parameters derived from the crystal structure of a [2Fe-2S] ferredoxin from *Aquifex aeolicus*²⁷ then adjusted by a least-squares fitting process to match the data (using the EXAFSPAK programs by G. N. George, SSRL). The experimental energy threshold, E_0 , was fixed at 7130 eV. The structural parameters that were varied during the refinement include the bond distance (R) and the bond variance (σ^2). The σ^2 parameter is related to the Debye-Waller factor, which is a measure of thermal vibration and static disorder of the absorbers and scatterers. Coordination numbers were varied systematically during the course of the analysis, but were not allowed to vary within a given fit.

EPR Spectroscopy. MMOR-Fd and MMOR in 25 mM potassium phosphate buffer (pH 7.0) were made anaerobic by vacuum gas exchange with O₂-free N₂. In an anaerobic chamber, protein, anaerobic buffer, and sodium dithionite were combined to yield 258 μM protein solutions containing a two-fold molar excess of dithionite (i.e. 500 μM for MMOR-Fd and 1.5 mM for MMOR). After equilibration for several minutes,

aliquots of the reduced protein samples were transferred to EPR tubes and frozen in liquid nitrogen.

By estimating the MMOR (and MMOR-FAD) midpoint potentials as -174 mV, -206 mV (MMOR only), and -265 mV (vide infra), the maximum amount of semiquinone species that can be stabilized was calculated. Plots of species concentration (FAD_{ox} , FAD_{sq} , and FAD_{hq} for MMOR-FAD; also Fd_{ox} and Fd_{red} for MMOR) vs solution potential were constructed with KaleidaGraph, v. 3.0 or 3.51 (Synergy Software, Reading, PA). Wavelengths (590 nm for MMOR-FAD; 640 nm for MMOR) for monitoring the titrations were selected such that maximum absorbance and maximum fraction of semiquinone species (0.75) coincided. A 900- μ L quantity of MMOR-FAD (159 μ M in 25 mM potassium phosphate, pH 7.0) was made anaerobic in a sealed quartz cuvette by vacuum gas exchange and titrated with sodium dithionite (ca. 4 mM) to maximize the FAD_{sq} species; this objective was achieved by reducing the sample until A_{590} reached a maximum. In a similar fashion, the MMOR protein (900 μ L of 170 μ M protein in 25 mM potassium phosphate, pH 7.0) was reduced to the point of maximum FAD_{sq} species by maximizing A_{640} . After dithionite additions, the MMOR-FAD and MMOR concentrations were calculated as 148 μ M and 153 μ M, respectively, of which about 75% of the FAD cofactor (ca. 110 μ M) was expected to be in the semiquinone oxidation state. In an anaerobic chamber aliquots of the semiquinone samples were transferred to EPR tubes.

EPR spectra of the four samples, MMOR- Fd_{red} , MMOR_{3e-}}, MMOR- $FAD_{sq,max}$, and MMOR_{sq,max}} were recorded with a Bruker EMX X-band spectrometer fitted with an Oxford ESR 900 liquid helium cryostat. The temperature was maintained at 10 K for the first two samples (reduced [2Fe-2S]) and 100 K for the latter two samples (FAD_{sq}).

The power saturation behavior of each protein sample was examined, and a high-quality spectrum was collected at a power at which the signal was not saturated.

Determination of FAD_{sq} Optical Spectrum by Evolving Factor Analysis. To examine the optical spectra of MMOR-FAD in various oxidation states, anaerobic reductive titrations were performed. A 1.00-mL aliquot of 90 μ M MMOR-FAD in 25 mM potassium phosphate (pH 7.0) was transferred to a sealed quartz cuvette and made anaerobic by 10-12 cycles of vacuum gas exchange with O₂-free N₂. Aliquots of 1-2 mM sodium dithionite were added with a gas-tight Hamilton titrating syringe. After each addition, optical spectra were collected until no further changes were observed (usually less than 5 min), and the final spectrum was saved for data analysis. The temperature for the titration experiments was held constant at 25 °C with a circulating water bath.

After subtracting the average absorbance between 800 and 900 nm from each spectrum, dilution corrections were applied. The evolving factor analysis (EFA) function resident in the Specfit Global Analysis software suite (v. 2.10U or 3.0.16; Spectrum Software Associates, Chapel Hill, NC) was used to extract component spectra for the MMOR-FAD domain, corresponding to the oxidized (FAD_{ox}), semiquinone (FAD_{sq}), and hydroquinone (FAD_{hq}) forms of the protein. Non-iterative EFA was performed for each data set to generate extinction coefficient profiles for the three spectroscopically distinct MMOR-FAD oxidation states. The extinction coefficients were scaled such that $\epsilon_{458} = 11,000 \text{ M}^{-1} \text{ cm}^{-1}$ for FAD_{ox}. To test the validity of this method, the individual spectra collected during the reductive titrations were fit with linear combinations of the oxidized, semiquinone, and hydroquinone component spectra (KaleidaGraph).

pH Effects on MMOR Domains Optical Spectra. In order to investigate the effects of pH on the optical spectra of the MMOR-Fd and MMOR-FAD proteins, samples of the oxidized and reduced domains were examined at varying pH values. Fourteen buffers were prepared for these experiments: 100 mM sodium citrate (pH 4.92, 5.06, 5.21, 5.47, and 5.81), 100 mM potassium phosphate (pH 6.00, 6.49, 6.98, 7.50, and 8.02), and 100 mM TAPS (pH 8.07, 8.50, 8.98, and 9.10). MMOR-FAD_{ox} (214 μ M) in 1 mM potassium phosphate (pH 7.0) was combined with each of these buffers to yield \sim 40 μ M protein solutions. Each solution was allowed to equilibrate for about 2 min, and an optical spectrum (300-900 nm) was recorded. The temperature was maintained at 25 °C with a circulating water bath. To determine the pK_a for the observed optical change, plots of A_{450} or A_{500} vs pH were fit with the expressions shown in eqs 2 and 3,

$$A = A_{\max} \frac{A_{\max} - A_{\min}}{1 + 10^{(pH - pK_a)}} \quad (2)$$

$$A = A_{\min} + \frac{A_{\max} - A_{\min}}{1 + 10^{(pH - pK_a)}} \quad (3)$$

respectively, by using the program KaleidaGraph. To yield \sim 45 μ M MMOR-Fd_{ox} solutions, MMOR-Fd in 1 mM potassium phosphate (pH 7.0) was mixed with 100 mM sodium citrate (pH 5.47), 100 mM potassium phosphate (pH 6.00, 6.98, or 8.02), or 100 mM TAPS (pH 8.98). After brief equilibration, optical spectra (300-900 nm) were collected at room temperature.

Fd_{red} and FAD_{hq} samples were prepared at varying pH values by reducing the proteins with sodium dithionite in an anaerobic chamber, dialyzing away excess dithionite, and combining aliquots of the reduced proteins with strong buffers (same used for Fd_{ox} experiment described above). Sealed MMOR-Fd_{red} and MMOR-FAD_{hq}

samples were removed from the box, and optical spectra (300-900 nm) were recorded. For all samples, the temperature was held constant at 25 °C with a circulating water bath.

To examine the effects of pH on the MMOR-FAD_{sq} optical spectrum, anaerobic reductive titrations of MMOR-FAD were performed at varying pH. The following buffers were used in these experiments: 80 mM potassium phosphate (pH 6.00), 60 mM potassium phosphate (pH 6.49), 75 mM potassium phosphate (pH 6.98), 70 mM potassium phosphate (pH 8.02), and 75 mM TAPS (pH 8.50, 8.98, or 9.31). The MMOR-FAD domain (ca. 50 μM) in a total volume of 1.00 mL was reduced with dithionite exactly as described above. After each addition of reductant, equilibrium was usually achieved in 5-10 min, but took as long as 40 min at high pH values. Data were processed as described, and EFA afforded FAD_{ox}, FAD_{sq}, and FAD_{hq} component spectra for each titration data set.

Redox Potential Determinations for the MMOR Domains. The equilibrium midpoint potentials of the MMOR-Fd and MMOR-FAD domains were determined by using a series of reductive titrations. All of the titrations were performed in 25 mM potassium phosphate (pH 7.0) buffer because MOPS, the standard buffer used in sMMO studies, interferes with electron equilibration. Each titration included one or more redox-active indicator dyes with known midpoint potentials to permit calculation of the solution potential throughout the titration. Dyes used for MMOR-Fd potential determination included anthraquinone-2-sulfonate (AQ2S; $E^{\circ\prime} = -226$ mV), phenosafranine ($E^{\circ\prime} = -252$ mV), and anthraquinone-2,6-disulfonate (AQ2,6S; $E^{\circ\prime} = -184$ mV) in combination with phenosafranine (15-20% relative to AQ2,6S).

The MMOR-Fd domain (ca. 40 μM) and dye(s) (ca. 35 μM for AQ2S and AQ2,6S; ca. 12 μM for phenosafranine) in a total volume of 1.00 mL were placed in a sealed

quartz cuvette and made anaerobic by twelve cycles of vacuum gas exchange with O₂-free N₂. A gas-tight Hamilton titrating syringe was filled with a solution of sodium dithionite (1-2 mM) in phosphate buffer and then transferred to the cuvette under positive pressure. After the solution had equilibrated to 25 °C, an initial visible spectrum (300-900 nm) of the oxidized material was collected. Dithionite was added to the protein-dye solution in 5- μ L aliquots, the solution was mixed thoroughly, and a spectrum was recorded. Multiple scans were taken after each dithionite addition until the system had reached equilibrium (usually 5-10 min, but as long as 40 min). The final spectrum was saved for data analysis. This process was repeated until the protein and dye(s) were reduced completely. In addition, the MMOR-Fd potential was measured in the presence of MMOH (0.5 equiv) and/or MMOB (1 equiv) with AQ2S as the solution potential indicator.

The equilibrium midpoint potentials of the MMOR-FAD domain were determined by using the same method. The indicator dyes AQ2S, anthraquinone-1,5-disulfonate (AQ1,5S; $E^{\circ} = -172$ mV), phenosafranine, safranine O ($E^{\circ} = -289$ mV), and AQ2,6S in combination with phenosafranine (15-20% relative to AQ2,6S) were used for the MMOR-FAD domain reductive titrations. The MMOR-FAD protein (ca. 30 μ M) and dye(s) (ca. 35 μ M for AQ2S, AQ1,5S, and AQ2,6S; ca. 12 μ M for phenosafranine and safranine O) were titrated at 25 °C with sodium dithionite.

To obtain dye component spectra, an anaerobic solution of each dye (1.00 mL; 65-70 μ M for the anthraquinone dyes, 20 μ M for phenosafranine and safranine O) was titrated with 1-2 mM sodium dithionite. The initial spectrum was taken as the oxidized dye component spectrum. After performing baseline and dilution corrections, the first spectrum for which no optical changes were observed upon dithionite addition was selected as the fully reduced dye spectrum. The MMOR-Fd component spectra, Fd_{ox}

and Fd_{red} were also determined by titration with dithionite; the MMOR-FAD component spectra, FAD_{ox} , FAD_{sq} , and FAD_{hq} were obtained by EFA as described above. For each redox couple (dye_{ox}/dye_{red} , Fd_{ox}/Fd_{red} , FAD_{ox}/FAD_{sq} and FAD_{sq}/FAD_{hq}), a difference spectrum, $\Delta\epsilon(\lambda)$, was calculated by subtracting the extinction coefficients of the oxidized species from those of the reduced species.

Dilution corrections were applied to each spectrum in a titration data set. To eliminate any errors due to inaccurate extinction coefficients, the initial species concentrations were determined by fitting the initial oxidized spectrum with a linear combination of oxidized protein and oxidized indicator spectra (KaleidaGraph). A difference spectrum for each titration point was generated by subtracting the starting oxidized spectrum from each spectrum in the data set. These difference spectra (350 nm \leq λ \leq 800 nm) were then fit with linear combinations of component difference spectra, as shown in eq 4.

$$\Delta A(\lambda) = \sum \Delta\epsilon_i(\lambda) (\Delta c_i) \quad (4)$$

The concentration differences, Δc_i , returned by fitting with eq 4 were readily converted to species concentrations by comparison with the total concentrations of protein and dye(s). The solution potential and MMOR domain midpoint potentials were computed for each titration point with modified Nernst equations.¹⁶ Average MMOR-Fd and MMOR-FAD midpoint potentials were calculated by including only those data for which the solution potential was within 40 mV of both the approximate MMOR-Fd or MMOR-FAD domain potential and the indicator potential.

Relative redox potentials were determined for the FAD domain at varying pH values. For each MMOR-FAD reductive titration (vide supra), a species fraction (FAD_{ox} , FAD_{sq} , or FAD_{hq}) vs percent reduction plot was constructed, where the latter

was computed according to eq 5. The FAD_{sq} vs % reduction plots were fit manually by

$$\% \text{ reduction} = 100 \frac{0.5[FAD_{sq}] + [FAD_{hq}]}{[FAD]_T} \quad (5)$$

generating a series of curves representing different ΔE° values (difference between the $FAD_{ox/sq}$ and $FAD_{sq/hq}$ redox potentials). First, given various ΔE° values, theoretical fractions of FAD_{ox} , FAD_{sq} , and FAD_{hq} were calculated over a range of solution potentials (E_h ; -500 mV to +100 mV) with eqs 6-8, respectively. For each E_h value, the

$$f_{ox} = \frac{[FAD_{ox}]}{[FAD]_T} = \frac{\exp\left(-\frac{F}{RT}(FAD_{ox/sq} - E_h)\right)}{\exp\left(-\frac{F}{RT}(FAD_{ox/sq} - E_h)\right) + 1 + \exp\left(\frac{F}{RT}(FAD_{sq/hq} - E_h)\right)} \quad (6)$$

$$f_{sq} = \frac{[FAD_{sq}]}{[FAD]_T} = \frac{1}{\exp\left(-\frac{F}{RT}(FAD_{ox/sq} - E_h)\right) + 1 + \exp\left(\frac{F}{RT}(FAD_{sq/hq} - E_h)\right)} \quad (7)$$

$$f_{hq} = \frac{[FAD_{hq}]}{[FAD]_T} = \frac{\exp\left(\frac{F}{RT}(FAD_{sq/hq} - E_h)\right)}{\exp\left(-\frac{F}{RT}(FAD_{ox/sq} - E_h)\right) + 1 + \exp\left(\frac{F}{RT}(FAD_{sq/hq} - E_h)\right)} \quad (8)$$

percent reduction (eq 5) was calculated. Finally, the theoretical mole fraction vs % reduction curves were compared to the experimental data in KaleidaGraph; the ΔE° value used to generate the best-fitting curve was taken as the difference in redox potentials at that pH.

Isothermal Titration Calorimetry. A VP-ITC isothermal titration calorimeter (MicroCal, Inc., Northampton, MA) was used to measure the binding affinity of the FAD_{ox} - NAD^+ complex. All titrations were performed at 4.2 °C in 25 mM MOPS (pH 7.0). Titrant (1.89 mM NAD^+) was injected in 10- μ L aliquots from a 250- μ L stirred titration syringe into the 1.430-mL sample cell containing 43 μ M MMOR-FAD. Stirring

was maintained at 310 rpm throughout the titrations. In order to measure the heat of dilution for NAD^+ , the experiment was repeated with buffer in the sample cell. Data were integrated and fit with the MicroCal Origin v. 5.0 software package.

MMOR-FAD Reaction with NADH. To examine intramolecular electron transfer for the reduction of MMOR-FAD with NADH, several stopped-flow experiments were performed. A Hi-Tech Scientific SF-61 DX2 double-mixing stopped-flow spectrophotometer configured for either single-wavelength photomultiplier or multi-wavelength diode-array collection was used for all experiments. Prior to use, the stopped-flow apparatus was made anaerobic by flushing the syringes and flow cell with a solution of ca. 5 mM sodium dithionite. The dithionite was then flushed from the system with anaerobic buffer. Oxidized MMOR-FAD protein in 25 mM MOPS (pH 7.0) was made anaerobic by 12-15 cycles of vacuum gas exchange with O_2 -free N_2 . Anaerobic NADH solutions were prepared by bubbling with nitrogen for at least 15 min. Concentrations of MMOR-FAD were 20-40 μM after mixing; NADH concentrations were ~ 10 times that of MMOR-FAD, except where noted. The MMOR-FAD reaction with NADH was monitored at 458, 625, and 725 nm in single-wavelength photomultiplier mode. Data points (512) were collected in 1-s shots on a log time scale. The experiment was repeated with the stopped-flow apparatus in multi-wavelength diode array mode. For each 1.4- or 2-s shot, 160 spectra (295-705 nm or 370-740 nm) were recorded with a logarithmic time base. The temperature was maintained at 4 $^\circ\text{C}$ with a constant temperature circulating water bath for all experiments. Single-wavelength absorbance data were fit to a sum of two or three exponential decays with the program KinetAsyst 2, v. 2.2 (Hi-Tech Limited, Salisbury, England). The Specfit program was used to analyze diode array data and second-order reaction data.

MMOR-FAD reduction with NADH was also investigated over a range of pH values. For these experiments, the FAD domain was prepared in 1 mM MOPS (pH 7.0), 49 mM NaCl and mixed with strongly buffered NADH solutions at the desired pH. Buffers included were 50 mM MES (pH 5.47, 5.93, and 6.29), 50 mM MOPS (pH 6.70, 7.00, and 7.40), and 50 mM TAPS (pH 7.77, 8.21, and 8.47). Ionic strength was maintained at 50 mM by addition of appropriate quantities of NaCl to each buffer. pK_a values for pH-dependent effects were calculated by using eqs 2 and 3.

Interdomain Electron Transfer Reactions. Electron transfer reactions between a) MMOR-FAD_{hq} and MMOR-Fd_{ox}; b) MMOR-FAD_{hq} and MMOR-FAD_{ox}; and c) MMOR-Fd_{ox}/MMOR-FAD_{ox} and NADH were investigated by stopped-flow optical spectroscopy. All experiments were performed in 25 mM MOPS (pH 7.0) or 25 mM potassium phosphate (pH 7.0) at 4 °C and/or 25 °C. Single-wavelength photomultiplier data collection was used for reactions b) and c); multi-wavelength diode array mode was employed for reactions a) and b). Protein concentrations after mixing were 20-30 μ M, except where noted.

RESULTS

General Characterization of MMOR Domains. Both MMOR-Fd (MMOR residues 1-98) and MMOR-FAD (MMOR residues 99-348) were prepared in good yield from recombinant expression systems. Protein purity and cofactor content were monitored effectively by examining absorbance ratios. For MMOR-Fd, an A_{276}/A_{332} ratio of 1.05 indicates pure, fully complemented protein; pure MMOR-FAD has an A_{270}/A_{458} ratio of \sim 6.7. Molecular weights within experimental error of the calculated values for the apoproteins (N-terminal methionine intact for the Fd domain and cleaved for the FAD domain) were obtained by mass spectrometric analysis (Table 3.1).

Iron and FAD determinations were used to calculate extinction coefficients for the domains, assuming 2.0 mol Fe/mol MMOR-Fd and 1.0 mol FAD/mol MMOR-FAD. The Fe K-edge, EXAFS, and Fourier transform spectra of MMOR-Fd and MMOR show only very small differences between the two samples (data not shown). The Fe–Fe and Fe–S distances determined for the fully reduced domain and full-length proteins, are essentially identical (Table 3.1). A second fit, with three long Fe–S distances (ca. 2.3 Å) and one short Fe–S distance (ca. 2.2 Å) was also possible, but the Fe–S paths were just within the resolution of the data for MMOR-Fd and not resolvable for MMOR. It is likely that there is one short Fe–S bond in the [2Fe-2S] cluster; however, the quality of the data does not allow this statement to be made with assurance. The EPR spectra of fully reduced MMOR-Fd and full-length MMOR exhibit rhombic signals characteristic of mixed-valent [2Fe-2S]⁺ centers with nearly identical *g* values. Although the EPR spectra of FAD_{sq,max} and MMOR_{sq,max} are essentially identical, the power saturation behavior for these samples is somewhat different (Figure 3.2), presumably due to the presence of EPR-active [2Fe-2S]⁺ (ca. 60% of total [2Fe-2S]) in the MMOR_{sq,max} sample.²⁸ The UV-visible spectra for the MMOR domains can be added to yield a spectrum identical to that of full-length MMOR (Figure 3.3). Full-length MMOR is not very fluorescent, a property that was previously believed²⁹ to be due to quenching of the FAD fluorescence by the nearby [2Fe-2S] center. Fluorescence studies of MMOR-FAD and free FMN demonstrated that the FAD domain is also a weak fluorophore; therefore, the protein environment around the FAD cofactor must quench most of the flavin fluorescence.

Evolving Factor Analysis for MMOR-FAD Component Spectra. Selected spectra from a reductive titration of MMOR-FAD at pH 7.0 are shown in Figure 3.4A. The FAD_{ox}, FAD_{sq}, and FAD_{hq} component spectra extracted by evolving factor analysis

are displayed in Figure 3.4B. The generated component spectra fit the original titration data extremely well; in addition, the total calculated concentration of MMOR-FAD (the sum of the FAD_{ox} , FAD_{sq} , and FAD_{hq} concentrations) is constant for all of the titration spectra, showing that the component spectra are correctly scaled with respect to each other.

Effect of pH on MMOR Domains Optical Spectra. Below pH 5.5, the Fd and FAD domains precipitate from solution, so the effective range for the pH investigations was 5.5 to 9.3. Over this pH range, the oxidized and reduced MMOR-Fd spectra did not exhibit pH-dependent optical changes. The UV-visible spectra of all three MMOR-FAD chromophores (FAD_{ox} , FAD_{sq} , and FAD_{hq}) are altered by pH (Figure 3.5A). Data corresponding to the wavelengths at which maximum absorbance changes occur reflect processes having pK_a values of 6.55 ± 0.05 (Figure 3.5B) and 7.1 ± 0.2 (Figure 3.5C) for FAD_{ox} and FAD_{hq} respectively. Above pH 8.5, the FAD_{sq} spectra provide evidence for deprotonation of the blue neutral semiquinone species to form a red anionic semiquinone.³⁰ There were not enough data to determine an accurate pK_a for this transition, but the value must be at least 9.

Redox Potentials of MMOR-Fd and MMOR-FAD. Figure 3.6 shows selected difference spectra from a reductive titration of MMOR-FAD in the presence of the indicator phenosafranine. To examine the accuracy of difference fitting, global fits to both difference spectra and the original titration spectra were performed for a reductive titration of MMOR-Fd and AQ2S. The returned $[2Fe-2S]_{ox/red}$ E° values (-205.1 ± 1.3 mV for difference fitting; -208.3 ± 3.8 mV for direct fitting) are essentially identical, except that direct fitting results in a larger standard deviation. Difference spectra emphasize the changes in a sample, so that even small spectral differences can be fit accurately when not obscured by much larger (and unchanged) features. In

addition, difference fitting in many cases reduces the number of independent variables in a fit so that a unique solution may be calculated. Therefore, fitting difference spectra is the method used to calculate component concentrations for all of the redox potential determinations.

Plots of MMOR domain potential versus solution potential were constructed to aid in selecting the data range included in the overall midpoint potential averages. Only those titration points that returned a relatively constant potential over a range of solution potentials were selected. In general, this linear range correlates well with the arbitrary selection of data points with solution potentials within 40 mV of both the estimated domain potential and indicator potential. It was necessary to correct the safranin O range from the calculated -250 to -304 mV to a range of -266 to -322 mV. The calculated midpoint potentials for MMOR-Fd ($[2\text{Fe-2S}]_{\text{ox/red}}$) and MMOR-FAD ($\text{FAD}_{\text{ox/sq}}$ and $\text{FAD}_{\text{sq/hq}}$) are displayed in Table 3.1. Within experimental error, addition of 0.5 equiv MMOH and/or 1 equiv MMOB to MMOR-Fd does not alter the Fd domain potential. MMOH forms complexes with both MMOB^{11} and MMOR-Fd^{31} ; by analogy to MMOR,^{11,16,32} MMOR-Fd is not expected to bind MMOB.

Relative MMOR-FAD redox potentials were determined by analyzing reductive titrations of the FAD domain performed at varying pH values. Because no indicator dye was included in these titrations, the solution potential at each titration point is unknown, and only the difference between the $\text{FAD}_{\text{ox/sq}}$ and $\text{FAD}_{\text{sq/hq}}$ potentials may be computed. Fits to mole fraction vs % reduction plots generated ΔE° ($\text{FAD}_{\text{ox/sq}} - \text{FAD}_{\text{sq/hq}}$) values for each titration, as shown in Figure 3.7A. The MMOR-FAD ΔE° values increase from 80 mV at pH 6.0, the lowest pH examined, to a maximum of 94 mV at pH 7.0, and then decrease to 32 mV at pH 9.0, the highest pH examined (Figure

3.7B). Additional titrations to extend the pH range could not be performed due to protein precipitation at low pH and extremely slow equilibration at high pH.

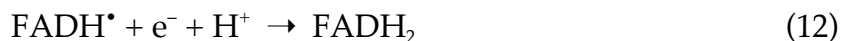
To analyze these data further, it was necessary to account for protons involved in the redox equilibria. For a reductive reaction including a single proton, the measured midpoint potential varies linearly with pH, as shown in eq 9. Therefore, the

$$E_m = E^{\circ} + \frac{RT}{nF} \ln[H^+] = E^{\circ} - \frac{2.303RT}{nF} pH \quad (9)$$

redox potential for a one-electron ($n = 1$), one-proton process exhibits a pH dependence of -59 mV/pH unit at 25 °C. Scheme 3.1 depicts the relevant redox equilibria for MMOR-FAD. At pH values below the FAD_{sq} pK_a (> 9), reduction of FAD_{ox} to the neutral semiquinone state requires a proton (eq 10); above this pK_a value, formation of anionic semiquinone is proton-independent (eq 11). Thus, the $FAD_{ox/sq}$ redox potential



should vary by -59 mV/pH unit at low pH and not at all at high pH (Figure 3.7C, dotted line). For semiquinone reduction to hydroquinone, there are three possible redox equilibria (eqs 12-14). At low and high pH values (eqs 12 and 14, respectively),



the redox reactions include protons. Between the FAD_{hq} and FAD_{sq} pK_a values (6.0 and > 9 , respectively; vide infra), reduction proceeds without protonation (eq 13). Therefore, the $FAD_{sq/hq}$ potential should be constant between pH 6 and ~ 9 and vary by -59 mV/pH unit at low and high pH (Figure 3.7C, dashed line). Combining these

processes yields a ΔE value ($\text{FAD}_{\text{ox/sq}} - \text{FAD}_{\text{sq/hq}}$) that is constant below pH 6, decreases by 59 mV/pH unit between pH 6 and ~9, and increases by 59 mV/pH unit above pH ~9 (Figure 3.7C, solid line).

In order to identify pH-dependent changes in MMOR-FAD redox potentials due to the protein environment, the contributions to ΔE° by the redox equilibria were subtracted from the ΔE° vs pH data. An appropriate ΔE correction curve was constructed with slopes of 0, -59, and +59 mV/pH unit at low, middle, and high pH, respectively, with transitions corresponding to $\text{p}K_a$ values of 6.0 and ≥ 9 (Figure 3.7C). Because the precise FAD_{sq} $\text{p}K_a$ value is unknown, this procedure was repeated for thirteen $\text{p}K_a$ values between 9.0 and 11.4. Subtracting the ΔE correction curves from the MMOR-FAD ΔE° vs pH data yielded titration curves that reflect a process with a $\text{p}K_a$ of 6.8 ± 0.1 and redox potential change of 119 ± 4 mV (Figure 3.7D).

Measurement of the MMOR-FAD_{ox}-NAD⁺ Binding Constant. The binding affinity of NAD⁺ for MMOR-FAD_{ox} was determined by isothermal titration calorimetry. Figure 3.8A shows the power required to compensate for the exothermic binding reaction after each addition of titrant to the sample cell. By integrating these heat pulses with respect to time, the incremental heat change for each injection was calculated. A plot of these data as a function of the NAD⁺/MMOR-FAD molar ratio is presented in Figure 3.8B. Fitting with the one-site model resident in the Origin software yielded the following thermodynamic parameters for the MMOR-FAD_{ox}-NAD⁺ binding reaction: $K_d = 43 \pm 2 \mu\text{M}$; $N = 1.00 \pm 0.05$ binding sites per FAD_{ox} molecule; $\Delta G = -5.5 \text{ kcal mol}^{-1}$; $\Delta H = -7.7 \pm 0.4 \text{ kcal mol}^{-1}$; $T\Delta S = -2.2 \text{ kcal mol}^{-1}$ (solid line in Figure 3.8B).

Kinetics of MMOR-FAD Reduction with NADH. Reduction of the MMOR-FAD domain with NADH was studied by diode array stopped-flow UV-visible

spectroscopy. A typical data set collected for this reaction at pH 7.0 and 4 °C is shown in Figure 3.9A. Spectra corresponding to four intermediates were resolved with Specfit software by using a sequential four-component model with a fixed FAD_{ox} spectrum as the initial species (Figure 3.9B). Upon NADH binding to the MMOR-FAD domain, species CT1, which is characterized by a charge transfer interaction between the NADH nicotinamide ring and flavin isoalloxazine group ($\lambda_{\text{max}} \approx 570 \text{ nm}$), is formed. Hydride transfer from NADH to the oxidized FAD produces intermediate CT2, which exhibits a lower-energy charge transfer band ($\lambda_{\text{max}} > 700 \text{ nm}$) between the NAD⁺ and reduced flavin (FAD_{hq}) groups. The CT2 species decays as NAD⁺ is released from the fully reduced MMOR-FAD protein. The NADH reaction with the FAD domain is summarized in Scheme 3.2.

Single-wavelength stopped-flow data collected at 458, 625, and 725 nm were fit with sums of two or three exponential decays (Figure 3.9C). CT1 formation is observed as an increase in A_{625} at $t < 7 \text{ ms}$; CT2 formation produces an increase in A_{725} at $t < 10 \text{ ms}$. Decreases in both A_{625} and A_{725} at $t > 10 \text{ ms}$ correspond to CT2 decay to FAD_{hq}. All three transitions are reflected as decreases in A_{458} . Rate constants of $350 \pm 20 \text{ s}^{-1}$ (vide infra), $188 \pm 7 \text{ s}^{-1}$, and $89 \pm 4 \text{ s}^{-1}$ were determined for CT1 formation, CT1 decay/CT2 formation, and CT2 decay, respectively, at pH 7.0 and 4 °C.

To investigate NADH binding to MMOR-FAD, single-wavelength stopped-flow experiments were performed with varying concentrations of NADH. The rate of CT1 formation increases hyperbolically with NADH concentration (Figure 3.10), which indicates that a spectroscopically silent intermediate, denoted MC1 for Michaelis complex 1, must precede CT1, the first observed intermediate. By fitting these data with a hyperbolic expression, a K_d value of $25 \pm 4 \mu\text{M}$ was calculated for the FAD domain–NADH binding interaction at 4 °C. Under saturating NADH conditions, the

rate constant for CT1 formation, k_1 , approaches 350 s^{-1} . In addition, at low NADH concentrations the rate of CT2 formation converges with the slower CT1 formation rate (data not shown), further substantiating the kinetic model.

Effect of pH on the Reaction of MMOR-FAD with NADH. Reduction of MMOR-FAD with NADH was also investigated at nine pH values in the range 5.5-8.5. Reaction rates were determined from single-wavelength stopped-flow data collected at each pH value; these results are displayed in Figure 3.11A. CT1 formation (k_1) and CT2 formation (k_2) are somewhat faster at low pH; in addition, k_1 , and possibly k_2 , may increase slightly at high pH. The variation of k_1 with respect to pH reflects either two processes having $\text{p}K_a$ values of 6.61 ± 0.07 and 7.09 ± 0.08 (solid line in Figure 3.11A) or a single process with a $\text{p}K_a$ of 6.2 ± 0.1 (fit not shown). The minimum k_1 value, 230 s^{-1} , occurs near pH 7.0. At low and high pH, k_1 approaches 372 s^{-1} and 274 s^{-1} , respectively. The k_2 data can also be fit fairly well with these $\text{p}K_a$ values, yielding maxima of 330 s^{-1} and 200 s^{-1} at low and high pH values, respectively. The rate of CT2 decay, k_3 , is unchanged throughout this pH range.

Diode array stopped-flow experiments were performed for this reaction at five pH values between 5.5 and 8.5. Spectra corresponding to the FAD_{ox} , CT1, CT2, and FAD_{hq} intermediates were resolved with Specfit software by using a sequential four-component model with a fixed FAD_{ox} spectrum (initial species) determined at the appropriate pH. CT1 spectra are essentially unchanged over this pH range; FAD_{hq} spectra vary as determined above (Figures 3.5A and 3.5C). The CT2 intermediate spectrum, however, is significantly altered as a function of pH, as shown in Figure 3.11B. Large increases in CT2 absorbance between 400 and 500 nm accompany pH decreases. Reducing the pH also converts the CT2 charge transfer band from one characteristic of a FADH^- - NAD^+ complex ($\lambda_{\text{max}} > 700 \text{ nm}$) to one very similar to the

FAD–NADH charge transfer band ($\lambda_{\text{max}} \approx 570 \text{ nm}$) of CT1. In fact, the CT1 and CT2 intermediates determined for data sets collected at pH 5.47 have nearly identical charge transfer bands; therefore, these data can be fit equally well with a sequential three-component model. The changes in CT2 λ_{470} and λ_{700} values with pH reflect a $\text{p}K_{\text{a}}$ of 6.0 ± 0.1 (Figure 3.11C).

Interdomain Electron Transfer Reactions. Reduction of full-length MMOR with NADH proceeds in exactly the same manner described for MMOR-FAD, except that NAD^+ release (CT2 decay) is accompanied by electron transfer from the FAD_{hq} cofactor to the $[\text{2Fe-2S}]^{2+}$ cluster, yielding the FAD_{sq} and $[\text{2Fe-2S}]^+$ oxidation states.^{11,14,16,33} Therefore, electron transfer between the MMOR domains was investigated to determine the effects of separating the domains. Electron transfer from MMOR-FAD_{hq} to Fd_{ox} at 25 °C can be fit as a second-order reaction ($\text{A} + \text{B} \rightarrow \text{C}$) with observed rate constant $k = 1500 \pm 100 \text{ M}^{-1} \text{ s}^{-1}$ (Figure 3.12A). Within a reasonable range of Fd_{ox} concentrations (12.5–50 μM), the second-order rate constant for electron transfer from 12.5 μM MMOR-FAD_{hq} is unchanged. A pseudo-first-order rate constant could not be determined for this reaction due to the high concentration of MMOR-Fd, estimated to be greater than 0.2 M, required to saturate the MMOR-FAD binding site. To examine the possibility that interdomain electron transfer is slow because MMOR-FAD–MMOR-Fd binding is slow, the domains were pre-complexed and allowed to react with NADH in a stopped-flow experiment. Although the CT1 and CT2 formation and decay rate constants are unchanged, electron transfer to the Fd domain is still extremely slow, even at increased temperature. For the comproportionation reaction of MMOR-FAD_{ox} and MMOR-FAD_{hq} to form MMOR-FAD_{sq} at 4 °C, there is a single observed step, which was fit with a second-order model (Figure 3.12B). The observed rate constant for electron transfer, $k = 100 \pm$

$15 \text{ M}^{-1} \text{ s}^{-1}$, describes a slow reaction that should not interfere with the NADH reaction kinetics reported above for MMOR-FAD.

DISCUSSION

Recombinant MMOR Domains. High-yield recombinant expression systems were developed for both the ferredoxin and FAD/NADH domains of MMOR. The NMR solution structure of the MMOR-Fd domain shows that this protein adopts a compact three-dimensional fold similar to that of other plant-type ferredoxins.³⁴ Preliminary NMR studies of the MMOR-FAD protein demonstrate that it too forms a well-defined structure in solution.³⁵ In nearly every respect examined, MMOR-Fd and MMOR-FAD are extremely good models for these domains in the full-length reductase. As judged by optical, EXAFS, and EPR spectroscopy, the domain cofactors are in protein environments nearly identical to those of MMOR. By separating the MMOR domains, the complexity of the full-length protein is reduced without compromising the integrity of most biochemical properties. For some experiments, the domains afford more straightforward data interpretation when compared to the corresponding MMOR study; for others, the MMOR domains provide data that could not have been obtained with the full-length reductase.

For example, the domains have been instrumental in structurally characterizing MMOR. The solution structure of the 10.9-kDa Fd domain was completed recently,³⁴ a feat that would have been far more challenging for the 38.5-kDa MMOR. Determination of high-quality Fd_{ox} , Fd_{red} , FAD_{ox} , FAD_{sq} , and FAD_{hq} component spectra required separation of the [2Fe-2S] and flavin cofactors; these component spectra were essential for accurate determinations of the MMOR redox potentials.¹⁶ Furthermore,

pH-associated optical changes observed for MMOR could not be assigned to individual chromophores without examining MMOR-Fd and MMOR-FAD separately.

Redox Potentials of MMOR-Fd and MMOR-FAD. The redox potentials measured for MMOR-Fd and MMOR-FAD match closely those reported previously for full-length MMOR (Table 3.1).^{13,16} Therefore, it appears that the ferredoxin domain of MMOR exerts no effect on the FAD midpoint potentials (or vice versa). Because data fitting for the MMOR domains required fewer independent parameters (two or three) than for MMOR (four or five), the domain potentials are more precise, as reflected by the significantly smaller standard deviations. The $FAD_{ox/sq}$ potential for MMOR-FAD (-172 ± 2 mV) agrees better with the value reported recently for MMOR, -176 ± 7 mV,¹⁶ than with a previous determination, -150 ± 20 mV,¹³ although all three potentials are within experimental error of each other. The method employed for the MMOR domain and recent MMOR¹⁶ redox potential studies has several advantages, including the avoidance of dyes that bind to the investigated proteins, simultaneous data fitting over the entire visible region, the production of multiple potential measurements for each experiment, and collection of all data at a single regulated temperature. For these reasons, the lower $FAD_{ox/sq}$ midpoint potential determined with this method is probably more accurate. Addition of MMOH or MMOB does not affect the MMOR-Fd midpoint potential within experimental error. A lag phase preceding Fd reduction was observed in titrations including MMOH, presumably due to electron transfer to the MMOH diiron sites mediated by the Fd domain.

Reaction of MMOR-FAD with NADH. The following kinetic model, which accounts for the results of stopped-flow optical experiments, is proposed for the reduction of the FAD domain with NADH at pH 7.0 and 4 °C (Scheme 3.2). The chemistry for this reaction corresponds directly with the first steps of the

MMOR–NADH reaction.^{11,16} In the first step, NADH binds rapidly to MMOR-FAD, forming a Michaelis complex, MC1, with an optical spectrum identical to that of FAD_{ox}. The K_d value for this interaction is $25 \pm 4 \mu\text{M}$ (Figure 3.10). Isothermal titration calorimetry experiments yielded a K_d of $43 \pm 2 \mu\text{M}$ for NAD⁺ binding to FAD_{ox} (Figure 3.8). MMOR binds NADH significantly more tightly with a measured K_d value of $3.8 \mu\text{M}$.¹⁶ This result suggests that the NADH binding site of MMOR-FAD differs from that of the full-length MMOR. Possibilities for this reduced NADH–FAD_{ox} binding affinity include structural or hydrogen bonding perturbations near the NADH binding site.

A conformational change, which occurs with an observed rate constant of 350 s^{-1} at pH 7.0, gives rise to the FAD–NADH charge transfer interaction of intermediate CT1. Due to the relatively weak FAD_{ox}–NADH binding ($K_d = 25 \mu\text{M}$), a 30-fold excess of NADH is required to approach the 350 s^{-1} limit for CT1 formation. Because many experiments were performed with only a 10-fold excess of NADH, the observed rate constant for this step was typically $290 \pm 20 \text{ s}^{-1}$ (Figure 3.9). In the MMOR–NADH reaction, CT1 formation proceeds at the same rate ($k = 350 \text{ s}^{-1}$ at 4 °C) with saturating NADH.¹⁶

Hydride transfer from NADH to FAD produces the CT2 intermediate with a rate constant of 188 s^{-1} . This species is characterized by a FADH[−]–NAD⁺ charge transfer band that is more intense and lower in energy than the FAD–NADH charge transfer band of CT1. Release of NAD⁺, yielding the hydroquinone form of MMOR-FAD, occurs with a rate constant of 89 s^{-1} . The rate constants for the corresponding steps of the MMOR–NADH reaction, 190 s^{-1} and 90 s^{-1} , respectively, are nearly identical.¹⁶ It appears that, once NADH binds to MMOR-FAD, the electron transfer steps proceed exactly as reported for MMOR. In full-length MMOR, CT2 decay is accompanied by

electron transfer from the reduced flavin cofactor to the [2Fe-2S] cluster, generating a species, SQ, comprising mainly FAD_{sq} and Fd_{red} .^{11,16} Electron transfer between the two MMOR cofactors occurs with a rate constant of 130 s^{-1} , as measured in a pH jump experiment.¹⁶ Based on this result, it was proposed that the slower electron transfer rate constant (90 s^{-1}) observed in the MMOR–NADH reaction is limited by the rate of NAD^+ release. The CT2 decay rate constant reported here for the isolated NAD^+ release step in MMOR-FAD (89 s^{-1}) supports this theory.

Influence of pH on MMOR-FAD Spectral, Redox, and Kinetic Properties. The UV-visible spectra of FAD_{ox} , FAD_{sq} , and FAD_{hq} species all exhibit pH-dependent changes, as depicted in Figure 3.5, with $\text{p}K_{\text{a}}$ values of 6.55 ± 0.05 , > 9 , and 7.1 ± 0.2 , respectively. As observed by extinction coefficient increases around 300 nm and decreases above 500 nm at high pH, the FAD_{sq} optical transition represents deprotonation of the blue neutral semiquinone to form a red species characteristic of anionic flavin semiquinone (Scheme 3.1). The macroscopic $\text{p}K_{\text{a}}$ values observed for the FAD_{ox} and FAD_{hq} chromophores are most likely associated with protonatable groups near or hydrogen bonded to the flavin isoalloxazine moiety rather than direct protonation of the flavin itself. Protonation of protein-bound flavins in the hydroquinone oxidation state typically occurs with a $\text{p}K_{\text{a}}$ below 6,³⁶ so the $\text{p}K_{\text{a}}$ of 7.1 noted for the FAD_{hq} optical spectrum probably corresponds to a different protonation event.

Equilibrium reductive titrations of MMOR-FAD at varying pH show that ΔE° ($\text{FAD}_{\text{ox/sq}} - \text{FAD}_{\text{sq/hq}}$) is maximized near pH 7.0 (Figure 3.7B). Above or below this pH, the difference in potentials is diminished. By correcting for the flavin redox equilibria-linked ΔE contributions, a protein-dependent $\text{p}K_{\text{a}}$ of 6.8 ± 0.1 for the MMOR-FAD ΔE° values is revealed (Figure 3.7D). This $\text{p}K_{\text{a}}$ value may reflect the combined effects of the

two protein-associated pK_a values (6.6 and 7.1) determined for the MMOR-FAD optical spectra and CT1 formation rate constant (*vide infra*). Because the measured ΔE° values reflect the difference between $FAD_{ox/sq}$ and $FAD_{sq/hq}$ either or both potentials may be affected by protonation of the protein environment. The corresponding MMOR ΔE° values exhibit a similar trend, with reported pK_a values of 6.6 ± 0.5 and 7.6 ± 0.9 .¹⁶ Analyzing the MMOR ΔE° vs pH data (Figure 8 in ref 16) in the same manner described here for MMOR-FAD yields a single pK_a of 6.5 ± 0.2 for ΔE° variation.³⁷

Kinetic studies of the MMOR-FAD reduction with NADH at varying pH values revealed several interesting pH-dependent features of this reaction. The CT1 formation rate constant, k_1 in Scheme 3.2, increases at low pH and possibly also at high pH. In addition, the CT1 decay/CT2 formation rate constant exhibits a similar, but less pronounced, variation with pH. The k_1 data could be fit as either one ($pK_a = 6.2 \pm 0.1$) or two ($pK_a = 6.61 \pm 0.07$ and 7.09 ± 0.08) pH-dependent processes (Figure 3.11A). Compared to the single- pK_a model, the two- pK_a model generates a better fit to the k_1 versus pH data and is therefore favored. In support of this assignment, the pK_a values calculated for this fit exactly match those determined for pH-dependent changes in the FAD_{ox} ($pK_a = 6.55 \pm 0.05$) and FAD_{hq} ($pK_a = 7.1 \pm 0.2$) optical spectra. Formation of the CT1 intermediate is presumed to represent a conformational change that orients the pyridine nucleotide and flavin isoalloxazine groups for efficient electron transfer, as indicated by the appearance of a FAD–NADH charge transfer band. Such a conformational reorganization step could easily be influenced by protonatable amino acid side chains hydrogen bonded to or in the vicinity of the prosthetic groups. The nature of these processes may be clarified when the structure of MMOR-FAD is available. At $pH < 6$, the k_1 value for the MMOR-FAD reaction with NADH reaches the value reported for this step (350 s^{-1}) in the corresponding MMOR reaction.¹⁶ The amino

acid side chain responsible for the k_1 variation in MMOR-FAD may be protected from deprotonation or have an altered pK_a in MMOR. Alternatively, a more extensive hydrogen bonding network in MMOR, including contacts between the Fd and FAD domains, may make this residue less relevant for orienting the cofactors in MMOR. The weaker binding of NADH to MMOR-FAD compared to MMOR (25 μM vs 3.8 μM) may also arise from a slightly perturbed hydrogen bonding network in the NADH binding cavity, possibly due to the same side chain that affects the CT1 formation rate constant. In fact, the variation in k_1 with pH may simply reflect differences in NADH binding affinity such that the NADH binding site is saturated only at low pH.

Spectra corresponding to the kinetic intermediates observed in the MMOR-FAD reaction with NADH were resolved by global analysis of diode array stopped-flow data. Over the pH range 5.5-8.5, the CT1 spectrum is unchanged; the CT2 intermediate, however, undergoes significant optical changes that reflect a pK_a of 6.0 ± 0.1 (Figures 3.11B and 3.11C). At pH 5.5, the CT2 optical spectrum closely resembles the CT1 intermediate, particularly at $\lambda > 530$ nm. The charge transfer bands for these two species are essentially indistinguishable. This phenomenon arises from protonation at flavin position N1 of anionic FAD_{hq} (FADH^-) to form FADH_2 (Scheme 3.1). The charge transfer interaction between neutral FADH_2 and NAD^+ is significantly weaker than that between FADH^- and NAD^+ but quite similar to the FAD -NADH charge transfer interaction of CT1. The measured FAD_{hq} pK_a for MMOR-FAD is within the range of values determined by NMR for N1 protonation in other flavoproteins.³⁶ A similar pK_a of 6.2 ± 0.1 was attributed to protonation of the flavin N1 site in MMOR.¹⁶

The pK_a values of ~ 6.5 and 6.8 noted for the FAD_{ox} optical spectrum and ΔE° values, respectively, may correspond to one or more carboxylate groups near the N1 and/or N3 position(s) of the flavin isoalloxazine ring system. Similar pK_a values have

been attributed to carboxylate moieties near the flavin cofactors of other flavoproteins.^{38,39} Deprotonation of the carboxylate(s) would destabilize the anionic FAD_{hq} , thereby decreasing the $\text{FAD}_{\text{sq/hq}}$ potential and increasing ΔE° at high pH, as observed for MMOR-FAD. In flavodoxin, neutralization of individual acidic residues via amide substitution does not eliminate the redox-linked $\text{p}K_{\text{a}}$ observed for the flavin semiquinone/hydroquinone redox potential.^{40,41} Increasing numbers of acid-to-amide flavodoxin mutations, however, increase this potential in an additive manner, with average contributions of about 15 mV per substitution.⁴² Moreover, the pH dependence of the semiquinone/hydroquinone potential decreases progressively with the number of charge neutralizations.⁴⁰ Thus, for flavodoxin, modulation of this redox potential appears to be controlled by the collective effect of multiple acidic residues surrounding the flavin cofactor.^{40,41} The $\text{p}K_{\text{a}}$ values determined for MMOR-FAD may also be macroscopic quantities that reflect multiple protonation events with similar microscopic $\text{p}K_{\text{a}}$ values.

The MMOR- FAD_{hq} $\text{p}K_{\text{a}}$ of 6.0 is higher than that observed in many flavoproteins, most of which exhibit a $\text{p}K_{\text{a}} < 5$ for the hydroquinone oxidation state.³⁶ Placement of a negative electrostatic field near the flavin cofactor could contribute to this phenomenon by destabilizing the anionic hydroquinone species (Scheme 3.1). In addition, removing a negative charge from this position in the flavodoxin E60Q mutant produces an optical change for the oxidized protein³⁹ very similar to that observed for FAD_{ox} at low pH, where the putative charge(s) would be neutralized by protonation. The $\text{p}K_{\text{a}}$ of 7.1 observed for the FAD_{hq} optical spectrum might even correspond to the same carboxylate group(s); the presence of a negative charge on the flavin would be expected to increase the $\text{p}K_{\text{a}}$ of nearby carboxylate groups, as suggested for flavodoxin.³⁸

By comparing the preliminary MMOR-FAD NMR structure and the structures of homologous proteins, including PDR,¹⁹ *Alcaligenes eutrophus* flavohemoglobin,⁴³ and *Azotobacter vinelandii* NADPH:ferredoxin reductase,⁴⁴ candidates for the negatively charged MMOR-FAD residue(s) were identified as Asp52, Glu85, and Asp90. In the other flavoproteins, these non-conserved residues are in or near homologous sequences having atoms ≤ 7 Å from the isoalloxazine N1, N3, or N5 positions. Subsequent analysis of the nearly completed MMOR-FAD NMR structure⁴⁵ revealed three carboxylate side chains within 10 Å of the FAD cofactor: Glu243 (4.5-5.0 Å), Asp52 (5.0-5.5 Å), and Asp59 (7.5-10.0 Å). The Glu243 and Asp52 residues are completely conserved in sMMO reductases, whereas Asp59 is replaced by His or Thr in other MMOR proteins. Addition/removal of other charges near the flavin cofactor, or a conformational change that alters hydrogen bonding or solvent accessibility to the isoalloxazine ring system, may also contribute to the pH dependence observed for the MMOR-FAD optical spectra and redox potentials.^{39,46-49} More definitive assignment of the pK_a effects to specific protein residues awaits completion of the MMOR-FAD structure and site-directed mutagenesis studies.

Interdomain Electron Transfer. Electron transfer from MMOR-FAD_{hq} to either Fd_{ox} or MMOR-FAD_{ox} occurs on a very slow time scale ($k = 1500 \text{ M}^{-1} \text{ s}^{-1}$ at 25 °C and $100 \text{ M}^{-1} \text{ s}^{-1}$ at 4 °C, respectively). It is particularly interesting to compare the interdomain electron transfer rates for the separated domains with the corresponding step in MMOR reduction with NADH ($k = 90 \text{ s}^{-1}$ at 4 °C).¹⁶ Presumably, the [2Fe-2S] and flavin cofactors in MMOR are positioned in an orientation amenable to electron transfer with minimal structural reorganization. The large effective rate decrease (at 25 °C) for the noncovalently linked domains suggests that cofactor proximity is extremely important for efficient electron transfer in MMOR.

In FNR (Figure 3.1), a flavoprotein electron transferase protein with a dissociable one-electron carrier, ferredoxin, transient noncovalent complexes between the flavin and [2Fe-2S] proteins afford relatively fast electron transfer ($k \approx 1500\text{-}7000\text{ s}^{-1}$)¹⁹ between cofactors. The X-ray structure of a complex between maize leaf ferredoxin and FNR reveals an intermolecular interface comprising mainly electrostatic interactions in the form of salt bridges and a hydrophobic region between the cofactors.⁵⁰ Precomplexing MMOR-Fd and MMOR-FAD before reduction with NADH did not significantly increase the observed interdomain electron transfer rates. This result implies that, unlike the ferredoxin:FNR system, the separated MMOR domains do not form a specific complex or that the complex that forms is unsuitable for efficient electron transfer. For full-length MMOR, in which the Fd and FAD domains are covalently tethered, high-affinity interdomain interactions are apparently unnecessary. Therefore, it appears that proximity rather than affinity facilitates interdomain electron transfer in MMOR.

Conclusions. This work demonstrates that the modular structure of MMOR can be exploited to simplify and extend characterization of a complex protein. Except for interdomain electron transfer, the separated MMOR-Fd and MMOR-FAD proteins retain essentially identical biochemical properties to the corresponding domains in MMOR. In simplifying a complicated system, these domains have already proved valuable for characterizing the structure and intramolecular electron transfer properties of the full-length reductase.^{16,34} By examining electron transfer to MMOH from both MMOR and MMOR-Fd, elucidation of the carefully orchestrated intermolecular electron transfer steps in the sMMO catalytic cycle will be possible.

ACKNOWLEDGMENT

This work was supported by National Institutes of Health Research Grant GM32134 (S.J.L.). J.L.B. was a Howard Hughes Medical Institute predoctoral fellow. We thank Dr. George T. Gassner for many helpful discussions and critical reading of the manuscript, Dr. Jens Müller and Lisa L. Chatwood for help with structural analysis, Dr. Maarten Merkx for EXAFS sample preparation and assistance in collecting EPR data, and Deanne Jackson Rudd, Dr. Britt Hedman, and Prof. Keith O. Hodgson for EXAFS data collection and analysis. We also acknowledge the Multiuser Facility for the Study of Complex Macromolecular Systems (NSF-0070319) for access to an isothermal titration calorimeter.

REFERENCES

- (*) This work has appeared previously in slightly altered form in reference (†).
Samples for XAS were prepared by Maarten Merkx, and EXAFS data collection and analysis were performed at Stanford University by Deanne Jackson Rudd, Britt Hedman, and Keith O. Hodgson.
- (†) Blazyk, J. L.; Lippard, S. J. *Biochemistry* **2002**, *41*, 15780-15794.
- (1) Higgins, I. J.; Best, D. J.; Hammond, R. C. *Nature* **1980**, *286*, 561-564.
- (2) Nguyen, H.-H. T.; Elliott, S. J.; Yip, J. H.-K.; Chan, S. I. *J. Biol. Chem.* **1998**, *273*, 7957-7966.
- (3) Prior, S. D.; Dalton, H. J. *Gen. Microbiol.* **1985**, *131*, 155-163.
- (4) Woodland, M. P.; Dalton, H. J. *Biol. Chem.* **1984**, *259*, 53-59.
- (5) Green, J.; Dalton, H. J. *Biol. Chem.* **1985**, *260*, 15795-15801.
- (6) Liu, K. E.; Lippard, S. J. In *Adv. Inorg. Chem.*; Sykes, A. G., Ed.; Academic Press: San Diego, 1995; Vol. 42, pp 263-289.
- (7) Feig, A. L.; Lippard, S. J. *Chem. Rev.* **1994**, *94*, 759-805.
- (8) Wallar, B. J.; Lipscomb, J. D. *Chem. Rev.* **1996**, *96*, 2625-2657.
- (9) Merkx, M.; Kopp, D. A.; Sazinsky, M. H.; Blazyk, J. L.; Müller, J.; Lippard, S. J. *Angew. Chem. Int. Ed.* **2001**, *40*, 2782-2807.
- (10) Colby, J.; Dalton, H. *Biochem. J.* **1978**, *171*, 461-468.
- (11) Gassner, G. T.; Lippard, S. J. *Biochemistry* **1999**, *38*, 12768-12785.
- (12) Merkx, M.; Lippard, S. J. *J. Biol. Chem.* **2002**, *277*, 5858-5865.
- (13) Lund, J.; Dalton, H. *Eur. J. Biochem.* **1985**, *147*, 291-296.
- (14) Lund, J.; Woodland, M. P.; Dalton, H. *Eur. J. Biochem.* **1985**, *147*, 297-305.
- (15) Stainthorpe, A. C.; Lees, V.; Salmond, G. P. C.; Dalton, H.; Murrell, J. C. *Gene* **1990**, *91*, 27-34.

- (16) Kopp, D. A.; Gassner, G. T.; Blazyk, J. L.; Lippard, S. J. *Biochemistry* **2001**, *40*, 14932-14941.
- (17) Andrews, S. C.; Shipley, D.; Keen, J. N.; Findlay, J. B. C.; Harrison, P. M.; Guest, J. R. *FEBS Lett.* **1992**, *302*, 247-252.
- (18) Karplus, P. A.; Daniels, M. J.; Herriott, J. R. *Science* **1991**, *251*, 60-66.
- (19) Correll, C. C.; Batie, C. J.; Ballou, D. P.; Ludwig, M. L. *Science* **1992**, *258*, 1604-1610.
- (20) Gassner, G. T.; Ballou, D. P. *Biochemistry* **1995**, *34*, 13460-13471.
- (21) Massey, V. *J. Biol. Chem.* **1957**, *229*, 763-770.
- (22) Stookey, L. L. *Anal. Chem.* **1970**, *42*, 779-781.
- (23) Thompson, J. D.; Higgins, D. G.; Gibson, T. J. *Nucleic Acids Res.* **1994**, *22*, 4673-4680.
- (24) Stainthorpe, A. C.; Murrell, J. C.; Salmond, G. P. C.; Dalton, H.; Lees, V. *Arch. Microbiol.* **1989**, *152*, 154-159.
- (25) Rehr, J. J.; Mustre de Leon, J.; Zabinsky, S. I.; Albers, R. C. *J. Am. Chem. Soc.* **1991**, *113*, 5135-5140.
- (26) Mustre de Leon, J.; Rehr, J. J.; Zabinsky, S. I.; Albers, R. C. *Phys. Rev. B* **1991**, *44*, 4146-4156.
- (27) Yeh, A. P.; Chatelet, C.; Soltis, S. M.; Kuhn, P.; Meyer, J.; Rees, D. C. *J. Mol. Biol.* **2000**, *300*, 587-595.
- (28) Galli, C.; Innes, J. B.; Hirsh, D. J.; Brudvig, D. J. *J. Magn. Reson. Ser. B* **1996**, *110*, 284-287.
- (29) Gassner, G. T.; Lippard, S. J., unpublished results.
- (30) Massey, V.; Hemmerich, P. *Biochem. Soc. Trans.* **1980**, *8*, 246-257.
- (31) Blazyk, J. L.; Gassner, G. T.; Lippard, S. J. **2003**, manuscript in preparation.

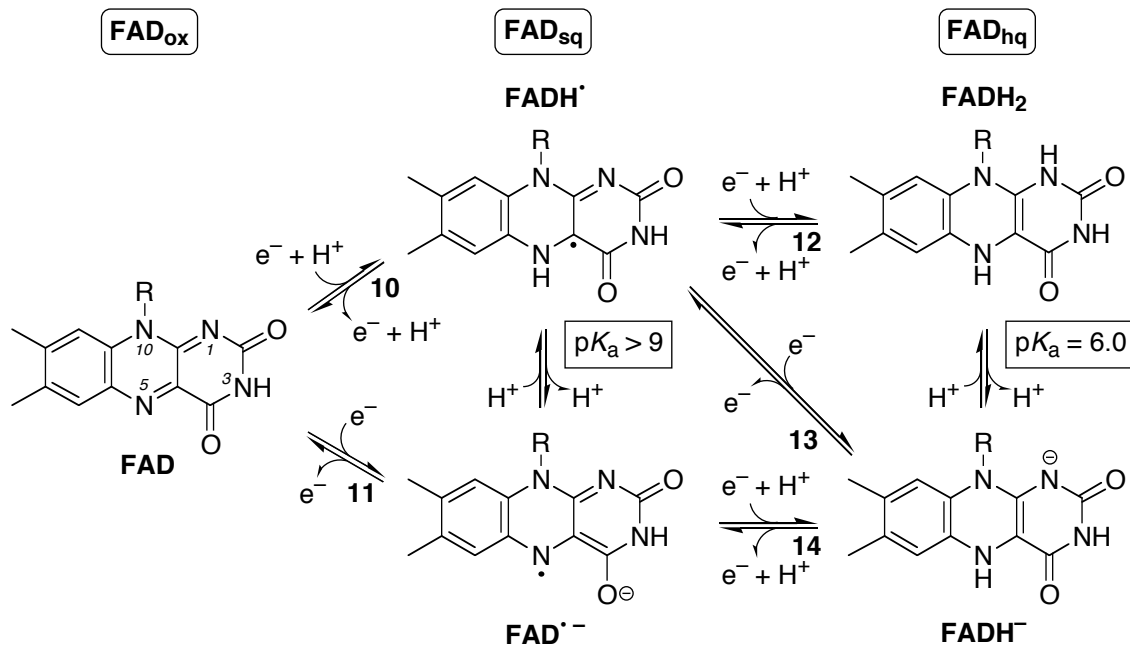
- (32) Walters, K. J.; Gassner, G. T.; Lippard, S. J.; Wagner, G. *Proc. Natl. Acad. Sci. USA* **1999**, *96*, 7877-7882.
- (33) Green, J.; Dalton, H. *Biochem. J.* **1989**, *259*, 167-172.
- (34) Müller, J.; Lugovskoy, A. A.; Wagner, G.; Lippard, S. J. *Biochemistry* **2002**, *41*, 42-51.
- (35) Müller, J.; Wagner, G.; Lippard, S. J., unpublished results.
- (36) Müller, F. In *Chemistry and Biochemistry of Flavoenzymes*; Müller, F., Ed.; CRC Press: Boca Raton, FL, 1992; Vol. 3, pp 557-595.
- (37) Blazyk, J. L.; Kopp, D. A.; Lippard, S. J., unpublished results.
- (38) Ludwig, M. L.; Schopfer, L. M.; Metzger, A. L.; Pattridge, K. A.; Massey, V. *Biochemistry* **1990**, *29*, 10364-10375.
- (39) Geoghegan, S. M.; Mayhew, S. G.; Yalloway, G. N.; Butler, G. *Eur. J. Biochem.* **2000**, *267*, 4434-4444.
- (40) Swenson, R. P.; Zhou, Z. In *Flavins and Flavoproteins*; Stevenson, K. J., Massey, V., Williams, C. H., Jr., Eds.; University of Calgary Press: Calgary, Canada, 1997, pp 427-436.
- (41) Bradley, L. H.; Swenson, R. P. *Biochemistry* **1999**, *38*, 12377-12386.
- (42) Zhou, Z.; Swenson, R. P. *Biochemistry* **1995**, *34*, 3183-3192.
- (43) Ermler, U.; Siddiqui, R. A.; Cramm, R.; Friedrich, B. *EMBO J.* **1995**, *14*, 6067-6077.
- (44) Prasad, G. S.; Kresge, N.; Muhlberg, A. B.; Shaw, A.; Jung, Y. S.; Burgess, B. K.; Stout, C. D. *Protein Sci.* **1998**, *7*, 2541-2549.
- (45) Chatwood, L. L.; Müller, J.; Gross, J. D.; Wagner, G.; Lippard, S. J., unpublished results.
- (46) Bradley, L. H.; Swenson, R. P. *Biochemistry* **2001**, *40*, 8686-8695.
- (47) Zhou, Z.; Swenson, R. P. *Biochemistry* **1996**, *35*, 15980-15988.

- (48) Hoover, D. M.; Drennan, C. L.; Metzger, A. L.; Osborne, C.; Weber, C. H.; Pattridge, K. A.; Ludwig, M. L. *J. Mol. Biol.* **1999**, *294*, 725-743.
- (49) Ludwig, M. L.; Pattridge, K. A.; Metzger, A. L.; Dixon, M. M.; Eren, M.; Feng, Y.; Swenson, R. P. *Biochemistry* **1997**, *36*, 1259-1280.
- (50) Kurisu, G.; Kusunoki, M.; Katoh, E.; Yamazaki, T.; Teshima, K.; Onda, Y.; Kimata-Arigo, Y.; Hase, T. *Nature Struct. Biol.* **2001**, *8*, 117-121.

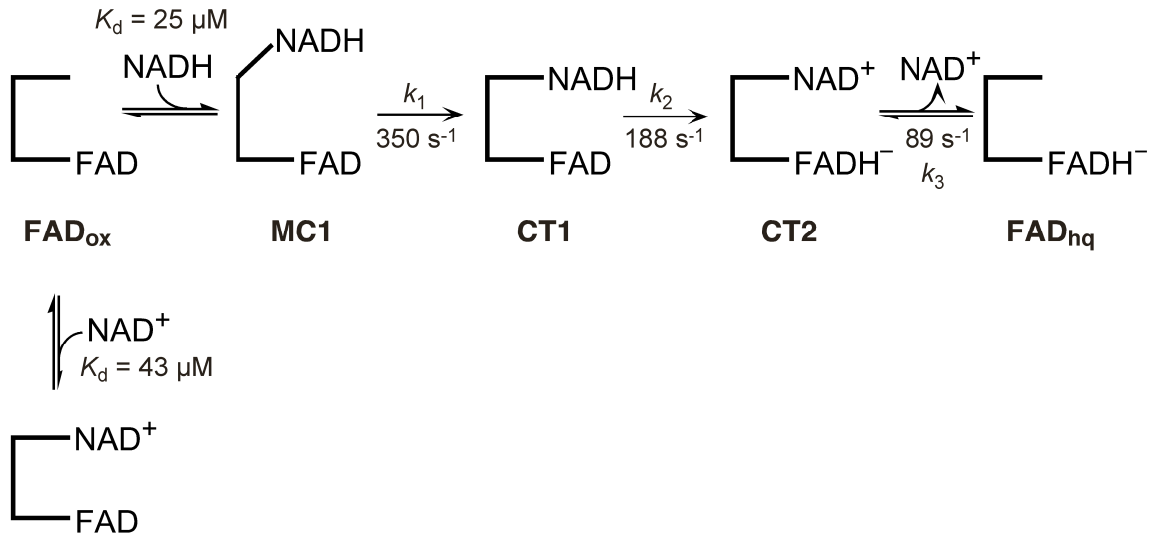
Table 3.1: Properties of MMOR-Fd, MMOR-FAD, and MMOR

	MMOR-Fd	MMOR-FAD	MMOR
MW measured (Da)	10,929.0 ^a ± 1.1	27,629.0 ^b ± 2.4	38,546.9 ± 3.9 ^c
ϵ_{458} (M ⁻¹ cm ⁻¹), pH 7.0, 25 °C	9550 ± 200	11,000 ± 500	20,800 ± 1000 ^d
ϵ_{\max} (nm), pH 7.0, 25 °C	332, 418, 467	394, 458	332, 394, 458 ^c
Fe-Fe (Å, fully reduced)	2.73	n/a	2.74
Fe-S (Å, fully reduced)	2.29	n/a	2.29
g values (fully reduced) ^e	2.049, 1.958, 1.888	n/a	2.047, 1.958, 1.871
g values (maximum FAD _{sq})	n/a	2.004 ^f	2.005 ^g
FAD _{ox/sq} (mV), pH 7.0, 25 °C	n/a	-172.4 ± 2.0	-176 ± 7 ^c
[2Fe-2S] _{ox/red} (mV), pH 7.0, 25 °C	-205.2 ± 1.3	n/a	-209 ± 14 ^c
FAD _{sq/hq} (mV), pH 7.0, 25 °C	n/a	-266.4 ± 3.5	-266 ± 15 ^c

^aExpected 10,931.3 Da for apoprotein with N-terminal methionine intact. ^bExpected 27,628.3 Da for apoprotein with N-terminal methionine cleaved. ^cAs reported in ref 16. ^dAs reported in ref 11. ^eEPR recorded at 10 K, 500 μ W at 9.478 GHz, 10.0-G modulation amplitude. ^fEPR recorded at 100 K, 32 μ W at 9.478 GHz, 2.0-G modulation amplitude. ^gEPR recorded at 100 K, 127 μ W at 9.482 GHz, 2.0-G modulation amplitude.



Scheme 3.1



Scheme 3.2

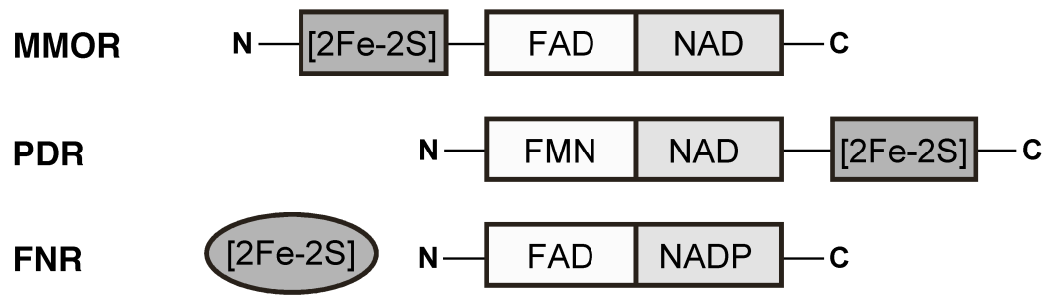


Figure 3.1. Examples of alternative connectivities between the one-electron carrier and flavin/NAD(P) binding domains of flavoprotein electron transferases.

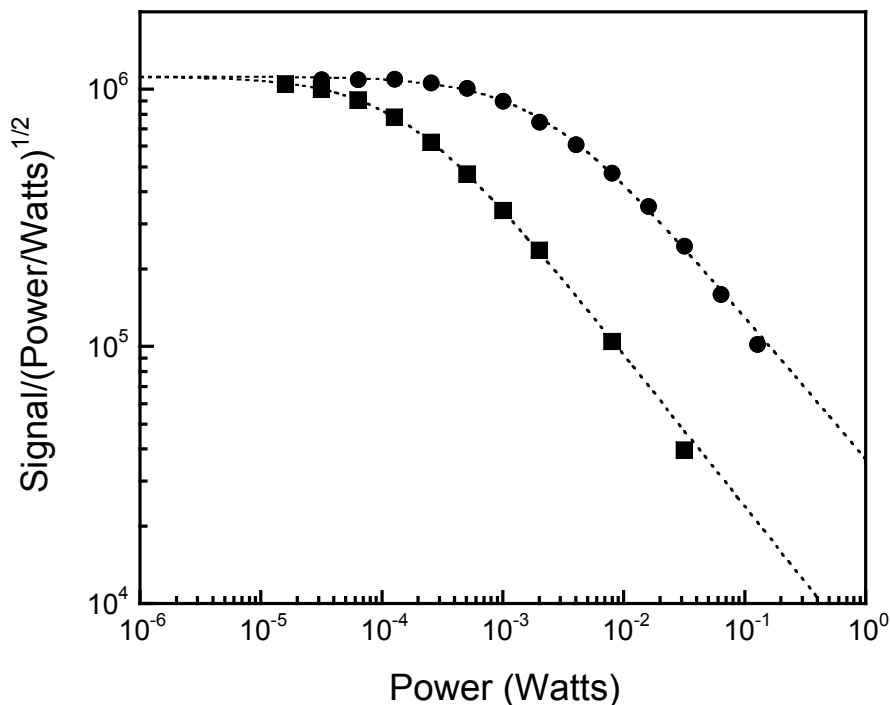


Figure 3.2. Microwave progressive power saturation data for MMOR-FAD_{sq,max} (squares) and MMOR_{sq,max} (circles) collected at 100 K, 9.48 GHz, 2.0-G modulation amplitude. The dotted lines are least-squares fits to the equation, $S'/P^{1/2} = K/[1 + (P/P_{1/2})^b]$, where S' is the EPR derivative signal amplitude, P is the microwave power, K is a constant, $P_{1/2}$ is the microwave power at half-saturation, and b is the inhomogeneity parameter, as described in ref 28. Compared to MMOR-FAD_{sq,max}, the MMOR_{sq,max} sample requires higher power to saturate the EPR signal.

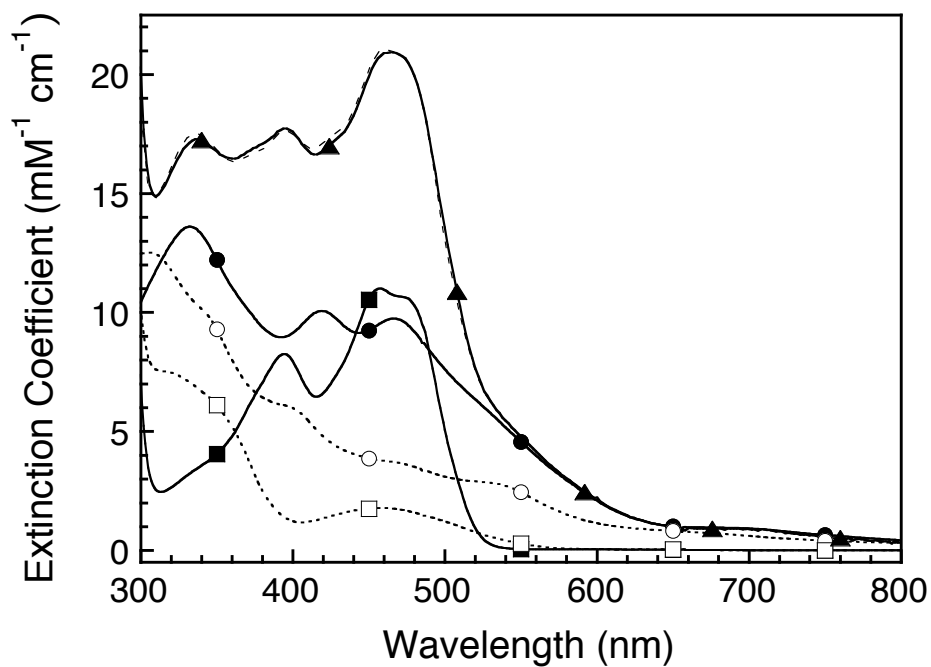


Figure 3.3. Optical spectra at pH 7.0 of MMOR-Fd (circles) and MMOR-FAD (squares) in the fully oxidized (closed symbols and solid lines) and fully reduced (open symbols and dotted lines) oxidation states. The sum of the two oxidized domain spectra (dashed line) is superimposed on the MMOR optical spectrum (triangles).

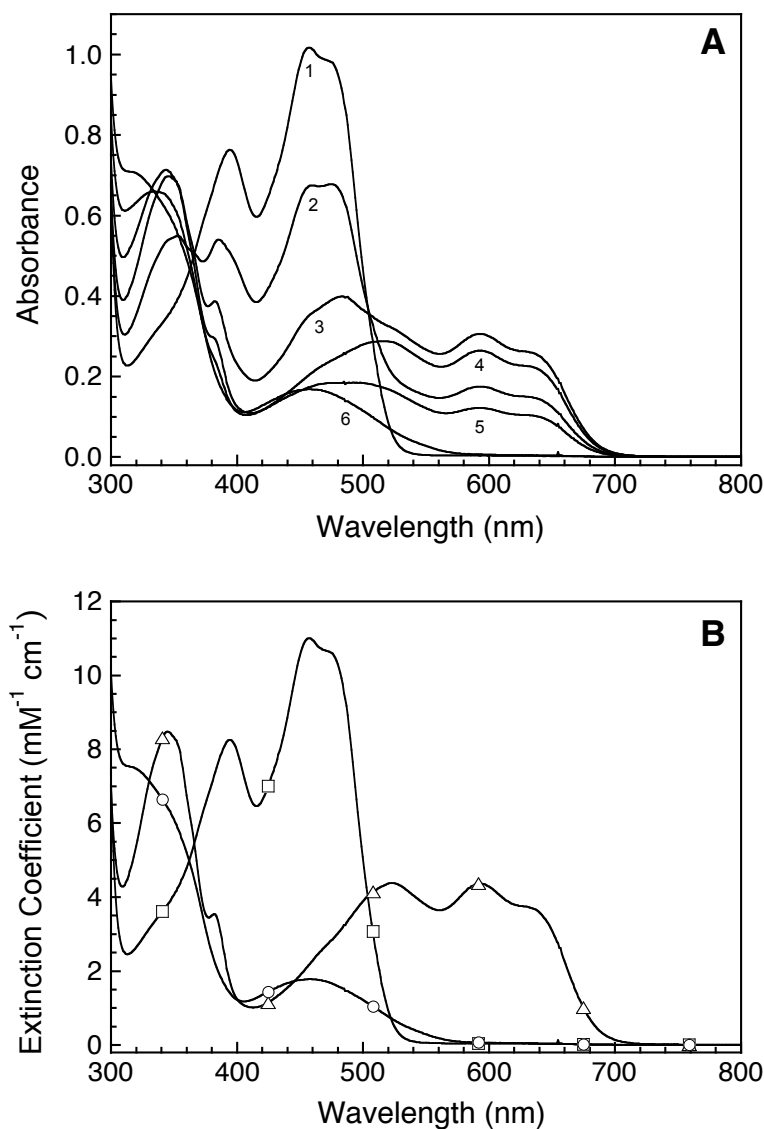


Figure 3.4. Determination of the FAD_{sq} optical spectrum at pH 7.0. (A) Selected spectra from an anaerobic reductive titration of 91 μM MMOR-FAD with ~ 2 mM dithionite at 25 $^{\circ}\text{C}$. (B) Component spectra, which correspond to the FAD_{ox} (squares), FAD_{sq} (triangles), and FAD_{hq} (circles) oxidation states, derived from evolving factor analysis of the titration data.

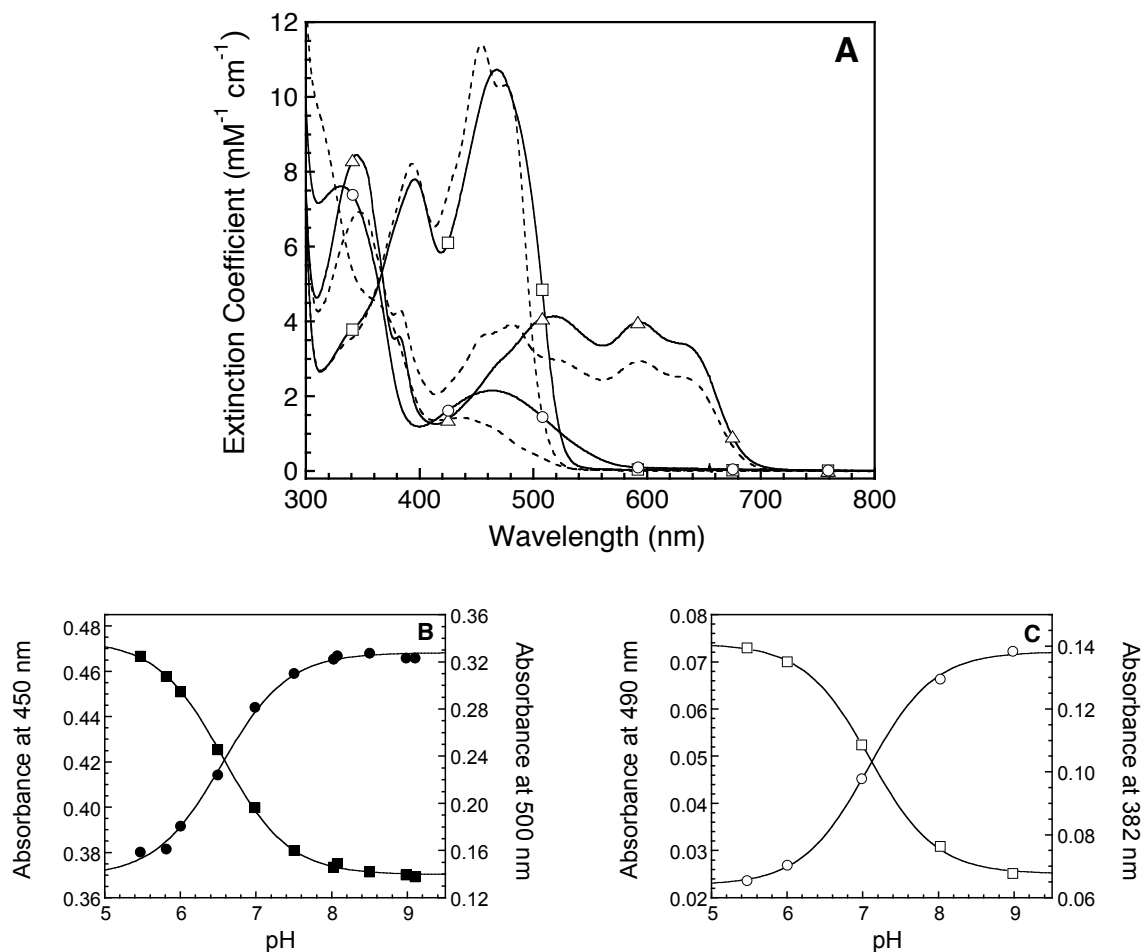


Figure 3.5. Effect of pH on the MMOR-FAD optical spectra. (A) FAD_{ox} (squares), FAD_{sq} (triangles), and FAD_{hq} (circles) component spectra determined at pH 6 (solid lines) and pH 9 (dashed lines). (B) FAD_{ox} absorbance at 450 (circles) and 500 nm (squares) as a function of pH. (C) Variation of FAD_{hq} absorbance at 382 (circles) and 490 nm (squares) with pH. Solid lines in panels B and C are fits to eqs 2 and 3.

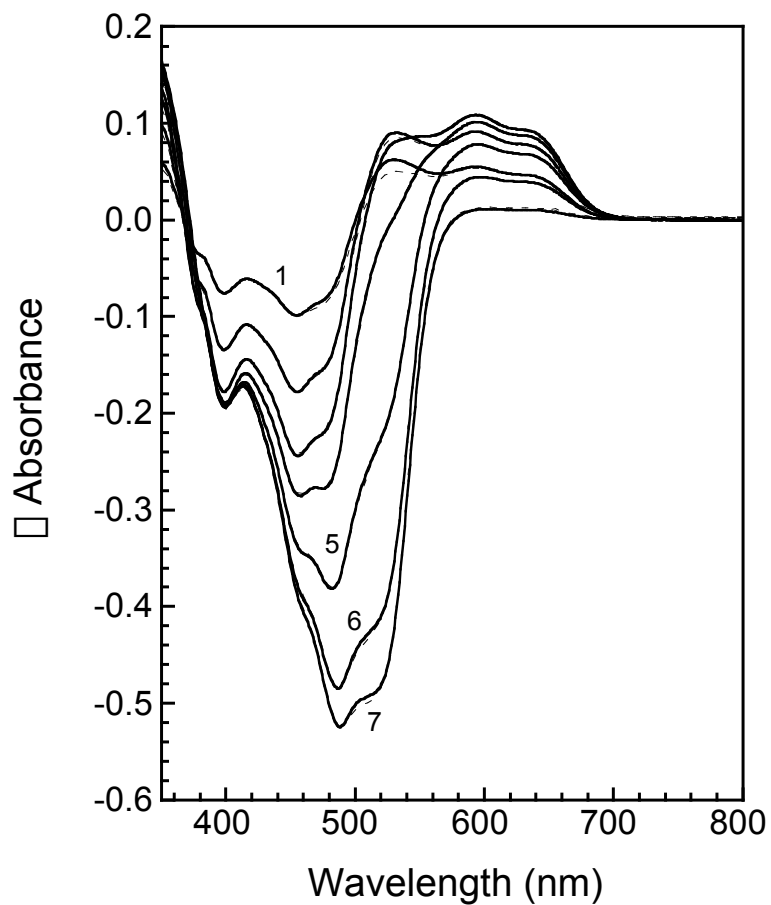


Figure 3.6. Difference spectra for the reductive titration of a 1-mL mixture of 30 μM MMOR-FAD and 11 μM phenosafranine by dithionite at pH 7.0 and 25 $^{\circ}\text{C}$. Spectra 1-7 correspond to the addition of 20, 30, 40, 50, 70, 90, and 110 μL of ~ 2 mM dithionite, respectively. Fits (dashed lines) are superimposed on the difference spectra.

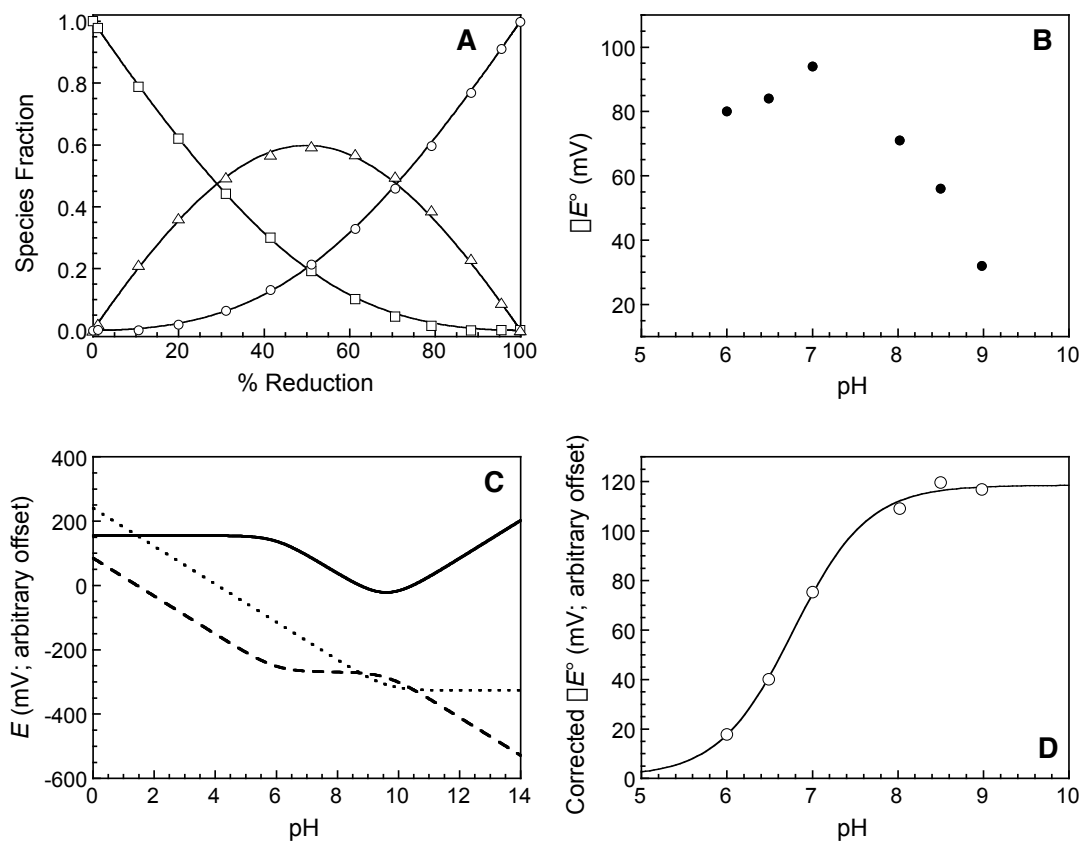


Figure 3.7. pH dependence of the relative redox potentials of MMOR-FAD. (A) MMOR-FAD reductive titration data obtained at pH 8.5 with fits (solid lines) determined by using eqs 5-8: FAD_{ox} (squares), FAD_{sq} (triangles), and FAD_{hq} (circles). (B) Variation of the difference between the two MMOR-FAD redox potentials with pH. (C) Theoretical curves reflecting the pH dependence of $FAD_{ox/sq}$ (dotted line), $FAD_{sq/hq}$ (dashed line), and ΔE ($FAD_{ox/sq} - FAD_{sq/hq}$; solid line) due to the inclusion of protons in some of the redox equilibria (Scheme 3.1). FAD_{hq} and FAD_{sq} pK_a values of 6.0 and 9.6, respectively, are shown. (D) pH dependence of ΔE° values after subtracting redox equilibria-related effects (panel C). The solid line represents a fit to eq 3.

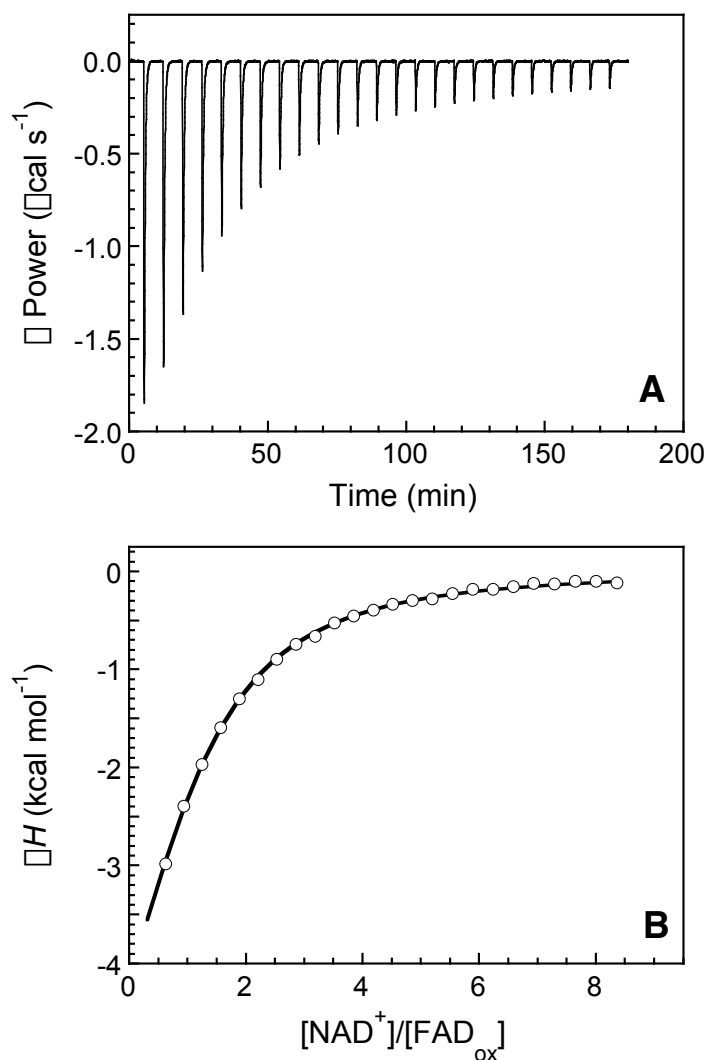


Figure 3.8. Determination of MMOR-FAD_{ox}-NAD⁺ binding constant by isothermal titration calorimetry. (A) Data recorded for the complex formation between MMOR-FAD_{ox} (43 μM in the calorimeter cell) and NAD⁺ (1.89 mM in a 250- μL injection syringe) at 4.2 $^{\circ}\text{C}$. Each heat pulse corresponds to a 10- μL injection into the 1.430-mL sample cell. (B) Integrated enthalpy data (circles) fit with a one-site binding model (solid line).

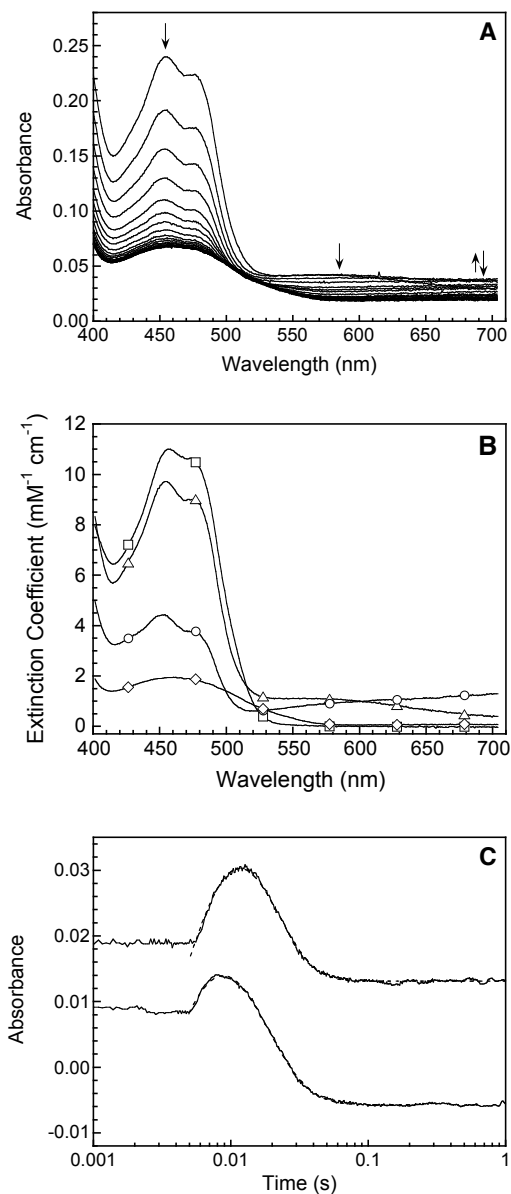


Figure 3.9. Kinetics of MMOR-FAD reduction with NADH. (A) Spectra recorded at ~ 3 -ms intervals by diode array stopped-flow spectroscopy in the first 67 ms after mixing $25 \mu\text{M}$ FAD_{ox} with $250 \mu\text{M}$ NADH at 4°C and pH 7.0. (B) Spectra of intermediates resolved by global analysis of the diode array kinetic data: FAD_{ox} (squares), CT1 (triangles), CT2 (circles), and FAD_{hq} (diamonds). (C) Time-dependent absorbance changes at 625 (lower trace) and 725 nm for this reaction. For clarity, the 725-nm trace was offset by 0.02 AU. Dashed lines represent fits to the data.

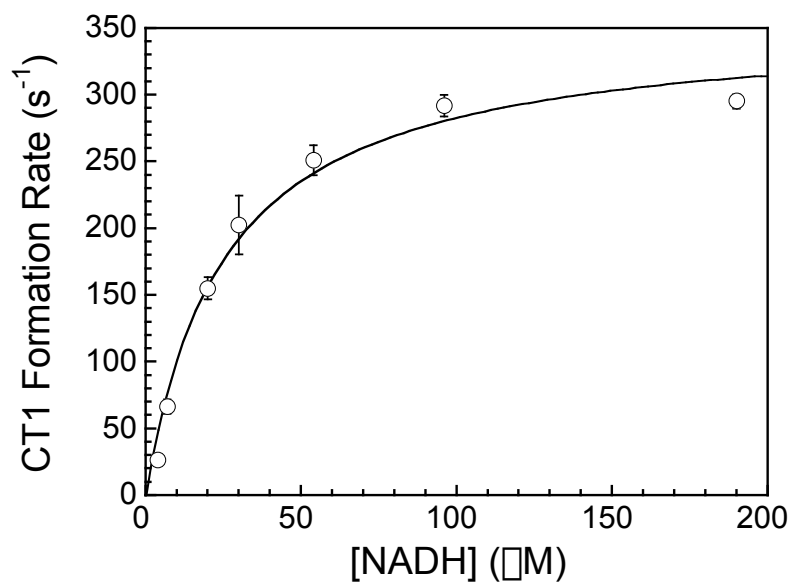


Figure 3.10. Dependence of the CT1 formation rate constant, k_1 , on NADH concentration for the reduction of MMOR-FAD with NADH at 4 °C and pH 7.0. The solid line represents a hyperbolic fit to the data.

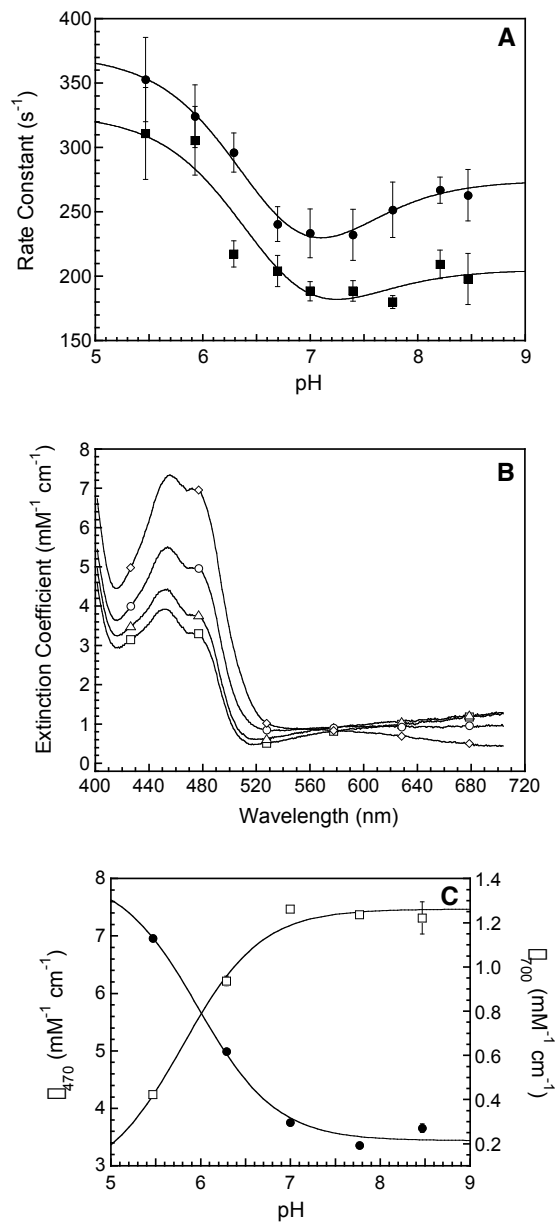


Figure 3.11. Influence of pH on the reaction of MMOR-FAD with NADH at 4 °C. (A) Variation of k_1 (CT1 formation, circles) and k_2 (CT2 formation, squares) with pH. Solid lines are fits of the type defined in eqs 2 and 3. (B) CT2 spectra determined at pH values of 7.77 (squares), 7.00 (triangles), 6.29 (circles), and 5.47 (diamonds). (C) CT2 extinction coefficients at 470 (closed circles) and 700 nm (open squares) with respect to pH. Solid lines are fits to eqs 2 and 3.

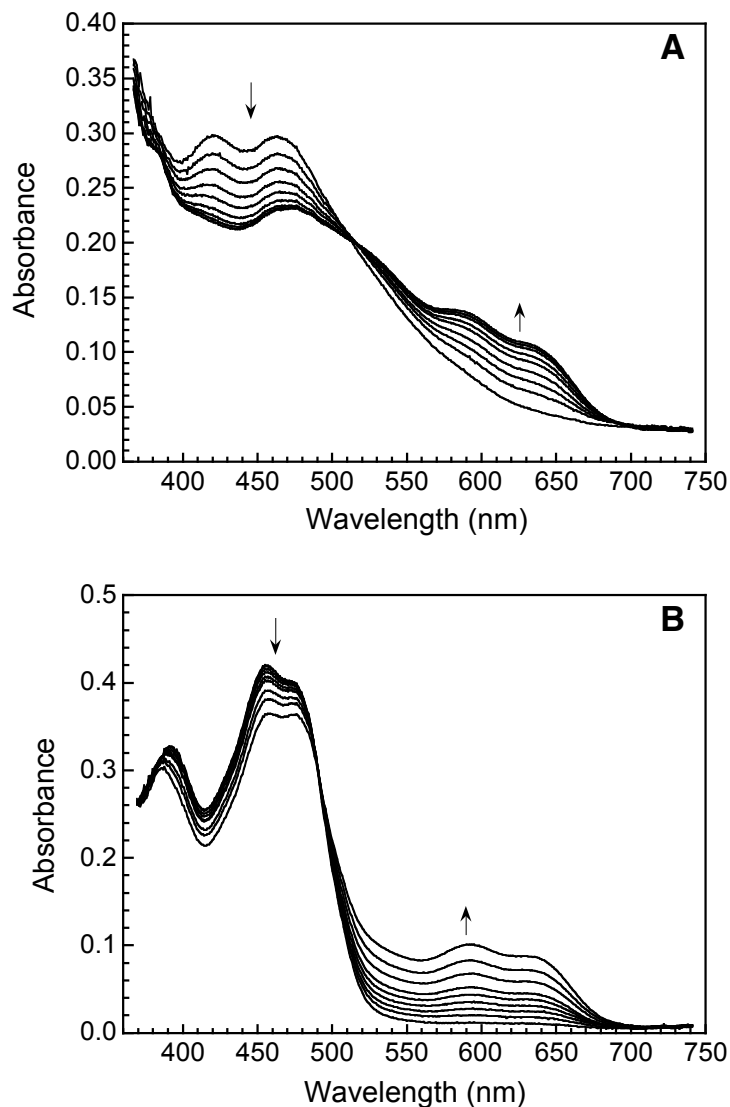


Figure 3.12. Electron transfer from MMOR-FAD_{hq} to Fd_{ox} or MMOR-FAD_{ox}. (A) Diode array spectra collected on a log time scale during the first 380 s after mixing 30 μ M MMOR-FAD_{hq} and 30 μ M Fd_{ox} at 25 °C and pH 7.0. (B) Diode array spectra collected on a log time scale during the first 380 s after mixing 30 μ M MMOR-FAD_{hq} and 30 μ M MMOR-FAD_{ox} at 4 °C and pH 7.0. Second-order rate constants were determined by fitting the data with second-order kinetic models in Specfit.

Chapter 4

**Intermolecular Electron Transfer Reactions in Soluble Methane Monooxygenase
from *Methylococcus capsulatus* (Bath): A Role for Hysteresis in Protein Function**

INTRODUCTION

Long-range electron transfer is an essential process in many physiological pathways, including respiration, photosynthesis, and intermediary metabolism.¹ Biological electron transfer reactions often proceed via bimolecular interactions between donor and acceptor proteins containing redox-active prosthetic groups. In order to achieve efficient interprotein electron transfer, steps such as specific protein–protein binding, conformational rearrangements, and chemical transformations may be required.^{2,3} A common strategy in bacterial mono- and dioxygenase systems is separation of the reductase and oxygenase functionalities into individual protein components.⁴ In this manner, the rate of electron transfer to the oxygenase active site can be finely controlled by intricate intermolecular interactions. In addition, the reductant can be physically separated from being consumed by active oxygen species generated in the oxygenase component.

Among the best-studied of these multicomponent oxygenase systems is soluble methane monooxygenase (sMMO), which catalyzes the selective oxidation of methane to methanol at ambient temperature and pressure (eq 1).^{5,6} By using methane as their



primary source of carbon and energy, methanotrophs significantly reduce the amount of this potent greenhouse gas that reaches the atmosphere.⁷ All methanotrophic bacteria can express a copper-containing membrane-bound MMO (pMMO),⁸⁻¹⁰ whereas the sMMO system is used by only a few species under copper-limited conditions.¹¹ The relative ease of purifying and stabilizing the sMMO proteins has facilitated detailed reactivity, spectroscopic, structural, kinetic, and theoretical studies of these enzymes from *Methylococcus capsulatus* (Bath) and *Methylosinus trichosporium* OB3b.¹²⁻¹⁵

Both sMMO systems comprise three proteins that are required for optimal catalysis,¹⁶⁻¹⁸ a hydroxylase (MMOH, 251 kDa), a reductase (MMOR, 38.5 kDa), and a regulatory protein (MMOB, 15.9 kDa). The inclusion of a fourth protein (MMOD) in the *M. capsulatus* (Bath) sMMO system was demonstrated recently.¹⁹ MMOH, a dimeric ($\alpha\alpha$)₂ protein, houses in its α subunits carboxylate-bridged non-heme diiron sites where dioxygen activation and substrate hydroxylation occur. MMOR is an iron-sulfur flavoprotein that shuttles electrons from NADH to the hydroxylase to prime the enzyme system for reaction with dioxygen. A [2Fe-2S] cluster is located in the N-terminal reductase domain, which exhibits sequence homology with ferredoxins of plants, cyanobacteria, and archaeobacteria.²⁰ To begin the series of electron transfer reactions necessary for steady-state sMMO turnover (Scheme 4.1), the flavin adenine dinucleotide (FAD) cofactor bound to the C-terminal portion of MMOR accepts two electrons from NADH. Electrons are then transmitted sequentially from the reduced flavin through the one-electron carrier [2Fe-2S] center to the diiron(III) hydroxylase active sites.^{18,21-23} After reduction by MMOR, a complex formed between the diiron(II) state of MMOH, H_{red}, and MMOB reacts with dioxygen to generate a series of oxygenated high-valent diiron intermediates.²⁴⁻²⁷ The final transient species hydroxylates methane, producing methanol and water and returning the hydroxylase to the resting, diiron(III) state. To complete the cycle, the MMOH diiron centers are reduced by MMOR and methanol is discharged from the active site. Interactions between the three sMMO components modulate the rates, efficiency, and substrate regioselectivity of the reaction.^{18,25,28-30}

MMOR is a member of a class of modular electron transferases, also called the ferredoxin:NADP⁺ oxidoreductase (FNR) family. These proteins are distinguished by a core flavin domain that transports electrons between a nicotinamide dinucleotide and a

one-electron carrier domain, which may be either linked or dissociable (Figure 4.1A).³¹⁻³³ Distinct flavin mononucleotide (FMN), NADH binding, and [2Fe-2S] domains are revealed in the crystal structure of *Burkholderia cepacia* phthalate dioxygenase reductase (PDR), demonstrating the structural and functional modularity of FNR proteins.³³ In order to simplify and extend the characterization of MMOR, the ferredoxin (MMOR-Fd, referred to hereafter as MMOR-Fd(1-98)) and FAD/NADH (MMOR-FAD) domains were expressed as separate proteins.³⁴ Except for interdomain electron transfer, the reductase domain proteins exhibit redox, spectroscopic, and kinetic properties nearly identical to those of full-length MMOR.³⁴ In addition, NMR studies of MMOR-Fd(1-98)³⁵ and MMOR-FAD³⁶ show that the separated domains adopt compact structures in solution with folds similar to homologous FNR proteins.

Previous studies of intermolecular electron transfer in the sMMO system allowed pre-formed MMOR–MMOH or MMOR–MMOH–MMOB complexes to react with NADH and monitored absorbance changes associated with multiple intra- and intermolecular kinetic steps.¹⁸ In the present work, reactions were conducted by rapidly mixing chemically reduced MMOR with oxidized MMOH, thereby affording direct observation of intermolecular electron transfer events while avoiding the complicating kinetics of the reductive half reaction of MMOR. Three MMOR-Fd analogs (Figure 4.1B) were also investigated to explore the features that modulate the inaugural electron transfer to the hydroxylase. Mechanisms for the intermolecular electron transfer reaction and roles for MMOB and MMOD in regulating the rate and extent of electron transfer are presented.

MATERIALS AND METHODS

Protein Purification. MMOH was isolated from *M. capsulatus* (Bath) cell paste by following a published protocol.¹⁸ Pure hydroxylase contained 3.8-4.0 mol Fe per mol protein, as determined by ferrozine iron assays,^{37,38} and exhibited specific activities of 250-350 nmol min⁻¹ mg⁻¹ of MMOH for the conversion of propylene to propylene oxide at 45 °C. MMOR,²³ MMOR-Fd(1-98),³⁴ and MMOD¹⁹ were expressed in recombinant *Escherichia coli* systems and purified as previously reported. FAD-depleted reductase, MMOR(apoFAD), was separated from MMOR by Sepharose 5'-AMP affinity chromatography.

Recombinant MMOB was expressed in *E. coli* as described³⁹ and purified by using a modified protocol. Cells from eight 1-L JM105/pWWB \square cultures were suspended in 100 mL of cracking buffer [25 mM 3-(*N*-morpholino)propanesulfonic acid (MOPS; pH 7.0), 1 mM 1,4-dithiothreitol (DTT), 75 mM NaCl, and 5 mM MgCl₂] containing DNase (1.5 units/mL), 1 mM Pefabloc SC (Roche Molecular Biochemicals, Indianapolis, IN), and 1 mM phenylmethylsulfonyl fluoride (PMSF). The cell suspension was sonicated on ice at 40% maximum output (Branson Sonifier Model 450 equipped with a 3/4-inch horn) with three 2-min pulses, which were spaced at 5-min intervals to prevent overheating. The lysed cells were centrifuged at 98,000g for 40 min in order to separate the soluble and insoluble materials. The soluble portion was decanted immediately, filtered through 0.2 μ m membranes, and applied to a DEAE Sepharose CL-6B (Amersham Pharmacia Biotech, Piscataway, NJ) column (2.6 \square 15 cm) equilibrated in buffer A [25 mM MOPS (pH 7.0), 1 mM DTT, 1 mM ethylenediaminetetraacetic acid (EDTA), and 75 mM NaCl]. Following a 100-mL wash with buffer A, proteins were eluted with a 750-mL linear gradient from buffer A to buffer B [25 mM MOPS (pH 7.0), 1 mM DTT, 1 mM EDTA, and 350 mM NaCl].

Fractions containing MMOB were identified by SDS-PAGE, pooled with additional Pefabloc SC (ca. 1 mM), and concentrated to 4 mL by ultrafiltration. This crude MMOB solution was resolved on a Superdex 75 (Amersham Pharmacia) size-exclusion column (2.6 × 60 cm) equilibrated in buffer A. Pure MMOB was pooled based on SDS-PAGE analysis, concentrated by ultrafiltration, and stored at -80 °C.

Construction and Purification of the MMOR-Fd(1-120+tail) Fragment. In an attempt to correct by site-directed mutagenesis a *Taq* DNA polymerase-introduced mutation (T123I) in the original MMOR expression vector, a one-base deletion was inadvertently introduced in the reductase gene. In pRED-C1, the error produced a tail of 19 frame-shifted amino acids (ATPSSFFCRSGPTSAATVA) following codon 120 which was terminated by an out-of-frame stop codon; thus, only the ferredoxin portion of MMOR (calculated MW, 15.0 kDa) was expressed. Expression and anion exchange chromatography were performed exactly as described for recombinant MMOR-Fd(1-98).³⁴ The MMOR-Fd(1-120+tail) protein was highly purified (> 95%) by resolution on a DEAE Sepharose CL-6B column. The Fd fragment eluted from the column at about 350 mM NaCl; fractions were identified by SDS-PAGE analysis and by the characteristic plant-type ferredoxin absorbance spectrum in the 300-700 nm region. An extinction coefficient ($\epsilon_{458} = 9300 \text{ M}^{-1} \text{ cm}^{-1}$) was estimated for MMOR-Fd(1-120+tail) by determining the iron content with ferrozine assays and assuming a full complement of two iron atoms per protein molecule.

Isothermal Titration Calorimetry. The binding affinity of the MMOH-MMOR-Fd(1-98) complex was measured with a VP-ITC isothermal titration calorimeter (MicroCal, Inc., Northampton, MA). All titrations were performed at 4.2 °C in 25 mM MOPS (pH 7.0), 2 mM tri(2-carboxyethyl)phosphine hydrochloride (TCEP; Sigma, St. Louis, MO). Titrant (368 μM MMOR-Fd(1-98)) was injected in 10- μL aliquots from a

250- μ L stirred titration syringe into the 1.430-mL sample cell containing 11.1 μ M MMOH. Stirring was maintained at 310 rpm throughout the titration. The experiment was repeated with buffer in the sample cell in order to measure the heat of dilution for MMOR-Fd(1-98). Data were integrated and fit with the MicroCal Origin v. 5.0 software package.

Kinetic Measurements of Intermolecular Electron Transfer. Intermolecular electron transfer in the sMMO system was examined by stopped-flow optical spectroscopy. A Hi-Tech Scientific SF-61 DX2 double-mixing stopped-flow spectrophotometer configured for either single-wavelength photomultiplier or multi-wavelength diode-array collection was used for all experiments. To make the stopped-flow apparatus anaerobic, the syringes and flow cell were flushed first with a solution of ca. 5 mM sodium dithionite and then with anaerobic buffer. Proteins were exchanged into either 25 mM MOPS (pH 7.0), 1 mM DTT (initial studies) or 25 mM MOPS (pH 7.0) with Biogel P6 desalting columns (Bio-Rad, Hercules, CA). A solution of oxidized MMOR, MMOR-Fd(1-98), MMOR-Fd(1-120+tail), or MMOR(apoFAD) in a sealed quartz cuvette was made anaerobic by 12 cycles of vacuum gas exchange with O₂-free N₂. Aliquots (5 μ L) of 2-5 mM sodium dithionite were added with a gas-tight Hamilton titrating syringe. After each addition, optical spectra were recorded until no further changes were observed (typically less than 2 min). This process was repeated until the protein was reduced completely. Anaerobic MMOH solutions were prepared by 10-12 cycles of vacuum gas exchange with nitrogen. Concentrations of MMOH were 10 μ M after mixing; reductase or ferredoxin concentrations were 20 μ M, except where noted. The reaction of reduced MMOR or MMOR-Fd with oxidized MMOH was monitored at 470 nm (both MMOR and MMOR-Fd) and 625 nm (MMOR only) in single-wavelength photomultiplier mode. Data points (512 or 640) were collected on a

logarithmic time scale (1 to 500 s, depending on the reaction). The experiment was repeated with the stopped-flow apparatus in multi-wavelength diode array mode. For each shot (2 to 800 s), 160 spectra (380-800 nm) were recorded; during data sets that required long collection times, an anti-bleaching shutter apparatus was employed. The temperature was maintained at 4 °C with a constant temperature circulating water bath for all experiments, except where noted. The effects of MMOB and MMOD on intermolecular electron transfer were investigated by including these proteins in the same syringe as oxidized hydroxylase. In some initial studies, MMOB was included with reduced MMOR or MMOR(apoFAD).

Single-wavelength absorbance data were fit to a sum of two (MMOR-Fd and MMOR(apoFAD)) or four (MMOR) exponentials with the program KinetAsyst (v. 2.2 or 3.04, Hi-Tech Limited, Salisbury, England). Rate constants and intermediate spectra were extracted from diode array data by using the global analysis routines resident in the Specfit software suite (v. 2.10U or 3.0.16; Spectrum Software Associates, Chapel Hill, NC). Compositions of intermediate spectra were calculated by fitting with linear combinations of [2Fe-2S] and FAD component spectra (Figure 4.2)³⁴ in KaleidaGraph (v. 3.0 or 3.6, Synergy Software, Reading, PA).

RESULTS

MMOR Domain Separation. Fortuitously, a site-directed mutagenesis reaction inadvertently yielded the truncated reductase, MMOR-Fd(1-120+tail), a 15-kDa protein comprising only the [2Fe-2S] domain of full-length MMOR (Figure 4.1B). This serendipitous ferredoxin fragment was competent for electron transfer to MMOH, demonstrating that the MMOR [2Fe-2S] domain can function as an independent modular unit. Because this truncated protein was expressed only in low yield (3 mg/L

of *E. coli* culture), we cloned the MMOR-Fd(1-98) domain in part to aid characterization of intermolecular electron transfer from MMOR to MMOH.³⁴ FAD-depleted MMOR, MMOR(apoFAD), was also employed to study the initial events in the MMOR–MMOH electron transfer reaction.

Measurement of MMOH–MMOR-Fd(1-98) Binding Affinity. The affinity of oxidized MMOR-Fd(1-98) for oxidized MMOH was determined by isothermal titration calorimetry. Figure 4.3A shows the power required to compensate for the exothermic binding reaction after each addition of titrant to the sample cell. The incremental heat change for each injection was calculated by integrating the heat pulses with respect to time. A plot of these data as a function of the MMOR-Fd(1-98)/MMOH molar ratio is presented in Figure 4.3B. Preliminary fitting of the enthalpy data with a non-interacting binding sites model in the Origin software suggested that only ca. 70% of the hydroxylase participated in binding MMOR-Fd(1-98). The same phenomenon was observed previously for full-length MMOR and MMOB interactions with MMOH.¹⁸ After correcting the MMOH concentration for the nonbinding fraction, a two-site sequential (interacting sites) model was used to obtain an excellent fit to the enthalpy data (solid line in Figure 4.3B). Thermodynamic parameters for the binding reaction are given in Table 4.1.

Protein Concentration Dependence of Intermolecular Electron Transfer. Protein–protein binding and structural reorganization are prerequisites of efficient intermolecular electron transfer reactions. The possibility that the kinetics of protein complex formation might affect electron transfer reactions between sMMO components was investigated by reacting various concentrations of chemically reduced MMOR-Fd(1-98) with oxidized MMOH in the stopped-flow instrument at 4 °C (Figure 4.4A). The kinetic traces could not be fit well with single exponential expressions;

using two exponential decays yielded high-quality fits to the data. As shown in Figure 4.4B, there is no significant effect of MMOR-Fd concentration on the observed rates of intermolecular electron transfer. Examination of the preexponential factors returned from data fitting showed that partitioning of electrons between the “fast” (1.0 s⁻¹) and “slow” (0.26 s⁻¹) reaction phases is altered by the concentration of MMOR-Fd (Figure 4.4C). Similar results were obtained for full-length MMOR (data not shown).

Intermolecular Electron Transfer from Ferredoxin Analogs to MMOH.

Because the [2Fe-2S] cofactor of MMOR is a one-electron carrier, the ferredoxin center must transfer two electrons sequentially to MMOH to reduce fully each diiron(III) hydroxylase active site. Several MMOR analogs lacking the FAD cofactor (Figure 4.1B) were implemented to observe the kinetics of the inaugural electron transfer from the ferredoxin domain to MMOH uncomplicated by the flavin moiety of the full-length reductase. All three ferredoxin proteins transferred electrons to the hydroxylase in a biphasic manner with varying rate constants (Table 4.2; see Discussion section for reaction schemes). The temperature dependence of these electron transfer reactions was investigated for MMOR-Fd(1-98), MMOR-Fd(1-120+tail), and MMOR(apoFAD), and activation energies were calculated with Arrhenius plots (Figures 4.5A and 4.5B, Table 4.3). For MMOR-Fd(1-98), the fractions of the total absorbance change associated with the rapid and slow pathways vary slightly with temperature (Figure 4.5C). Analysis using electron transfer theory expressions¹ was performed by fitting temperature-dependence data to eqs 2 and 3 (Figure 4.5D and Table 4.4), where h is

$$k_{ET} = \frac{4\pi^2 H_{AB}^2}{h\sqrt{4\pi RT}} e^{[\Delta(G^\ddagger + D)^2 / 4RT]} \quad (2)$$

$$k_{ET} = k_0 e^{\pi(r\pi r_0)} e^{[\Delta(G^\ddagger + D)^2 / 4RT]} \quad (3)$$

Planck's constant, R is the gas constant, T is temperature, k_0 is the characteristic frequency of the nuclei, usually assigned a value of 10^{13} s^{-1} , and r_0 is the close contact distance, generally set to 3.0 \AA . H_{AB} is the electronic coupling between redox centers, Δ is the reorganizational energy, and r is the distance between the donor and acceptor sites. A value of 1.4 \AA^{-1} was used for Δ ⁴⁰ a global parameter related to the nature of the medium between electron transfer partners.

Spectra from the global analysis of diode array data for the reaction of $20 \text{ }\mu\text{M}$ MMOR-Fd(1-98) with $10 \text{ }\mu\text{M}$ MMOH at $4 \text{ }^\circ\text{C}$ are shown in Figure 4.6A. Rate constants of $k_1 = 1.0 \pm 0.1 \text{ s}^{-1}$ and $k_2 = 0.28 \pm 0.02 \text{ s}^{-1}$ were determined to give the best fit through the biphasic data. The composition of each intermediate was calculated by fitting the spectra with linear combinations of the oxidized and reduced MMOR-Fd component spectra (Figure 4.2).³⁴ In the first electron transfer phase, the hydroxylase was reduced by 23% (with four-electron reduced MMOH corresponding to 100%); after the second electron transfer phase, 35% hydroxylase reduction was realized. Since each ferredoxin protein can transfer only one electron to MMOH, the theoretical maximum for hydroxylase reduction in this reaction is 50%. At the end of the electron transfer reaction, total MMOH reduction was generally only 30-40%, however. This result is in accord with other binding and kinetic data that demonstrate that a significant fraction (20-40%) of MMOH does not bind MMOB and MMOR.¹⁸ Therefore, if the nonbinding portion of MMOH is taken into account, full reduction of the active MMOH fraction was achieved. This experiment was repeated for MMOR(apoFAD) (Table 4.5).

Effect of MMOB on Intermolecular Electron Transfer from Ferredoxins.

Reactions that included MMOB in the same syringe as MMOH (2 mol MMOB per mol MMOH) exhibited the same biphasic behavior observed in the absence of MMOB. For MMOR-Fd(1-98), the two intermolecular electron transfer reactions occur with rate

constants of $k_1 = 1.1 \pm 0.2 \text{ s}^{-1}$ and $k_2 = 0.056 \pm 0.005 \text{ s}^{-1}$ (Figure 4.6B). The extent of hydroxylase reduction after each stage of this reaction was 5% and 34%, respectively. Thus, the majority (ca. 85%) of electrons were transferred during the slow phase. The effect of MMOB on this reaction is therefore twofold. First, the rate constant for the second electron transfer phase is decreased by a factor of about five. Moreover, the partitioning of electrons between the rapid and slow phases is shifted significantly toward the slow pathway. Adding MMOB to the experiment involving MMOR(apoFAD) yielded similar but less pronounced results. A fivefold reduction in the k_2 value was determined for electron transfer to MMOH, but only a slight shift in electron partitioning was noted (Table 4.5). Time courses of MMOH reduction measured for three MMOR ferredoxin analogs and the effects of MMOB on two of those reactions are illustrated in Figure 4.7A.

Kinetic traces recording intermolecular electron transfer from MMOR-Fd(1-98) to MMOH in the presence of increasing concentrations of MMOB are presented in Figure 4.8A. Rate constants from parallel two-exponential fits of these data are altered significantly as a function of MMOB concentration (Figure 4.8B). The first equivalent of MMOB reduces the rate constant for rapid electron transfer by 50%; adding a second equivalent of MMOB restores this rate constant to values determined in the absence of MMOB. The rate constant for the slow reaction phase decreases with increasing concentrations of MMOB such that an 8- to 10-fold reduction is observed at high [MMOB]. The extent of the fast and slow reaction phases, as measured by the fractional contributions of preexponential factors, is also highly dependent on MMOB concentration (Figure 4.8C). At high MMOB concentrations, electron transfer proceeds almost entirely through the slow pathway. Thus, the effective electron transfer rate decreases steadily with increasing MMOB concentration (triangles, Figure 4.8B). The

effect of MMOB on electron transfer from MMOR(apoFAD) to MMOH was also examined. With saturating MMOB, rate constants for the rapid and slow electron transfer phases are reduced by 15% and 200%, respectively. In the absence of MMOB, approximately 70% of this reaction takes place at the fast rate. Increasing the MMOB concentration inverts the distribution so that in the presence of saturating MMOB, only 30% of the reaction occurs via the rapid pathway.

Intermolecular Electron Transfer from MMOR_{3e-} to MMOH. The reaction of 20 μ M reduced MMOR (MMOR_{3e-}) with 10 μ M oxidized MMOH at 4 °C was studied by diode array stopped-flow spectroscopy. Intermediate spectra derived from globally fitting the data with a sequential five-component model are displayed in Figure 4.9A. Fits converged on rate constant values of $k_1 = 70 \pm 10 \text{ s}^{-1}$, $k_2 = 18.5 \pm 1.5 \text{ s}^{-1}$, $k_3 = 2.5 \pm 1.5 \text{ s}^{-1}$, and $k_4 = 0.11 \pm 0.09 \text{ s}^{-1}$. The oxidation state of each intermediate was determined by fitting the spectra with linear combinations of [2Fe-2S]_{ox}, [2Fe-2S]_{red}, FAD_{ox}, FAD_{sq}, and FAD_{hq} component spectra (dashed lines in Figure 4.9A). A graphical representation of the electron distribution in each intermediate species and the extent of electron transfer to MMOH at each stage of the reaction is given in Figure 4.9B. In the four reaction phases, the hydroxylase diiron sites are reduced by 30%, 25%, 11%, and 11%, respectively, for a total of 77% reduction. After correcting for the nonparticipating fraction of MMOH, the extent of hydroxylase reduction after each electron transfer step was recalculated (Table 4.6). The first two reaction phases each account for the transfer of about 1.5 electrons to MMOH. The final electron is passed to MMOH in two slow steps.

Kinetic traces for the electron transfer reaction from MMOR_{3e-} to MMOH at varying temperature (4-37 °C) were fit with sums of two (625 nm) or four (470 nm) exponentials (Table 4.2). An Arrhenius plot was constructed (Figure 4.10A), and

activation energies for the first three electron transfer steps were determined (Table 4.3). Inspection of the preexponential factors demonstrated that electron partitioning through the first and second reaction phases is significantly affected by temperature (Figure 4.10B). Comparison to temperature-induced partitioning in the MMOR-Fd(1-98) reaction with MMOH (Figure 4.5C) reveals nearly identical trends. Fitting the temperature dependence data to eqs 2 and 3 generated values for the electron transfer parameters H_{AB} , Δ , and r (Figures 4.10C and 4.10D; Table 4.4).

Effects of MMOB and MMOD on Electron Transfer from MMOR_{3e-} to MMOH. When two equivalents of MMOB or MMOD were added to MMOH before mixing with MMOR_{3e-} in the stopped-flow instrument, intermolecular electron transfer was inhibited. Intermediate spectra obtained from global analysis of diode array data for the reaction of 20 μ M MMOR_{3e-} with 10 μ M MMOH/20 μ M MMOB at 4 °C are shown in Figure 4.11A. Rate constants for the four electron transfer steps are only slightly lower than those determined in the absence of MMOB ($k_1 = 52 \pm 7 \text{ s}^{-1}$, $k_2 = 10.5 \pm 1.5 \text{ s}^{-1}$, $k_3 = 1.5 \pm 0.5 \text{ s}^{-1}$, $k_4 = 0.03 \pm 0.01 \text{ s}^{-1}$). The inhibitory effects of MMOB on intermolecular electron transfer instead arise primarily from a large shift in the fraction of electrons traveling through the four reaction phases (Figure 4.11B). The initial three electron transfer steps combine to transmit a single electron to MMOH; the remaining three electrons are transferred at the slowest rate (Table 4.6). MMOD is an even more potent inhibitor of intermolecular electron transfer in the sMMO system. Diode array data recorded for the reaction of 20 μ M MMOR_{3e-} with 10 μ M MMOH/20 μ M MMOD were fit with a sequential four-component model to give rate constants of $k_1 = 3 \pm 1 \text{ s}^{-1}$, $k_2 = 0.06 \pm 0.02 \text{ s}^{-1}$, and $k_3 = 0.009 \pm 0.003 \text{ s}^{-1}$ (Figure 4.12A). These rate constants are substantially diminished compared to those determined in the absence of MMOD. Like MMOB, MMOD induces a change in electron partitioning between the various

reaction phases (Figure 4.12B and Table 4.6). During the first two steps, a total of one electron is transferred to the two hydroxylase diiron sites. Two more electrons are transmitted to MMOH in the slow third step, resulting in 75% reduced hydroxylase. Transfer of a fourth electron was not observed but may occur eventually beyond the examined time range (400 s). The full extent of electron transfer inhibition by MMOB and MMOD can be appreciated by plotting percent MMOH reduction vs time (Figure 4.7B).

The MMOB concentration dependence for electron transfer from MMOR_{3e^-} to oxidized MMOH was investigated with single wavelength stopped-flow experiments. Kinetic traces (470 nm) for this reaction were collected at 4 °C with MMOB included in the same syringe as MMOH (Figure 4.13A). Rate constants extracted from parallel four-exponential fitting are only mildly perturbed by increasing concentrations of MMOB (Figure 4.13B). As noted for MMOR-Fd(1-98), the extent of the fast and slow reaction phases exhibits considerable dependence on MMOB concentration, such that electron transfer proceeds nearly completely via slow pathways with saturating MMOB (Figure 4.13C). Including MMOB in the syringe with MMOR_{3e^-} produced a similar but smaller interconversion effect. At high MMOB concentrations, 30% of electron transfer occurs through the rapid pathway compared to < 5% when MMOB is pre-mixed with MMOH.

DISCUSSION

Comparison of MMOH–MMOR-Fd and MMOH–MMOR Binding Interactions. The ferredoxin domain of MMOR was employed in this study to model the initial electron transfer steps from MMOR to MMOH. To ensure that MMOR-Fd(1-98) retains an affinity for MMOH similar to that of full-length MMOR, the

MMOH–MMOR-Fd(1-98) binding interaction at 4.2 °C was examined by isothermal titration calorimetry. By fitting the calorimetric data with an interacting sites binding model, dissociation constants of 0.6 μM and 3.2 μM were determined for the first and second MMOR-Fd(1-98) binding interactions, respectively, with the dimeric MMOH protein. These values are about 1.5- to 4.5-fold greater, indicating weaker binding, than those measured by the same method for the MMOH–MMOR interaction at 3.3 °C (0.4 μM and 0.7 μM).¹⁸ Furthermore, the MMOR-Fd protein binds to MMOH in an exothermic reaction, whereas the MMOH–MMOR binding reaction is endothermic (Table 4.1). Possible reasons accounting for these differences in thermodynamic binding parameters include different coverage of the MMOH surface owing to the larger full-length MMOR protein, altered structural features in MMOR-Fd compared to the [2Fe-2S] domain and adjacent peptide regions of MMOR, and more extensive conformational changes induced by MMOH–MMOR binding.

Our previous NMR titration studies of MMOR-Fd(1-98) with MMOH revealed a face of the ferredoxin protein, including Asp26 and Glu73, involved in binding to the hydroxylase.³⁵ Mutating either of these residues to alanine in full-length MMOR resulted in decreased affinity for MMOH, demonstrating that MMOR-Fd(1-98) and MMOR contact the hydroxylase in a similar fashion.⁴¹ Both MMOR-Fd(1-98) and MMOR from *M. capsulatus* (Bath) cross-link to the MMOH alpha subunit, providing further evidence for shared binding interactions.⁴² We therefore conclude that MMOR-Fd(1-98) and MMOR minimally bind to the same sites on MMOH. Additional protein contacts involving the MMOH–MMOR interface and/or changes in structure as a consequence of complex formation are probably responsible for the altered thermodynamic properties noted in the calorimetry experiments.

Formation of Electron Transfer Complexes. Protein–protein binding typically precedes intermolecular electron transfer in biological systems. Thus, for stopped-flow experiments in which the donor and acceptor pair is combined by mixing, rate constants associated with protein–protein binding and orientation may contribute to the observed rate constant for intermolecular electron transfer. This feature was avoided in previous studies of electron transfer from MMOR to MMOH by allowing the pre-formed MMOH–MMOR complex to react with NADH.¹⁸ When fully reduced MMOR-Fd(1-98) or MMOR is rapidly mixed with MMOH, the measured rate constants for the intermolecular electron transfer reactions are independent of protein concentration (Figure 4.4B). This result indicates that MMOR-Fd(1-98) and MMOR associate rapidly with MMOH to form a tight complex prior to the electron transfer reactions.

The rate constant determined for the first electron transfer step from MMOR_{3e^-} to MMOH at 4 °C ($k = 65 \pm 5 \text{ s}^{-1}$) is significantly less than that observed for the initial electron transfer from MMOR to MMOH in the NADH-initiated reaction ($k = 106 \pm 13 \text{ s}^{-1}$).¹⁸ Since there is greater driving force for electron transfer from chemically reduced MMOR, this smaller rate constant is somewhat surprising. We propose that the initial rapid association of MMOH and MMOR is followed by a slower reorganization of the protein complex that limits the observed rate constant for intermolecular electron transfer. On the basis of kinetic and thermodynamic studies of MMOH complex formation with MMOB and MMOR, a similar two-step binding process was postulated.¹⁸ Isomerization of the initial MMOH–MMOR precomplex at 25 °C was estimated to occur with forward and reverse rate constants of $k_f = 0.38 \text{ s}^{-1}$ and $k_r = 0.057 \text{ s}^{-1}$, respectively.¹⁸ Rate constants for electron transfer from MMOR_{3e^-} to MMOH at 25 °C determined in this study are $k_1 = 205 \pm 16 \text{ s}^{-1}$, $k_2 = 18 \pm 4 \text{ s}^{-1}$, $k_3 = 4.6 \pm 1.2 \text{ s}^{-1}$, and $k_4 =$

$0.28 \pm 0.10 \text{ s}^{-1}$. The comparable values of k_4 and the approximate MMOH–MMOR precomplex forward isomerization rate constant suggest that the last intermolecular electron transfer step, corresponding to the transmission of ca. 0.5 electrons to MMOH (Table 4.6), may be controlled primarily by slow complex reorganization. Rates for the initial three reaction phases may not require as stringent cofactor positioning in the MMOH–MMOR precomplex.

Modeling Intermolecular Electron Transfer in the sMMO System. Multiple kinetic steps are detected for electron transfer from chemically reduced MMOR or MMOR-Fd to oxidized MMOH. The data reported here were fit by using both parallel (single wavelength data) and sequential (diode array data) mechanisms for the intermolecular electron transfer reactions. Rate constants returned from both fitting methods were quite similar. In addition, global fitting of diode array data with sequential models yielded internally consistent sets of composite intermediate spectra, which are well described by linear combinations of the previously determined oxidized and reduced iron-sulfur and flavin component spectra.³⁴ Multi-wavelength data sets for the four-step reaction of MMOR_{3e^-} with MMOH_{ox} could also be fit well with various alternative mechanisms (*vide infra*), but these models generally failed to converge upon unique solutions.

For the simple case of MMOR ferredoxin analogs transferring electrons to MMOH, a discrete hydroxylase intermediate that is 25-35% reduced and a final state that is 50% reduced are observed. These results are consistent with an asynchronous mechanism (half-sites reactivity) in which a mixed-valent iron center is generated at one hydroxylase protomer in the first reaction phase and at the other protomer in the second reaction phase (Scheme 4.2A, upper pathway). A concerted mechanism (Scheme 4.2A, lower pathway), defined by simultaneous electron transfer to both

MMOH protomers, is also possible and cannot be ruled out with certainty based on the present data. A third option invokes two hydroxylase populations that exhibit intrinsically different intermolecular electron transfer rates (Scheme 4.2B). Because temperature or MMOR-Fd concentration variations can alter the partitioning of electrons through the rapid and slow reaction pathways, the electron transfer steps are interchangeable, probably by means of conformational changes in the hydroxylase component.

The sequence of electron transfer steps and the species compositions determined for the MMOH–MMOR reaction at 4 °C are presented graphically in Scheme 4.3. The first two reaction phases each correspond to the transmission of 1.5 electrons to MMOH. The final electron is transferred in two distinct steps. The oxidation levels of the MMOR cofactors were assessed throughout the electron transfer reaction by fitting the optical spectra of intermediates with combinations of the well-established reductase [2Fe-2S] and FAD component spectra.^{18,34} The oxidized, mixed-valent, and reduced forms of MMOH are virtually silent in the visible region examined in these stopped-flow experiments. Although the total number of electrons transferred to MMOH can be calculated with precision from the MMOR composition, the distribution of electrons within the hydroxylase diiron sites cannot be ascertained. As described for the MMOR-Fd analogs, both asynchronous (Scheme 4.3A) and parallel (Scheme 4.3B) electron transfer mechanisms are plausible. Furthermore, because there are four discrete steps, various types of half-sites reactivity can be imagined, including differential (Scheme 4.3B, upper and center pathways) or alternating (Scheme 4.3B, lower pathway) electron transfer to the two hydroxylase protomers. Further spectroscopic studies of the MMOH diiron center will be necessary to distinguish between these mechanisms. Since X-ray structural investigations have revealed

substantial amino acid side chain repositioning during reduction of H_{ox} to H_{mv} to H_{red} .⁴³ It is likely that these conformational changes contribute to the kinetic features observed in the present work.

Interconversion of Rapid and Slow Electron Transfer Pathways. The binding of MMOB to the hydroxylase induces structural changes that are coupled energetically to the redox equilibria of the MMOH diiron centers.⁴⁴⁻⁴⁶ For the sMMO system from *M. trichosporium* OB3b, the equilibrium midpoint potential of MMOH ($E_m = +48$ mV, relative to the normal hydrogen electrode) is decreased by 132 mV ($E_m = -84$ mV) upon binding MMOB. Adding MMOR to either MMOH or an MMOH–MMOB complex raises the hydroxylase midpoint potential to ca. +100 mV.²⁹ Moreover, MMOR inverts the relative values of the two MMOH redox potentials such that the transfer of two electrons is thermodynamically favored.⁴⁵ Both MMOB and MMOD alter the structure of the MMOH diiron site, as indicated by several spectroscopic techniques. EPR, MCD, and EXAFS studies provide evidence for MMOB-induced changes at the hydroxylase active site.^{28,30,47,48} Optical spectroscopy reveals that a small fraction (ca. 15%) of hydroxo-bridged diiron sites is converted to (μ -oxo)diiron(III) centers when MMOD binds to MMOH.¹⁹ Formation of the oxo-bridged species is also supported by EXAFS spectroscopy.⁴⁹ In contrast, MMOR does not alter the spectroscopic properties of the hydroxylase diiron center.¹⁴ MMOB and MMOR profoundly affect steady-state sMMO catalysis and efficiency, single-turnover reaction rates, and product distribution by means of intricate interactions that are still not fully understood.^{18,25,28-30} By competing with MMOB for binding to the hydroxylase, MMOD inhibits sMMO activity in steady-state assays.¹⁹

A role for MMOB in modulating the rate of intermolecular electron transfer in steady-state sMMO reactions has been suggested.^{17,21,50} Previous stopped-flow studies

of electron transfer from MMOR to MMOH involved rapidly mixing pre-assembled MMOR–MMOH or MMOR–MMOH–MMOB complexes with NADH and monitoring absorbance changes associated with MMOR reduction by NADH and reoxidation as electrons were transferred to MMOH.¹⁸ Four kinetic steps corresponding to the transfer of two electrons into a single hydroxylase diiron site were observed. Increasing concentrations of MMOB in the reactions increased the latter three electron transfer rate constants to a point of saturation. In contrast to these findings, when chemically reduced MMOR is allowed to react with pre-mixed MMOH and MMOB, electron transfer to the hydroxylase is substantially slower than in the absence of MMOB (Figure 4.7B). This inhibitory effect is produced primarily by shifting the bulk of electron transfer from the initial, faster reaction phases to the fourth, slowest phase.

MMOB and MMOR from *M. capsulatus* (Bath) do not bind to each other and have separate binding sites on MMOH.¹⁸ Therefore, the effect of MMOB on intermolecular electron transfer must be transmitted through structural changes of the hydroxylase component. The fully equilibrated MMOR–MMOH–MMOB complex exhibits relatively fast intermolecular electron transfer rates ($k_1 = 106 \text{ s}^{-1}$, $k_2 = 24.5 \text{ s}^{-1}$, $k_3 = 15.8 \text{ s}^{-1}$, and $k_4 = 6.4 \text{ s}^{-1}$) when reduced by NADH at 4 °C.¹⁸ The significantly lower rate constants ($k_1 = 50 \text{ s}^{-1}$, $k_2 = 9.4 \text{ s}^{-1}$, $k_3 = 1.6 \text{ s}^{-1}$, and $k_4 = 0.02 \text{ s}^{-1}$) measured in the present study for electron transfer from MMOR_{3e^-} to a pre-formed MMOH–MMOB complex suggest that isomerization of the initial ternary complex is required for maximal intermolecular electron transfer rates. By extrapolation from binding data collected at 25 °C (vide supra),¹⁸ the rate constant for this isomerization reaction may correspond to k_4 . Thus, in the presence of MMOB, 75% of electron transfer from MMOR_{3e^-} to MMOH may be gated by a slow conformational change, compared to just 14% without MMOB (Table 4.6). This effect can be explained by a simple model that includes two

interconvertible populations of MMOH, H_{ox} and H_{ox}' , which exhibit rapid and slow electron transfer rates, respectively (Scheme 4.3B). Addition of MMOB to this heterogeneous MMOH mixture would shift the equilibrium between the two species toward H_{ox}' , such that more electrons are transferred by the slow mechanism. The presence of MMOR would counteract the effect of MMOB by moving the equilibrium toward H_{ox} . This intermolecular electron transfer model mimics closely the changes in the hydroxylase redox potentials produced by MMOB and/or MMOR.^{29,44}

The MMOB-induced structural changes in MMOH appear to block the two fastest electron transfer routes in the ternary pre-complex, presumably by physical disruption of the relevant pathways or thermodynamic modulation of the diiron center redox potentials. Neither MMOH nor MMOB affects the MMOR redox potentials.²³ Although MMOB causes a large decrease in the hydroxylase midpoint potential, the complete transfer of two electrons from $MMOR_{3e-}$ is still thermodynamically favorable: $FAD (E^{\circ'} = -266 \text{ mV} / -176 \text{ mV}) \rightarrow [2Fe-2S] (E^{\circ'} = -209 \text{ mV}) \rightarrow \text{MMOH-MMOB complex} (E^{\circ'} = -84 \text{ mV})$.^{23,34} Therefore, even if MMOR were to increase the MMOH redox potentials only slowly with respect to the stopped-flow mixing and reaction times, this effect would not wholly account for the delayed electron transfer (*vide infra*). Another possibility is that the MMOR–MMOH binding isomerization reaction comprises multiple steps, the initial ones of which align useful electron transfer pathways. In this scenario, MMOB would slow these processes without drastically altering the rate of the macroscopic conformational change. Conversely, MMOB might serve to lock in the structural changes induced by MMOR. Interruption of important electron transfer pathways in the MMOH–MMOB complex is the most reasonable explanation for inhibition of electron transfer from $MMOR_{3e-}$ to pre-mixed MMOH and MMOB. After

MMOR binds to the MMOH–MMOB complex, a slow conformational reorganization must occur to align the redox sites for efficient electron transfer.

A small fraction (ca. 12%) of hydroxylase reduction occurs by the two fastest routes in the presence of two equivalents of MMOB, which suggests that a dynamic equilibrium exists between the blocked (H_{ox}') and unblocked (H_{ox}) forms of MMOH, as presented in Scheme 4.3B. Evidence exists for a third population of oxidized hydroxylase, which is not involved in the equilibria between H_{ox} and H_{ox}' . A nearly constant percentage (13-17%) of intermolecular electron transfer occurs during the step described by k_3 (with and without MMOB) or k_2 (with MMOD). The magnitudes of these rate constants are affected by MMOB (Figure 4.13B) and MMOD (Table 4.6), demonstrating that this population of MMOH (H_{ox}^+) binds both proteins; however, the fraction of electron transfer to H_{ox}^+ is unchanged by either MMOB or MMOD. A more complex model that accounts for this third hydroxylase population is shown in Scheme 4.4. H_{ox}^+ may be interchangeable with the other populations of MMOH or may represent permanently damaged protein. By excluding the H_{ox}^+ portion, relative amounts of the equilibria-related H_{ox} and H_{ox}' were calculated. In the absence of MMOB, 84% of intermolecular electron transfer from $MMOR_{3e-}$ to oxidized MMOH takes place through the two fast pathways associated with H_{ox} ; slow reduction of H_{ox}' accounts for the remaining 16%. When two equivalents of MMOB are pre-mixed with MMOH, the partitioning of electron transfer through the fast (15%) and slow (85%) pathways is inverted. For a mixture of 10 μ M oxidized MMOH and 20 μ M MMOB ($K_d = 0.3 \mu$ M and 0.7 μ M),¹⁸ MMOB is bound to about 86% of the hydroxylase protomers. Therefore, we assign H_{ox}' as the hydroxylase population with structural features like those induced by MMOB binding. When $MMOR_{3e-}$ is mixed with the pre-formed

MMOH–MMOB complex, rapid electron transfer (at k_1 and k_2) occurs only to those hydroxylase protomers without bound MMOB.

There are several spectroscopic indications of heterogeneity in both oxidized and reduced hydroxylase samples. In freeze-quench Mössbauer studies of the reaction of $H_{\text{red}}/2B$ with dioxygen, two distinct populations of H_{red} were observed.²⁵ Only the minority species (30-40% of the iron that participated in the reaction) generated high-valent intermediates at rates fast enough to support steady-state turnover numbers. In addition, a third fraction (ca. 12% of the total iron) did not react with dioxygen at all. The occurrence of two populations of H_{ox} from *M. capsulatus* (Bath) was previously detected by EPR spectral analysis of cryoreduced samples.⁵¹ Moreover, this study indicated that the effects of MMOB did not involve significant alterations in the primary coordination sphere of the diiron center. EXAFS spectroscopy of oxidized hydroxylase from *M. trichosporium* OB3b revealed two populations of diiron sites with Fe–Fe distances of 3.01 Å (60%) and 3.36 Å (40%).⁵² Only ca. 15% of $MMOH_{\text{ox}}$ is converted to the μ -oxo species by MMOD, even though two equivalents of MMOD bind to each hydroxylase molecule.¹⁹ Therefore, the multiple populations of hydroxylase proposed for intermolecular electron transfer reactions (Schemes 4.3B and 4.4) are not unreasonable.

When $MMOR_{3e-}$ and MMOB are mixed simultaneously with oxidized MMOH, a smaller inhibitory effect on electron transfer is observed. This result correlates well with the proposal that MMOB produces a conformational change in MMOH that limits electron transfer in the ternary pre-complex. The forward rate constant for MMOH–MMOB isomerization at 4 °C is quite small ($k_f = 0.0056 \text{ s}^{-1}$),¹⁸ such that the full effects of MMOB binding are not realized immediately after mixing with MMOH. In addition, the hydroxylase redox potentials undergo a significantly smaller shift when

MMOH is not pre-mixed with MMOB (Scheme 4.5). Any effect on intermolecular electron transfer arising from decreased MMOH midpoint potentials (E_m) would be largely muted by avoiding equilibration of the MMOH–MMOB complex.

Incubating MMOH with two equivalents of MMOD inhibits electron transfer from MMOR_{3e^-} even more severely than MMOB (Figure 4.7B). Several possibilities exist for inhibition of intermolecular electron transfer by MMOD: (i) MMOD binding to MMOH obscures the MMOR binding site; (ii) MMOD binding to MMOH induces a conformational change in MMOH that makes MMOR binding and/or electron transfer unfavorable; (iii) MMOD alters the MMOH redox potentials; (iv) MMOD binds to MMOR; and (v) MMOD alters the MMOR redox potentials. The inclusion of MMOD in the sMMO enzyme system was established only recently;¹⁹ for this reason, its component interactions have not been studied in as much detail as those of MMOB and MMOR. MMOD competes with MMOB for binding sites on the hydroxylase and cross-links to both the MMOH alpha and beta subunits.¹⁹ There is no evidence for binding to MMOR or MMOB, a finding that argues against proposals iv and v. The effect of MMOD on the hydroxylase redox potentials is currently unknown. After reaction with MMOR_{3e^-} in the presence of MMOD, the hydroxylase is reduced by only 75%. Therefore, a large decrease in the midpoint potential of the MMOH–MMOD complex that cannot be overcome by MMOR binding is possible. One of the first two proposals, competitive binding with MMOR or a conformational change that prevents electron transfer, probably accounts for the majority of electron transfer inhibition noted for MMOD.

Hysteresis in Intermolecular Electron Transfer Reactions. In the absence of MMOB or MMOD, MMOR_{3e^-} transmits two electrons to MMOH at 4 °C in about 31 ms, which corresponds to a maximum turnover number of 32 s^{-1} for the complete reduction

of one of the two hydroxylase diiron centers. Pre-mixing two equivalents of MMOB with MMOH increases the time for two-electron transfer to 11.2 s (maximum turnover number of 0.089 s^{-1}). In steady-state sMMO reactions with methane, a turnover number of ca. 0.3 s^{-1} is achieved with similar ratios of the MMO components at $4\text{ }^{\circ}\text{C}$.¹⁸ If the effects of reductase binding to the MMOH–MMOB complex rapidly dissipated upon dissociation of MMOR, steady-state catalysis would be limited by electron transfer to a rate at least threefold lower than actually observed. Therefore, either MMOR does not dissociate from the ternary MMOH–MMOB–MMOR complex during steady-state turnover or relaxation of the MMOH–MMOR complex to the free hydroxylase conformational state is slow with respect to the binding and dissociation of MMOR. Because steady-state sMMO activity can be maximized in the presence of only 0.1–0.2 equivalents of MMOR per hydroxylase,^{17,18,28} a single reductase molecule must service multiple MMOH molecules during each turnover of the enzyme, a process that requires rapid binding to and dissociation from MMOH–MMOB complexes. We conclude that hysteresis of the conformational changes imparted to MMOH by MMOR is necessary for sustained rapid intermolecular electron transfer in the sMMO system. By this mechanism, the ungated hydroxylase structure would be retained throughout the catalytic cycle so that slow MMOH–MMOR isomerization reactions do not inhibit turnover. Furthermore, the equilibrated $\text{MMOH}_{\text{ox}}:2\text{MMOB}$ complex cannot be a catalytically relevant structure in steady-state sMMO reactions because electron transfer to this species is too slow to support observed reaction rates. This complex may represent a subset of the hydroxylase population but cannot be the majority species. The present work was performed at $4\text{ }^{\circ}\text{C}$; it is possible that at higher temperatures a step other than MMOH–MMOR isomerization becomes rate-limiting. A comprehensive study of component interactions over a wide temperature range (4–45

°C) suggested that the regulatory mechanism of hydroxylase activity by MMOB and MMOR is conserved with respect to temperature, however.¹⁸ An alternative and seemingly unlikely explanation is that a large portion of MMOH does not participate in steady-state turnover.

Hysteresis has been invoked for several other aspects of the sMMO system. For example, just 0.6 equivalents of MMOB effect the full conversion of the reduced MMOH EPR spectrum to that of the $\text{MMOH}_{\text{red}}\text{-MMOB}$ complex.³⁰ Substrate hydroxylation regioselectivity is also controlled by substoichiometric quantities of MMOB.³⁰ The complete effects of MMOR on the hydroxylase redox potentials, single-turnover product yields, and MMOH_{red} reactivity with O_2 are achieved with a 0.2:1 MMOR:MMOH ratio.²⁹ On the basis of these hysteretic changes induced by MMOR, a mechanism in which MMOR converts MMOH to a different conformation (MMOH'') with distinct physical properties was proposed.²⁹ At physiological ratios of sMMO components (1:2:0.2 for MMOH:MMOB:MMOR),^{17,29} the hydroxylase would exist primarily in the MMOH'' form with increased and inverted redox potentials, thereby favoring two-electron transfer. In addition to these features of MMOH'' , we propose that this hydroxylase conformation supports rapid intermolecular electron transfer in the initial MMOH–MMOR or MMOH–MMOB–MMOR precomplex.

MMOR Ferredoxins as Models for Intermolecular Electron Transfer. Several reductase ferredoxin analogs ranging in length from a 98-residue MMOR-Fd truncate to FAD-depleted full-length MMOR were examined as models for intermolecular electron transfer in the sMMO system (Figure 4.1B). These proteins, which contain only a [2Fe-2S] cluster, facilitate interpretation of data for the inaugural interprotein electron transfer event. Electron transfer to MMOH from all three ferredoxin constructs proceeds via biphasic reactions similar to the multiple phases observed for

wild-type MMOR. Rate constants for these electron transfer steps vary significantly from protein to protein (Figure 4.7A and Table 4.2). The particularly low electron transfer rates measured for MMOR-Fd(1-98) ($k_1 = 1.0 \text{ s}^{-1}$ and $k_2 = 0.24 \text{ s}^{-1}$) were somewhat surprising; the slightly longer MMOR-Fd(1-120+tail) transfers electrons to MMOH at 30-fold higher rates. Spectroscopic (optical, EPR, and EXAFS) and redox potential studies demonstrate that the [2Fe-2S] center of MMOR-Fd(1-98) is identical to the corresponding cofactor in MMOR.^{34,49} The NMR structure of this short MMOR-Fd domain reveals a fold typical of plant-type ferredoxins.³⁵ We postulate that the discrepancy in intermolecular electron transfer rates arises from the involvement of MMOR residues 99-120 in complex formation with MMOH. To test this hypothesis, we are preparing the MMOR-Fd(1-120) construct in order to investigate intermolecular electron transfer from this longer ferredoxin domain to MMOH.

Application of ET Theory to Intermolecular Electron Transfer in sMMO. ET theory may be applied to interprotein electron transfer reactions provided that the observed rate constants are not limited by preceding adiabatic processes such as proton transfer. Because it is not practical to vary ΔG° systematically in most biological systems, ET parameters can be determined instead by examining the reaction at varying temperatures.⁵³ There are several important caveats to this type of analysis. Temperature-dependent changes in ΔG° , H_{AB} , or λ or the rate-limiting step can invalidate the results of analysis by ET theory. For most biological electron transfer reactions, including those of the sMMO system (vide infra), $-\Delta G^\circ$ is small compared to λ . Therefore, changes in the value of ΔG° with temperature have very little effect on the calculated ET parameters. In addition, any uncertainty in the ΔE° value, even as large as $\pm 100 \text{ mV}$, is of little importance.⁵³ The possibility of temperature-dependent protein conformational changes that alter the values of H_{AB} or λ is often reduced by the limited

range of temperatures over which biological systems can be studied. Despite the many stipulations, analysis of interprotein electron transfer reactions by ET theory can be a useful diagnostic tool to distinguish between true, gated, and coupled electron transfer.^{2,53}

Electron transfer from MMOR to MMOH is additionally complex, with multiple hydroxylase populations giving rise to four electron transfer rate constants. A value for ΔE° (+281 mV) was selected to represent the initial electron transfer from the [2Fe-2S] cluster ($E^{\circ'} = -205$ mV)³⁴ to oxidized MMOH ($E_1^{\circ'} = +76$ mV).⁴⁴ Other possible ΔE° values for the sMMO system range from +226 mV to +319 mV, corresponding to a difference in ΔG° values of only 2.1 kJ/mol. As discussed above, the magnitude of the potential error in ΔG° is not significant in this analysis. The H_{AB} , Δ , and r values determined for electron transfer from two MMOR-Fd analogs and MMOR to MMOH are all reasonable for true electron transfer reactions (Table 4.4). The significantly larger values obtained for H_{AB} and Δ in the MMOR-Fd(1-98) (k_1 and k_2) and MMOR (k_4) reactions may indicate gated or coupled electron transfer reactions. The ET parameters for the remaining reactions are fairly similar. Of particular interest is r , the distance between the reductase [2Fe-2S] and hydroxylase diiron centers in the MMOH-MMOR complex. For MMOR (k_1 and k_3) and MMOR-Fd(1-120+tail) (k_1), an average r value of 11.0 ± 0.3 Å was determined. This distance falls within the 14-Å requirement for efficient electron transfer in biological systems.⁵⁴ In addition, the shortest path from the MMOH diiron site to the hydroxylase surface is ca. 12 Å.⁵⁵ Thus, only a small conformational change in MMOH would be required to accommodate the reductase in a position suitable for rapid electron transfer. If the ET theory-derived r values are accurate, MMOR must bind in the central hydroxylase canyon region, as suggested previously.^{42,56} The rather large Δ values determined for intermolecular electron

transfer (1.5-2.0 eV) suggest that considerable conformational changes accompany hydroxylase reduction. Oxidation of the reductase [2Fe-2S] is not expected to require significant reorganization. Upon formation of reduced and mixed-valent MMOH, carboxylate shifts and severe distortion of the diiron site occur, respectively, as observed in crystal structures of the hydroxylase in different oxidation states.^{43,57,58} These types of sizeable structural perturbations at the MMOH active site could account for the large λ values. Alternatively, the observed electron transfer rate constants could represent kinetically coupled ET reactions, in which case λ would contain contributions from both the electron transfer event and the preceding reaction step.

Concluding Remarks. Electron transfer from chemically reduced MMOR to oxidized MMOH occurs in four discrete kinetic phases corresponding to the transfer of four electrons into the two dinuclear iron centers of the hydroxylase. Both MMOB and MMOD severely diminish intermolecular electron transfer rates by shifting the majority of electron transfer to the slowest reaction phase, suggesting a function for one or both of these proteins in regulating electron transfer in the sMMO system. A model in which MMOR-induced conformational changes to MMOH are retained throughout the steady-state catalytic cycle is proposed to account for slow intermolecular electron transfer observed in the ternary MMOH–MMOB–MMOR pre-complex. In order to distinguish between the various possible asynchronous, concerted, and parallel electron transfer mechanisms, freeze-quench EPR, Mössbauer, and XAS spectra are required to characterize the MMOH diiron sites throughout the reactions. Using flash photolysis to initiate electron transfer in pre-formed MMOH–MMOR complexes may be valuable for determining intrinsic intermolecular electron transfer rates in the absence of slow binding isomerization reactions.

ACKNOWLEDGMENT

This work was supported by National Institute of General Medical Sciences grant GM32134 (S.J.L.). J.L.B. was a Howard Hughes Medical Institute predoctoral fellow, and George T. Gassner was an NIH postdoctoral fellow. We acknowledge Dr. Maarten Merkx for providing the MMOD used in this study and the Multiuser Facility for the Study of Complex Macromolecular Systems (NSF-0070319) for access to an isothermal titration calorimeter.

REFERENCES

- (*) A slightly modified version of this work will be submitted for publication.
Blazyk, J. L.; Gassner, G. T.; Lippard, S. J. **2003**. George T. Gassner performed the initial electron transfer experiments with MMOR and MMOR(apoFAD).
- (1) Marcus, R. A.; Sutin, N. *Biochim. Biophys. Acta* **1985**, *811*, 265-322.
- (2) Davidson, V. L. *Acc. Chem. Res.* **2000**, *33*, 87-93.
- (3) Hoffman, B. M.; Ratner, M. A. *J. Am. Chem. Soc.* **1987**, *109*, 6237-6243.
- (4) Batie, C. J.; Ballou, D. P.; Correll, C. C. In *Chemistry and Biochemistry of Flavoenzymes*; Müller, F., Ed.; CRC Press: Boca Raton, FL, 1992; Vol. III, pp 543-556.
- (5) Higgins, I. J.; Best, D. J.; Hammond, R. C.; Scott, D. *Microbiol. Rev.* **1981**, *45*, 556-590.
- (6) Hanson, R. S.; Hanson, T. E. *Microbiol. Rev.* **1996**, *60*, 439-471.
- (7) Higgins, I. J.; Best, D. J.; Hammond, R. C. *Nature* **1980**, *286*, 561-564.
- (8) Murrell, J. C. *Biodegradation* **1994**, *5*, 145-159.
- (9) Nguyen, H.-H. T.; Elliott, S. J.; Yip, J. H.-K.; Chan, S. I. *J. Biol. Chem.* **1998**, *273*, 7957-7966.
- (10) Lieberman, R. L.; Shrestha, D. B.; Doan, P. E.; Hoffman, B. M.; Stemmler, T. L.; Rosenzweig, A. C. *Proc. Nat. Acad. Sci. USA* **2003**, *100*, 3820-3825.
- (11) Prior, S. D.; Dalton, H. J. *Gen. Microbiol.* **1985**, *131*, 155-163.
- (12) Feig, A. L.; Lippard, S. J. *Chem. Rev.* **1994**, *94*, 759-805.
- (13) Wallar, B. J.; Lipscomb, J. D. *Chem. Rev.* **1996**, *96*, 2625-2657.
- (14) Merckx, M.; Kopp, D. A.; Sazinsky, M. H.; Blazyk, J. L.; Müller, J.; Lippard, S. J. *Angew. Chem. Int. Ed.* **2001**, *40*, 2782-2807.
- (15) Baik, M.-H.; Newcomb, M.; Friesner, R. A.; Lippard, S. J. *Chem. Rev.* **2003**, *103*, 2385-2419.

- (16) Colby, J.; Dalton, H. *Biochem. J.* **1978**, *171*, 461-468.
- (17) Fox, B. G.; Froland, W. A.; Dege, J. E.; Lipscomb, J. D. *J. Biol. Chem.* **1989**, *264*, 10023-10033.
- (18) Gassner, G. T.; Lippard, S. J. *Biochemistry* **1999**, *38*, 12768-12785.
- (19) Merckx, M.; Lippard, S. J. *J. Biol. Chem.* **2002**, *277*, 5858-5865.
- (20) Stainthorpe, A. C.; Lees, V.; Salmond, G. P. C.; Dalton, H.; Murrell, J. C. *Gene* **1990**, *91*, 27-34.
- (21) Lund, J.; Woodland, M. P.; Dalton, H. *Eur. J. Biochem.* **1985**, *147*, 297-305.
- (22) Green, J.; Dalton, H. *Biochem. J.* **1989**, *259*, 167-172.
- (23) Kopp, D. A.; Gassner, G. T.; Blazyk, J. L.; Lippard, S. J. *Biochemistry* **2001**, *40*, 14932-14941.
- (24) Lee, S.-K.; Nesheim, J. C.; Lipscomb, J. D. *J. Biol. Chem.* **1993**, *268*, 21569-21577.
- (25) Liu, K. E.; Valentine, A. M.; Wang, D.; Huynh, B. H.; Edmondson, D. E.; Salifoglou, A.; Lippard, S. J. *J. Am. Chem. Soc.* **1995**, *117*, 10175-10185.
- (26) Shu, L.; Nesheim, J. C.; Kauffmann, K.; Münck, E.; Lipscomb, J. D.; Que, L., Jr. *Science* **1997**, *275*, 515-518.
- (27) Valentine, A. M.; Stahl, S. S.; Lippard, S. J. *J. Am. Chem. Soc.* **1999**, *121*, 3876-3887.
- (28) Fox, B. G.; Liu, Y.; Dege, J. E.; Lipscomb, J. D. *J. Biol. Chem.* **1991**, *266*, 540-550.
- (29) Liu, Y.; Nesheim, J. C.; Paulsen, K. E.; Stankovich, M. T.; Lipscomb, J. D. *Biochemistry* **1997**, *36*, 5223-5233.
- (30) Froland, W. A.; Andersson, K. K.; Lee, S.-K.; Liu, Y.; Lipscomb, J. D. *J. Biol. Chem.* **1992**, *267*, 17588-17597.
- (31) Andrews, S. C.; Shipley, D.; Keen, J. N.; Findlay, J. B. C.; Harrison, P. M.; Guest, J. R. *FEBS Lett.* **1992**, *302*, 247-252.
- (32) Karplus, P. A.; Daniels, M. J.; Herriott, J. R. *Science* **1991**, *251*, 60-66.

- (33) Correll, C. C.; Batie, C. J.; Ballou, D. P.; Ludwig, M. L. *Science* **1992**, *258*, 1604-1610.
- (34) Blazyk, J. L.; Lippard, S. J. *Biochemistry* **2002**, *41*, 15780-15794.
- (35) Müller, J.; Lugovskoy, A. A.; Wagner, G.; Lippard, S. J. *Biochemistry* **2002**, *41*, 42-51.
- (36) Chatwood, L. L.; Müller, J.; Gross, J. D.; Wagner, G.; Lippard, S. J., unpublished results.
- (37) Massey, V. *J. Biol. Chem.* **1957**, *229*, 763-770.
- (38) Stookey, L. L. *Anal. Chem.* **1970**, *42*, 779-781.
- (39) Coufal, D. E.; Blazyk, J. L.; Whittington, D. A.; Wu, W. W.; Rosenzweig, A. C.; Lippard, S. J. *Eur. J. Biochem.* **2000**, *267*, 2174-2185.
- (40) Moser, C. C.; Keske, J. M.; Warncke, K.; Farid, R. S.; Dutton, P. L. *Nature* **1992**, *355*, 796-802.
- (41) Blazyk, J. L.; Lippard, S. J., unpublished results.
- (42) Kopp, D. A.; Berg, E. A.; Costello, C. E.; Lippard, S. J. *J. Biol. Chem.* **2003**, *278*, 20939-20945.
- (43) Whittington, D. A.; Lippard, S. J. *J. Am. Chem. Soc.* **2001**, *123*, 827-838.
- (44) Paulsen, K. E.; Liu, Y.; Fox, B. G.; Lipscomb, J. D.; Münck, E.; Stankovich, M. T. *Biochemistry* **1994**, *33*, 713-722.
- (45) Liu, K. E.; Lippard, S. J. *J. Biol. Chem.* **1991**, *266*, 12836-12839; 24859.
- (46) Liu, K. E.; Lippard, S. J. In *Adv. Inorg. Chem.*; Sykes, A. G., Ed.; Academic Press: San Diego, 1995; Vol. 42, pp 263-289.
- (47) Pulver, S. C.; Froland, W. A.; Lipscomb, J. D.; Solomon, E. I. *J. Am. Chem. Soc.* **1997**, *119*, 387-395.
- (48) DeWitt, J. G.; Rosenzweig, A. C.; Salifoglou, A.; Hedman, B.; Lippard, S. J.; Hodgson, K. O. *Inorg. Chem.* **1995**, *34*, 2505-2515.

- (49) Rudd, D. J.; Merckx, M.; Hedman, B.; Lippard, S. J.; Hodgson, K. O., unpublished results.
- (50) Green, J.; Dalton, H. *J. Biol. Chem.* **1985**, *260*, 15795-15801.
- (51) Davydov, R.; Valentine, A. M.; Komar-Panicucci, S.; Hoffman, B. M.; Lippard, S. J. *Biochemistry* **1999**, *38*, 4188-4197.
- (52) Shu, L.; Liu, Y.; Lipscomb, J. D.; Que, L., Jr. *J. Biol. Inorg. Chem.* **1996**, *1*, 297-304.
- (53) Davidson, V. L. *Biochemistry* **1996**, *35*, 14035-14039.
- (54) Page, C. C.; Moser, C. C.; Chen, X.; Dutton, P. L. *Nature* **1999**, *402*, 47-52.
- (55) Sazinsky, M. H.; Lippard, S. J., unpublished results.
- (56) Rosenzweig, A. C.; Frederick, C. A.; Lippard, S. J.; Nordlund, P. *Nature* **1993**, *366*, 537-543.
- (57) Rosenzweig, A. C.; Nordlund, P.; Takahara, P. M.; Frederick, C. A.; Lippard, S. J. *Chem. & Biol.* **1995**, *2*, 409-418.
- (58) Rosenzweig, A. C.; Frederick, C. A.; Lippard, S. J. In *Microbial Growth on C₁ Compounds*; Lidstrom, M. E., Tabita, F. R., Eds.; Kluwer Academic Publishers: Dordrecht, Germany, 1996, pp 141-149.

Table 4.1: Thermodynamic Parameters for MMOH–MMOR-Fd and MMOH–MMOR Interactions^a

Protein	K_{d1} (μM)	ΔG_1 (kcal mol^{-1})	ΔH_1 (kcal mol^{-1})	$T\Delta S_1$ (kcal mol^{-1})	K_{d2} (μM)	ΔG_2 (kcal mol^{-1})	ΔH_2 (kcal mol^{-1})	$T\Delta S_2$ (kcal mol^{-1})
Fd(1-98) ^b	0.6	-7.9	-4.4	3.5	3.2	-7.0	-5.0	2.0
MMOR ^c	0.4	-8.1	4.5	12.6	0.7	-7.8	2.4	10.1

^a Isothermal titration data were fit with an interacting sites model after correcting for the nonbinding fraction of MMOH; see text for details. ^b Measured at 4.2 °C. ^c From ref 18; measured at 3.3 °C.

Table 4.2: Intermolecular Electron Transfer Rate Constants for MMOR-Fd and MMOR^a

Protein	aa ^b	k_1 (s ⁻¹)	k_2 (s ⁻¹)	k_3 (s ⁻¹)	k_4 (s ⁻¹)
MMOR-Fd(1-98)	98	1.0 ± 0.1	0.24 ± 0.04	n/a	n/a
MMOR-Fd(1-120+tail) ^c	139	35 ± 4	7.1 ± 1.1	n/a	n/a
MMOR(apoFAD)	348	17 ± 2	2.9 ± 0.3	n/a	n/a
MMOR	348	65 ± 5	12 ± 3	1.3 ± 0.2	0.032 ± 0.007

^aMeasured at pH 7.0 and 4 °C in single-wavelength stopped-flow experiments. ^baa, amino acid residues. ^cTail sequence: ATPSSFFCRSGPTSAATVA.

Table 4.3: Activation Energies for Intermolecular Electron Transfer^a

Protein	aa ^b	E_{a1} (kcal mol ⁻¹)	E_{a2} (kcal mol ⁻¹)	E_{a3} (kcal mol ⁻¹)
MMOR-Fd(1-98)	98	11.6	12.8	n/a
MMOR-Fd(1-120+tail)	139	7.9	7.1	n/a
MMOR(apoFAD)	348	13.5	11.8	n/a
MMOR	348	8.3	9.3	10.1

^aMeasured at pH 7.0 in single-wavelength stopped-flow experiments. ^baa, amino acid residues.

Table 4.4: Electron Transfer Parameters from Temperature Dependence Studies^a

Reaction	Rate Constant (s ⁻¹) ^b	H_{AB} (cm ⁻¹) ^c	Δ (eV) ^c	r (Å) ^c
Fd(1-98) _{red} + H _{ox}	k_1 (1.0)	7.5 ± 3.3	2.3 ± 0.1	8.3 ± 0.6
	k_2 (0.24)	5.7 ± 1.3	2.4 ± 0.1	8.7 ± 0.3
Fd(1-120+tail) _{red} + H _{ox}	k_1 (35)	0.9 ± 0.5	1.6 ± 0.1	11.2 ± 0.8
	k_2 (7)	0.2 ± 0.1	1.5 ± 0.2	13.3 ± 0.9
MMOR _{3e-} + H _{ox}	k_1 (65)	1.1 ± 0.3	1.5 ± 0.1	11.0 ± 0.4
	k_2 (12)	2.5 ± 5.2	1.9 ± 0.4	9.9 ± 3.0
	k_3 (1.3)	1.3 ± 0.3	2.0 ± 0.1	10.7 ± 0.4
	k_4 (0.032)	7 ± 21	2.6 ± 0.6	8.5 ± 4.2

^aMeasured at pH 7.0 in single-wavelength stopped-flow experiments. ^bNumbers in parentheses measured at 4 °C. ^cValues of H_{AB} , Δ , and r were determined by fitting rate constant vs temperature plots with eq 2 or 3; $\Delta E^\circ = +0.281$ V (Fd_{ox/red} = -0.205 V, H_{ox/mv} = +0.076 V), $\Delta G^\circ = -6.48$ kJ mol⁻¹, $k_0 = 10^{13}$ s⁻¹, $\Delta = 1.4$ Å⁻¹, and $r_0 = 3.0$ Å. Because $\Delta \gg \Delta G^\circ$, altering ΔE° by ± 0.1 V yields only small changes in H_{AB} , Δ , and r .

Table 4.5: Effect of MMOB on Intermolecular Electron Transfer for MMOR Ferredoxin Analogs^a

Protein	k_1 (s ⁻¹)	% MMOH reduction ^b	k_2 (s ⁻¹)	% MMOH reduction
MMOR-Fd(1-98)	1.0 ± 0.1	23 (66) ^c	0.28 ± 0.02	35 (34)
+ MMOB (2 eq.) ^d	1.1 ± 0.2	5 (15)	0.056 ± 0.005	34 (85)
MMOR(apoFAD)	8.3 ± 0.7	19 (50)	1.2 ± 0.1	38 (50)
+ MMOB (2 eq.)	7.3 ± 0.2	20 (42)	0.25 ± 0.01	48 (58)

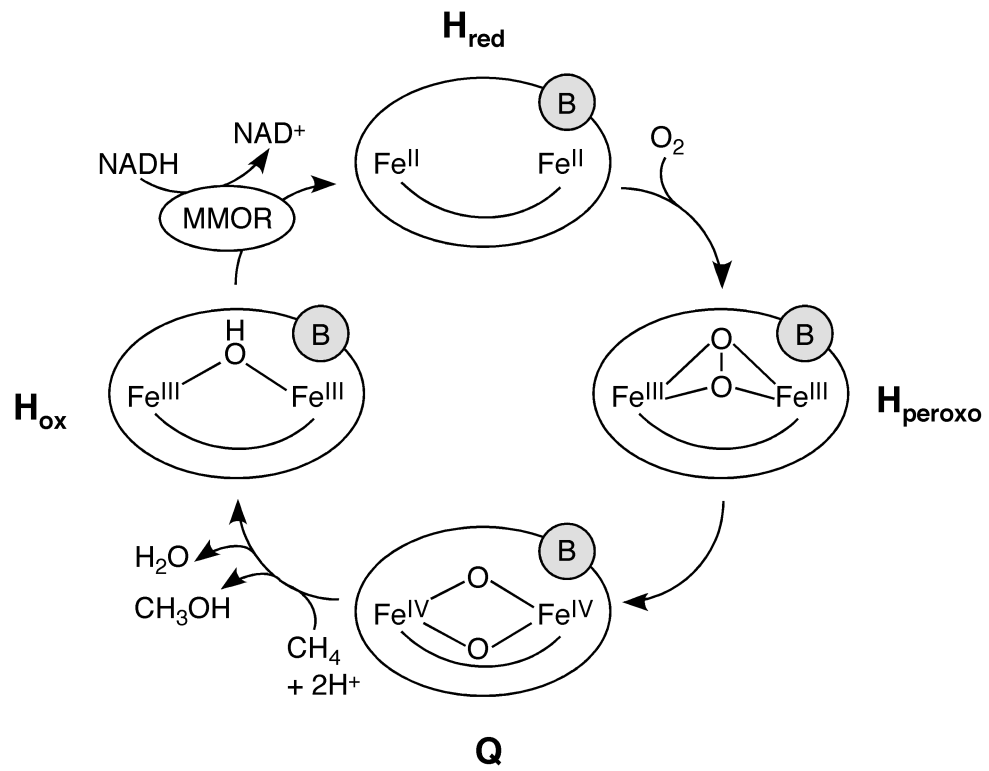
^aMeasured at 4 °C and pH 7.0 in diode array stopped-flow experiments. ^bPercent reduction of MMOH at the completion of each reaction phase, with four-electron reduced MMOH corresponding to 100%. ^cNumbers in parentheses represent the percentage of electrons transferred at that rate.

^dEquilibrated mixture of MMOH and two mole equivalents of MMOB.

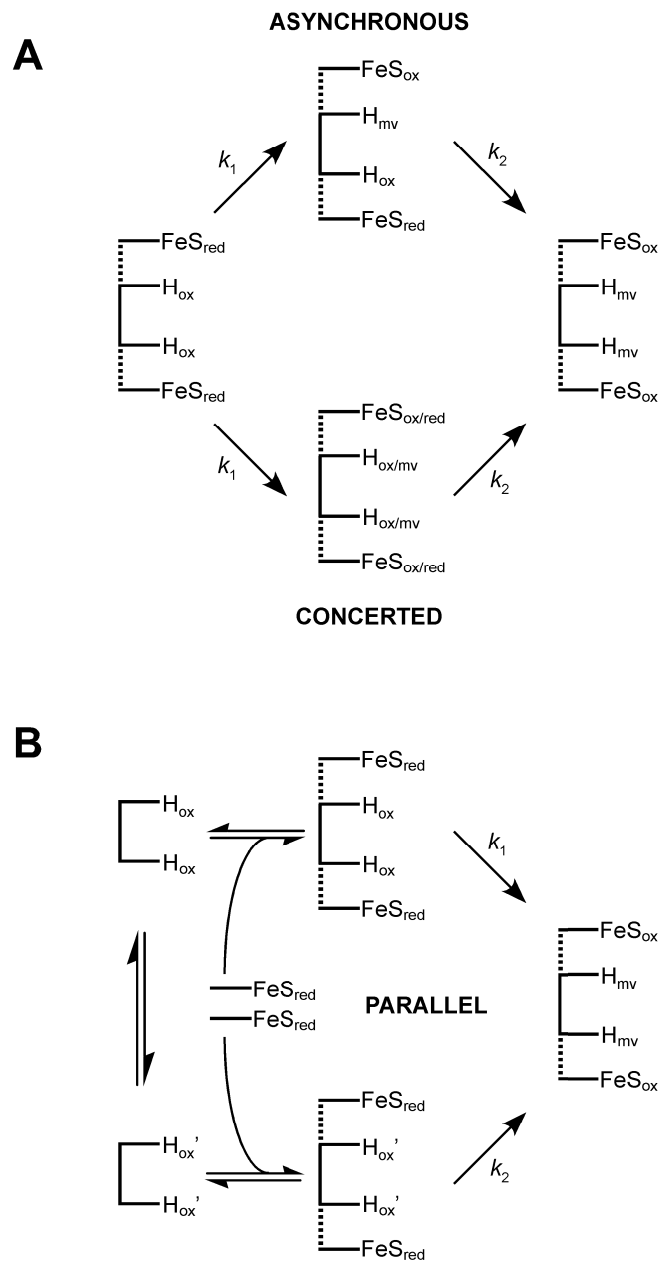
Table 4.6: Distribution of Electrons in Intermolecular Electron Transfer Intermediates^a

Species	k_f (s ⁻¹)	% total Fe ₂ S ₂		% total FAD ^b			% MMOH reduction ^b	
		Fd _{ox}	Fd _{red}	FAD _{ox}	FAD _{sq}	FAD _{hq}	Step ^c	Total ^c
$2R_{3e^-} + H_{ox}$								
A	—	6	94	0	2	98	—	4 (0)
B	65	40	60	3	21	75	30 (39)	34 (39)
C	20	41	59	10	57	34	25 (32)	59 (71)
D	3	55	45	15	55	30	12 (15)	70 (86)
E	0.2	65	35	22	53	25	11 (14)	81 (100)
$2R_{3e^-} + H_{ox}/2B^d$								
A	—	0	100	0	0	100	—	0 (0)
B	50	4	96	0	1	99	3 (4)	3 (4)
C	9	4	96	0	14	86	6 (8)	9 (12)
D	1.5	2	98	6	24	70	10 (13)	19 (25)
E	0.04	52	48	16	63	21	54 (70)	73 (95)
$2R_{3e^-} + H_{ox}/2D^e$								
A	—	1	99	0	0	100	—	1 (0)
B	3	2	98	0	11	89	6 (8)	7 (8)
C	0.08	2	98	3	31	66	13 (17)	20 (25)
D	0.01	38	62	7	62	31	37 (48)	57 (73)

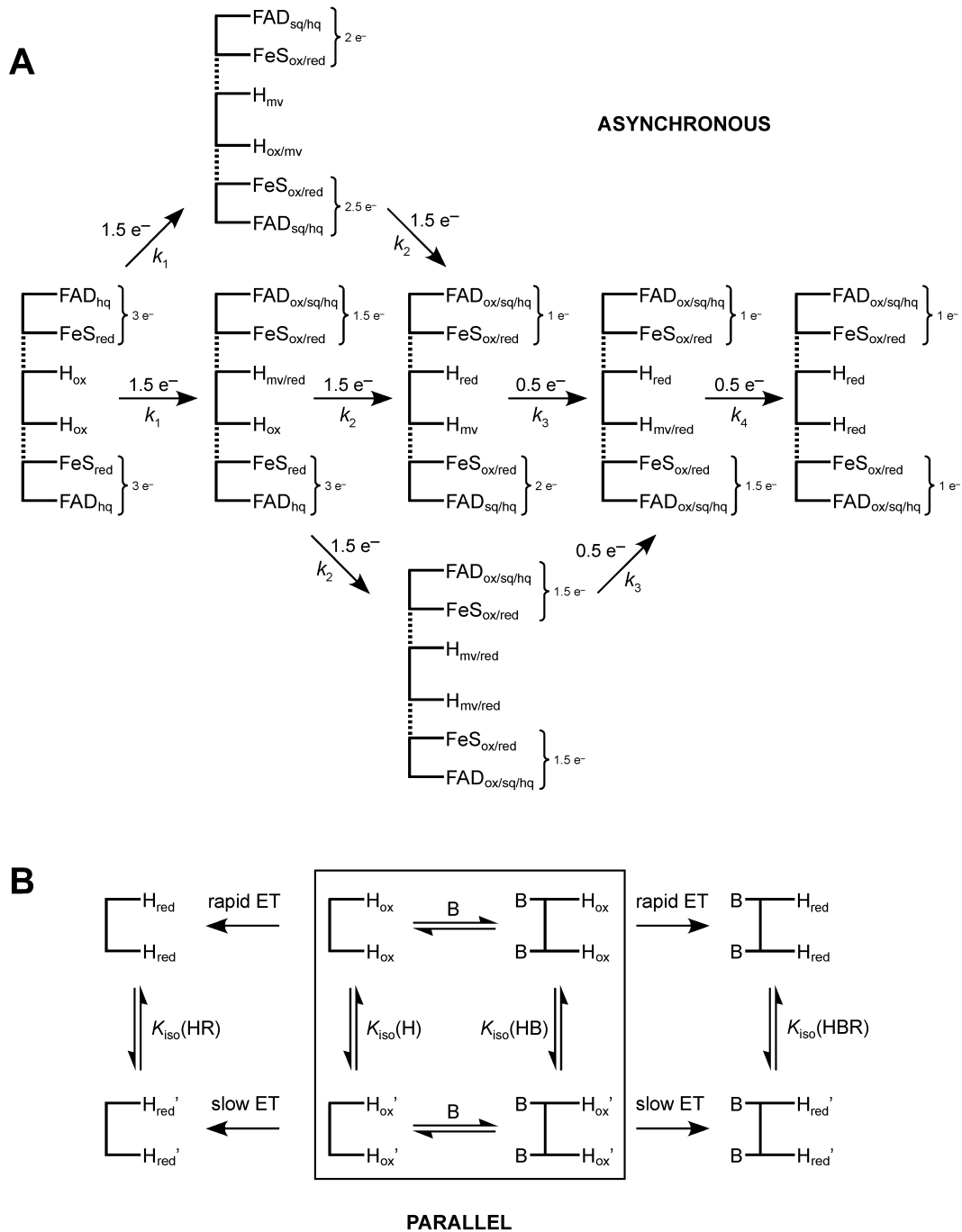
^aMeasured at pH 7.0 and 4 °C in diode array stopped-flow experiments. Intermediates are for sequential kinetic schemes. ^bIn some cases, percentages do not total 100 due to rounding. ^cNumbers in parentheses represent percent MMOH reduction after correcting for the nonbinding hydroxylase fraction. ^dMMOB pre-equilibrated with MMOH. ^eMMOD pre-equilibrated with MMOH.



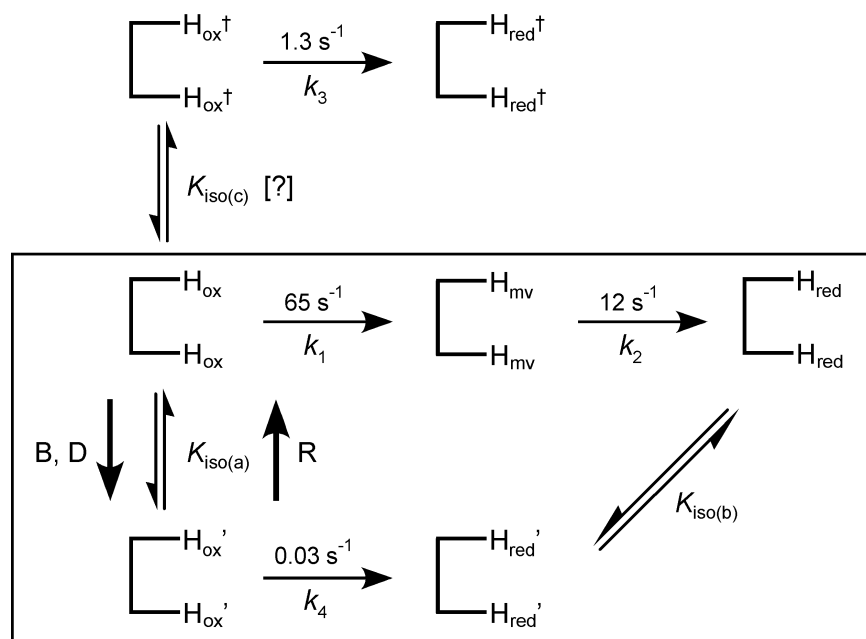
Scheme 4.1



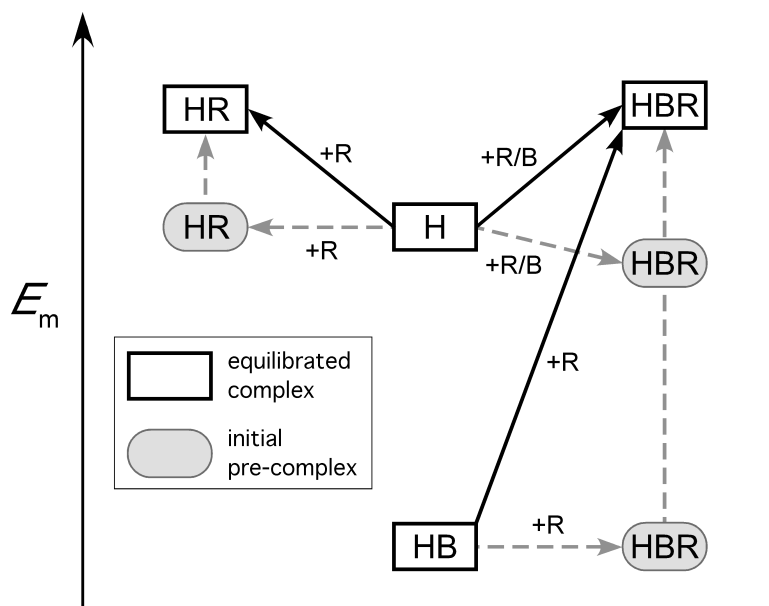
Scheme 4.2



Scheme 4.3



Scheme 4.4



Scheme 4.5

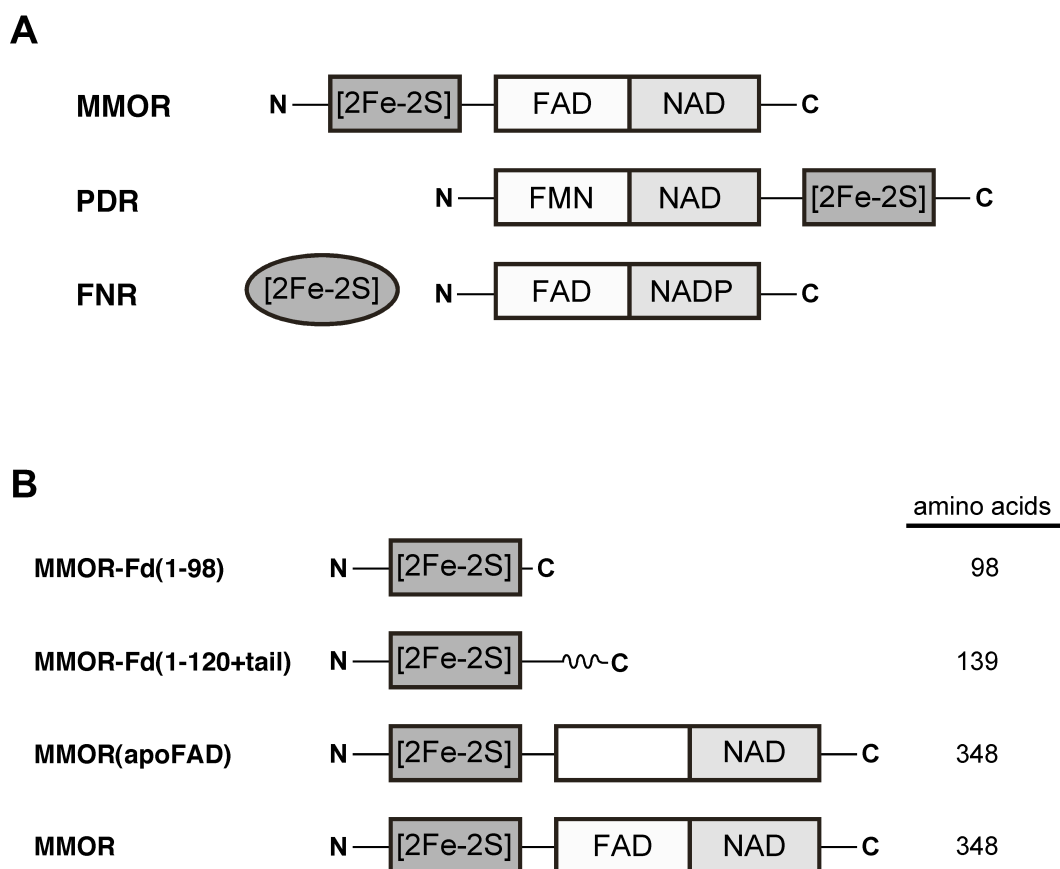


Figure 4.1. (A) Examples of alternative connectivities between the one-electron carrier and flavin/NAD(P) binding domains of flavoprotein electron transferases. (B) MMOR proteins examined in this study.

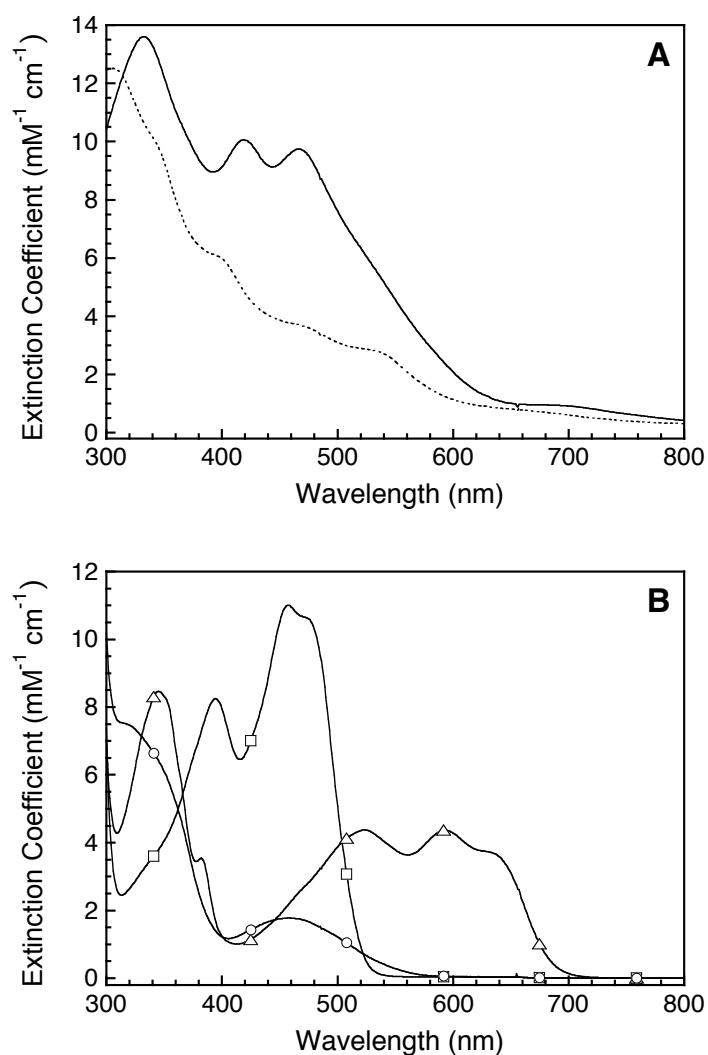


Figure 4.2. Component spectra determined for the MMOR domain proteins. (A) Oxidized (Fd_{ox} ; solid line) and reduced (Fd_{red} ; dotted line) optical spectra for MMOR-Fd. (B) MMOR-FAD in the oxidized (FAD_{ox} ; squares), semiquinone (FAD_{sq} ; triangles), and hydroquinone (FAD_{hq} ; circles) oxidation states. From ref 34.

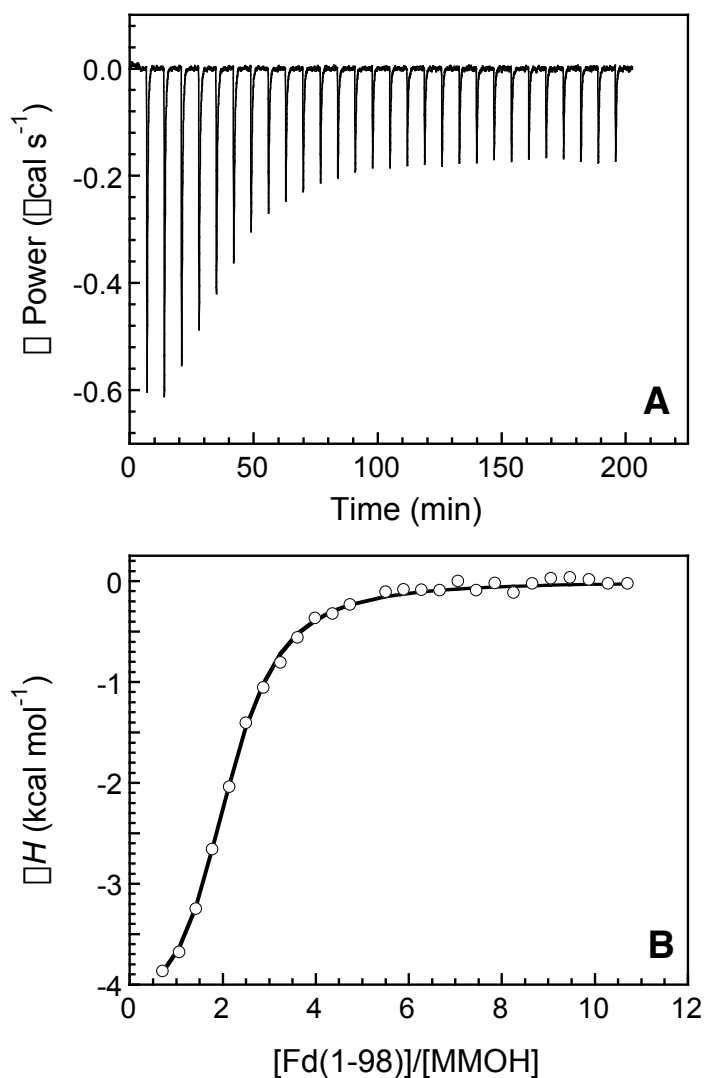


Figure 4.3. Determination of MMOH–MMOR–Fd(1-98) binding constant by isothermal titration calorimetry. (A) Data recorded for complex formation between MMOH (11.1 μM in the calorimeter cell) and MMOR–Fd(1-98) (368 μM in a 250- μL injection syringe) at 4.2 $^{\circ}\text{C}$. Each heat pulse corresponds to a 10- μL injection into the 1.430-mL sample cell. (B) Integrated enthalpy data (circles) fit with an interacting sites binding model after correction of the MMOH concentration for the nonbinding fraction of hydroxylase (solid line).

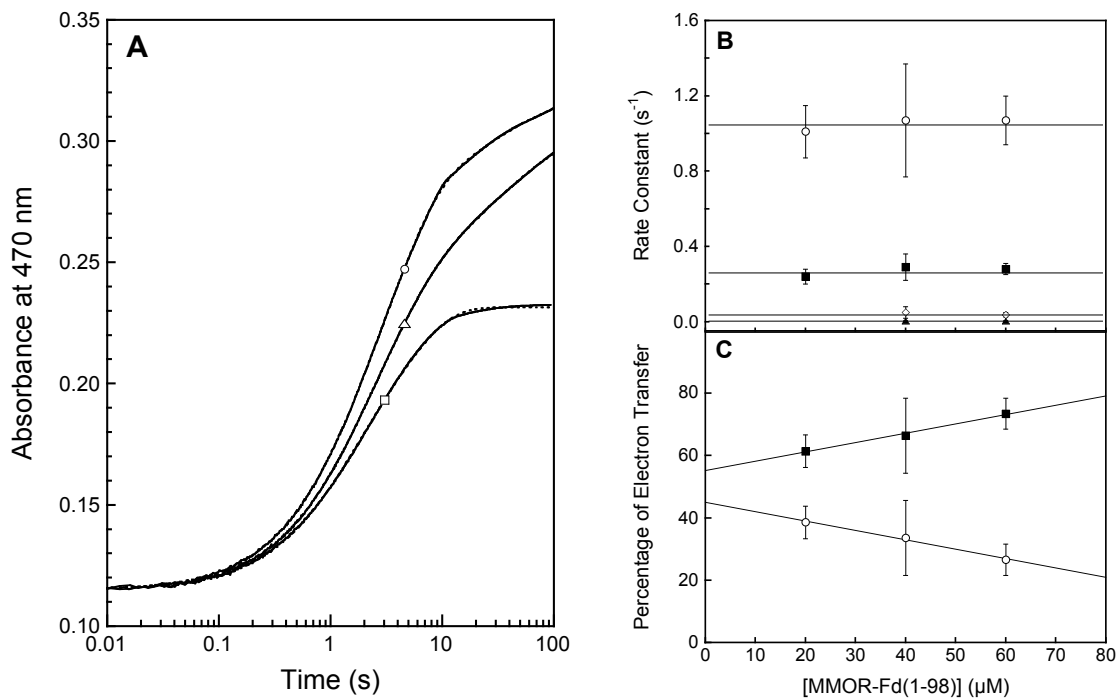


Figure 4.4. Effect of MMOR-Fd concentration on electron transfer from chemically reduced MMOR-Fd(1-98) to oxidized MMOH at 4 °C. (A) Parallel fits through kinetic traces recorded at 470 nm for 20 μM (squares), 40 μM (triangles), and 80 μM (circles) MMOR-Fd(1-98) reacting with 10 μM MMOH. Symbols are for identification purposes only. (B) Variation of rate constants with respect to MMOR-Fd(1-98) concentration: k_1 (circles), k_2 (squares), k_3 (diamonds), and k_4 (triangles). (C) Partitioning of electrons between the rapid (k_1 , circles) and slow (k_2 , squares) reaction phases as a function of MMOR-Fd(1-98) concentration.

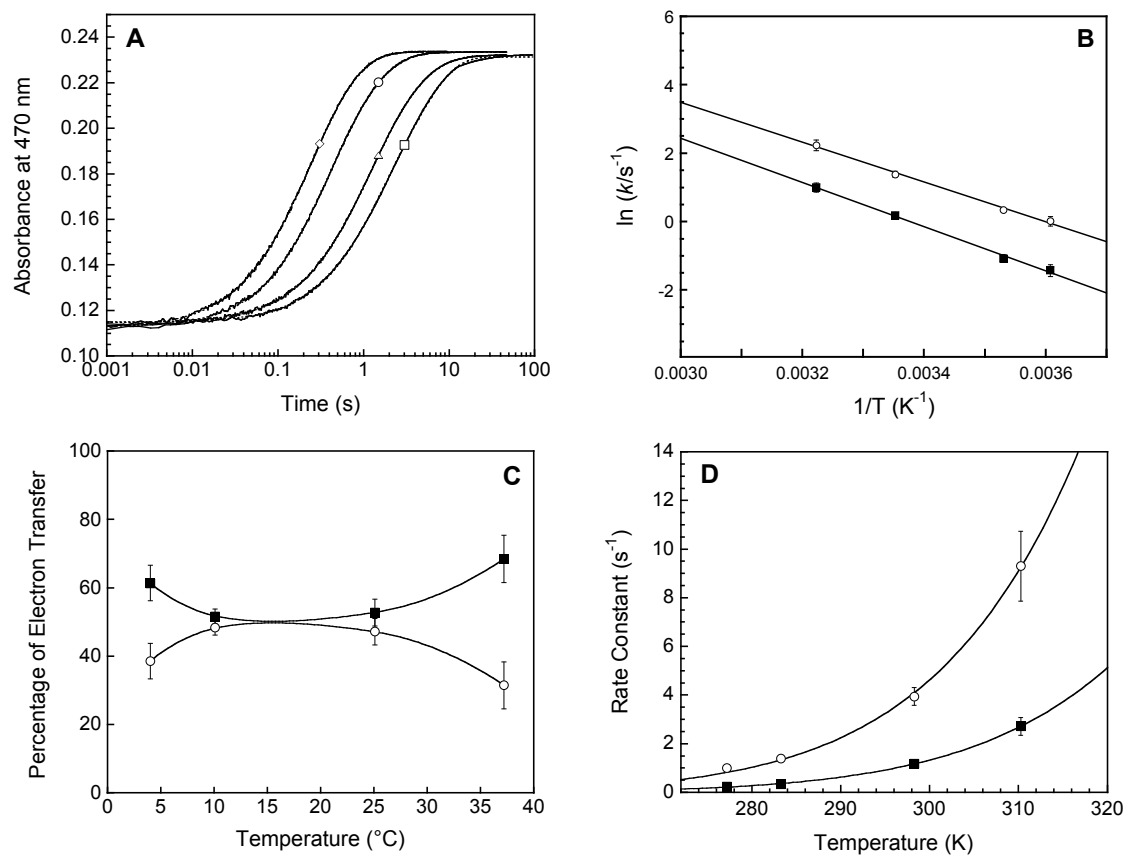


Figure 4.5. Effect of temperature on intermolecular electron transfer from reduced MMOR-Fd(1-98) to oxidized MMOH. (A) Parallel fits through kinetic traces recorded at 470 nm for the reaction of 20 μ M MMOR-Fd(1-98) with 10 μ M MMOH at 4 $^{\circ}C$ (squares), 10 $^{\circ}C$ (triangles), 25 $^{\circ}C$ (circles), and 37 $^{\circ}C$ (diamonds). (B) Arrhenius plot for determination of activation energies: k_1 (circles) and k_2 (squares). (C) Electron partitioning between the rapid (circles) and slow (squares) reaction phases as a function of temperature. (D) Analysis by electron transfer theory (see text) of the temperature dependence of rate constants: k_1 (circles) and k_2 (squares). The solid lines are fits to eqs 2 and 3. Fits to the two equations are superimposable.

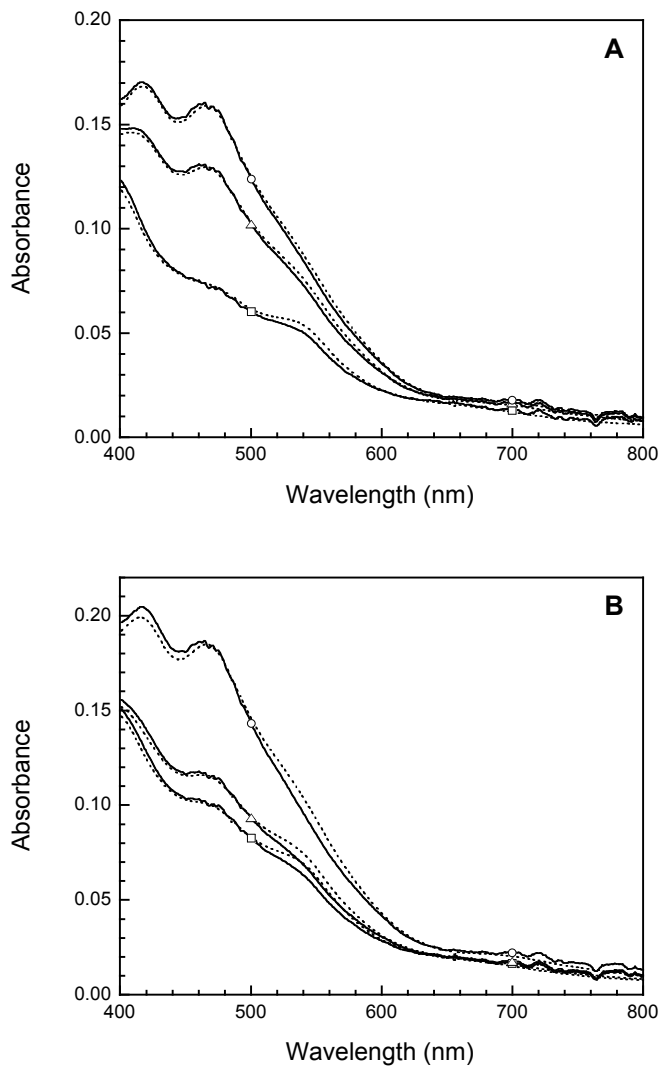


Figure 4.6. Spectra of intermediates resolved by global analysis of diode array kinetic data for the reaction of chemically reduced MMOR-Fd(1-98) with oxidized MMOH in the (A) absence and (B) presence of two equivalents of MMOB: first intermediate (squares), second intermediate (triangles), and third intermediate (circles). Dashed lines represent the best fitting linear combinations of component Fd_{ox} and Fd_{red} spectra.

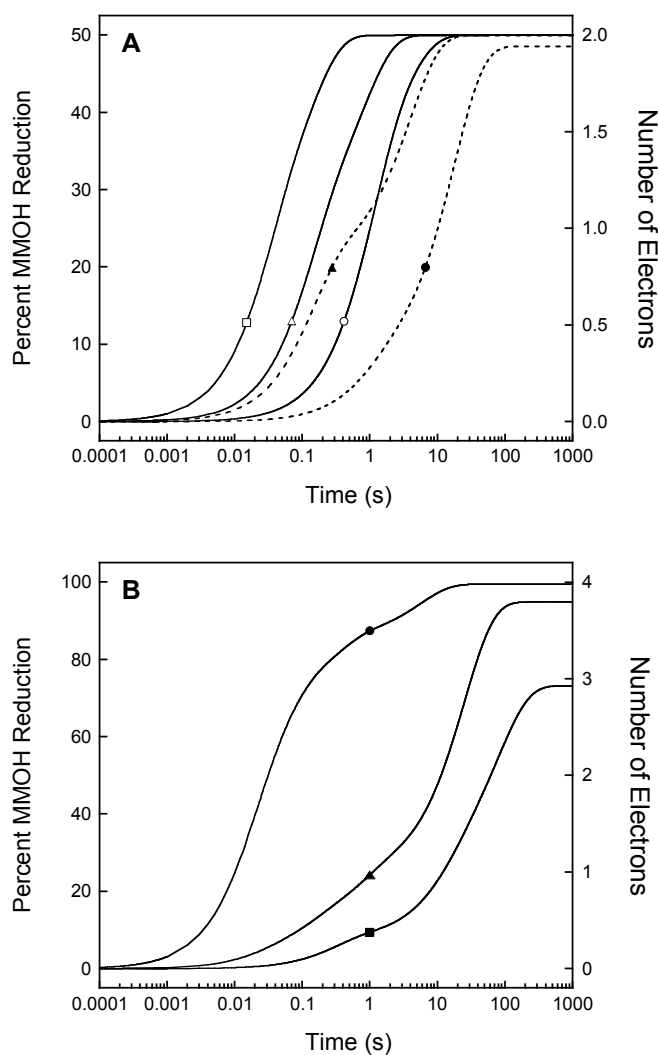


Figure 4.7. Time courses for MMOH reduction by (A) MMOR ferredoxin analogs and (B) MMOR at 4 °C. (A) Electron transfer reactions in the absence (solid lines) and presence (dashed lines) of two equivalents of MMOB for MMOR-Fd(1-120+tail) (squares), MMOR(apoFAD) (triangles), and MMOR-Fd(1-98) (circles). (B) Progression of electron transfer from MMOR_{3e^-} in reactions including MMOH alone (circles) and with two equivalents of MMOB (triangles) or MMOD (squares).

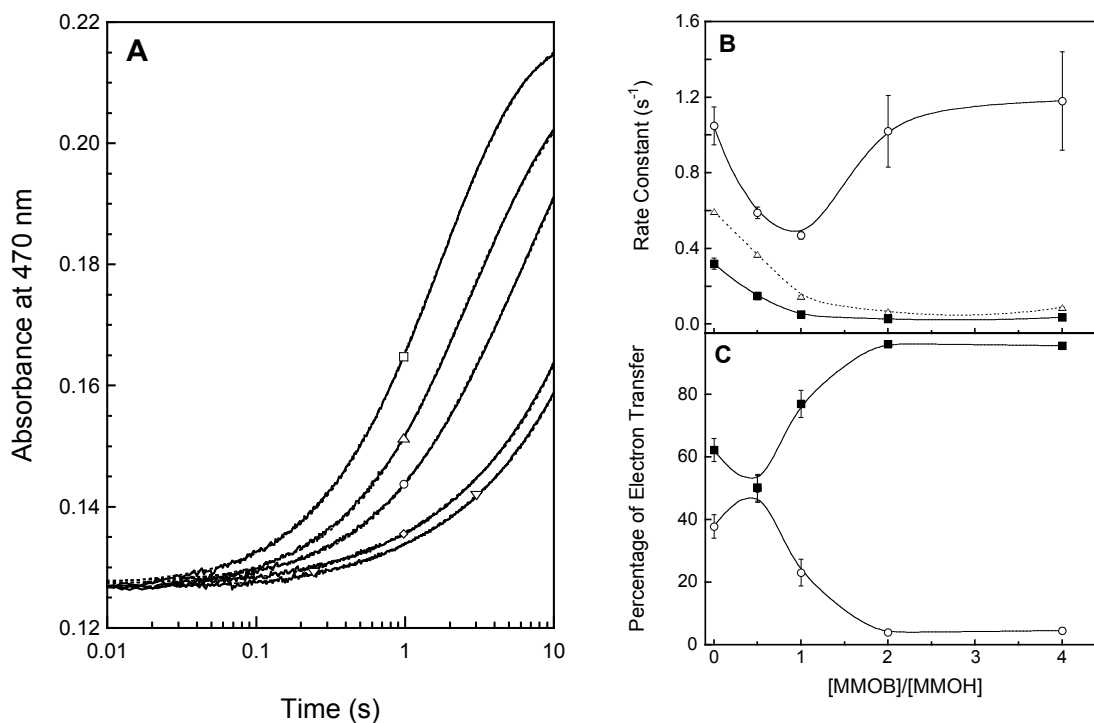


Figure 4.8. Effect of MMOB on electron transfer from reduced MMOR-Fd(1-98) to oxidized MMOH at 4 °C. (A) Parallel fits through kinetic traces recorded at 470 nm for the reaction of 20 μM MMOR-Fd(1-98) with 10 μM MMOH in the presence of no MMOB (squares), 5 μM MMOB (triangles), 10 μM MMOB (circles), 20 μM MMOB (diamonds), and 40 μM MMOB (inverted triangles). (B) Variation of rate constants with MMOB concentration: k_1 (circles), k_2 (squares), and weighted average (triangles). (C) Partitioning of electrons through the rapid (circles) and slow (squares) reaction phases as a function of MMOB concentration.

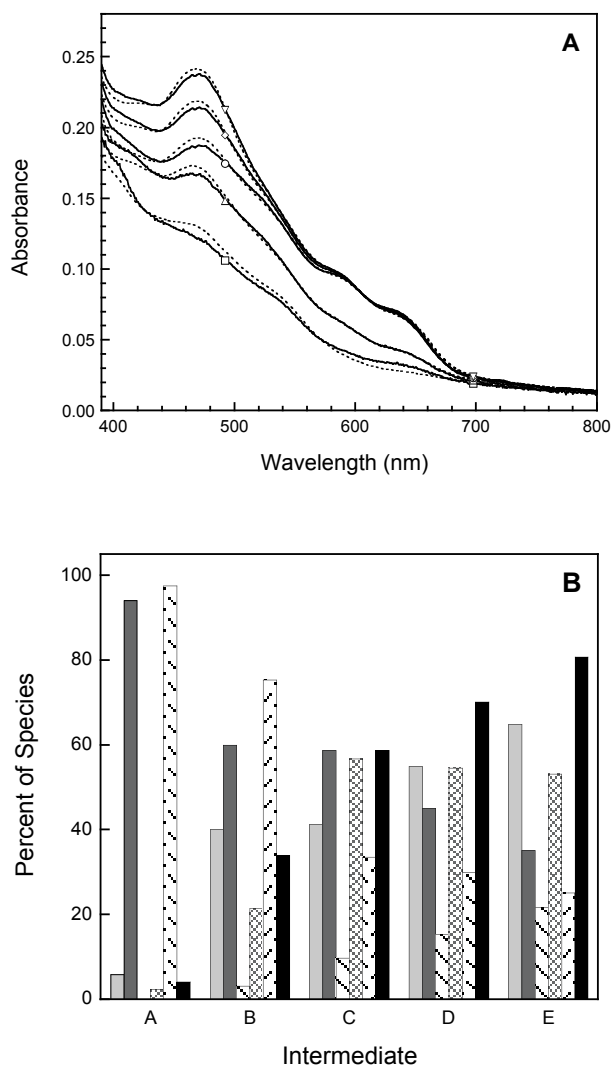


Figure 4.9. (A) Spectra of intermediates resolved by global analysis of diode array kinetic data for the reaction of MMOR_{3e^-} with oxidized MMOH: intermediates A (squares), B (triangles), C (circles), D (diamonds), and E (inverted triangles). Dashed lines are fits with linear combinations of MMOR component spectra (Fd_{ox} , Fd_{red} , FAD_{ox} , FAD_{sq} , and FAD_{hq}). (B) Composition of each intermediate: Fd_{ox} (light gray), Fd_{red} (dark gray), FAD_{ox} (diagonal lines), FAD_{sq} (narrow hatches), FAD_{hq} (wide hatches), and MMOH reduction (black).

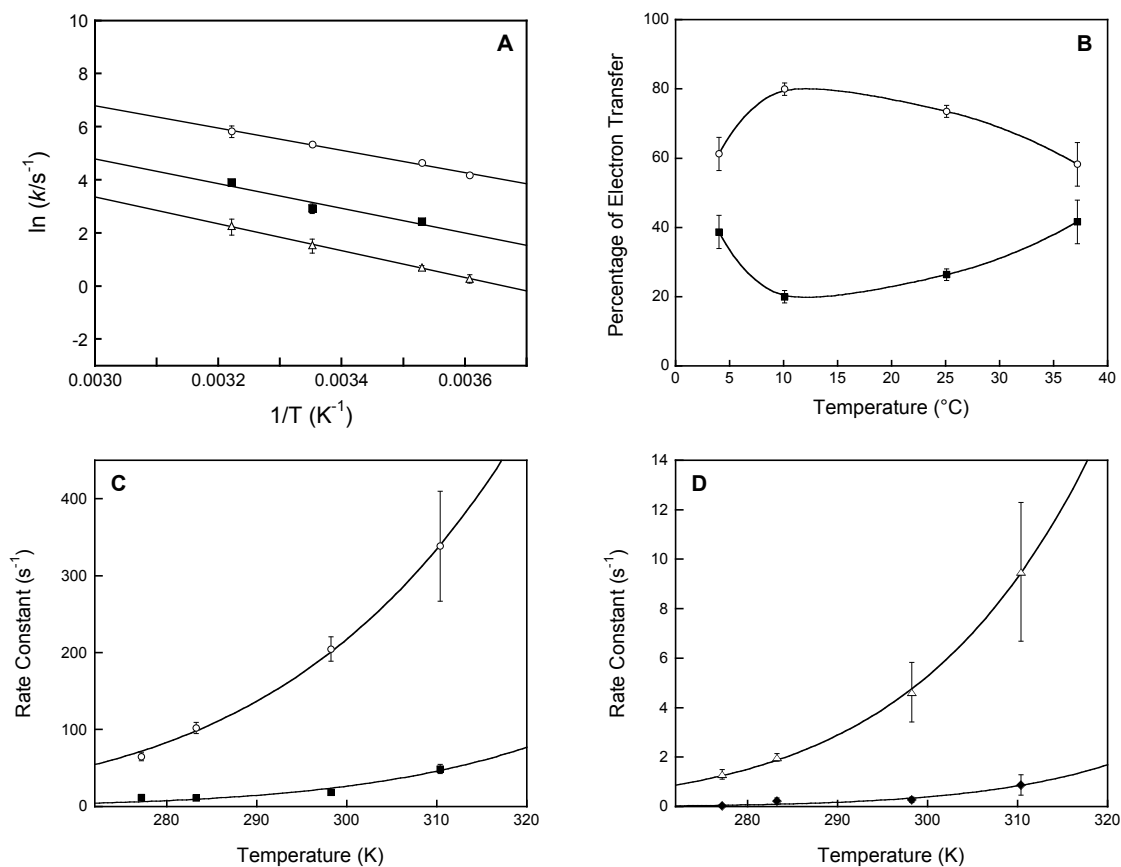


Figure 4.10. Effect of temperature on intermolecular electron transfer from MMOR_{3e-} to oxidized MMOH. (A) Arrhenius plot for determination of activation energies: k_1 (circles), k_2 (squares), and k_3 (triangles). (B) Electron partitioning between the fast (circles) and slow (squares) reaction phases as a function of temperature. (C) and (D) Analysis by electron transfer theory (see text) of the temperature dependence of rate constants: k_1 (C, circles), k_2 (C, squares), k_3 (D, triangles), and k_4 (D, diamonds). The solid lines are fits to eqs 2 and 3. Fits to the two equations are superimposable.

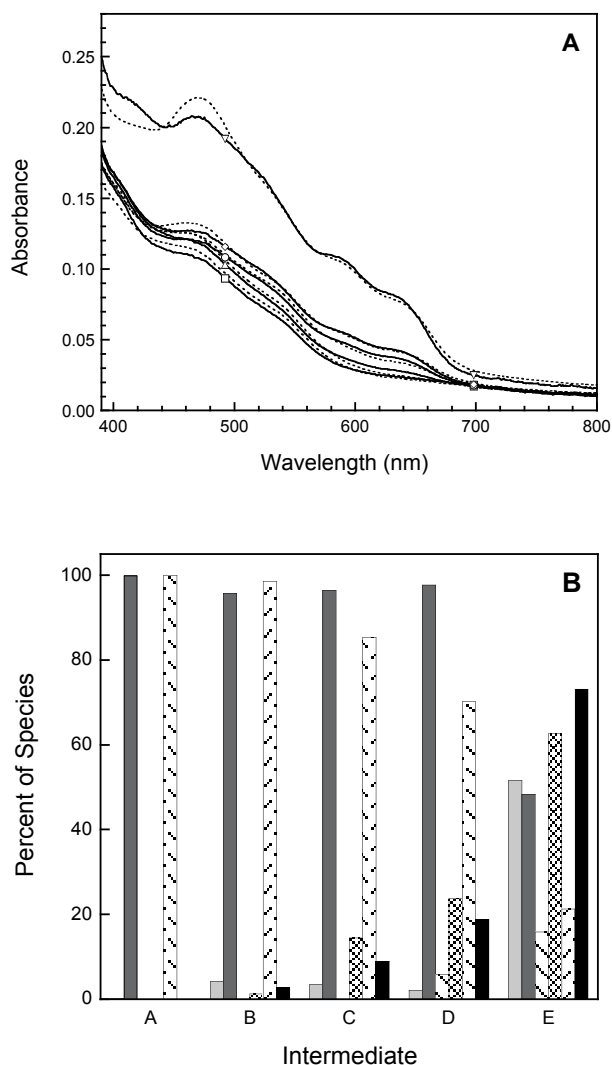


Figure 4.11. (A) Spectra of intermediates resolved by global analysis of diode array kinetic data for the reaction of MMOR_{3e^-} with a pre-equilibrated mixture of oxidized MMOH and two equivalents of MMOB: intermediates A (squares), B (triangles), C (circles), D (diamonds), and E (inverted triangles). Dashed lines are fits with linear combinations of MMOR component spectra (Fd_{ox} , Fd_{red} , FAD_{ox} , FAD_{sq} , and FAD_{hq}). (B) Composition of each intermediate: Fd_{ox} (light gray), Fd_{red} (dark gray), FAD_{ox} (diagonal lines), FAD_{sq} (narrow hatches), FAD_{hq} (wide hatches), and MMOH reduction (black).

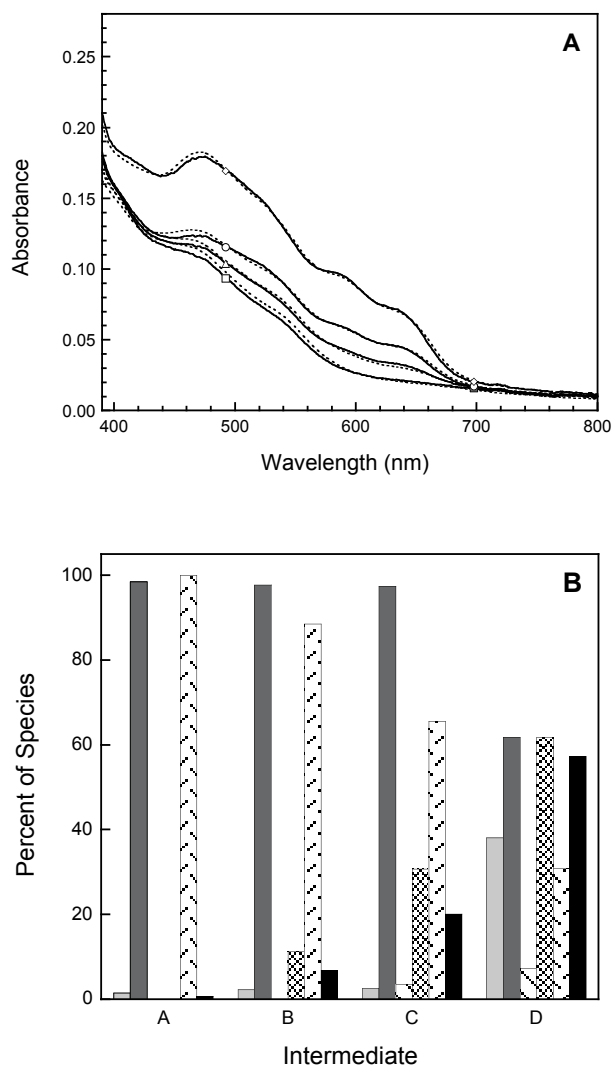


Figure 4.12. (A) Spectra of intermediates resolved by global analysis of diode array kinetic data for the reaction of MMOR_{3e^-} with a pre-equilibrated mixture of oxidized MMOH and two equivalents of MMOD: intermediates A (squares), B (triangles), C (circles), and D (diamonds). Dashed lines are fits with linear combinations of MMOR component spectra (Fd_{ox} , Fd_{red} , FAD_{ox} , FAD_{sq} , and FAD_{hq}). (B) Composition of each intermediate: Fd_{ox} (light gray), Fd_{red} (dark gray), FAD_{ox} (diagonal lines), FAD_{sq} (narrow hatches), FAD_{hq} (wide hatches), and MMOH reduction (black).

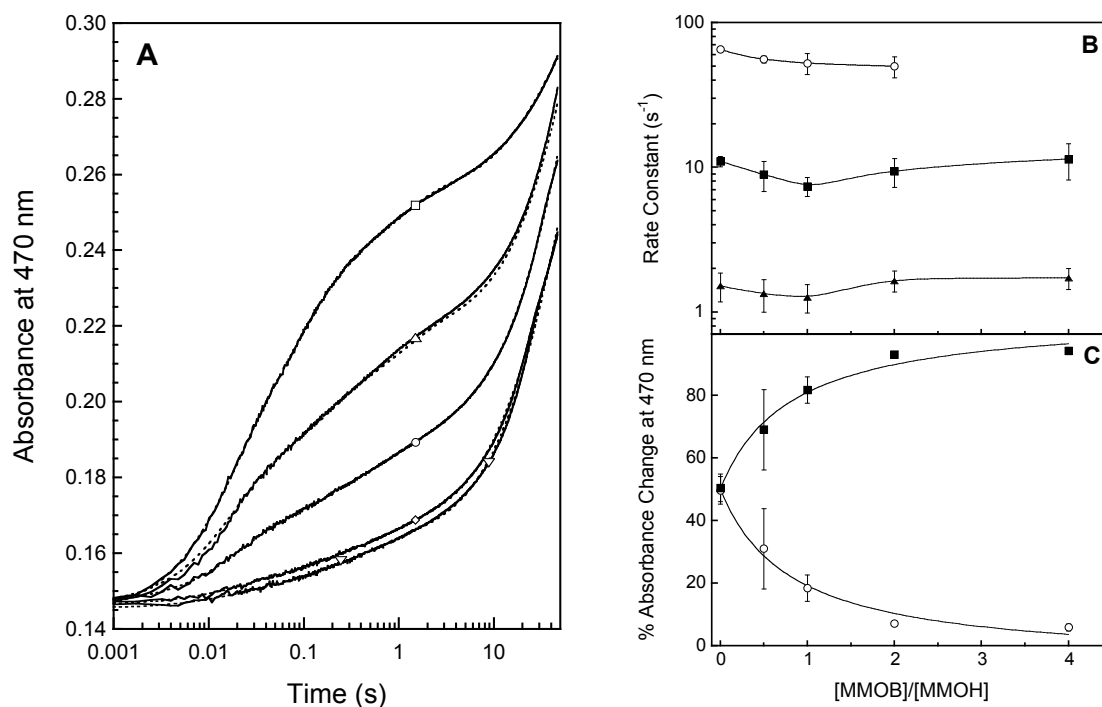


Figure 4.13. Effect of MMOB on electron transfer from MMOR_{3e-} to oxidized MMOH at 4 °C. (A) Parallel fits through kinetic traces recorded at 470 nm for the reaction of 20 μM MMOR with 10 μM MMOH in the presence of no MMOB (squares), 5 μM MMOB (triangles), 10 μM MMOB (circles), 20 μM MMOB (diamonds), and 40 μM MMOB (inverted triangles). (B) Variation of rate constants with MMOB concentration: k_1 (circles), k_2 (squares), and k_3 (triangles). (C) Partitioning of electrons through the rapid (circles) and slow (squares) reaction phases as a function of MMOB concentration.

Chapter 5

Domain Engineering of the Reductase Component of Soluble Methane Monooxygenase from *Methylococcus capsulatus* (Bath)*

INTRODUCTION

The first step in the catabolic pathway of methanotrophs is the conversion of methane to methanol by soluble or membrane-bound methane monooxygenases (MMOs).^{1,2} Although the soluble MMO (sMMO) system is expressed by only a few organisms under low-copper conditions,³ it has been characterized far more extensively than the particulate form (pMMO) due to difficulties purifying and stabilizing the pMMO enzymes.^{4,6} The sMMO proteins from two methanotrophic bacteria, *Methylococcus capsulatus* (Bath)^{7,8} and *Methylosinus trichosporium* OB3b,^{9,10} have been studied in great detail.¹¹⁻¹⁸ Both systems comprise three components: a dimeric ($\square\square$)₂ hydroxylase (MMOH, 251 kDa) with dinuclear, carboxylate-bridged iron centers where dioxygen activation and methane hydroxylation occur; a regulatory protein (MMOB, 15.9 kDa); and a reductase (MMOR, 38.5 kDa) that transfers electrons from NADH to the MMOH diiron sites, thereby priming the hydroxylase for reaction with dioxygen. The N-terminal domain of MMOR, which houses a [2Fe-2S] cluster, shares sequence,¹⁹ spectroscopic,^{16,20-23} and structural²⁴ properties with ferredoxins of plants, cyanobacteria, and archaeobacteria. A flavin adenine dinucleotide (FAD) cofactor located in the C-terminal portion of MMOR accepts two electrons from NADH. These electrons are passed sequentially from the reduced FAD moiety through the MMOR [2Fe-2S] center into the hydroxylase active sites by means of a series of intra- and intermolecular electron transfer reactions.^{16,23,25,26}

MMOR is a member of a class of modular flavoprotein electron transferases, also known as the ferredoxin:NADP⁺ oxidoreductase (FNR) family. These proteins contain a flavin domain that transfers electrons between a nicotinamide dinucleotide and a one-electron carrier domain, which may be linked or dissociable.²⁷⁻²⁹ Because the electron carrier domain can be attached to either the N- or C-terminal end of the core

flavin/NAD(P) unit, this domain appears to be an independent modular element. In support of this designation, the crystal structure of *Burkholderia cepacia* phthalate dioxygenase reductase (PDR), an FNR family member with C-terminal electron carrier connectivity, shows distinct flavin mononucleotide (FMN), NADH binding, and [2Fe-2S] domains (Figure 5.1).²⁹ To examine the modular nature of MMOR and facilitate characterization of this complex protein, the ferredoxin (MMOR-Fd) and FAD/NADH (MMOR-FAD) domains were expressed as separate polypeptides.³⁰ NMR studies reveal that both MMOR-Fd and MMOR-FAD form well-defined structures in solution.^{24,31} In nearly every respect examined, the individual MMOR domains retain biochemical properties essentially identical to those of the corresponding portions of full-length MMOR. Without a covalent tether between the domains, however, the MMOR-Fd and MMOR-FAD proteins are unable to form a complex suitable for rapid interdomain electron transfer, since $k = 1500 \text{ M}^{-1} \text{ s}^{-1}$ at 25 °C, compared to 90 s^{-1} at 4 °C for internal electron transfer between cofactors in MMOR.³⁰

In order to explore further the modularity of the sMMO reductase, MMOR constructs were prepared in which the wild-type arrangement of [2Fe-2S] and FAD/NADH domains is reversed to reproduce the connectivity of PDR. The goal for this project was to determine the extent to which the rapid interdomain electron transfer of wild-type MMOR could be restored by connecting the domain proteins in a non-native fashion observed in a related protein. In this work, four linker sequences, encompassing a variety of chemical and geometric properties, were employed to tether the reversed domains; the spectroscopic, redox, and electron transfer properties of these reversed-domains MMOR constructs were determined. Through such domain engineering, the relative effects of domain orientation, affinity, and proximity to interdomain electron transfer may be delineated.

MATERIALS AND METHODS

MMOR Reversed-Domains Construct Design. To define the Fd and FAD/NADH domain boundaries of *M. capsulatus* (Bath) MMOR and *B. cepacia* PDR, sections of MMOR were aligned with the full-length PDR protein sequence (PDB code 2PIA) by using CLUSTAL W.³² In addition, the approximate MMOR domain sequences (residues 1-114, Fd domain; residues 89-348, FAD/NADH domain) were compared to and aligned with other protein sequences in the non-redundant National Center for Biotechnology Information (NCBI) protein databases with the PSI-BLAST program. The final domain definition technique involved examination of the PDR secondary structural features to ensure that the selected domain linker region was not the terminus of an existing α -helical or β -sheet structure. Once the domain boundaries were set, the PDR and reversed-domains MMOR sequences were aligned. A short seven-amino acid linker sequence between the domains was selected based on lower homology and lack of defined secondary structure in that region.

Four different linker sequences were designed for the reversed-domains MMOR mutants. The first two seven-residue linkers were chosen with the principle of minimal perturbation. One linker was selected as the sequence in the PDR interdomain region and another as the MMOR sequence in that part. A third seven-residue linker was designed to incorporate a factor X_a protease cleavage site, which would allow the domains to be disconnected if desired. Finally, to investigate the importance of domain proximity in the MMOR intramolecular electron transfer reactions, a longer fourteen-residue linker was generated with the program LINKER.³³ The primary amino acid sequences and basic properties of the four MMOR reversed-domains constructs (MMOR-RD) are displayed in Table 5.1.

DNA Primer Synthesis and Purification. All of the primers used for cloning and DNA sequencing were designed manually and synthesized on an Applied Biosystems Model 392 DNA/RNA synthesizer. Each primer was purified by polyacrylamide gel electrophoresis on a 12% denaturing polyacrylamide gel, extracted from the gel slices by using a crush and soak method, then precipitated to remove most of the salt added during extraction. The DNA pellets were suspended in appropriate quantities of deionized distilled water and stored at $-20\text{ }^{\circ}\text{C}$.

Construction of pTrc-Fd1 and pTrc-Fd2 Plasmids. A four-step procedure was devised for constructing the four MMOR-RD expression vectors, as depicted in Scheme 5.1. The *mmo* genes, which code for all five components of the MMO system, are contained on a 5.5-kb section of pCH4.³⁴ Two variations (Fd1 and Fd2) of the Fd portion of the *mmoC* gene, which codes for the MMO reductase protein, were amplified from pCH4 by polymerase chain reaction (PCR) with the primers LKFB10 (Fd1; 5'-CT-**GCGGATCC**CACACTATCACGGCGGTG) or LKFB20 (Fd2; 5'-AGTT**GGATCC**GGCC-**ATGTTAGCGTTATTCGCGAGTTC**CACACTATCACGGC) and FdRH10 (5'-CCTCTC-**CAAAGCTT**TATGCGTCAATGGGTATAG). The resulting 313-bp (Fd1) and 341-bp (Fd2) fragments were flanked by *Bam*HI and *Hind*III sites (bold; underlined regions are base mismatches with template DNA), which were introduced by LKFB10/LKFB20 and FdRH10, respectively. PCR was performed with *Pfu* Turbo DNA polymerase (Stratagene, La Jolla, CA), which has 3' → 5' proofreading capability, with the following thermal cycler conditions: 45 s at 96 °C; 45 s at 96 °C, 45 s at 61 °C, and 30 s at 72 °C for 25 cycles, followed by extension for 10 min at 72 °C. Each *mmoC*-Fd PCR product was isolated with the QIAQuick PCR purification kit (Qiagen, Inc., Valencia, CA) and digested with *Bam*HI (New England Biolabs, Inc., Beverly, MA) by following the provided instructions. After completion of the digest reaction, the restriction

enzyme was inactivated by incubating the samples for 20 min at 80 °C. The DNA was isolated from the reactions (QIAQuick PCR purification kit) and then digested with *Hind*III (New England Biolabs). The high-copy-number plasmid pTrc99A (Amersham Pharmacia, Piscataway, NJ) was digested with *Bam*HI and *Hind*III by using the same two-step procedure. To inactivate *Hind*III, the Fd1, Fd2, and pTrc99A samples were incubated for 20 min at 65 °C. The pTrc99A digest was treated with alkaline phosphatase (AP; Boehringer Mannheim, Indianapolis, IN) to prevent recircularization in the subsequent ligation reaction. After inactivating the AP by adding 20 mM ethylene glycol-bis[β -aminoethyl ether]-*N,N,N',N'*-tetraacetic acid (EGTA) and heating at 65 °C for 10 min, DNA in the *mmoC*-Fd1, *mmoC*-Fd2, and pTrc99A digests was purified once more (QIAQuick PCR purification kit) and ligated with T4 DNA ligase (New England Biolabs) to yield pTrc-Fd1 (pTrc99A + Fd1) and pTrc-Fd2 (pTrc99A + Fd2) (Scheme 5.1). The ligase was heat-inactivated by incubation for 20 min at 65 °C, and the ligation mixtures were transformed into supercompetent *E. coli* XL10-Gold cells (Stratagene), which were selected on Luria-Bertani (LB)-ampicillin (Ap; 100 μ g/mL) agar plates. Positive clones were identified by restriction digests of DNA isolated from plasmid minipreps.³⁵ The sequences of the *mmoC*-Fd inserts were verified by DNA sequencing (MIT Biopolymers Laboratory).

Construction of pTrc-RD1m, pTrc-RD2m, pTrc-RD3m, and pTrc-RD4 Vectors.

To introduce different linker regions into the MMOR-RD constructs, four versions (FAD1, FAD2, FAD3, and FAD4) of the FAD/NADH region of *mmoC* were PCR-amplified from pCH4 with the primers FNFE10 (5'-CGAAGACCGACCTGGAATTCTAAGGAGGTTATAATATGTGCCGCATCAGTTTTGGTGAG) and LKRB10 (FAD1; 5'-GTTAGGATCCGCGCATTCGTGTTGGTTGCGCCGAATTTTTCGAAGAAGACCTGTTTCG), LKRB20 (FAD2; 5'-GTTAGGATCCGCTGTGCGGCGCCGCTGGGCAAGA-

ATTTTTCGAAGAAGACCTGTTTCG), LKRB30 (FAD3; 5'-GTTAGGATCCGACCCTC-
AATGGTTTCATCGCCGAATTTTTCGAAGAAGACCTGTTTCG), or LKRB40 (FAD4;
 5'-GTTAGGATCCACCGCTACCAATGCCGAATTTTTCGAAGAAGACCTGTTTCG).

The 802-bp (FAD1, FAD2, and FAD3) and 795-bp (FAD4) products were flanked by *EcoRI* and *BamHI* sites (bold; underlined regions are base mismatches with template DNA), which were introduced by FNFE10 and LKRB10/LKRB20/LKRB30/LKRB40, respectively. The double-underlined 'A' in LKRB10, LKRB20, and LKRB30, which was required to incorporate the *BamHI* site, added a point mutation in the MMOR sequence that was corrected by site-directed mutagenesis at a later stage in the cloning process. PCR was performed with the thermal cycler conditions: 45 s at 96 °C; 45 s at 96 °C, 45 s at 61 °C, and 1 min at 72 °C for 25 cycles, followed by extension for 10 min at 72 °C. The amplified DNA was purified from the PCR reactions by using the QIAquick PCR purification kit. All four PCR products were digested with the restriction enzymes *EcoRI* (New England Biolabs) and *BamHI* by following the manufacturer's instructions. The enzymes were heat-inactivated by incubating the samples for 20 min at 80 °C, and the DNA was purified with the QIAquick PCR purification kit. The plasmids pTrc-Fd1 and pTrc-Fd2 were digested with the same restriction enzymes, then treated with AP. Following AP inactivation, the DNA was isolated with the QIAquick PCR purification kit. The AP-treated pTrc-Fd1, pTrc-Fd2, and *mmoC*-FAD digests were ligated by using T4 DNA ligase to yield pTrc-RD1m (pTrc-Fd1 + FAD1), pTrc-RD2m (pTrc-Fd1 + FAD2), pTrc-RD3m (pTrc-Fd1 + FAD3), and pTrc-RD4 (pTrc-Fd2 + FAD4) (Scheme 5.1). The ligation products were transformed into supercompetent *E. coli* XL10-Gold cells, and potential positive clones were identified by plating onto LB-Ap (100 µg/mL) agar plates. Colonies with ampicillin resistance were analyzed further by restriction

mapping of DNA isolated from plasmid minipreps and DNA sequencing (MIT Biopolymers Laboratory).

Site-Directed Mutagenesis to Yield pTrc-RD1, pTrc-RD2, and pTrc-RD3 Expression Vectors. Site-directed mutagenesis (GGATCC → GGGTCC) was performed to remove the point mutation required to introduce the *Bam*HI site into the RD1, RD2, and RD3 reversed-domains constructs. Mutagenesis of pTrc-RD1m, pTrc-RD2m, and pTrc-RD3m was accomplished by using the QuikChange kit (Stratagene) and following the manufacturer's instructions. The primers listed in Table 5.2 were designed and purified for use in the *Pfu* DNA polymerase-catalyzed PCR mutagenesis reaction. Subsequent isolation and DNA sequencing (MIT Biopolymers Laboratory) of pTrc-RD1, pTrc-RD2, and pTrc-RD3 (Scheme 5.1) confirmed that the gene sequences contained only the desired mutations.

Construction of pRED-RD1, pRED-RD2, pRED-RD3, and pRED-RD4 Expression Vectors. The final step in the reversed-domains MMOR cloning scheme (Scheme 5.1) involved transferring the RD1, RD2, RD3, and RD4 genes from the pTrc-RD plasmids into pKK223-3 (Amersham Pharmacia), the expression vector used for the recombinant MMOR, MMOR-Fd, and MMOR-FAD expression systems.^{23,30} The plasmids pKK223-3, pTrc-RD1, pTrc-RD2, pTrc-RD3, and pTrc-RD4 were each digested with *Eco*RI and *Hind*III. The *mmoC*-RD digests were separated from pTrc99A by resolution on a 1% agarose-ethidium bromide gel and then extracted from the gel with a QIAEX II kit (Qiagen). The pKK223-3 digest was treated with AP to prevent recircularization in the ligation reaction, the AP was inactivated as described above, and the plasmid digest was isolated with a QIAquick PCR purification kit. T4 DNA ligase was used to ligate each *mmoC*-RD digest into the digested pKK223-3 vector. After the ligation reactions had proceeded for 3.5 h at room temperature, the ligase was

heat-inactivated by incubating the solutions for 20 min at 65 °C. The resulting plasmid solutions were transformed into supercompetent *E. coli* XL10-Gold cells, which were then spread on LB-Ap (100 µg/mL) agar plates to select for pKK223-3-containing cells. Colonies containing pRED-RD constructs were identified by restriction mapping of DNA obtained from plasmid minipreps.

Expression Trials for the Reversed-Domains MMOR Proteins. The pTrc99A, pTrc-RD1, pTrc-RD2, pTrc-RD3, pTrc-RD4, pKK223-3, pRED-RD1, pRED-RD2, pRED-RD3, and pRED-RD4 plasmids (Scheme 5.1) were transformed into *E. coli* JM105 cells for expression trials. The ten clones were grown to saturation in 4-mL LB-Ap (100 µg/mL) cultures. Aliquots (100 µL) of the saturated starter cultures were used to inoculate 50-mL quantities of LB medium supplemented with 100 µg/mL of Ap and 500-µL quantities of 10 mM Fe(NH₄)₂(SO₄)₂·6H₂O in 100 mM sodium citrate (pH 7.0), and the cells were incubated at 37 °C with shaking (200 rpm). When the OD₆₆₀ of the JM105/pTrc99A and JM105/pKK223-3 cultures reached ~0.6, MMOR-RD expression was induced by adding 80 µM FeSO₄ and 1.0 mM isopropyl β-D-thiogalactopyranoside (IPTG). Samples (1.0 mL) were collected from each culture just before induction, 15 min after induction, and then at 60-min intervals for the following 5 h. To separate the soluble and insoluble fractions of the MMOR-RD time-course expression samples, BugBuster protein extraction reagent (Novagen, Inc., Madison, WI) was used according to the manufacturer's instructions. In brief, each cell pellet was thawed and suspended in 100 µL of BugBuster solution to which DNase had been added. The samples were gently agitated at room temperature for ca. 12 min, centrifuged for 20 min at 16,000g to separate the soluble and insoluble cellular components, and decanted into clean tubes. The pellets were washed with 100 µL of 25 mM potassium phosphate (pH 7.0) and then

suspended in 100 μ L of the same buffer. The samples were analyzed by SDS-PAGE on 12% polyacrylamide gels.

Expression and Purification of MMOR-RD Proteins. A JM105/pRED-RD1 clone was grown to saturation in 100 mL of LB-Ap (100 μ g/mL) medium at 37 °C with 200 rpm shaking. To each of six 1-L quantities of LB-Ap (100 μ g/mL) medium were added 10 mL of 10 mM $\text{Fe}(\text{NH}_4)_2(\text{SO}_4)_2 \cdot 6\text{H}_2\text{O}$ in 100 mM sodium citrate (pH 7.0) and 10 mL of the saturated JM105/pRED-RD1 starter culture. When the OD_{660} reached ca. 0.6, the cultures were supplemented with 80 μ M FeSO_4 , added as 2 mL of 40 mM $\text{FeSO}_4 \cdot 7\text{H}_2\text{O}$ in 12.5 mM H_2SO_4 per L of cell culture, and induction was started by adding IPTG to a final concentration of 1.0 mM. After 4 h, the cells were collected by centrifugation, drained briefly, and then suspended in 100 mL of cold cracking buffer [25 mM 3-(*N*-morpholino)propanesulfonic acid (MOPS; pH 7.0), 1 mM 1,4-dithiothreitol (DTT), 5 mM MgCl_2 , and 200 μ M $\text{Fe}(\text{NH}_4)_2(\text{SO}_4)_2 \cdot 6\text{H}_2\text{O}$] containing DNase (1.5 U/mL) and 1 mM Pefabloc SC (Boehringer Mannheim). The cells were sonicated on ice with three 2-min pulses at 40% output (Branson Sonifier Model 450 equipped with a 3/4-inch horn) and then centrifuged for 40 min at 98,000g to separate the soluble and insoluble materials. The soluble cell extract was filtered through 0.2 μ m membranes before loading onto a DEAE Sepharose CL-6B (Amersham Pharmacia) column (2.6 \times 15 cm) equilibrated in buffer A [25 mM MOPS (pH 7.0), 1 mM DTT, and 50 mM NaCl]. After a 120-mL wash with buffer A, proteins were eluted with a 740-mL linear gradient from buffer A to buffer B [25 mM 3-(*N*-morpholino)propanesulfonic acid (MOPS; pH 7.0), 1 mM DTT, and 500 mM NaCl]. Fractions containing the RD1 protein were identified by SDS-PAGE and UV-visible spectroscopy, pooled, and concentrated by ultrafiltration. This crude RD1 protein solution was diluted fivefold with 25 mM MOPS (pH 7.0), 2 mM DTT and applied to a 5'-AMP Sepharose (Sigma, St.

Louis, MO) column (2.6 × 18 cm) equilibrated with buffer A. After washing the column with buffer A to remove protein contaminants, pure MMOR-RD1 was eluted with buffer B containing 0.8 mM NADH. Fractions containing the MMOR-RD1 protein (PDR linker), as identified by color and SDS-PAGE, were pooled and exchanged into 25 mM MOPS (pH 7.0), 2 mM DTT with a Biogel P6 desalting column (Bio-Rad, Hercules, CA). The MMOR-RD2 (MMOR linker), MMOR-RD3 (factor X_a site), and MMOR-RD4 (long linker) proteins were expressed from JM105/pRED-RD2, JM105/pRED-RD3, and JM105/pTrc-RD4, respectively, and purified by following the same protocol.

Purification of MMOH, MMOB, and MMOR. MMOH was isolated from *M. capsulatus* (Bath) by using a slightly modified published protocol.¹⁶ Pure hydroxylase contained 3.9-4.0 mol Fe per mol protein, as determined by ferrozine iron assays,^{36,37} and exhibited a specific activity of 250-300 nmol min⁻¹ mg⁻¹ of MMOH for the conversion of propylene to propylene oxide at 45 °C. MMOB was expressed from a recombinant *E. coli* system³⁸ and purified as described in Chapter 4. Recombinant MMOR was expressed and purified as published,²³ except that the iron additions were performed as described above for the MMOR-RD expression systems.

Basic Characterization of MMOR-RD Constructs. To assess the purity of the reversed-domains proteins, SDS-PAGE and native PAGE gels were run for the four MMOR-RD constructs with wild-type MMOR (MMOR-wt) included for comparison. The MMOR-RD proteins in 25 mM MOPS (pH 7.0), 0.3 mM DTT were submitted to the MIT Biopolymers Laboratory for analysis by electrospray ionization mass spectrometry (ESI-MS). To remove cofactors which separated from the proteins upon treatment with formic acid, ammonium acetate, and acetonitrile, HPLC purification was necessary. The protein component was analyzed with a Sciex model API 365 triple-stage mass

spectrometer. Iron assays were carried out to determine whether the MMOR-wt extinction coefficient ($\epsilon_{458} = 20,800 \text{ M}^{-1} \text{ cm}^{-1}$) was altered in the MMOR-RD proteins.

Optical Spectra of Oxidized and Reduced MMOR-RD Proteins. All UV-visible spectra were obtained with a Hewlett Packard 8453 diode array spectrophotometer. To examine the MMOR-RD optical spectra in various oxidation states, anaerobic reductive titrations were performed. A 1-mL aliquot of 40 μM MMOR (RD1, RD2, RD3, or RD4) in 25 mM potassium phosphate (pH 7.0) was transferred to a sealed quartz cuvette and made anaerobic by 12 cycles of vacuum gas exchange with O_2 -free N_2 . Aliquots of 2 mM sodium dithionite were added with a gastight Hamilton titrating syringe. After each addition, optical spectra (300-900 nm) were collected until no further changes were observed (generally less than 5 min), and the final spectrum was saved for analysis. This process was repeated until the protein was reduced completely. The temperature was maintained at 25 $^\circ\text{C}$ with a circulating water bath.

Previous studies of the individual MMOR-FAD domain revealed that its optical spectrum is quite sensitive to buffer composition, whereas the optical properties of MMOR-Fd remain unchanged by varying pH or ionic strength.³⁰ Therefore, it was assumed that the [2Fe-2S] cofactors in the MMOR-RD constructs have optical spectra identical to that of MMOR-Fd (Figure 5.2). In order to determine component spectra for the fully oxidized MMOR-RD flavin domains (FAD_{ox}), a scaled oxidized MMOR-Fd (Fd_{ox}) spectrum was subtracted from the initial titration spectrum such that the absorbance above 550 nm was zero in each calculated spectrum. In the same manner, fully reduced component spectra (FAD_{hq}) were obtained by subtracting appropriately scaled reduced MMOR-Fd (Fd_{red}) spectra from the fully reduced MMOR-RD spectra.

Relative Redox Potential Determinations. The differences between the three reductase equilibrium midpoint potentials were determined for each MMOR-RD

construct by analyzing reductive titration data. In addition to the FAD_{ox} and FAD_{hq} component spectra calculated for the MMOR-RD constructs (vide supra), the Fd_{ox} , Fd_{red} and FAD_{sq} component spectra determined previously for the separate MMOR domains (Figure 5.2)³⁰ were employed. For each redox couple (Fd_{ox}/Fd_{red} , FAD_{ox}/FAD_{sq} and FAD_{sq}/FAD_{hq}), a difference spectrum, $\Delta A(\lambda)$, was generated by subtracting the extinction coefficients of the oxidized species from those of the reduced species.

First, dilution corrections were applied to each spectrum in a titration data set. A difference spectrum for each titration point was calculated by subtracting the initial oxidized spectrum from each spectrum in the data set. These difference spectra ($350 \leq \lambda \leq 800$ nm) were then fit with linear combinations of component difference spectra (KaleidaGraph, version 3.51; Synergy Software, Reading, PA), as shown in eq 1. The

$$\Delta A(\lambda) = \sum \epsilon_i(\lambda) \Delta c_i \quad (1)$$

concentration differences, Δc_i , returned by fitting with eq 1 were readily converted to species concentrations by comparison to total cofactor concentrations. Relative MMOR-RD redox potentials ($\Delta E^{\circ'}$) were calculated with modified Nernst equations. Average $\Delta E^{\circ'}$ values were computed by including only those data for which all four relevant species were present at greater than 10% of the total cofactor concentrations.

Redox Potential Determinations for MMOR-RD Constructs. Because many of the MMOR-RD $\Delta E^{\circ'}$ values were significantly altered from those of MMOR-wt, absolute values for the redox potentials were determined. Anaerobic reductive titrations of the MMOR proteins were repeated exactly as described except for the inclusion of one or more redox-active indicator dyes with known midpoint potentials to permit calculation of the solution potential throughout the titrations. Dyes used for MMOR-RD potential determination included anthraquinone-2-sulfonate (AQ2S; $E^{\circ'}$ =

-226 mV), phenosafranine ($E^{\circ} = -252$ mV), safranine O ($E^{\circ} = -289$ mV; RD3 only), and anthraquinone-2,6-disulfonate (AQ2,6S; $E^{\circ} = -184$ mV; RD2 only) in combination with phenosafranine (15-20% relative to AQ2,6S). Dye concentrations were ca. 40 μ M for AQ2S and AQ2,6S and ca. 10 μ M for phenosafranine and safranine O. The MMOR-RD concentration was 30 μ M in all titrations including redox dyes.

The titration data were converted to difference spectra as described and fit with linear combinations of component difference spectra for the four redox couples (dye_{ox}/dye_{red}, Fd_{ox}/Fd_{red}, FAD_{ox}/FAD_{sq} and FAD_{sq}/FAD_{hq}). Modified Nernst equations were used to calculate the solution potential and MMOR-RD midpoint potentials for each titration point. Only those data for which the solution potential was within 40 mV of both the indicator potential and approximate MMOR-RD potential were included in average E° calculations.

Steady-State Dye Reduction Activity Assays. The ability of the MMOR-RD constructs to transfer electrons from NADH to redox-active dyes was investigated with steady-state assays. Reductase (83 nM), dichlorophenolindophenol (DCPIP, Sigma; 47 μ M, $E^{\circ} = +217$ mV), and 25 mM MOPS (pH 7.0) were combined in a masked cuvette. NADH (160 μ M) was introduced to initiate the reaction, and DCPIP reduction was monitored at 600 nm ($\epsilon_{600} = 22,000$ M⁻¹ cm⁻¹) for 30 s with a 1-s integration time. The assays were repeated with K₃Fe(CN)₆ (92 μ M, $E^{\circ} = +360$ mV) in place of DCPIP. Reduction of [Fe(CN)₆]³⁻ was observed at 420 nm ($\epsilon_{420} = 1020$ M⁻¹ cm⁻¹) for 60 s. Duplicate samples were analyzed for each MMOR-RD construct as well as wild-type MMOR. The temperature was held constant at 15 °C with a circulating water bath for all assays. The absorbance vs time data were fit with lines in the spectrophotometer software to obtain rate constants for the dye reduction reactions.

Steady-State sMMO Activity Assays. To determine the competence of the MMOR-RD constructs for binding and transferring electrons to the hydroxylase, steady-state sMMO assays were performed. In a quartz cuvette, 1 μM MMOH, 1 μM MMOB, 0.8 mM propylene, and 25 mM MOPS (pH 7.0) were mixed. The reductase concentration was varied from 0 to 3.2 μM ; nine different concentrations were assayed. NADH (160 μM) was added to initiate the propylene epoxidation reaction, and NADH consumption was monitored at 340 nm ($\epsilon_{340} = 6220 \text{ M}^{-1} \text{ cm}^{-1}$) for 60 s. The temperature was maintained at 25 °C with a circulating water bath. Kinetic traces were fit with lines in the spectrophotometer software. Plots of activity vs [MMOR] were constructed and fit with a hyperbola plus a line (MMOR-wt) or a line (MMOR-RD constructs) in KaleidaGraph.

In addition, sMMO activity assays were carried out with nitrobenzene as the substrate. MMOH (1 μM), MMOB (2 μM), reductase (0.4 μM or 2 μM), and nitrobenzene (1 mM), were combined in 25 mM MOPS (pH 7.7). After adding NADH (150 μM), *p*-nitrophenol formation was monitored at 404 nm ($\epsilon_{404} = 15,000 \text{ M}^{-1} \text{ cm}^{-1}$) for 180 s. The temperature was held constant at 25 °C. Rates were determined by fitting the kinetic traces with lines in the spectrophotometer software. Upon complete oxidation of NADH, a visible spectrum was collected for each reaction.

MMOR-RD Reactions with NADH. Interdomain electron transfer rates for the MMOR-RD constructs were determined in stopped-flow experiments. A Hi-Tech Scientific SF-61 DX2 double-mixing stopped-flow spectrophotometer configured in either single-wavelength photomultiplier or multiwavelength diode array mode was used for all data collection. The stopped-flow apparatus was made anaerobic by flushing the flow cell and syringes first with a solution of ca. 5 mM sodium dithionite and then with anaerobic buffer to remove the dithionite. Oxidized MMOR (wild-type,

RD1, RD2, RD3, or RD4) in 25 mM MOPS (pH 7.0) was made anaerobic by 10-12 cycles of vacuum gas exchange with O₂-free N₂. Anaerobic NADH solutions were prepared by bubbling with N₂ for at least 15 min. After mixing, concentrations of MMOR and NADH were 20 μM and 200 μM, respectively. The reaction of reductase with NADH was monitored at 458, 625, and 725 nm in single-wavelength mode. Data points (512) were collected in 1- to 500-s shots with a logarithmic time base. The experiment was repeated with the stopped-flow configured for diode array mode. For each 1.5- to 300-s shot, 160 spectra (350-800 nm) were recorded on a log time scale. The temperature was maintained at 4 °C with a constant-temperature circulating water bath for all experiments. Single-wavelength kinetic traces were fit with a sum of three to five exponential decays with the program KinetAsyst, version 3.04 (Hi-Tech Limited, Salisbury, England). Diode array data analysis was performed with Specfit, version 3.0.16 (Spectrum Software Associates, Chapel Hill, NC).

RESULTS

Expression of MMOR-RD Constructs. Eight plasmids (pTrc-RD n and pRED-RD n , where $n = 1-4$) were prepared for expressing the engineered reversed-domains MMOR constructs in *E. coli* hosts. In each of the initial expression tests, there was a time-dependent buildup of protein of the appropriate molecular weight in the soluble cell extract. The recombinant MMOR-RD n proteins represented the major soluble protein in all of the systems. Only in JM105/pRED-RD4 cells did a significant amount of recombinant protein accumulate in the insoluble fraction. Therefore, the JM105/pTrc-RD4 expression system, for which inclusion bodies were not observed, was used to express the MMOR-RD4 (long linker) construct.

Initial Characterization of MMOR-RD Constructs. All four MMOR-RD proteins were expressed and purified in good yield (Table 5.3). On SDS-PAGE and native PAGE gels, the reversed-domains reductases migrated like wild-type MMOR. The molecular weights of the apoproteins determined by ESI-MS matched closely the expected values. Each MMOR-RD construct contained nearly stoichiometric iron (Table 5.3), demonstrating that the MMOR-wt extinction coefficient ($\epsilon_{458} = 20,800 \text{ M}^{-1} \text{ cm}^{-1}$) was relatively unperturbed by domain swapping. Only MMOR-RD2, with 1.86 mol Fe per mol protein, was slightly iron depleted. Upon storage of samples at 4 °C, the [2Fe-2S] clusters in the MMOR-RD proteins were significantly less stable than the same cofactor in MMOR-wt, as revealed by accelerated loss of the pinkish-brown ferredoxin color in the mutants.

MMOR-RD Optical Spectra. Optical spectra recorded for the oxidized MMOR-RD proteins could be fit reasonably well with a linear combination of the oxidized MMOR-Fd (Fd_{ox}) and MMOR-FAD (FAD_{ox}) component spectra (Figure 5.2).³⁰ An extremely good fit to the MMOR-RD2 spectrum was obtained (Figure 5.3), suggesting that the RD2 [2Fe-2S] and flavin cofactors are in environments essentially identical to those of wild-type MMOR. Small but significant deviations between the combined component spectra and the RD1, RD3, and RD4 visible spectra were noted. By subtracting the [2Fe-2S] contributions from the fully oxidized and fully reduced MMOR-RD optical spectra, FAD_{ox} and FAD_{hq} component spectra were generated (Figure 5.4). In both cases, the RD2 spectra were identical to those of wild-type MMOR, whereas the RD1 and, to a greater extent, RD3 and RD4 spectra displayed differences, indicating slight perturbation of the flavin site with respect to that of MMOR-wt.

Redox Potentials of MMOR-RD Constructs. Relative redox potentials of each reversed-domains reductase were determined with reductive titrations (Table 5.4). Many of the ΔE° values were significantly altered compared to those measured for MMOR²³ or the individual MMOR domains.³⁰ In particular, the $\text{FAD}_{\text{ox/sq}} - [\text{2Fe-2S}]_{\text{ox/red}}$ and $\text{FAD}_{\text{ox/sq}} - \text{FAD}_{\text{sq/hq}}$ difference potentials of RD1, RD3, and RD4 were considerably lower (ca. 30 mV), suggesting decreased $\text{FAD}_{\text{ox/sq}}$ potentials in these mutants. A key limitation of this method is the difficulty of accurately measuring ΔE° values for widely separated potentials, since there are few solution potentials at which significant amounts of all four relevant species are present.

Therefore, a series of reductive titrations including indicator dyes was performed to establish absolute values for the MMOR-RD redox potentials. Figure 5.5 shows selected difference spectra obtained from a titration of MMOR-RD2 with the indicator AQ2S. Calculated midpoint potentials for the three redox couples of each protein are displayed in Table 5.5. There is generally good agreement between the relative and absolute redox potential measurements, with a mean deviation of 6.8 mV. The $\text{FAD}_{\text{ox/sq}}$ potentials of RD1, RD3, and RD4 are 32, 44, and 33 mV, respectively, lower than that of MMOR-wt.²³ In addition, a 27-mV decrease in the $\text{FAD}_{\text{sq/hq}}$ potential was measured for the RD3 construct. All four MMOR-RD proteins have moderately lower $[\text{2Fe-2S}]_{\text{ox/red}}$ potentials (9-18 mV) compared to wild-type MMOR.

Steady-State Diaphorase Activity. The reversed-domains reductases were able to transfer electrons from NADH to redox-active dyes at rates similar to those measured for MMOR-wt (Table 5.6). With DCPIP as the electron acceptor, MMOR-RD2 was 26% less active and MMOR-RD4 was 20% more active than the wild-type, RD1, and RD3 reductases. Assays with ferricyanide revealed enhanced activity

for the RD4 (86%) and RD2 (15%) constructs and substantially decreased activity for RD3 (26% of wild-type).

Steady-State sMMO Activity. To investigate electron transfer to MMOH, assays were performed for the steady-state sMMO reaction with propylene at 25 °C at various reductase concentrations. As shown in Figure 5.6, none of the four MMOR-RD proteins behaved like wild-type MMOR in this experiment. For MMOR-wt, the NADH consumption vs [MMOR] plot could be fit with a hyperbolic function representing NADH oxidation coupled to propylene oxide formation (sMMO activity) plus a line representing dioxygen reduction to hydrogen peroxide by excess reductase (oxidase activity). All four MMOR-RD NADH consumption curves could be fit extremely well without the hyperbolic function, suggesting that electron transfer to the hydroxylase was negligible. The oxidase activities of the RD1, RD3, and RD4 reductases were 4-8 times higher than that measured for MMOR-wt (Table 5.6). The RD2 construct, however, reduced dioxygen to peroxide at only half the wild-type rate. When nitrobenzene was used as a substrate, *p*-nitrophenol formation was not observed for any of the reactions including MMOR-RD constructs, confirming that the reversed-domains reductases are not competent for electron transfer to the hydroxylase.

Kinetics of MMOR-RD Reduction with NADH. The reaction of the MMOR-RD constructs with NADH was studied by stopped-flow UV-visible spectroscopy. Figures 5.7A and 5.7B show typical data sets collected for the reduction of MMOR-wt and MMOR-RD4, respectively, with NADH at pH 7.0 and 4 °C. The kinetic steps for this reaction, which were determined previously for wild-type MMOR^{16,23} and MMOR-FAD,³⁰ are depicted in Scheme 5.2. Spectra corresponding to four or five intermediates were resolved with Specfit software by using a sequential four- (RD4) or five-component (wt, RD1, RD2, and RD3) model (Figures 5.7C and

5.7D). When NADH binds to MMOR, species CT1, which is characterized by a charge transfer interaction between the NADH nicotinamide ring and the FAD isoalloxazine moiety ($\lambda_{\text{max}} \approx 575 \text{ nm}$), is formed. Hydride transfer from NADH to the oxidized flavin (FAD_{ox}) yields intermediate CT2, which exhibits a lower-energy charge transfer band ($\lambda_{\text{max}} \approx 740 \text{ nm}$) between the reduced FAD (FAD_{hq}) and NAD^+ cofactors. Upon NAD^+ release, species CT2 decays to form intermediate HQ, which has FAD_{hq} and $[\text{2Fe-2S}]_{\text{ox}}$ cofactors. Interdomain electron transfer produces the final species, SQ, with a spectrum characteristic of FAD_{sq} and $[\text{2Fe-2S}]_{\text{red}}$. In MMOR-wt, ca. 65% of the total electron transfer from FAD_{hq} to the oxidized $[\text{2Fe-2S}]$ cluster occurs simultaneously with NAD^+ release.

Single-wavelength stopped-flow data were collected at 458, 625, and 725 nm for each of the MMOR-RD proteins, as well as MMOR-wt (Figure 5.8). The kinetic traces were fit with sums of three to five exponential decays. CT1 formation is observed as an increase in A_{625} ; CT2 formation produces an increase in A_{725} . Subsequent decreases in both A_{625} and A_{725} correspond to CT2 decay/HQ formation. Intramolecular electron transfer to form SQ yields an increase in A_{625} and a decrease in A_{725} . All four transitions are marked by decreases in A_{458} . A fifth step describing a slow process, such as reaction with excess NADH to form three-electron reduced MMOR, was required for data fitting at long time points. The rate constants determined for the five reductases are summarized in Table 5.7.

DISCUSSION

MMOR-RD Constructs. All four MMOR-RD constructs were prepared in good yield and with nearly full cofactor occupancy. The optical spectra of the oxidized RD1, RD3, and RD4 reductases show changes in the flavin component with respect to the

MMOR-wt spectrum (Figure 5.4). The altered MMOR-RD FAD_{ox} spectra, which exhibit increased extinction coefficients at 394 nm, resemble free flavin mononucleotide more closely than does the wild-type FAD_{ox} spectrum. Therefore, this optical change may correspond to an increase in solvent accessibility to the flavin cofactor in the RD1, RD3, and RD4 constructs. In fact, the largest optical changes are observed for RD3 (long linker) and RD4 (negatively charged linker); the RD1 (uncharged polar linker) spectrum is moderately perturbed. Only RD2, with a largely hydrophobic linker, displays an unchanged optical spectrum. Thus, in the reversed-domains reductases, the linker sequence appears to influence the flavin environment either by direct contact or by structural perturbations that decrease hydrophobicity near the cofactor.

MMOR-RD Redox Potentials. Measurements of both relative and absolute redox potentials for the four MMOR-RD proteins revealed substantial decreases in many of the flavin potentials compared to those of MMOR-wt²³ and MMOR-FAD³⁰ (Tables 5.4 and 5.5). The $\text{FAD}_{\text{ox/sq}}$ redox potential in the RD1, RD3, and RD4 constructs is lowered by 30-45 mV, a result that correlates well with the optical changes observed for these proteins. Like the 350-450 nm region of the FAD_{ox} visible spectrum, the $\text{FAD}_{\text{ox/sq}}$ potential seems to be modulated by the hydrophobicity of the flavin environment. The first residue of the linker sequence is probably the key determinant in these shifted flavin properties. Analysis of a preliminary MMOR-FAD NMR structure indicates that the side chain of Leu246 (residue 343 in full-length MMOR) packs against the FAD cofactor; residues Pro247 and Ser248 may also contact the flavin.³¹ In MMOR-RD2 (MMOR linker), the Leu, Pro, and Ser residues are preserved, and the optical and redox features of MMOR-wt are retained. The first linker residue in RD1, RD3, and RD4 is glycine, which cannot make hydrophobic contacts with the isoalloxazine group. Moreover, the conformational flexibility afforded by this amino

acid probably increases solvent accessibility to the flavin ring. The possibility that the remainder of the RD2 linker/MMOR-FAD sequence (Pro247, Ser248, Gly249, Ala250, and Ala251) affects the flavin cofactor cannot be ruled out, however.

In addition, the $FAD_{sq/hq}$ potential of MMOR-RD3 is decreased by 26 mV relative to MMOR-wt. This effect is most likely due to destabilization of the anionic flavin hydroquinone species by the presence of three carboxylate groups on the RD3 linker. All four MMOR-RD constructs exhibit moderately lower (9-18 mV) $[2Fe-2S]_{ox/red}$ potentials than wild-type MMOR. Although these differences are small and largely within experimental error of each other, they may reflect a slight perturbation in the $[2Fe-2S]$ environment. The significantly decreased stability of the iron-sulfur clusters in the MMOR-RD proteins lends support for this possibility. Because the redox and stability effects on the $[2Fe-2S]$ cofactor are quite similar in all of the reversed-domains reductases, a minor change in structure or orientation of the Fd domain, rather than direct interaction with linker residues, might be expected.

Steady-State MMOR-RD Activity. Altering the connectivity of the MMOR domains did not seriously disrupt steady-state electron transfer from NADH to redox-active dyes. As indicated by increased activities in both DCPIP and $K_3Fe(CN)_6$ assays, the long, flexible RD4 linker may afford better accessibility of substrates to the reductase cofactors. Conversely, the protected flavin cofactor of RD2 may prevent efficient interaction with DCPIP, resulting in a 26% decrease in diaphorase activity compared to MMOR-wt. The substantial rate decrease observed for MMOR-RD3 (26% of wild-type activity) in the ferricyanide experiment is probably the result of repulsion between the three negatively charged residues in the RD3 linker sequence and the negatively charged $[Fe(CN)_6]^{3-}$ substrate.

Although the MMOR-RD constructs were predicted to retain activity in steady-state sMMO reactions, no evidence of productive electron transfer to MMOH was observed in propylene or nitrobenzene assays. Even with somewhat altered reductase redox potentials, the normal electron transfer pathway, $\text{NADH} \rightarrow \text{FAD} \rightarrow [\text{2Fe-2S}] \rightarrow \text{MMOH}$, is thermodynamically favored in the MMOR-RD constructs. Therefore, either interdomain electron transfer is blocked in MMOR-RD proteins or the reversed-domains constructs do not make suitable complexes with MMOH. Attaching a His₆ tag to the N-terminus of MMOR-Fd abolishes cross-linking to MMOH,³⁹ which suggests that the N-terminal portion of the ferredoxin domain is involved in binding MMOH. If so, linking the 27-kDa MMOR-FAD domain at this position, as done in this work, would interfere with MMOH–MMOR complex formation.

In the steady-state sMMO assays, the RD1, RD3, and RD4 reductases exhibited considerably elevated oxidase activities relative to that of wild-type MMOR (Table 5.6). The MMOR-RD1 construct, with an uncharged polar linker, showed a fourfold increase in dioxygen reduction. More hydrophilic (RD3) and longer (RD4) linkers afforded even larger (6- to 8-fold) enhancements. Again, this behavior can be explained by increased solvent/substrate accessibility to the reductase cofactors. On the other hand, the low oxidase activity measured for the MMOR-RD2 protein indicates that its cofactors are well isolated from solvent.

Reaction of MMOR-RD Constructs with NADH. Reduction of the MMOR-RD constructs with NADH at pH 7.0 and 4 °C proceeds via the same kinetic steps described previously for wild-type MMOR,^{16,23} except that NAD⁺ release and interdomain electron transfer do not coincide (Scheme 5.2). By analogy to MMOR²³ and MMOR-FAD,³⁰ NADH is presumed to bind rapidly to MMOR-RD, forming a Michaelis complex, MC1, with an optical spectrum identical to that of oxidized

reductase. Next, a conformational rearrangement gives rise to the FAD–NADH charge transfer interaction of species CT1. This step occurs at 350–400 s⁻¹ in both MMOR-wt and MMOR-FAD, but for the FAD domain protein, relatively weak binding to NADH ($K_d = 25 \mu\text{M}$ vs 3.8 μM for MMOR) reduces the observed rate constant to $290 \pm 20 \text{ s}^{-1}$ in the presence of a 10-fold excess of NADH.³⁰ All four MMOR-RD proteins exhibit reduced CT1 formation rates, ranging from 96 s⁻¹ for RD3 to 229 s⁻¹ for RD2 (Table 5.7). Because NADH concentration dependence experiments were not performed for the reversed-domains reductases, this decrease in the observed rate constant cannot be assigned definitively to either reduced affinity for NADH or a slower conformational change. It was noted during purification, however, that the MMOR-RD proteins, particularly the RD3 construct, did not bind well to the Sepharose 5'-AMP affinity column. This observation suggests that weak affinity for NADH is at least partly responsible for the depressed CT1 formation rates.

Hydride transfer from NADH to the flavin cofactor yields intermediate CT2, which is characterized by a charge transfer interaction between NAD⁺ and FADH⁻. This electron transfer step proceeds at 180–190 s⁻¹ in MMOR-wt and MMOR-FAD, as well as MMOR-RD2. The other MMOR-RD proteins have nearly identical CT1 and CT2 formation rates, indicating that the rate of hydride transfer may be limited by generation of the initial charge transfer complex. Release of NAD⁺ to form intermediate HQ, which has FAD_{hq} and [2Fe-2S]_{ox} cofactors, occurs at 90 s⁻¹ in MMOR and MMOR-FAD. Rates ranging from 75 s⁻¹ (RD2) to 14 s⁻¹ (RD3) were observed for the reversed-domains constructs, reflecting varying affinities for NAD⁺. In MMOR-wt, a fraction of intramolecular electron transfer from FAD_{hq} to [2Fe-2S]_{ox} (ca. 65% of total) takes place upon NAD⁺ release; no electron transfer was detected for any of the MMOR-RD constructs in this kinetic step.

The final step, interdomain electron transfer to yield species SQ with cofactors largely in the FAD_{sq} and $[\text{2Fe-2S}]_{\text{red}}$ oxidation states, proceeds at 25 s^{-1} for wild-type MMOR, corresponding to ca. 35% of the total observed intramolecular electron transfer. This reaction is significantly slower in all four MMOR-RD proteins. A rate constant of 0.9 s^{-1} was measured for MMOR-RD4 (long linker), which represents a 28-fold decrease with respect to MMOR-wt. Participation of the histidine and tyrosine residues of the RD4 linker in electron transfer is possible, although rather unlikely. The other reversed-domains reductases exhibit far slower interdomain electron transfer rates: 0.036 s^{-1} for RD1 (700-fold decrease), 0.0062 s^{-1} for RD2 (4000-fold decrease), and 0.038 s^{-1} for RD3 (660-fold decrease). Electron transfer in the three extremely slow reactions may actually involve bimolecular processes. If this step were to occur by a second-order reaction in the RD1, RD2, and RD3 constructs, the sequestered flavin ring in MMOR-RD2 may contribute to the especially low interdomain electron transfer rate observed for this protein.

Regardless of the electron transfer pathway, none of the MMOR-RD constructs with a short, 7-residue linker sequence is able to transfer electrons efficiently between the flavin and $[\text{2Fe-2S}]$ cofactors. The short linkers apparently do not allow the reductase domains to align properly for rapid electron transfer. Tethering the reductase domains with a long, flexible linker, however, afforded an engineered protein, MMOR-RD4, with a reasonably fast interdomain electron transfer rate (0.9 s^{-1} at $4 \text{ }^\circ\text{C}$). This result suggests that the orientation of domains in MMOR may be different than that in PDR. There is precedence for such variable interdomain contacts among FNR family proteins. For instance, in the maize leaf ferredoxin (Fd)–FNR complex, the Fd protein is rotated ca. 180° about the $[\text{2Fe-2S}]$ –flavin axis with respect to the PDR domain arrangement.⁴⁰ Alternatively, a longer linker may be required in

MMOR to accommodate the adenosine portion of FAD, which is absent from the FMN cofactor of PDR.

Conclusions. By reattaching the separated [2Fe-2S] and FAD domains of MMOR in a non-native configuration, interdomain electron transfer can be restored, at least in part, thereby demonstrating the truly modular nature of the FNR family proteins. The requirement of a long, flexible linker for efficient electron transfer between MMOR-RD cofactors provides the first information about domain orientation in full-length MMOR, the structure of which has not yet been determined. Changing Leu343 (MMOR numbering) to glycine in three of the MMOR-RD constructs reveals a role for this residue in modulating the flavin optical spectrum, FAD_{ox}/FAD_{sq} redox potential, and reactivity with electron acceptors. This work opens the road to a more systematic investigation of MMOR-RD proteins with long linker sequences to establish the roles of affinity, proximity, and orientation in the interdomain electron transfer reaction.

ACKNOWLEDGMENT

This work was supported by National Institute of General Medical Sciences grant GM32134 (S.J.L.). J.L.B. was a Howard Hughes Medical Institute predoctoral fellow. We thank Lisa L. Chatwood for many helpful discussions and assistance with structural analysis and Jane H. Maduram for performing the initial cloning step.

REFERENCES

- (*) A slightly altered version of this work will be submitted for publication. Blazyk, J. L.; Lippard, S. J. **2003**.
- (1) Higgins, I. J.; Best, D. J.; Hammond, R. C.; Scott, D. *Microbiol. Rev.* **1981**, *45*, 556-590.
- (2) Hanson, R. S.; Hanson, T. E. *Microbiol. Rev.* **1996**, *60*, 439-471.
- (3) Prior, S. D.; Dalton, H. J. *Gen. Microbiol.* **1985**, *131*, 155-163.
- (4) Murrell, J. C. *Biodegradation* **1994**, *5*, 145-159.
- (5) Nguyen, H.-H. T.; Elliott, S. J.; Yip, J. H.-K.; Chan, S. I. *J. Biol. Chem.* **1998**, *273*, 7957-7966.
- (6) Lieberman, R. L.; Shrestha, D. B.; Doan, P. E.; Hoffman, B. M.; Stemmler, T. L.; Rosenzweig, A. C. *Proc. Nat. Acad. Sci. USA* **2003**, *100*, 3820-3825.
- (7) Colby, J.; Dalton, H. *Biochem. J.* **1978**, *171*, 461-468.
- (8) Pilkington, S. J.; Dalton, H. *Methods Enzymol.* **1990**, *188*, 181-190.
- (9) Fox, B. G.; Froland, W. A.; Dege, J. E.; Lipscomb, J. D. *J. Biol. Chem.* **1989**, *264*, 10023-10033.
- (10) Fox, B. G.; Froland, W. A.; Jollie, D. R.; Lipscomb, J. D. *Methods Enzymol.* **1990**, *188*, 191-202.
- (11) Woodland, M. P.; Dalton, H. J. *Biol. Chem.* **1984**, *259*, 53-59.
- (12) Feig, A. L.; Lippard, S. J. *Chem. Rev.* **1994**, *94*, 759-805.
- (13) Liu, K. E.; Lippard, S. J. In *Adv. Inorg. Chem.*; Sykes, A. G., Ed.; Academic Press: San Diego, 1995; Vol. 42, pp 263-289.
- (14) Wallar, B. J.; Lipscomb, J. D. *Chem. Rev.* **1996**, *96*, 2625-2657.
- (15) Valentine, A. M.; Lippard, S. J. *Dalton Trans.* **1997**, *21*, 3925-3931.
- (16) Gassner, G. T.; Lippard, S. J. *Biochemistry* **1999**, *38*, 12768-12785.

- (17) Solomon, E. I.; Brunold, T. C.; Davis, M. I.; Kemsley, J. N.; Lee, S.-K.; Lehnert, N.; Neese, F.; Skulan, A. J.; Yang, Y.-S.; Zhou, J. *Chem. Rev.* **2000**, *100*, 235-349.
- (18) Merckx, M.; Kopp, D. A.; Sazinsky, M. H.; Blazyk, J. L.; Müller, J.; Lippard, S. J. *Angew. Chem. Int. Ed.* **2001**, *40*, 2782-2807.
- (19) Stainthorpe, A. C.; Lees, V.; Salmond, G. P. C.; Dalton, H.; Murrell, J. C. *Gene* **1990**, *91*, 27-34.
- (20) Colby, J.; Dalton, H. *Biochem J.* **1979**, *177*, 903-908.
- (21) Lund, J.; Dalton, H. *Eur. J. Biochem.* **1985**, *147*, 291-296.
- (22) Fox, B. G.; Hendrich, M. P.; Surerus, K. K.; Andersson, K. K.; Froland, W. A.; Lipscomb, J. D.; Münck, E. J. *Am. Chem. Soc.* **1993**, *115*, 3688-3701.
- (23) Kopp, D. A.; Gassner, G. T.; Blazyk, J. L.; Lippard, S. J. *Biochemistry* **2001**, *40*, 14932-14941.
- (24) Müller, J.; Lugovskoy, A. A.; Wagner, G.; Lippard, S. J. *Biochemistry* **2002**, *41*, 42-51.
- (25) Lund, J.; Woodland, M. P.; Dalton, H. *Eur. J. Biochem.* **1985**, *147*, 297-305.
- (26) Green, J.; Dalton, H. *Biochem. J.* **1989**, *259*, 167-172.
- (27) Andrews, S. C.; Shipley, D.; Keen, J. N.; Findlay, J. B. C.; Harrison, P. M.; Guest, J. R. *FEBS Lett.* **1992**, *302*, 247-252.
- (28) Karplus, P. A.; Daniels, M. J.; Herriott, J. R. *Science* **1991**, *251*, 60-66.
- (29) Correll, C. C.; Batie, C. J.; Ballou, D. P.; Ludwig, M. L. *Science* **1992**, *258*, 1604-1610.
- (30) Blazyk, J. L.; Lippard, S. J. *Biochemistry* **2002**, *41*, 15780-15794.
- (31) Chatwood, L. L.; Müller, J.; Gross, J. D.; Wagner, G.; Lippard, S. J., unpublished results.
- (32) Thompson, J. D.; Higgins, D. G.; Gibson, T. J. *Nucleic Acids Res.* **1994**, *22*, 4673-4680.

- (33) Crasto, C. J.; Feng, J.-a. *Prot. Eng.* **2000**, *13*, 309-312.
- (34) Stainthorpe, A. C.; Murrell, J. C.; Salmond, G. P. C.; Dalton, H.; Lees, V. *Arch. Microbiol.* **1989**, *152*, 154-159.
- (35) Sambrook, J.; Fritsch, E. F.; Maniatis, T. *Molecular Cloning: A Laboratory Manual*; 2nd ed.; Cold Spring Harbor Laboratory Press: Cold Spring Harbor, NY, 1989.
- (36) Massey, V. J. *Biol. Chem.* **1957**, *229*, 763-770.
- (37) Stookey, L. L. *Anal. Chem.* **1970**, *42*, 779-781.
- (38) Coufal, D. E.; Blazyk, J. L.; Whittington, D. A.; Wu, W. W.; Rosenzweig, A. C.; Lippard, S. J. *Eur. J. Biochem.* **2000**, *267*, 2174-2185.
- (39) Kopp, D. A.; Lippard, S. J., unpublished results.
- (40) Kurisu, G.; Kusunoki, M.; Katoh, E.; Yamazaki, T.; Teshima, K.; Onda, Y.; Kimata-Arigo, Y.; Hase, T. *Nature Struct. Biol.* **2001**, *8*, 117-121.

Table 5.1: Primary Sequences for Reversed-Domains MMOR Constructs

Protein	Linker Type	N-Terminal Sequence	Linker Residues	C-Terminal Sequence
RD1	PDR	MMOR(99-342)	GATNTNA	MMOR(3-98)
RD2	MMOR	MMOR(99-342)	LPSGAAQ ^a	MMOR(3-98)
RD3	factor X _a site	MMOR(99-342)	GDETIEG	MMOR(3-98)
RD4	long (14 aa) ^b	MMOR(99-342)	GIGSGGSGHVSGYS	MMOR(3-98)

^aLPSGAA, MMOR residues 343-348; Q, MMOR residue 2. ^bAbbreviation: aa, amino acid residues.

Table 5.2: Primers for Site-Directed Mutagenesis of MMOR-RD Sequences

Construct	Forward Primer ^a
RD1	5'-CCAACACGAATGCGCGG <u>G</u> TCCACACTATCACG
RD2	5'-CGCCGCACAGCGG <u>G</u> TCCACACTATCACG
RD3	5'-CCATTGAGGGTCGG <u>G</u> TCCACACTATCACGG

^a Forward primers are depicted; reverse primers are the reverse complements. The altered codon, which corresponds to Val4 of the Fd domain, is shown in bold with the altered base underlined.

Table 5.3: Properties of MMOR and MMOR-RD Constructs

Reductase	Linker	Yield (mg/L)	MW (Da), measured	Fe content (mol/mol protein)	λ_{\max} (nm) pH 7.0, 25 °C	A_{458}/A_{394} (FAD _{ox})
MMOR	n/a	15 ^a	38,547 ± 4 ^a	2.05 ± 0.05 ^a	337, 395, 465	1.33
RD1	PDR	25	38,413 ± 4 ^b	1.94 ± 0.02	337, 398, 458	1.25
RD2	MMOR	23	38,409 ± 4 ^c	1.86 ± 0.05	337, 397, 464	1.35
RD3	X _a site	19	38,484 ± 4 ^d	1.98 ± 0.11	339, 398, 463	1.11
RD4	long	13	38,985 ± 4 ^e	1.97 ± 0.02	339, 396, 458	1.14

^aAs reported in ref 23. ^bExpected 38,415 Da for apoprotein. ^cExpected 38,410 Da for apoprotein.
^dExpected 38,487 Da for apoprotein. ^eExpected 38,989 Da for apoprotein.

Table 5.4: Relative Redox Potentials for MMOR-RD Constructs^a

Protein	FAD _{ox/sq} – Fd _{ox/red} (mV)	Fd _{ox/red} – FAD _{sq/hq} (mV)	FAD _{ox/sq} – FAD _{sq/hq} (mV)
MMOR ^b	33 ± 21	57 ± 29	90 ± 22
domains ^c	33 ± 3	61 ± 5	94 ± 6
RD1	4 ± 6	58 ± 7	62 ± 13
RD2	45 ± 2	64 ± 1	109 ± 4
RD3	9 ± 6	53 ± 8	62 ± 14
RD4	19 ± 3	48 ± 8	67 ± 11

^aDifferences between MMOR redox potentials measured at pH 7.0 and 25 °C. FAD_{ox/sq} FAD_{ox}/FAD_{sq} redox couple; Fd_{ox/red} [2Fe-2S]_{ox}/[2Fe-2S]_{red} redox couple; FAD_{sq/hq} FAD_{sq}/FAD_{hq} redox couple. Bold values deviate significantly from those of the MMOR domains. ^bAs reported in ref 23. ^cAs reported in ref 30.

Table 5.5: Absolute Redox Potentials for MMOR-RD Constructs^a

Protein	FAD _{ox/sq} (mV) ^b	Δ (mV)	Fd _{ox/red} (mV)	Δ (mV)	FAD _{sq/hq} (mV)	Δ (mV)
MMOR ^c	-176 ± 7	n/a	-209 ± 14	n/a	-266 ± 15	n/a
domains ^d	-172 ± 2	n/a	-205 ± 1	n/a	-266 ± 4	n/a
RD1	-208 ± 1	-32	-219 ± 2	-10	-269 ± 5	-3
RD2	-166 ± 5	+10	-218 ± 7	-9	-270 ± 7	-4
RD3	-220 ± 4	-44	-227 ± 5	-18	-293 ± 6	-27
RD4	-209 ± 4	-33	-221 ± 3	-12	-272 ± 4	-6

^aMeasured at pH 7.0 and 25 °C. ^bFAD_{ox/sq}/FAD_{ox}/FAD_{sq} redox couple; Fd_{ox/red}, [2Fe-2S]_{ox}/[2Fe-2S]_{red} redox couple; FAD_{sq/hq}/FAD_{sq}/FAD_{hq} redox couple. Bold values deviate significantly from those of the MMOR domains. ^cAs reported in ref 23. ^dAs reported in ref 30.

Table 5.6: Steady-State Activities for MMOR-RD Proteins^a

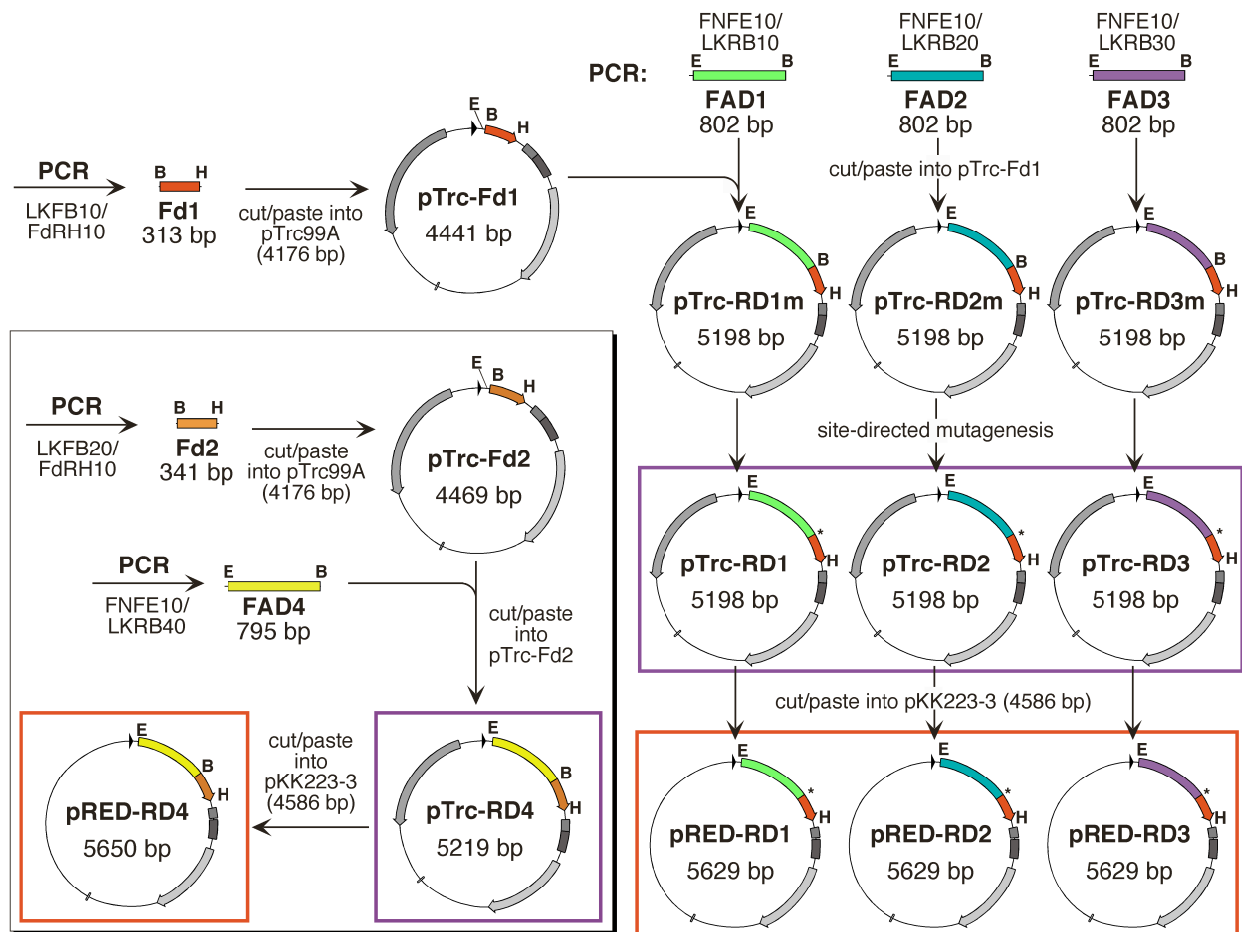
Protein	DCPIP reduction ^b ($\mu\text{mol min}^{-1} \text{mg}^{-1}$)	Rel. Act.	[Fe(CN) ₆] ³⁻ reduction ^b ($\mu\text{mol min}^{-1} \text{mg}^{-1}$)	Rel. Act.	oxidase activity ^c ($\mu\text{mol min}^{-1} \text{mg}^{-1}$)	Rel. Act.
MMOR	8.8 ± 0.2	1.00	10.7 ± 0.6	1.00	0.095 ± 0.013	1.00
RD1	8.4 ± 0.1	0.96	10.6 ± 0.5	1.00	0.377 ± 0.004	4.00
RD2	6.5 ± 0.3	0.74	12.3 ± 0.3	1.15	0.052 ± 0.009	0.53
RD3	9.2 ± 0.3	1.04	2.8 ± 0.1	0.26	0.619 ± 0.009	6.59
RD4	10.6 ± 0.3	1.20	19.8 ± 1.1	1.86	0.710 ± 0.004	7.55

^aBold values deviate significantly from those of MMOR-wt. ^bMeasured at 15 °C. ^cMeasured at 25 °C; sMMO propylene assay in the presence of 1 μM MMOH and 1 μM MMOB.

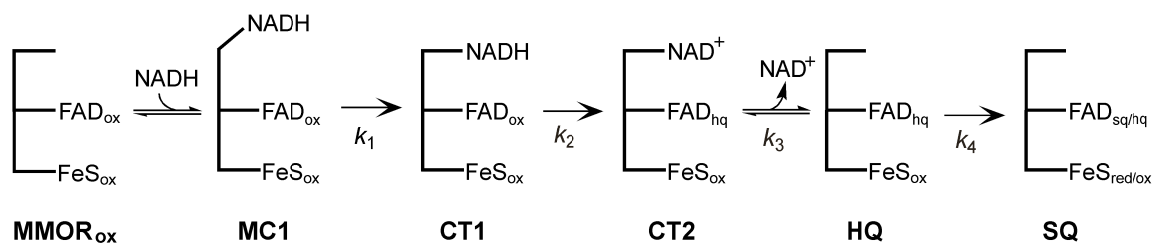
Table 5.7: Rate Constants for MMOR-RD Reaction with NADH^a

Protein	CT1 formation k_1 (s ⁻¹)	CT1 decay/CT2 form. k_2 (s ⁻¹)	CT2 decay k_3 (s ⁻¹)	Interdomain ET k_4 (s ⁻¹)	wild-type comparison ^b
MMOR	400 ± 50	179 ± 9	90 ± 3 ^c	90 ± 3 ^c /25 ± 2	1
RD1	160 ± 6	140 ± 5	33 ± 1	0.036 ± 0.003	0.0014
RD2	229 ± 26	177 ± 13	75 ± 3	0.0062 ± 0.0007	0.00025
RD3	96 ± 4	72 ± 2	14 ± 1	0.038 ± 0.003	0.0015
RD4	172 ± 7	169 ± 4	20 ± 1	0.9 ± 0.1	0.04

^aMeasured at pH 7.0 and 4 °C. Kinetic model depicted in Scheme 5.2. ^bDecrease in interdomain electron transfer relative to the slow MMOR-wt rate constant (25 s⁻¹). ^cApproximately 65% of interdomain electron transfer coincides with CT2 decay in MMOR-wt.



Scheme 5.1



Scheme 5.2

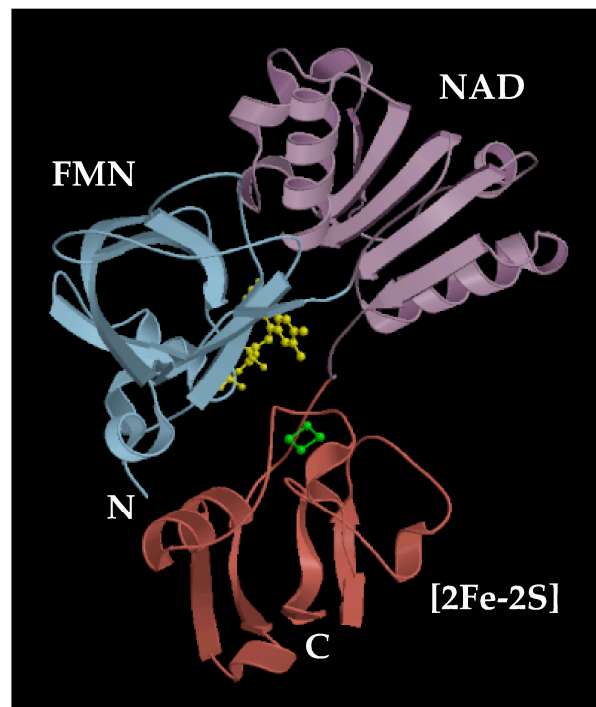
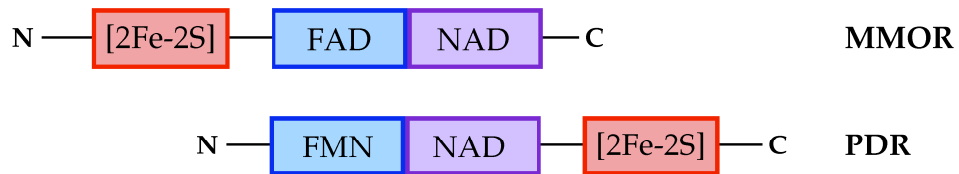


Figure 5.1. Reductase domain arrangement derived from the MMOR gene sequence and homology to members of the flavoprotein electron transferase family. The [2Fe-2S] domain is an independent modular unit which can be linked to either the N- or C-terminus of FNR-like proteins (top). X-ray crystal structure of phthalate dioxygenase reductase (bottom; ref 29). The FMN cofactor is shown in yellow, and the [2Fe-2S] cluster is colored green.

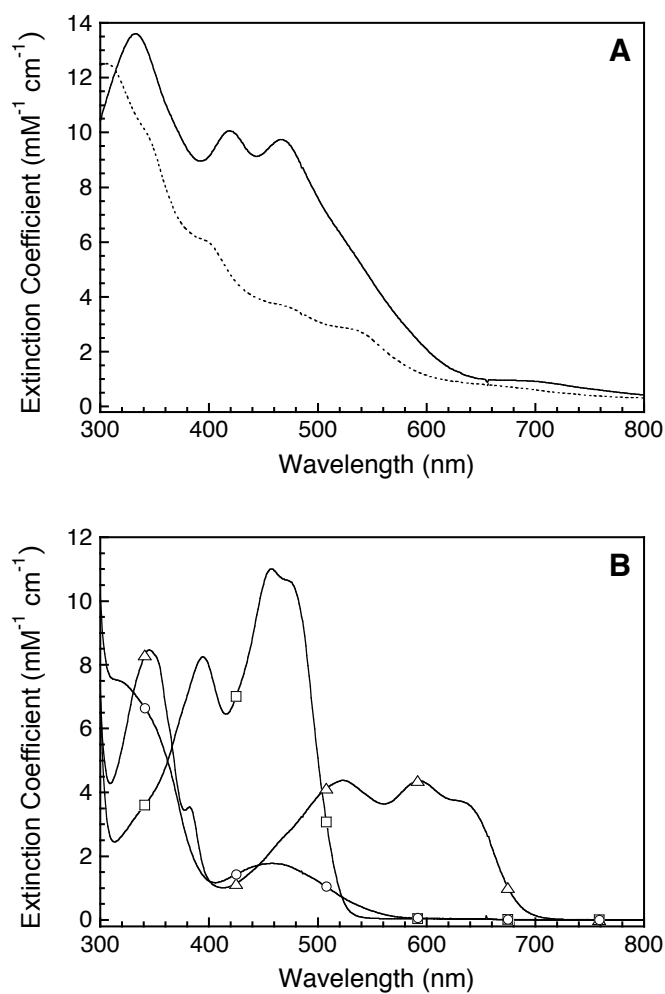


Figure 5.2. Component spectra determined for the MMOR domain proteins. (A) Oxidized (Fd_{ox} ; solid line) and reduced (Fd_{red} ; dotted line) optical spectra for MMOR-Fd. (B) MMOR-FAD in the oxidized (FAD_{ox} ; squares), semiquinone (FAD_{sq} ; triangles), and hydroquinone (FAD_{hq} ; circles) oxidation states. From ref 30.

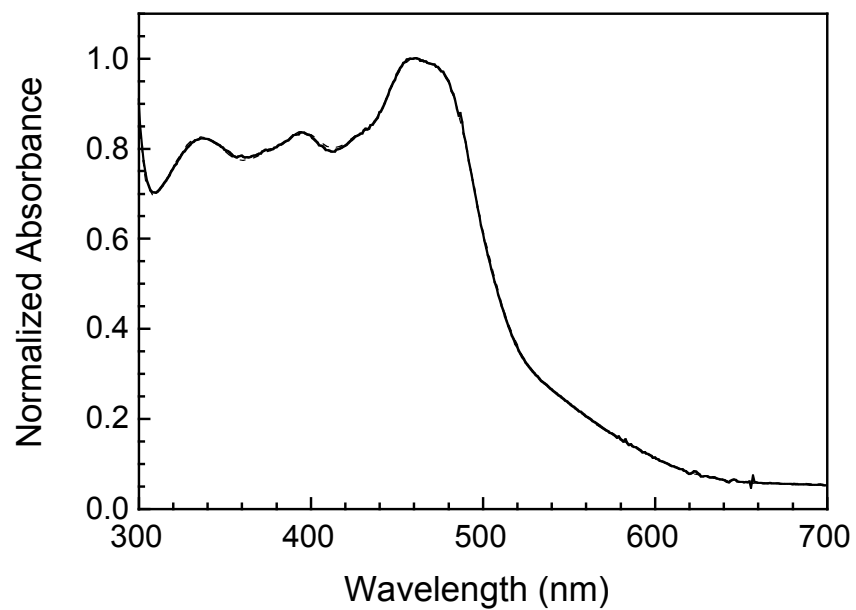


Figure 5.3. Optical spectrum of pure MMOR-RD2 fit with a linear combination of Fd_{ox} and FAD_{ox} component spectra (dashed line) determined previously for the separated MMOR domains (ref 30).

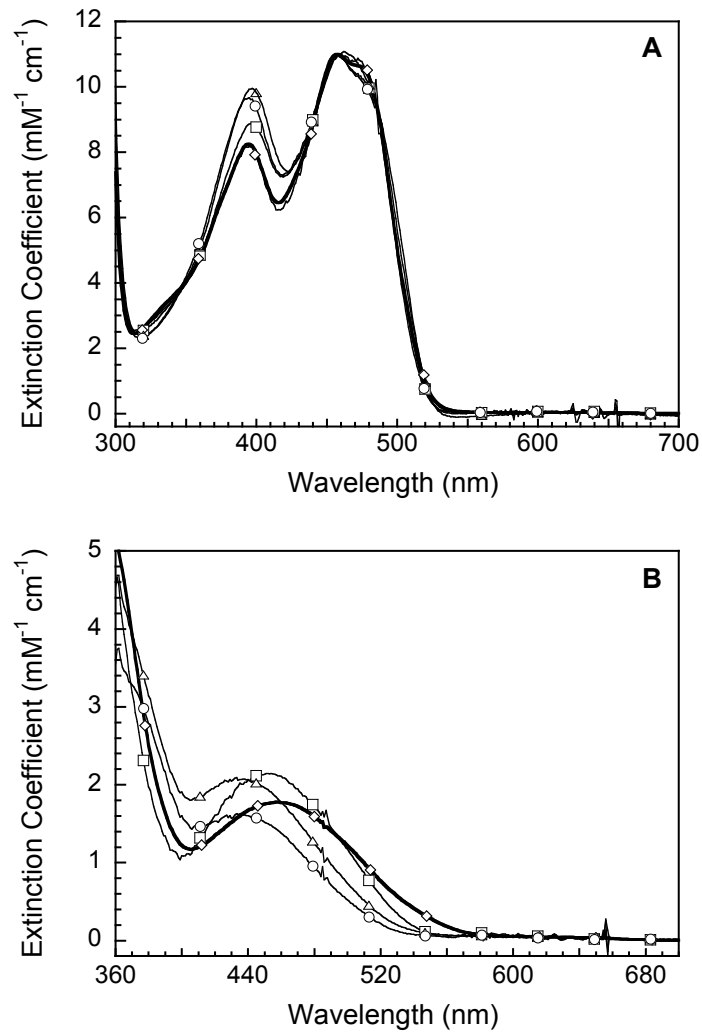


Figure 5.4. Calculated flavin component spectra in the (A) fully oxidized and (B) fully reduced oxidation states for MMOR-wt (heavy line), MMOR-RD1 (squares), MMOR-RD2 (diamonds), MMOR-RD3 (triangles), and MMOR-RD4 (circles).

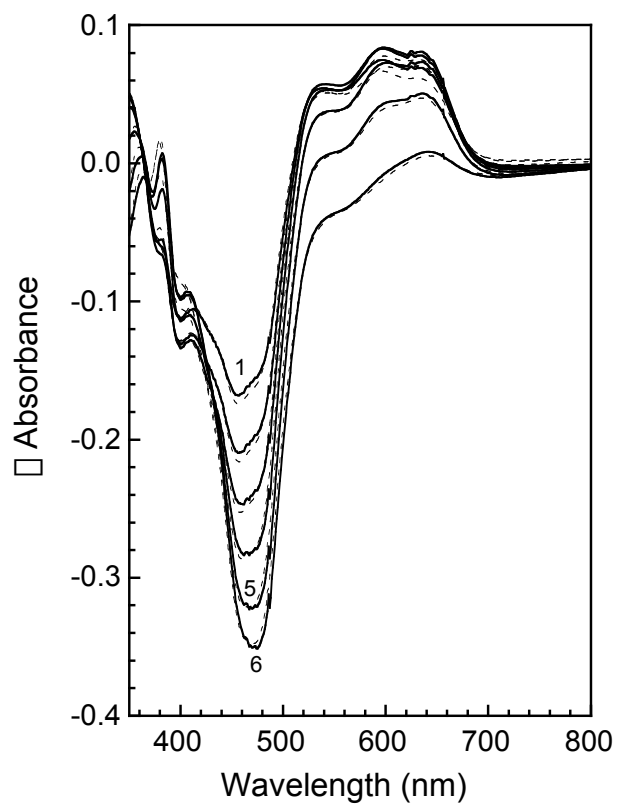


Figure 5.5. Difference spectra for the reductive titration of a 1-mL mixture of 30 μM MMOR-RD2 and 40 μM anthraquinone-2-sulfonate by dithionite at pH 7.0 and 25 $^{\circ}\text{C}$. Spectra 1-6 correspond to the addition of 10, 15, 25, 45, 70, and 80 μL of ~ 2 mM dithionite, respectively. Fits (dashed lines) are superimposed on the difference spectra.

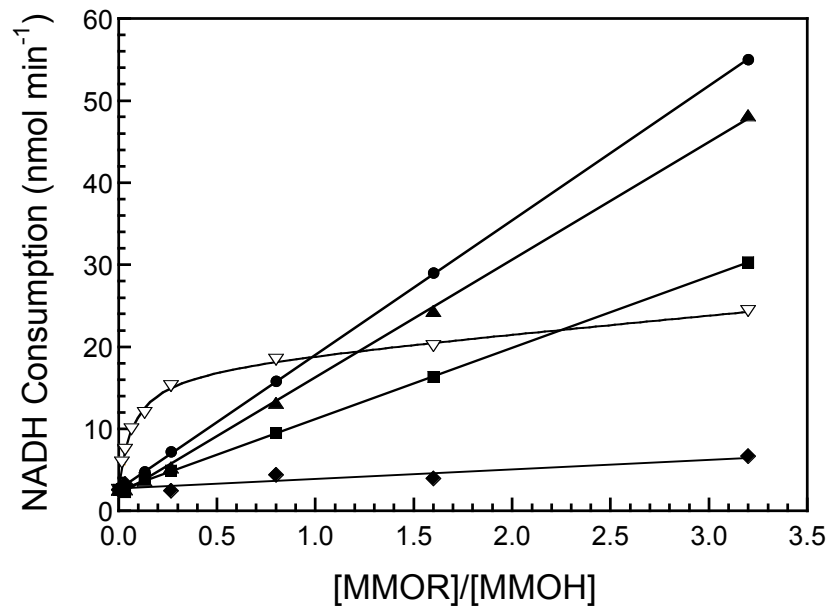


Figure 5.6. Dependence of the steady-state sMMO reaction with propylene at 25 °C on reductase concentration. Samples were air-saturated and contained 1 μ M MMOH, 1 μ M MMOB, 160 μ M NADH, and 0.8 mM propylene. Activity curves were fit with a hyperbola plus a line (MMOR-wt, open triangles) or a line (MMOR-RD constructs). MMOR-RD1, squares; MMOR-RD2, diamonds; MMOR-RD3, triangles; MMOR-RD4, circles.

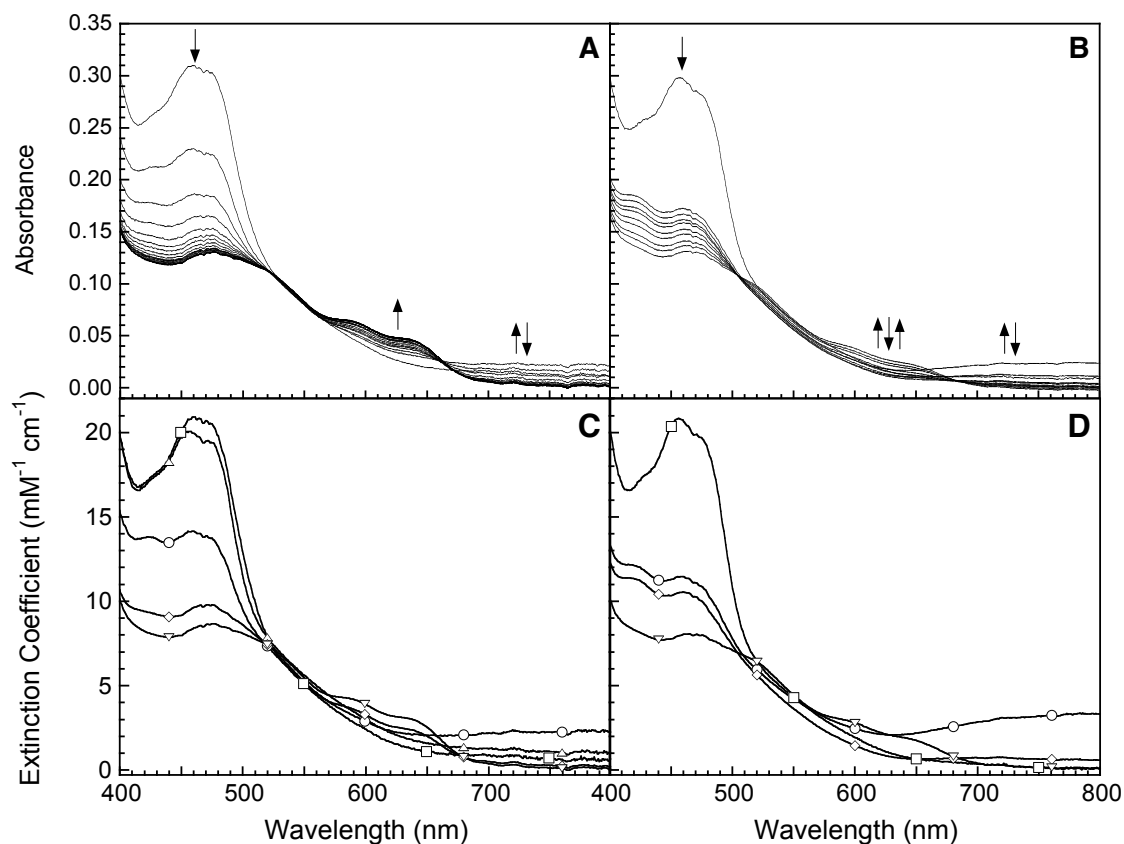


Figure 5.7. Kinetics of MMOR reduction with NADH at 4 °C and pH 7.0. Spectra recorded on a log time scale by diode array stopped-flow spectroscopy (A) in the first 350 ms after mixing 20 μM MMOR-wt with 200 μM NADH and (B) in the first 2.5 s after mixing 20 μM MMOR-RD4 with 200 μM NADH. Spectra of intermediates resolved by global analysis of the diode array kinetic data for (C) MMOR-wt and (D) MMOR-RD4: MMOR_{ox} (squares), CT1 (triangles; MMOR-wt only), CT2 (circles), HQ (diamonds), and SQ (inverted triangles).

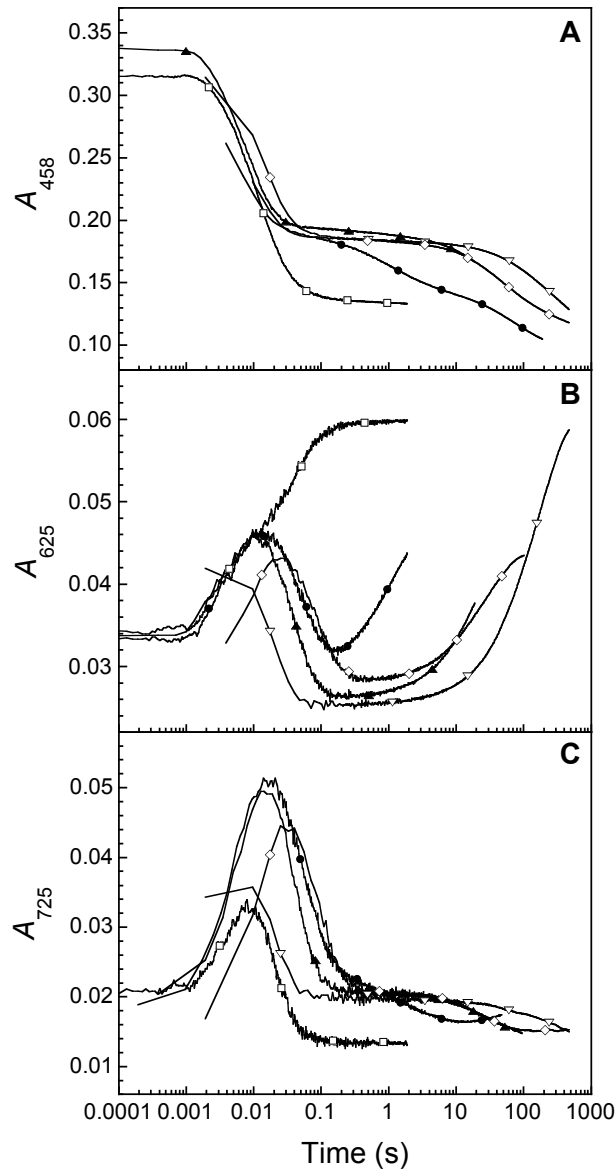


Figure 5.8. Kinetics of MMOR reduction with NADH at 4 °C and pH 7.0. Time-dependent absorbance changes at (A) 458 nm, (B) 625 nm, and (C) 725 nm for the reaction of 20 μM MMOR with 200 μM NADH: MMOR-wt (open squares), RD1 (closed triangles), RD2 (open triangles), RD3 (open diamonds), and RD4 (closed circles).

Chapter 6

**Expression in *Escherichia coli* of the Hydroxylase Component of Soluble
Methane Monooxygenase from *Methylococcus capsulatus* (Bath)***

INTRODUCTION

Methanotrophic bacteria thrive at the interface between aerobic and anaerobic sediments. These organisms use methane as their sole source of carbon and energy, such that only a small fraction of this greenhouse gas, which is generated by the anaerobic degradation of organic carbon, reaches the atmosphere.¹ The first step of their primary metabolic pathway, the selective oxidation of methane to methanol (eq 1), is catalyzed by the methane monooxygenase (MMO) enzyme system. Nearly all



methanotrophs express a copper-dependent membrane-bound particulate MMO (pMMO).^{2,3} At low copper-to-biomass ratios, a few species of methanotrophic bacteria produce instead a soluble form of MMO (sMMO), which contains iron.⁴

The sMMO complexes from two methanotrophs, *Methylococcus capsulatus* (Bath) and *Methylosinus trichosporium* OB3b, have been characterized extensively by many methodologies during the last twenty-five years.⁵⁻¹¹ Maximal catalytic activity is achieved in the presence of three protein components: a hydroxylase (MMOH, 251 kDa), a reductase (MMOR, 38.5 kDa), and a regulatory protein (MMOB, 15.9 kDa).¹²⁻¹⁴ The hydroxylase, a dimer of three subunits^{5,13} in an $\alpha_2\beta_2\gamma$ configuration (α , 60.6 kDa; β , 45.0 kDa; γ , 19.8 kDa), contains two carboxylate- and hydroxo-bridged dinuclear iron centers housed in the β subunits. Dioxygen activation and substrate hydroxylation occur at the diiron active sites. MMOR is an iron-sulfur flavoprotein which shuttles electrons from NADH through its flavin adenine dinucleotide (FAD) and [2Fe-2S] cofactors to the hydroxylase active site.¹⁴⁻¹⁷ The MMOB protein, which contains no prosthetic groups, modulates the MMO reaction by forming specific complexes with the hydroxylase^{14,18} that alter the environment and therefore the spectroscopic^{10,13,19-21} and chemical^{7,14,19,22-24} properties of the diiron site. In addition, a fourth protein

(MMOD, 11.9 kDa), for which no function has been established, was recently identified in the *M. capsulatus* (Bath) sMMO system.²⁵

The genes encoding the sMMO proteins of *M. capsulatus* (Bath),²⁶⁻²⁸ *M. trichosporium* OB3b,^{29,30} *Methylocystis* sp. strain M,³¹ *Methylocystis* sp. strain WI 14,³² and *Methylomonas* sp. strains KSPIII and KSWIII³³ have been identified and sequenced. In all of these organisms, the six sMMO genes, *mmoX*, *mmoY*, *mmoB*, *mmoZ*, *orfY*, and *mmoC*, which code for MMOH_□, MMOH_□, MMOB, MMOH_□, MMOD, and MMOR, respectively, are clustered on a 5.5-kb segment of DNA (Figure 6.1). Amino acid sequences of these six sets of sMMO proteins are universally conserved as follows: MMOH_□, 73.6%; MMOH_□, 46.8%; MMOB, 55.6%; MMOH_□, 35.7%; MMOD, 19.4%; and MMOR, 37.4%.¹¹ Although the overall percent identity for the putative MMOD products is fairly low (19.4%), there is a central region with a significantly greater number of conserved residues (44.4%).

sMMO expression in *M. capsulatus* (Bath) is controlled by a single □⁷⁰-dependent copper-regulated promoter located upstream of the *mmoX* gene, so that the sMMO system is produced only under conditions of low copper concentration.³⁴ Motifs resembling □-independent transcriptional terminators in the *mmoX/mmoY* (T₁) and *mmoZ/orfY* (T₂) intercistronic regions give rise to three mRNA transcripts differing only in their 3' ends in the native organism. Transcription of the homologous sMMO genes of *M. trichosporium*, however, is regulated by a □⁵⁴-dependent promoter upstream from *mmoX* and a □⁷⁰-dependent promoter located between *mmoX* and *mmoY*.³⁵

The roles of individual amino acids in catalysis or binding can be probed by using site-directed mutagenesis (SDM). In order to employ this method for the MMO system, however, the individual proteins must be expressed from controllable genes. High-yield *Escherichia coli* expression systems for MMOB,^{28,36-38} MMOR,¹⁷ and MMOD²⁵

have been reported, making mutagenesis of these proteins possible. Although the sMMO enzymes have been studied intensively for more than two decades, mutagenesis of the hydroxylase component, unquestionably the most interesting target in the sMMO system, has, until very recently,³⁹ been prevented by the lack of a useful recombinant expression system.

Despite much effort, attempts to express active MMOH in *E. coli* have not yet been successful.⁴⁰⁻⁴² Reports of robust expression in *E. coli* of similar monooxygenases, including toluene-4-monooxygenase,^{43,44} toluene-*o*-xylene monooxygenase,⁴⁵ and phenol hydroxylase,⁴⁶ suggest that the *E. coli* environment is not intrinsically unsuitable for folding and assembling multisubunit oxygenases. Other heterologous hosts can produce small quantities of active hydroxylase. Trichloroethylene and chloroform degradation was noted in a *Pseudomonas putida* strain expressing all of the sMMO proteins from *M. trichosporium* OB3b, but expression was irregular, and the proteins were not purified.⁴⁷ After optimizing this system, plasmid stability was increased, but no MMOH activity was detected in pseudomonad cell extracts.⁴⁸ Low-level sMMO activity was also detected in *Agrobacterium tumefaciens* A114,⁴⁸ *Rhizobium meliloti* 102F34,⁴⁸ *Methylobacterium album* BG8,⁴⁹ and *Methylocystis parvus* OBBP⁴⁹ cells complemented with the *M. trichosporium* OB3b *mmo* operon.

Expression of *M. trichosporium* OB3b MMOH in the native host has been accomplished recently.⁵⁰ The *mmoX* gene in the host strain was knocked out genetically through a double-crossover recombination experiment to eliminate background expression of the MMOH α subunit.⁵¹ By adding a plasmid carrying the *mmo* operon to the sMMO-minus *M. trichosporium* OB3b mutant, sMMO activity was restored to wild-type levels.⁵⁰ The first site-directed MMOH mutants, expressed from a slightly modified homologous system, were described very recently.³⁹

In the present work, we employed several strategies, including stringent regulation of expression, placing all six sMMO genes on the expression vector, and constructing artificial *mmo* operons, to facilitate production of active recombinant *M. capsulatus* (Bath) MMOH in *E. coli* strains.

MATERIALS AND METHODS

sMMO Purification and Characterization. MMOH and MMOR were isolated from *M. capsulatus* (Bath) with minor modifications to a published protocol.¹⁴ The iron content of MMOH was determined by the ferrozine method.^{52,53} Pure MMOR was exchanged into distilled deionized water with a Quick Spin Sephadex G-50 column (Boehringer Mannheim, Indianapolis, IN). Methanol and acetic acid were added to the desalted MMOR to yield a 15 pmol/ μ L solution in 50% methanol/0.1% acetic acid, and the sample was submitted to the MIT Biopolymers Laboratory for analysis by electrospray ionization mass spectrometry (ESI-MS). To remove cofactors that had separated from the reductase peptide during sample preparation, HPLC purification was necessary. The protein component was analyzed with a Sciex model API 365 triple stage mass spectrometer. Conditions for expression and purification of MMOB from a recombinant *E. coli* system are described in Chapter 2.

DNA Primer Synthesis and Purification. All of the primers used for cloning and DNA sequencing were designed manually and synthesized on an Applied Biosystems Model 392 DNA/RNA synthesizer. Each primer was purified by polyacrylamide gel electrophoresis on a 12% denaturing polyacrylamide gel, extracted from the gel slices by using a crush and soak method, then precipitated to remove most of the salt added during extraction. The DNA pellets were suspended in appropriate quantities of deionized distilled water and stored at -20°C .

Construction of pJLB001 for DNA Sequencing. The *mmo* genes, which code for all four components of the MMO system, are contained on a 5.5-kb section of pCH4.^{26,27} From the plasmid DNA the entire operon was amplified by polymerase chain reaction (PCR) with the primers MON30 (5'-GAATGCCTTC**GAATTC**GGAGGAAACAAGTAATGGCAC) and 40C30 (5'-CGTGCACCTTA**AGCTTTC**AGGCCGCCCGGACGGCA-G). The resulting 5401-bp operon fragment was flanked by *Eco*RI and *Hind*III restriction sites (boldface font), which were introduced by MON30 and 40C30, respectively. PCR was performed with *Taq* DNA polymerase (Gibco BRL, Gaithersburg, MD) and *Taq* extender (Stratagene, La Jolla, CA) with the following thermal cycler conditions: 2 min at 96 °C; 1 min at 96 °C, 1 min at 55 °C, and 6 min at 72 °C for 22 cycles, followed by extension for 15 min at 72 °C. Because *Taq* DNA polymerase lacks 3' → 5' proofreading capability, it produces DNA with one-base deoxyadenosine (dA) overhangs on the 3' ends. This feature was exploited to ligate the resulting *mmo* operon PCR product directly into the pCR2.1 vector (Invitrogen, Carlsbad, CA) by using T4 DNA ligase (New England Biolabs, Inc., Beverly, MA or Boehringer Mannheim). The ligation products were transformed into competent *E. coli* XL1-Blue cells and selected on Luria-Bertani (LB)-ampicillin (Ap; 100 µg/mL) followed by LB-kanamycin (Km; 50 µg/mL) agar plates. A positive clone was identified as pJLB001 (Figure 6.2; Table 6.1) by restriction mapping of DNA isolated from plasmid minipreps.⁵⁴

Site-Directed Mutagenesis of pJLB001 to “Correct” *mmoZ* Sequence. DNA sequencing of pJLB001 (vide infra) revealed a base inversion at positions 63-64 in the *mmoZ* gene. The protein expressed from this gene would have contained two mutations in the MMOH α subunit, H21Q and V22L. Site-directed mutagenesis was performed to “correct” (vide infra) this error by using the QuikChange kit (Stratagene)

and following the instructions provided by the manufacturer. Two primers, Z63INVF (5'-GGGTGAACAAGATCGCGCACGTCAACACCCTGG) and Z63INVR (5'-CCAGG-GTGTTGACCGTGCGCGATCTTGTTCACCC) were prepared for use in the *Pfu* DNA polymerase-catalyzed PCR mutagenesis reaction. Subsequent isolation and sequencing (MIT Biopolymers Laboratory) of pJLB001-C showed that the mutagenesis was successful.

Construction of Series I Vectors for MMOH Expression. The *mmo* operon PCR product (vide supra) was digested with the restriction enzymes *Eco*RI and *Hind*III by using the conditions suggested by the supplier (New England Biolabs). A wide-host-range low-copy-number plasmid, pMMB190,⁵⁵ was digested in the same manner. To inactivate the restriction enzymes, both digest reaction mixtures were incubated for 20 min at 65 °C. The PCR product was ligated into the pMMB190 fragment by using T4 DNA ligase, and the resulting plasmid solution was transformed into *E. coli* XL1-Blue cells and selected on LB-Ap (100 µg/mL) plates. Colonies with ampicillin resistance were analyzed further by restriction mapping of DNA isolated from plasmid minipreps. A plasmid with the correct insert was selected and named pJLB100 (Figure 6.3A).

To create MMO expression vectors with slightly different features, pJLB100 was digested with *Eco*RI and *Hind*III, and the resulting operon fragment was ligated into two similarly digested low-copy-number wide-host-range plasmids, pMMB206 and pMMB277.⁵⁵ Colonies containing plasmids were selected on LB-chloramphenicol (Cm; 10-20 µg/mL) plates. Restriction mapping was used to identify the positive clones pJLB200 (Figure 6.3B) and pJLB201 (Figure 6.3C), which were constructed from pMMB206 and pMMB277, respectively.

An expression vector containing the “corrected” *mmo* operon (vide supra) was prepared by transferring the *mmo* genes of pJLB001-C into the multiple cloning site (MCS) of pMMB277, exactly as described for constructing pJLB200 and pJLB201. A plasmid containing the desired DNA fragments, pJLB201-C, was identified by restriction mapping. To avoid the potential interference of *lacZ* peptide translation with MMOH subunit expression, a plasmid without the *lacZ* gene was constructed from pJLB001-C and pMMB207, which differs from pMMB277 only in the absence of this gene.⁵⁵ Cloning was performed as described above, and a positive clone was named pJLB207 (Figure 6.3D).

Construction of Series II Vectors for MMOH Expression. The series I expression plasmids described above included the entire *mmo* operon without alteration. The second series of plasmids made for MMOH expression was based on the same wide-host-range low-copy-number pMMB plasmids⁵⁵ used in the first series. Rather than the whole operon, new “artificial” operons were designed in an attempt to improve the folding and assembly of the recombinant MMOH subunits. Because the first plasmid series yielded a rather high MMOB-to-MMOH ratio in the soluble fraction and little if any MMOD or MMOR (vide infra), changes in the native gene sequence were implemented. The MCS present in most of the pMMB plasmids does not have enough restriction sites compatible with the *mmo* operon, so it was necessary to construct the new operon sequences in pTrc99A (Amersham Pharmacia, Piscataway, NJ), a high-copy-number plasmid with a more useful MCS.

First, an expression vector that contains only the hydroxylase genes (*mmoX*, *mmoY*, and *mmoZ*) was constructed (pJLB300, Figure 6.4C). From the pCH4 plasmid DNA the *mmoX*–*mmoY* segment was amplified by PCR with the primers XFE10 (5'-CA-TAGAATGGAATTCGGAGGAAACAAGTAATGGCAC) and YRK10 (5'-CGTCATAG-

GTACCCTATTATTTCAATCCTGCCAGAAC). The resulting 2877-bp fragment was flanked by *EcoRI* and *KpnI* sites (boldface font), which were introduced by XFE10 and YRK10, respectively. PCR was performed with *Pfu* DNA polymerase (Stratagene, La Jolla, CA), which possesses 3' → 5' proofreading capability, with the following thermal cyclers conditions: 45 s at 96 °C; 45 s at 96 °C, 45 s at 60 °C, and 8 min at 72 °C for 25 cycles, followed by extension for 10 min at 72 °C. The DNA was precipitated by adding 0.1 volume of 2.5 M sodium acetate (pH 5.2) and 2.2 volumes of cold ethanol to the PCR solution. After incubation at -20 °C and -80 °C, the precipitated PCR product was recovered by centrifugation for 30 min at 10,000g, 4 °C and dissolved in 10 mM Tris (pH 8.0), 1 mM ethylenediaminetetraacetic acid (EDTA) (TE buffer). The *mmoX*-*mmoY* PCR product was digested with the restriction enzymes *EcoRI* and *KpnI* (New England Biolabs) by following the provided instructions. pTrc99A, a high-copy-number expression vector, was digested with the same enzymes to remove the *EcoRI*-*KpnI* fragment from its MCS. The *KpnI* enzyme cannot be heat-inactivated, so the plasmid and PCR product digests were extracted with equal volumes of phenol:chloroform:isoamyl alcohol (25:24:1) to denature the enzymes. The aqueous layers were removed, and the DNA was precipitated as described above. The pTrc99A digest was treated with alkaline phosphatase (AP; Boehringer Mannheim) to prevent recircularization in the subsequent ligation reaction. After inactivating the AP by adding 20 mM ethylene glycol-bis[β -aminoethyl ether]-*N,N,N',N'*-tetraacetic acid (EGTA) and heating at 65 °C for 10 min, the DNA was extracted again and precipitated with ethanol. The AP-treated pTrc99A digest and *mmoX*-*mmoY* PCR product were ligated by using T4 DNA ligase, and the resulting plasmid solution was transformed into competent *E. coli* XL1-Blue cells. Potential positive clones were identified by plating onto LB-agar plates containing Ap (100 μ g/mL). Colonies with ampicillin

resistance were analyzed further by restriction mapping of DNA isolated from plasmid minipreps. A plasmid with the correct insert was selected and named pTXY, as depicted in Figure 6.4A.

The *mmoZ* gene was PCR-amplified from pCH4 with the primers ZFK10 (5'-CT-**GGTACCCCTTAAGGAGAATGACATGGCGAAACTGG**) and ZRH10 (5'-AGGATGA-**AGCTTCCTCCCTTCAGTGC GGCGAC**), resulting in a 558-bp segment flanked by *KpnI* and *HindIII* sites (boldface font). PCR was performed with the following thermal cycler conditions: 45 s at 96 °C; 45 s at 96 °C, 45 s at 60 °C, and 1.5 min at 72 °C for 25 cycles, followed by extension for 10 min at 72 °C. After ethanol precipitation, the PCR product was digested with *HindIII* and then heated at 65 °C for 20 min to inactivate the restriction enzyme. The digested PCR product was isolated by ethanol precipitation, dissolved in NEB buffer 1/BSA, and digested with *KpnI*. The pTXY plasmid was digested with *KpnI* and *HindIII* in the same two-step procedure. The NaCl concentration of the plasmid double digest was increased to 100 mM in order to inactivate the *KpnI*. AP was added to the plasmid digest, incubated for 60 min at 37 °C, and then heat-inactivated as described previously. Both the *mmoZ* and pTXY digests were extracted with equal volumes of phenol:chloroform:isoamyl alcohol (25:24:1); the DNA was recovered by ethanol precipitation and dissolved in 10 mM Tris (pH 8.0). The *mmoZ* segment was ligated into pTXY as described above, and the resulting plasmid solution was transformed into competent *E. coli* XL1-Blue cells. After performing plasmid minipreps, a vector with the correct insert was selected and named pTXYZ, as shown in Figure 6.4B.

To construct the low-copy-number expression vector pJLB300 (Figure 6.4C), pMMB277 and pTXYZ were digested with the restriction enzymes *EcoRI* and *HindIII*, and the enzymes in both samples were heat-inactivated. The pMMB277 digest was

treated with AP, which was inactivated as described. Both digests were extracted, ethanol precipitated, and then dissolved in 10 mM Tris (pH 8.0). The *mmoX*–*mmoY*–*mmoZ* segment was ligated into pMMB277 with T4 DNA ligase, and the resulting plasmid solution was transformed into competent *E. coli* XL1-Blue cells. Potential positive clones were selected on LB-Cm (10 µg/mL) agar plates. By restriction digest analysis of plasmid DNA isolated from minipreps, seven positive clones were identified and labeled pJLB300(*En*), where $n = 3, 4, 6, 7, 8, 9,$ and 11.

A second MMOH expression vector was constructed in a similar fashion. pJLB400 (Figure 6.5C) contains all of the genes in the *mmo* operon, but lacks the T₂ transcription termination site located between *mmoZ* and *orfY* in the native *M. capsulatus* (Bath) DNA (Figure 6.1). The *mmoX*–*mmoZ* segment was PCR-amplified from pCH4 with the primers XFE10 and ZRK10 (5'-GAGCGAGACTGGTACCCTTCA-GTGCGGCGAC) using conditions identical to those for the *mmoX*–*mmoY* PCR reaction, resulting in a 3847-bp segment flanked by *EcoRI* and *KpnI* sites. The PCR product was digested with *EcoRI* and *KpnI* and inserted into pTrc99A exactly as described above to form pTX-Z (Figure 6.5A). Primers OFK10 (5'-CCGGTACCTTTCGTAAGGAAATCA-CCATGGTC) and RRH10 (5'-TCACAGTACTTAAGCTTTTCAGGCCCGCCCCGGAC) were used to PCR-amplify the *orfY*–*mmoC* region from pCH4, yielding a 1415-bp product flanked by *KpnI* and *HindIII* sites. PCR was performed with the following thermal cycler conditions: 45 s at 96 °C; 45 s at 96 °C, 45 s at 60 °C, and 3 min at 72 °C for 25 cycles, followed by extension for 10 min at 72 °C. As described for pTXYZ, the PCR product was digested with *KpnI* and *HindIII* in a two-step procedure and ligated into pTX-Z to yield pTX-C, as shown in Figure 6.5B. To create pJLB400, the *mmoX*–*mmoC* operon (no T₂ site) was cut from pTX-C and ligated into pMMB277.

Plasmid minipreps and restriction digest analysis identified three positive clones, which were named pJLB400(*Fn*), where $n = 3, 7,$ and 8 .

DNA Sequencing of the *mmo* Operon. Because the low-copy-number expression plasmid pJLB201 could not be purified adequately for DNA sequencing, the high-copy-number pJLB001 vector constructed in parallel with the series I expression vectors was used for sequencing the *mmoX*, *mmoY*, *mmoB*, and *mmoZ* genes. In addition, the *mmoB*, *mmoZ*, *orfY*, and *mmoC* genes of pCH4 were analyzed. Sequencing was performed by automated fluorescent DNA sequencing on an Applied Biosystems model 377 DNA Sequencer (MIT Biopolymers Laboratory). Most of the sequencing primers had been prepared previously in this laboratory.⁵⁶ The DNA sequence data were analyzed manually by comparison to previously recorded data (*mmoX*, *mmoY*, *mmoZ*)²⁸ and the published sequences (*mmoC*;²⁷ region between *mmoY* and *mmoB*, *mmoB*²⁶). All of the DNA sequencing was performed for both strands. A discrepancy between previously obtained data and the *mmoZ* sequence in pCH4 (vide supra) was resolved by reanalyzing DNA sequencing gels.²⁸ To ensure that the series II expression vectors contained the correct sMMO gene sequences, pTXY (*mmoX* and *mmoY*), pTXYZ (*mmoZ*), pTX-Z (*mmoX*, *mmoY*, *mmoB*, and *mmoZ*), and pTX-C (*orfY* and *mmoC*) were submitted for sequencing.

Protein Characterization. Denaturing polyacrylamide gel electrophoresis (PAGE) was performed with 4-20% acrylamide precast gels (Bio-Rad, Hercules, CA) or hand-cast 12% polyacrylamide gels (Bio-Rad) using a Tris/glycine, sodium dodecyl sulfate (SDS) buffer system. Electrophoresis samples were prepared by incubation for 5 min at 100 °C in denaturing buffer [62.5 mM Tris (pH 6.8), 10% (v/v) glycerol, 0.2% SDS, 5% (v/v) β -mercaptoethanol, and 0.025% bromophenol blue]. The molecular weight markers used as standards for SDS-PAGE (Bio-Rad) were (substance, kDa):

phosphorylase B, 97.4; serum albumin, 66.2; ovalbumin, 45.0; carbonic anhydrase, 31.0; trypsin inhibitor, 21.5; and lysozyme, 14.4.

A Tris/glycine buffer system and non-denaturing sample buffer [62.5 mM Tris (pH 6.8), 10% (v/v) glycerol, and 0.025% bromophenol blue] were employed for native PAGE analyses. In order to prevent protein denaturation, samples were incubated on ice prior to loading onto 4-20% acrylamide precast gels (Bio-Rad). Since all native PAGE gels were run for analysis by Western blotting, native MMOH was included as the standard.

For both SDS-PAGE and native PAGE gels, blotting onto nitrocellulose was performed with a Mini Trans-Blot Electrophoretic Transfer Cell (Bio-Rad). Polyclonal MMOH antibodies⁴¹ were used in combination with horseradish peroxidase (HRP)-linked goat anti-rabbit antibodies in the standard development of Western blots. The Immun-Blot HRP Assay Kit (Bio-Rad), in which HRP converts 4-chloro-1-naphthol to a purple solid, afforded detection of proteins binding MMOH antigens.

Indirect ELISA quantification of recombinant MMOH was performed according to standard protocols. Protein A-alkaline phosphatase conjugate was added to antigen-bound MMOH antibodies, and color development was achieved by incubation with *p*-nitrophenyl phosphate (Sigma, St. Louis, MO) for about 17 h. Absorbance values were determined with a Titertek Multiskan microtiter plate reader (Labsystems, Helsinki, Finland) configured with a 405 nm filter.

MMOH Expression in *E. coli* Hosts: Series I Plasmids. The series I plasmid constructs pJLB100, pJLB200, and pJLB201, were transformed into competent *E. coli* JM105 cells and electroporated into electrocompetent *E. coli* BL21(DE3) cells for expression tests. For initial expression of sMMO proteins from pJLB100, the *E. coli* JM105 expression host was grown to saturation in a 5-mL LB-Ap (100 μ g/mL) culture.

A 1-mL aliquot of this culture was used to inoculate 100 mL of LB supplemented with 100 $\mu\text{g}/\text{mL}$ of ampicillin. After incubation at 37 °C for 3.25 h with shaking (200 rpm), isopropyl β -D-galactopyranoside (IPTG, 0.4 mM) was added to induce expression of the MMO proteins. Beginning 20 min after induction, 1-mL samples were collected at ca. 60-minute intervals for the following 16 h. The bacteria were pelleted in 1.5-mL Eppendorf tubes by centrifugation for 5 min at 4 °C, frozen in liquid nitrogen, and stored at -80 °C until completion of the time course experiment. The cells collected at each time point were suspended in SDS loading buffer, boiled for 5 min, and analyzed by SDS-PAGE.

Expression from pJLB100, pJLB200, and pJLB201 in *E. coli* JM105 was performed in a similar manner. Since pJLB200 and pJLB201 contain a gene for chloramphenicol resistance rather than ampicillin resistance, media for these expression systems were supplemented with 10 $\mu\text{g}/\text{mL}$ of chloramphenicol. LB-antibiotic media (100 mL) were inoculated with 1 mL of saturated 5-mL cultures and incubated for 3 h at 37 °C with shaking. Immediately prior to induction, 200 μL of an iron solution (0.56 g of $\text{FeSO}_4 \cdot 7\text{H}_2\text{O}$ dissolved in 47.5 mL of deionized water acidified with 2.5 mL of 0.25 M H_2SO_4) was added to the growth medium. Expression was induced by adding IPTG (0.05 mM), and the temperature was reduced to 25 °C. Bacteria were collected after 10 min or 7 h and pelleted by centrifugation. The harvested cells from each 100-mL culture were suspended in 50 mL of 25 mM 3-(*N*-morpholino)propanesulfonic acid (MOPS; pH 7.0) containing 5 mM MgCl_2 , DNase (2 units/mL), and 1 mM Pefabloc SC (Boehringer Mannheim) and transferred to 50-mL glass beakers in an ice bath. The cell suspensions were sonicated at 40% maximum output (Branson Sonifier model 450 equipped with a 3/4-inch horn) with three two-minute pulses, which were separated by several minutes to prevent overheating. The lysed cells were centrifuged at 98,000g

for 30 min in order to separate the soluble and insoluble materials. The supernatants were transferred to 50-mL Falcon tubes and stored at 4 °C. To denature insoluble proteins, about 5 mL of 6 M urea in 10 mM MOPS (pH 7.0) was added to each extract pellet, and the tubes were rotated overnight at 4 °C. SDS-PAGE gels and Western blots using polyclonal antibodies for MMOH were performed by following standard protocols. In addition, the amounts of hydroxylase produced in both the soluble and insoluble fractions were quantitated by indirect ELISA.

Similar expression experiments were carried out with the protease-deficient *E. coli* BL21(DE3) strain. Several variables, including induction time, IPTG concentration, temperature, growth medium (LB and M9 media), and collection time, were altered in subsequent expressions in both JM105 and BL21(DE3) hosts. To examine the subunit assembly of the recombinant hydroxylase, native PAGE Western blots using MMOH antibodies were carried out according to standard protocols.

MMOH Expression in *E. coli* Hosts: Series II Plasmids. The following plasmids were transformed into competent *E. coli* JM105 and BL21(DE3) cells: pJLB300(E3), pJLB300(E6), pJLB400(F3), pJLB400(F7), and pMMB277. For initial expression of the recombinant proteins, the *E. coli* JM105 expression hosts containing pMMB277, pJLB300(E3), and pJLB400(F3) were grown to saturation in 4-mL LB-Cm (10 µg/mL) cultures. Aliquots (1 mL) of these cultures were used to inoculate 100-mL quantities of LB-Cm (10 µg/mL) medium, which were transferred to a 37 °C incubator set to rotate at 200 rpm. Protein expression was induced with 0.5 mM IPTG and 80 µM FeSO₄ (vide supra) at OD₆₀₀ ~0.6. Beginning 15 min after induction, 1-mL samples were collected at ca. 60-min intervals for the following 5 h. In addition, samples were collected immediately prior to starting induction. The bacteria were pelleted in 1.5-mL Eppendorf tubes by centrifugation for 5 min at 4 °C, frozen in liquid nitrogen, and

stored at $-80\text{ }^{\circ}\text{C}$ until completion of the time course experiment. The whole-cell time course samples were analyzed by SDS-PAGE.

Expression from pJLB400 in JM105 and BL21(DE3) Hosts. Expression from pJLB400(F3) and pJLB400(F7) in both *E. coli* JM105 and BL21(DE3) was performed under conditions more suitable for MMOH expression and assembly. LB-Cm (10 $\mu\text{g}/\text{mL}$) cultures (100 mL) were inoculated with 100- μL aliquots of saturated 4-mL cultures and incubated at $37\text{ }^{\circ}\text{C}$ with shaking. When the OD_{600} of the two BL21(DE3) cultures reached ~ 0.8 (3.5 h after inoculation), expression of sMMO proteins was induced by adding 0.05 mM IPTG, 80 μM FeSO_4 , and reducing the temperature to $25\text{ }^{\circ}\text{C}$. Induction was started in the two JM105 cultures in the same manner when the OD_{600} was ~ 0.7 (4.75 h after inoculation). The bacteria were collected 4 h (JM105 cultures) or 5.25 h (BL21(DE3) cultures) after starting induction and pelleted by centrifugation. The harvested cells from each 100-mL culture were suspended in 25-mL quantities of cracking buffer [25 mM MOPS (pH 7.0), 8 mM sodium thioglycolate (NaTG), 5 mM MgCl_2 , and 200 μM $\text{Fe}(\text{NH}_4)_2(\text{SO}_4)_2 \cdot 6\text{H}_2\text{O}$] containing DNase (1.5 units/mL) and 1 mM Pefabloc SC and transferred to 125-mL stainless steel beakers. The cell suspensions were sonicated at 40% maximum output (Branson Sonifier model 450 equipped with a 3/4-inch horn) with three 2-min pulses, which were separated by 5 min to prevent overheating. The lysed cells were centrifuged at $120,000g$ for 30 min in order to separate the soluble and insoluble materials. The supernatants were filtered through 0.2 μm membranes, drop-frozen in liquid nitrogen, and stored at $-80\text{ }^{\circ}\text{C}$. The pelleted material was washed with buffer and transferred to clean ultracentrifuge tubes. To each tube 15 mL of 6 M urea in 25 mM MOPS (pH 7.0) was added, and the tubes were rotated overnight at $4\text{ }^{\circ}\text{C}$. SDS-PAGE and native PAGE Western blots using polyclonal antibodies to MMOH were performed by following standard protocols.

Expression from JM105/pJLB300+pRED and JM105/pJLB400+pRED. In the initial time course study for JM105/pJLB400(F3), there appeared to be little to no MMOD or MMOR production, even at relatively high IPTG levels. To investigate whether MMOR is necessary for proper folding and/or assembly of MMOH, competent *E. coli* JM105 cells were transformed with the high-copy-number pRED-K2 (MMOR expression plasmid)¹⁷ and either pJLB300(E3) or pJLB400(F3) and plated on LB-Ap (75 $\mu\text{g}/\text{mL}$)-Cm (10 $\mu\text{g}/\text{mL}$) agar plates. Duplicate 100-mL LB-Ap-Cm cultures were inoculated with 100- μL aliquots of saturated JM105/pJLB300(E3)+pRED-K2 or JM105/pJLB400(F3)+pRED-K2 starter cultures. The expression cultures were supplemented with 100 μM Fe^{2+} added as 1.0 mL of 10 mM $\text{Fe}(\text{NH}_4)_2(\text{SO}_4)_2 \cdot 6\text{H}_2\text{O}$ in 100 mM sodium citrate (pH 7.0). When the OD_{660} was ~ 0.6 , sMMO protein expression was induced by adding 0.5 mM or 0.05 mM IPTG and 200 μL of the FeSO_4 solution described above (80 μM final $[\text{Fe}^{2+}]$ addition). The cultures induced with 0.5 mM IPTG were used for a time course study in which samples were collected at approximately 60-min intervals after induction as described above. SDS-PAGE gels were run to examine protein production over the 5-h time course. About 5 h after induction, cells in the low-IPTG cultures were collected by centrifugation and then frozen with liquid nitrogen. The JM105/pJLB300(E3)+pRED-K2 and JM105/pJLB400(F3)+ pRED-K2 cells were sonicated and ultracentrifuged exactly as described above to isolate the soluble cell extracts, which were drop-frozen in liquid nitrogen and stored at -80°C . Urea (6 M) was added to the pelleted materials to solubilize denatured proteins. After overnight rotation at 4°C , the samples were centrifuged to remove insoluble lipids and other solids. SDS-PAGE and native PAGE Western blots were performed according to standard protocols.

Expression from pJLB300 in JM105 and BL21(DE3) Hosts. Expression from pJLB300(E3) and pJLB300(E6) was performed in the *E. coli* strains JM105 and BL21(DE3). Cultures (100 mL) of LB-Cm (10 $\mu\text{g}/\text{mL}$) were inoculated with 100- μL aliquots of 4-mL saturated overnight cultures. The cells were grown at 37 °C with shaking at 200 rpm until the OD_{600} reached ~ 0.7 . At this time, MMOH production was induced by the addition of 0.05 mM IPTG and 80 μM FeSO_4 , and the temperature was reduced to 30 °C. The cells were collected by centrifugation 5 h after starting induction and suspended in cracking buffer [25 mM MOPS (pH 7.0), 8 mM NaTG, 2 mM cysteine, 5 mM MgCl_2 , and 200 μM $\text{Fe}(\text{NH}_4)_2(\text{SO}_4)_2 \cdot 6\text{H}_2\text{O}$] containing DNase (1.5 units/mL) and 1 mM Pefabloc SC. The soluble and insoluble components were isolated as described above. MMOH production in the expression cells was analyzed with SDS-PAGE and native PAGE Western blots.

Large-scale expressions of BL21(DE3)/pJLB300(E3) were performed to produce protein for purification trials. A 100-mL LB-Cm (10 $\mu\text{g}/\text{mL}$) culture was inoculated with 100 μL of a saturated 4-mL BL21(DE3)/pJLB300(E3) culture and incubated overnight at 37 °C. Six 1-L quantities of LB-Cm (10 $\mu\text{g}/\text{mL}$) were inoculated with 1-mL aliquots of the saturated starter culture and transferred to a 37 °C incubator set to rotate at 200 rpm. When the OD_{600} was ~ 0.7 , induction was started with 0.05 mM IPTG and 80 μM FeSO_4 . The temperature was reduced to 30 °C approximately 4 h later. About 7.5 h after starting induction, the cells were collected by centrifugation, frozen with liquid nitrogen, and stored at -80 °C. The cells were thawed and suspended in 100 mL of cracking buffer (described above), transferred to a large stainless steel beaker, and sonicated on ice with three 2-min pulses at 40% output (Branson Sonifier model 450 equipped with a 3/4-inch horn). The lysed cells were centrifuged for 40 min at 98,000g to separate the soluble cell extract, which was then filtered through 0.2 μm

membranes to remove any remaining particulate matter. A 12-L expression was performed in nearly the same manner, except that 5 min before induction the temperature was reduced to ca. 27 °C and the FeSO₄ solution was added. In addition, the cells were sonicated immediately after collection.

Purification of Recombinant MMOH from JM105/pJLB201. The pJLB201 expression vector was selected for further study, since it yielded more soluble MMOH than the other series I plasmids. In addition, proteolysis was not as significant a problem with this system. Four 500-mL cultures of JM105/pJLB201 were grown to saturation, then induced as described previously. The cells were harvested, frozen in liquid nitrogen, and stored at -80 °C. The frozen expression cells were suspended in 100 mL of cracking buffer and sonicated for a total of 6 min. After centrifugation at 98,000g for 45 min, the soluble cell-free extract was filtered through a 0.2 μm membrane. This solution was loaded onto a Q-Sepharose Fast Flow (Amersham Pharmacia) column (2.5 × 11 cm) equilibrated with 25 mM MOPS (pH 7.0) containing 50 mM NaCl. The column was washed with 150 mL of the equilibration buffer, and a 500-mL linear gradient from 50 to 300 mM NaCl was applied. Fractions were pooled and analyzed for MMOH by SDS-PAGE, native PAGE, and Western blotting techniques. Purification was also attempted with the more complex buffer [25 mM MOPS (pH 7.0), 5 mM MgCl₂, 2 mM cysteine, 8 mM NaTG, and 200 μM Fe(NH₄)₂(SO₄)₂·6H₂O] used for purifying native MMOH, a shallower elution gradient, and a shorter column (2.5 × 8 cm).

Purification of Recombinant MMOH from BL21(DE3)/pJLB300. In the small-scale BL21(DE3)/pJLB300 expression trials, a very small band of properly assembled MMOH was detected by native PAGE Western blotting. A partial purification was attempted for a 6-L expression of BL21(DE3)/pJLB300(E3). The cells were grown,

induced, collected, and sonicated as described above. The soluble cell extract was loaded onto a DEAE Sepharose CL-6B (Amersham Pharmacia) column (2.6 × 15 cm) equilibrated with buffer A [25 mM MOPS (pH 7.0), 8 mM NaTG, 2 mM cysteine, and 200 μM Fe(NH₄)₂(SO₄)₂·6H₂O], and the column was washed with 120 mL of buffer A to remove unbound proteins. A 740-mL linear gradient from 0 to 300 mM NaCl was run, followed by a 160-mL wash with buffer B [buffer A plus 300 mM NaCl]. Fraction samples were pooled into fourteen groups, labeled A-N. SDS-PAGE and native PAGE gels and Western blots were run to examine the elution pattern for the recombinant MMOH.

A 12-L expression of BL21(DE3)/pJLB300(E3) was employed to purify the recombinant MMOH further. The soluble cell extract was resolved on a CL-6B column as described. Fractions eluting at 135-180 mM NaCl were pooled based on the elution profile of assembled MMOH determined in the previous 6-L purification. The pool of MMOH-containing fractions was concentrated to about 5 mL by ultrafiltration over a YM100 membrane. The sample was passed through a 0.2 μm filter and loaded onto a Superdex 200 (Amersham Pharmacia) size-exclusion column (2.6 × 80 cm). A 750-mL wash with 25 mM MOPS (pH 7.0), 120 mM NaCl, 1 mM DTT, and 5% glycerol was performed with the fraction collector set to high sensitivity. The concentrator and superloop were washed thoroughly before using to avoid contamination by native MMOH. In addition, a new YM100 membrane was used for concentrating the crude recombinant MMOH (rMMOH) sample. Fraction pools were analyzed for assembled MMOH with SDS-PAGE and native PAGE gels and Western blots. As a control, the cell extract from a 12-L BL21(DE3)/pMMB277 growth was resolved by column chromatography in exactly the same manner. Gels and Western blots were run to

determine whether contamination from native MMOH was introduced during purification.

Assays for Recombinant MMOH Activity. Several assays for recombinant MMO hydroxylase activity were performed. Conversion of propylene to propylene oxide by the MMO system was monitored by gas chromatography (GC). To soluble cell-free extracts, the following reagents were added (final concentration): MMOR (0.2 μ M), NADH (1.0 mM), propylene (0.5 mM), and NaTG (8.0 mM). A Western blot for MMOB showed that it was present at a significantly higher concentration than MMOH,⁵⁷ so no additional MMOB was included in the assay mixture. The samples were incubated for 3 h at 25 °C in small glass vials. Chloroform extraction separated the nonpolar propylene and potential propylene oxide product from the reaction components, and 5.0- μ L aliquots of the organic layers were analyzed by using a Hewlett Packard Model 5890A gas chromatograph with a Porapak Q column.

Propylene activity assays were also carried out for partially purified rMMOH from a BL21(DE3)/pJLB300 expression (vide supra). Because the total amount of assembled MMOH was estimated to be only 10 μ g, the seven fractions containing MMOH were each concentrated to ca. 30 μ L in Centricon 30 concentration devices (Amicon, Beverly, MA). The fractions were combined to make a single 210- μ L sample, which was analyzed by a propylene steady-state kinetics assay and by product analysis. Assaying an unknown amount of MMOH for activity is inherently difficult, since activity varies dramatically with the relative concentrations of MMOH, MMOB, and MMOR.¹⁴ A total of 10 μ g of MMOH yields a concentration of 0.1 μ M in a 400- μ L volume, which was deemed enough to monitor NADH consumption in a propylene steady-state assay. The following reagents were added (final concentration) for 400- μ L standard samples: MMOH (100 nM), MMOB (100 nM), MMOR (100 nM), propylene

(0.8 mM), and buffer [25 mM MOPS (pH 7.0) and 1 mM DTT]. These components were added to a 1-mL masked cuvette and mixed thoroughly by inverting. NADH (0.16 mM) was added to initiate the reaction, and NADH consumption was monitored at 340 nm ($\epsilon_{340} = 6220 \text{ M}^{-1} \text{ cm}^{-1}$) over a period of 6 min with a Hewlett Packard Model 8452A diode array spectrophotometer. Blank samples were prepared in the same manner, except that MMOH was excluded from the reaction contents. To the 210- μL recombinant MMOH sample, MMOB (100 nM), propylene (0.8 mM), and buffer were added (initially no MMOR). NADH (0.16 mM) was introduced, and the reaction was monitored for 3 min. MMOR (100 nM) was added to initiate MMO activity; at three points during the 18-min reaction, supplemental NADH was added to assure availability for the MMO system. Each 400- μL sample was extracted with 80 μL of chloroform to remove the propylene and potential propylene oxide product and centrifuged for 5 min at 10,000g to separate the organic and aqueous layers. Identification of the propylene oxide product was performed by GC, as described above.

Nitrobenzene assays were used to identify column fractions containing active MMOH from a JM105/pJLB201 expression. Reaction mixtures (700 μL) containing 200 μL of sample and 1.0 μM MMOB, 0.2 μM MMOR, 1.0 mM nitrobenzene, and 2 mM NaTG in 25 mM MOPS (pH 7.7) were prepared. A 600- μL aliquot was transferred to a cuvette, NADH (1.0 mM) was added to initiate the reaction, and formation of *p*-nitrophenol ($\epsilon_{\text{max}} = 404 \text{ nm}$) was monitored.

A colorimetric assay to detect naphthalene oxidation^{58,59} was employed to examine MMO activity in colonies on agar plates, whole cells grown in liquid culture, and cell-free extracts. In addition, since copper has been reported to inhibit MMOR irreversibly,^{4,60} some expression cells were transferred to M9 minimal medium⁵⁴ before

induction. In brief, solid naphthalene was added to 1.0-mL samples, which were incubated at room temperature for ca. 45 min. A 100- μ L aliquot of 1% (w/v) Fast Blue BN dye (tetrazotized *o*-dianisidine; Sigma), which reacts with naphthol to form purple diazo dyes, was added to each sample. The dye products were stabilized by addition of glacial acetic acid (300 μ L) after 15 s.

Indole assays were also attempted, although initial studies showed that indole is at best a poor substrate for the *M. capsulatus* (Bath) sMMO enzyme system.⁶¹ Bacteria containing pJLB expression vectors were spread on LB-agar plates which contained Cm (10 μ g/mL), IPTG (20 μ g/mL), and indole (100 μ g/mL). The plates were incubated overnight at 37 °C.

Search for ORFs Surrounding the *mmo* Operon. In an effort to identify key components for proper folding and assembly of MMOH, open reading frames in the DNA region encompassing the *mmo* operon were located. Preliminary sequence data for the entire *M. capsulatus* (Bath) genome (4600 kb) was obtained from The Institute for Genomic Research (TIGR) website (<http://www.tigr.org>). At the time this analysis was performed (August 2002), the TIGR search program provided a maximum of 1000 nt on either side of a search sequence. Therefore, starting with the published sMMO genes,²⁶⁻²⁸ a bootstrapping method was employed to reconstruct the DNA surrounding the *mmo* operon. A 1340-nt sequence that disrupted the *mmo* operon was also repeated multiple times throughout the genome, presumably an artifact of the incomplete stage of the sequencing. These repeats were removed to yield a 27.4-kb contiguous sequence including 4.1 kb upstream and 18 kb downstream of the sMMO genes. Putative open reading frames (ORFs) were identified on both DNA strands by using the ORF Finder function on the National Center for Biotechnology Information (NCBI) website (<http://www.ncbi.nlm.nih.gov>). For each ORF, protein BLAST and conserved domain

searches were performed against all available non-redundant databases on the NCBI site. Those gene-translated proteins with significant homology to other proteins were accepted as possible *M. capsulatus* (Bath) proteins. In some cases, the start site for the gene was unclear. To help resolve these discrepancies, the DNA was also analyzed for bacterial promoter regions with the Neural Network Promoter Prediction tool available at the Berkeley Drosophila Genome Project website (http://www.fruitfly.org/seq_tools/promoter.html).

RESULTS

Corrections to the *M. capsulatus* (Bath) sMMO Gene Sequences. Six errors were identified in the published DNA sequences of the *M. capsulatus* (Bath) sMMO genes,^{26,27} including four in the hydroxylase genes. Each of the changes could be verified by at least one method. The first error is a two-base inversion in codon 84 of *mmoX*, **GTA** → **GAT**, where the former is from the published gene sequence and the latter from the present work. This inversion results in a change in the α -subunit protein sequence from Q⁷⁸FGSLQVALTR to Q⁷⁸FGSLQ**D**ALTR. A double frame shift in *mmoY* (CGG ACG AGT TCA TGC AAC → CGG **GAC GAG TTC ATC AAC**) yields a R¹⁴¹**TSSCN** → R¹⁴¹**DEFIN** change in the hydroxylase α subunit. This frame-shift sequencing error at the end of *mmoY* was observed previously by X-ray crystallography.⁶² Finally, the α subunit has two altered residues, I¹⁹**AHVNT** → I¹⁹**AQLNT**, resulting from a two-base inversion at codons 21 and 22 of *mmoZ* (**CAC GTC** → **CAG CTC**). Therefore, site-directed mutagenesis to correct the *mmoZ* “error” in pJLB001 actually introduced a base inversion (vide supra). The alterations in the α and β subunits were used in refinements of the crystallographically determined *M. capsulatus* (Bath) sMMO hydroxylase structure. Reanalysis of the hydroxylase crystal

structure solved to 1.7 Å resolution⁶³ revealed that the α -subunit residues Gln21 and Leu22 identified here better fit the electron density than the His and Val residues deduced from the published gene sequence.²⁶

N-terminal sequencing of MMOB isolated from *M. capsulatus* (Bath) indicated that residue 12 is Ile rather than Phe.²⁸ Subsequent sequencing of the cDNA showed a one-base error in codon 12 (TTC → ATC), which would produce the observed change in the protein sequence. Mass spectrometric investigations also support this sequence change.^{38,64} The remainder of the gene sequence is correct as published.²⁶ A two-base inversion in codon 254 of *mmoC* (CAC → ACC) corresponds to a change from V²⁵²NHEP to V²⁵²NTEP in the protein sequence.²⁷ A reductase mass of 38,545.6 Da was obtained by ESI-MS, which is consistent with the sequence change. With the N-terminal methionine intact and the H254T sequence correction, the expected mass is 38,542.6 Da, less than a 0.01% difference from the observed value and within the accuracy range of the mass spectrometer. On the other hand, the published sequence would yield a mass of 38,578.7 Da, a difference of 33 Da (0.09%), which is well outside the expected accuracy of the instrument. No discrepancies were found between the published DNA sequence for *orfY*²⁷ and the sequencing reported here.

Expression of sMMO Proteins in *E. coli*: Series I Vectors. Cultures of *E. coli* JM105/pJLB100 expressed proteins with molecular weights corresponding to those of the α , β , and γ subunits of MMOH, as well as MMOB and MMOR (Figure 6.6). In addition, a faint ~12-kDa band on the SDS-PAGE time-course gel may be MMOD. Maximal expression of the MMO proteins occurred 5-7 h after IPTG addition. Because they appeared in a time-dependent fashion, it is highly likely that these proteins were expressed from the MMO operon insert. A significant number of inclusion bodies were formed in cells containing the pJLB100 expression vector, as indicated by a distinct

color change from yellow to fairly white soon after induction began. Therefore, even the low-copy-number expression system produced misfolded or misassembled MMO proteins when induced with 0.4 mM IPTG.

Reducing the IPTG concentration to 0.05 mM decreased visible inclusion body formation dramatically. Since so little recombinant protein was produced in samples expressed with low IPTG levels, however, identification of the MMOH proteins on SDS-PAGE gels was not possible. Western blots using antibodies to MMOH showed that all three subunits of the hydroxylase were clearly present in both the soluble and insoluble, misfolded fractions in each of the three initial JM105/pJLBxxx expression systems, where xxx = 100, 200, or 201 (Figure 6.7). Lack of hydroxylase in control cultures containing the pMMB plasmids without the MMO operon inserts showed that the hydroxylase antibodies do not cross-react with native *E. coli* proteins. Proteolysis which yielded specific cleavage products appeared to be a significant problem in this experiment. Because the SDS-PAGE gels used for this and similar Western blots had a 4-20% polyacrylamide gradient, estimation of the molecular weight of the cleavage fragments based on gel mobility was imprecise, making fragment identification difficult.

Apart from antibiotic resistance, the major difference in the pJLB100, pJLB200, and pJLB201 vectors is the strength of their inducible promoters. Both pJLB100 and pJLB200 have the *taclac* (*tac-lac* UV5 in tandem) promoter, which reaches only ~5% of the expression level of the *tac* promoter contained in pJLB201.⁵⁵ Both Western blot and ELISA studies indicated that the JM105/pJLB201 system yielded somewhat greater quantities of soluble hydroxylase than the other two systems. ELISA analysis of both the soluble and urea-denatured expression proteins showed that the maximum concentration of MMOH in the soluble JM105/pJLB201 fraction was 0.2 μ M, which

corresponds to 1 mg per 100-mL culture. Expression from pJLB100 and pJLB200 yielded 35% and 54% as much total MMOH (both soluble and insoluble) and 30% and 59% as much soluble MMOH, respectively, as the less tightly controlled pJLB201 system. In comparison, a semi-quantitative Western blot indicated that the concentration of MMOB in the JM105/pJLB201 soluble fraction was $\sim 8 \mu\text{M}$, about 40 times greater than the MMOH concentration.⁵⁷

As shown in Figure 6.8A, the protease-deficient *E. coli* BL21(DE3) host yielded recombinant MMOH which was far less proteolyzed than that recovered from JM105 cells (Figure 6.7). A native PAGE Western blot of the same BL21(DE3) and JM105 expression samples (Figure 6.8B) showed that no significant portion of the recombinant hydroxylase was present in the native $\alpha_2\beta_2$ form, however, which suggests that factors other than proteolysis are involved in the misfolding or misassembly of the MMOH subunits. Variation of several growth conditions, including induction time, growth medium, and collection time, made little difference in the quality of soluble hydroxylase expressed by the *E. coli* host. Either lowering the temperature or IPTG concentration slowed the rate of expression, thereby decreasing the total amount of insoluble protein produced. These strategies, however, failed to yield a significant increase in the amount of soluble recombinant MMOH.

Purification of rMMOH from JM105/pJLB201. Proteins in the JM105/pJLB201 cell-free extract were resolved by anion exchange chromatography. Western blots of pooled fractions indicated that although the MMOH subunits were expressed, the entire $\alpha_2\beta_2$ holoenzyme did not elute at a single salt concentration (Figure 6.9). Instead, the α subunit eluted from the column throughout the entire 50-300 mM NaCl gradient, while much of the β subunit did not bind strongly to the column and eluted in the column flowthrough and wash fractions. That which remained bound eluted in

a rather non-specific manner over the entire first half of the ionic gradient. Only the α subunit displayed an elution profile similar to that of native MMOH, which elutes at 150 mM NaCl under similar chromatographic conditions. The results of this experiment were reproduced, and native PAGE Western blot analysis of the fractions gave further proof that no significant portion of rMMOH was present in the native form. Varying the column size and elution profile did not improve recombinant hydroxylase recovery.

Assays for rMMOH Activity: Series I Vectors. None of the assays detected recombinant hydroxylase activity for the series I expression systems. Since the propylene oxide GC assay is quite sensitive, it is unlikely that the lack of activity in cell-free extracts and whole-cell assays can be attributed to extremely low concentrations of hydroxylase. A distinct possibility is that MMOH, which is inhibited by MMOB at molar ratios greater than 2:1,¹⁴ was completely inactivated by the high levels of MMOB in the extract (> 40:1). Hydroxylase activity was unaffected by attempts to remove excess protein B by buffer exchange. In the nitrobenzene assays, some of the Q-Sepharose column fractions yielded an initial increase in A_{440} followed by a net decrease in the absorbance at this wavelength. Whereas it is possible that the nitrophenol product was degraded by other components of the *E. coli* extracts, subsequent studies indicated that nitrophenol consumption is negligible. Although reported to be a substrate for MMO,^{58,59} naphthalene was not converted to naphthol under any of the assay conditions or by the native sMMO proteins. It is probable that very little naphthalene dissolved in the aqueous buffer, thus preventing its oxidation by MMO. Detergent solubilization of naphthalene⁵⁹ was unsuccessful. Finally, none of the MMO expression colonies grown on LB-Cm-IPTG-indole agar plates converted indole to indigo.

Expression of sMMO Proteins in *E. coli*: Series II Vectors. Cultures of *E. coli* JM105/pJLB300(E3) and JM105/pJLB400(F3) induced with 0.5 mM IPTG produced large quantities of proteins with molecular weights corresponding to those of the α , β , and γ subunits of MMOH (Figure 6.10). In addition, MMOB was expressed in the JM105/pJLB400(F3) culture. Expression from pJLB400, which lacks the transcription terminator region between *mmoZ* and *orfY*, yielded little to no MMOR or MMOD, however. Therefore, another factor, possibly the unusual *mmoC* ribosome binding site (RBS), appears to prevent reductase synthesis in *E. coli*.

By coexpressing from the pJLBxxx and pRED-K2 plasmids, the requirement for MMOR in MMOH folding and/or assembly was investigated. SDS-PAGE analysis of time course samples for the JM105/pJLB300+pRED-K2 and JM105/pJLB400+pRED-K2 expressions (0.5 mM IPTG) revealed production of large quantities of MMOR and smaller amounts of the MMOH α and β subunits. Very small bands for the MMOH γ subunits could be identified in the pJLB400+pRED gel. No assembled hydroxylase was apparent in native PAGE Western blots, which suggests that a lack of MMOR is not the primary difficulty in assembling MMOH in non-native hosts.

As observed for the series I expression vectors, reducing the IPTG concentration to 0.05 mM significantly decreased inclusion body formation, so this inducer concentration was used for all subsequent expression experiments. Western blots demonstrated that all three hydroxylase subunits were present in both the soluble and insoluble fractions in both the JM105/pJLB400 and BL21(DE3)/pJLB400 expression systems. Proteolysis appeared to be a considerable problem, although the proteolytic patterns were different in the two *E. coli* hosts. Native PAGE Western blots demonstrated that no significant portion of the recombinant hydroxylase expressed from pJLB400 was present in the native $\alpha_2\beta_2\gamma$ form. SDS-PAGE Western blot analysis

of the JM105/pJLB300 and BL21(DE3)/pJLB300 samples revealed that all three MMOH subunits were present in both the soluble and insoluble fractions of each expression culture (Figure 6.11A). Very small $\alpha_2\beta_2\gamma$ bands were present in the BL21(DE3)/pJLB300 cell extracts, as determined by native PAGE Western blot analysis (Figure 6.11B).

Purification of rMMOH from BL21(DE3)/pJLB300. The soluble cell extract from a 6-L BL21(DE3)/pJLB300(E3) expression culture was resolved on a Sepharose CL-6B column by FPLC. The fractions were combined into 13 pools, which were labeled A-N. These pools were analyzed by SDS-PAGE and native PAGE gels and Western blots (Figure 6.12). The $\alpha_2\beta_2\gamma$ MMOH holoenzyme eluted from the column in pools G and H, which corresponded to a NaCl concentration of about 150 mM. Thus, the recombinant MMOH behaved much like native MMOH in this purification. The amount of assembled MMOH was quite small compared to the relatively large portion of misfolded or misassembled hydroxylase. In addition, the amount of gamma subunit in these fractions seemed rather low.

A second 12-L BL21(DE3)/pJLB300(E3) expression was performed to provide enough material for purification of the recombinant MMOH. The cells were expressed, collected, and resolved on a Sepharose CL-6B column in exactly the same manner described for the 6-L culture. Fractions that eluted between 135 and 180 mM NaCl were pooled without further analysis, concentrated, and resolved on a Superdex 200 column. The initial 26 5-mL fractions (elution volumes between 130 and 240 mL) were divided into 9 pools labeled A-I. The pooled samples were analyzed by SDS-PAGE and native PAGE gels and Western blots (Figure 6.13). From the native Western blot, it was apparent that the assembled MMOH eluted mainly in pools D, E, and F (170-200 mL). This elution profile matched that of native MMOH quite closely.

GC Assays for rMMOH Activity: Series II Vectors. Steady-state propylene assays were performed for two blanks (no MMOH), two standards, and the sample of recombinant MMOH purified from BL21(DE3)/pJLB300. The blanks and standards exhibited linear degradation of NADH with respect to time. For the rMMOH sample, however, NADH consumption was fast and non-linear, even before MMOR was added to initiate the propylene epoxidation reaction. Therefore, the recombinant sample contained other enzymes capable of oxidizing NADH. Three extra additions of NADH were made throughout the 18-min reaction time to ensure that NADH would be available for putative MMO activity. Spectra taken during the rMMOH assay showed the presence of a cytochrome ($\lambda_{\text{max}} = 420 \text{ nm}$), rapid consumption of NADH (decrease in A_{340}), and a general increase in the absorbance between 380 and 700 nm, which was not readily explicable. Each propylene assay was extracted with chloroform, and the organic layers were analyzed by GC (Figure 6.14). In the positive control reaction containing 100 nM MMOH, propylene and the MMO oxidation product, propylene oxide, eluted at 2.13 and 6.37 min, respectively. The blank (no MMOH) exhibited a propylene peak (2.27 min) but no propylene oxide peak. In the recombinant MMOH assay, peaks for both propylene (2.20 min) and propylene oxide (6.44 min) were observed. The small propylene peak in the rMMOH sample was probably due to longer sample handling rather than degradation since propylene was shown previously to be stable in *E. coli* cell extracts.

Mock Purification of rMMOH from BL21(DE3)/pMMB277. The possibility that the MMOH observed in the BL21(DE3)/pJLB300 Superdex fractions and responsible for sMMO activity was not derived from the recombinant expression culture but from contamination by native MMOH-containing materials was noted. In order to investigate this scenario, a mock purification was performed for a 12-L

BL21(DE3)/pMMB277 expression. The cells were expressed, collected, and resolved on DEAE Sepharose CL-6B and Superdex 200 columns exactly as described for the BL21(DE3)/pJLB300(E3) expression cells. The initial 26 fractions from the size-exclusion column were grouped into nine pools labeled A-I and examined by SDS-PAGE and native PAGE gels and Western blots. Unfortunately, a small amount of assembled MMOH was detected in pools D-G, presumably introduced during the purification.

Identification of Genes Flanking the *mmo* Operon of *M. capsulatus* (Bath).

Nine genes encoding proteins with conserved domain sequences were identified in the 18-kb region of *M. capsulatus* (Bath) DNA downstream of the *mmo* operon (Figure 6.15). In the 4.1-kb DNA segment immediately upstream of *mmoX*, no ORFs with conserved domains were found. The putative proteins include a GroEL-like chaperonin, two proteins of a two-component sensory transduction system, a transcriptional regulator (σ^{54} activator), the three subunits of formate dehydrogenase, a protein L-isoaspartate carboxymethyltransferase (PCMT), and an RNA 3'-terminal phosphate cyclase (RTC) (Table 6.2). For formate dehydrogenase, PCMT, and RTC, extremely high homology to other known proteins indicates an unambiguous function. The larger protein of the sensory transduction system (129 kDa) exhibits nine conserved domains, including histidine kinase-related sequences in the C-terminal region (residues 500-1160). The smaller component (67 kDa) has three domains related to signal transduction and regulation of cGMP turnover.

A BLAST search revealed that the *M. capsulatus* (Bath) chaperonin has high sequence homology to many prokaryotic GroEL and heat shock proteins. The most similar database entry is a GroEL homolog from *M. trichosporium* OB3b (encoded by *mmoG*; NCBI accession number X55394),⁶⁵ which exhibits 43% identity to the *M.*

capsulatus (Bath) protein (Figure 6.16). Unlike bacterial GroEL,⁶⁶ there is no cochaperone (GroES) gene near the *M. capsulatus* (Bath) *mmoG* gene. In fact, there is a more highly conserved GroEL gene elsewhere in the *M. capsulatus* (Bath) genome (79% identity, 5% dissimilarity to *E. coli* GroEL) with an associated GroES gene. By comparison, the *M. capsulatus* (Bath) GroEL homolog has just 37% identity (27% dissimilarity) to *E. coli* GroEL. Aligning the *M. capsulatus* (Bath) *mmoG* product, GroEL from *M. capsulatus* (Bath), and GroEL from *E. coli* K12 (NCBI accession number NC_000913) demonstrates clearly this difference in sequence homology (Figure 6.17).

DISCUSSION

Corrections to the *M. capsulatus* (Bath) sMMO gene sequences. All six changes in the sMMO gene sequences are consistent with independent crystallographic, mass spectrometric, and N-terminal sequencing experiments. The four alterations in the MMOH protein sequences increase the masses of the α , β , and γ subunits by 16, 126, and 5 Da, respectively. A study of the *M. capsulatus* (Bath) sMMO hydroxylase by ESI-MS revealed precisely these mass differences.⁶⁷ Based on the ESI-MS data obtained, the authors correctly deduced the actual sequences of the α and β subunits, although they could not distinguish between isoleucine and leucine in the R¹⁴¹TSSCN → R¹⁴¹DEFIN correction to the β subunit. Because of apparent misinterpretation of MS/MS sequencing of the β -subunit peptides (data not shown in the published MS work), however, they misidentified L82 as T82 and Q83 as R83 and failed to correct V84 to D84. Although these suggested sequence changes (Q⁷⁸FGSTRVALTR) yield the observed peptide mass, they cannot be explained by simple DNA sequencing errors. In contrast, the two-base inversion found in *mmoX* codon 84 in the present work, which results in a Q⁷⁸FGSLQVALTR →

Q⁷⁸FGSLQDALTR sequence change, produces the same 16-Da increase in mass with only a minor DNA sequence change. In addition, the “corrected” residues identified⁶⁷ do not fit the MMOH crystal structure electron density as well as the Q⁷⁸FGSLQDALTR sequence (Figure 6.18). Although MS is a useful tool, it is best used in conjunction with other complementary techniques in order to minimize errors.

MMOH Expression in Heterologous Hosts. Prior to this work, it was established that large quantities of misfolded, insoluble hydroxylase subunit proteins could be produced in *E. coli* hosts.⁴¹ This ample protein synthesis suggested that the failure to express active MMOH was a post-translational problem, perhaps a result of expressing too much protein too quickly or in inappropriate ratios. The expression vectors used in these previous experiments were all high-copy-number plasmids with strong promoters. Therefore, in an effort to regulate MMOH expression more stringently, the *M. capsulatus* (Bath) sMMO genes were cloned into low-copy-number vectors with more tightly controlled promoters. In addition, the entire *mmo* operon was included, a technique that has been successful for robust expression of similar monooxygenases in *E. coli*.⁴³⁻⁴⁶

By using this approach of limiting the rate of MMOH expression, the amounts of insoluble inclusion bodies were indeed dramatically reduced in the series I JM105/pJLBxxx and BL21(DE3)/pJLBxxx systems (xxx = 100, 200, or 201). For the first time, all three hydroxylase subunits were expressed, albeit at low levels, in the soluble fraction of *E. coli* hosts (Figure 6.7). Complex component interactions¹⁴ make measuring sMMO activity of unpurified material inherently difficult. Thus, the assembly of recombinant hydroxylase was assessed directly with native Western blots. For *E. coli* systems using the first series of expression plasmids, neither folded MMOH nor sMMO activity was detected.

A second generation of plasmids (pJLB300 and pJLB400) was prepared in an effort to address unequal expression levels of the sMMO components. Small quantities of hydroxylase with the native $\alpha_2\beta_2\gamma$ form were observed in protease-deficient BL21(DE3)/pJLB300 (*mmoX*–*mmoY*–*mmoZ* insert) but not JM105/pJLB300 cell extracts (Figure 6.11). This finding represents the first report of *E. coli* expressing MMOH with native assembly, although only a very small fraction of the total soluble hydroxylase was folded correctly. After a two-step purification procedure, sMMO activity was detected in the rMMOH sample. Unfortunately, MMOH was also noted in a control purification, demonstrating that contamination from native MMOH was unavoidable on equipment routinely used with relatively enormous quantities of native MMOH. The partially purified rMMOH may indeed have been active, but the possibility of native MMOH introduction during purification precludes any claim of recombinant hydroxylase activity. These sMMO hydroxylase expression systems, although perhaps slightly better than many previous attempts, suffer from the same intractable problems encountered repeatedly in *E. coli* hosts. Too little rMMOH is expressed in a soluble form and of that, only a tiny fraction is assembled properly. Moreover, purifying or assaying activity of such minute amounts of material is extremely challenging. Improving the yield of soluble, folded recombinant hydroxylase is vital for generating a convenient system for producing site-directed mutants of MMOH.

A recent report states that knocking out a *groEL* gene (*mmoG*) located upstream of *mmoX* in *M. trichosporium* OB3b abolished sMMO activity in the mutant.⁶⁸ Therefore, it appears that a special chaperonin is essential for proper folding and assembly of the sMMO proteins. That *M. capsulatus* (Bath) also has a *groEL*-like gene adjacent to its *mmo* operon, although on the 3' side (Figure 6.15), strengthens the notion that this protein is part of the sMMO system. Because MMOB, MMOR, and MMOD can be

expressed in soluble form in *E. coli*, they are likely unaffected by the absence of the GroEL homolog in the knockout strain. On the other hand, without *mmoG*, as is the case for nearly every previous heterologous expression system, the hydroxylase does not assemble properly to any great extent. In particular, *E. coli* does not seem to have a hospitable environment for MMOH folding and assembly. Despite exhaustive efforts to develop a recombinant *E. coli* system for active MMOH expression, this goal has not yet been achieved.^{36,41,42,51} Low levels of sMMO activity were measured in several heterologous hosts, including *Pseudomonas putida* F1,^{47,48} *Agrobacterium tumefaciens* A114,⁴⁸ and *Rhizobium meliloti* 102F34,⁴⁸ that had been complemented with the *M. trichosporium* OB3b *mmo* operon (*mmoX*–*mmoC*). These species may contain a more suitable, but not ideal, chaperone for MMOH assembly, which affords small quantities of active MMOH. Heterologous expression of *M. trichosporium* OB3b sMMO in two methanotrophs, *Methylobacterium album* BG8 and *Methylocystis parvus* OBBP, yielded low-level production of active sMMO, but difficulty isolating and maintaining these transconjugate strains was also reported.⁴⁹ Although the putative *mmoG* chaperonin may not be the only factor required for assembling MMOH, its absence likely contributed to the low or nonexistent activities noted for non-native hosts.

Homologous Expression of MMOH in *M. trichosporium* OB3b. The only published high-yield hydroxylase expression system employs a sMMO-minus mutant of *M. trichosporium* OB3b in which the *mmoX* gene was disrupted by marker-exchange mutagenesis.⁵¹ Complementing this strain with a plasmid carrying the *M. trichosporium* OB3b *mmo* operon and native promoter sequences yielded transconjugates that expressed sMMO at wild-type levels and activities.⁵⁰ In this homologous host, innate factors necessary for correct MMOH folding and assembly were apparently present. The decreased copper sensitivity of these systems was attributed to a higher

concentration of active regulator protein, presumably encoded by the expression plasmid, or a larger sMMO promoter copy number.⁵⁰ A recent report of the first MMOH site-directed mutants demonstrated the usefulness of this homologous expression system.³⁹ Of the four α subunit mutants prepared (C151E, C151Y, T213A, and T213S), only MMOH(T213S), which was expressed in good yield, could be purified. Low-level expression was noted for the remaining three mutants; upon cell lysis, sMMO activity observed in whole-cell assays (C151E and T213A) was abolished.

The homologous expression systems for recombinant *M. trichosporium* OB3b MMOH represent an important step toward probing the roles of individual hydroxylase residues in sMMO catalysis. As observed in the initial mutagenesis experiments, preparing strains for MMOH mutant expression is a time-consuming, low-efficiency process.³⁹ More importantly, a major limitation is the requirement for high-level sMMO activity for growth of the host on methane under copper-limited conditions. For the three MMOH mutant-expressing strains that grew poorly without added copper (0.4 μ M), instability or inactivity prevented in vitro characterization of the hydroxylase mutants.³⁹ Although whole-cell assays are of some utility, a more robust method for obtaining large quantities of purified MMOH mutants will be necessary for comprehensive mechanistic studies.

Future Directions. During the last decade, systems for producing recombinant sMMO hydroxylase have improved dramatically, but high-yield MMOH expression in a heterologous host remains elusive. Hosts such as *E. coli* or *Pseudomonas* would afford much simpler construction of mutants as well as eliminate the requirement for sMMO activity that hampers the current homologous expression systems. Although many different heterologous hosts have been investigated already,⁴⁷⁻⁴⁹ broad-host-range expression plasmids facilitate screening additional species. The fact that only low-level

sMMO expression was observed in heterologous methanotroph systems⁴⁹ suggests that MMOH may need a special environment for proper folding and assembly. An intriguing possibility is the inclusion of a GroEL homolog in the sMMO system.⁶⁸ Identifying and coexpressing the protein(s) associated with assembling MMOH in the native hosts may afford heterologous systems for ample production of recombinant hydroxylase.

ACKNOWLEDGMENT

This work was supported by National Institutes of Health Research Grant GM32134 (S.J.L.). J.L.B. was a Howard Hughes Medical Institute predoctoral fellow. We thank Dr. David E. Coufal, Dr. Elisabeth Cadieux, Dr. Maarten Merckx, and Dr. Hans Brandstetter for many helpful discussions, Dr. Athanasios Salifoglou and Dr. David E. Coufal for the gift of numerous sequencing primers, and Dr. Douglas A. Whittington for crystallographic analysis. Sequencing of the *M. capsulatus* (Bath) genome (TIGR and University of Bergen, Norway) was accomplished with support from the U.S. Department of Energy Microbial Genome Project.

REFERENCES

- (*) Portions of this work have been published in altered form in reference (28). David E. Coufal performed the initial DNA sequencing of the MMOH genes in pCH4 with a manual dideoxy chain termination method.
- (1) Higgins, I. J.; Best, D. J.; Hammond, R. C. *Nature* **1980**, *286*, 561-564.
 - (2) Nguyen, H.-H. T.; Elliott, S. J.; Yip, J. H.-K.; Chan, S. I. *J. Biol. Chem.* **1998**, *273*, 7957-7966.
 - (3) Lieberman, R. L.; Shrestha, D. B.; Doan, P. E.; Hoffman, B. M.; Stemmler, T. L.; Rosenzweig, A. C. *Proc. Nat. Acad. Sci. USA* **2003**, *100*, 3820-3825.
 - (4) Prior, S. D.; Dalton, H. J. *Gen. Microbiol.* **1985**, *131*, 155-163.
 - (5) Woodland, M. P.; Dalton, H. J. *Biol. Chem.* **1984**, *259*, 53-59.
 - (6) Feig, A. L.; Lippard, S. J. *Chem. Rev.* **1994**, *94*, 759-805.
 - (7) Liu, K. E.; Lippard, S. J. In *Adv. Inorg. Chem.*; Sykes, A. G., Ed.; Academic Press: San Diego, 1995; Vol. 42, pp 263-289.
 - (8) Wallar, B. J.; Lipscomb, J. D. *Chem. Rev.* **1996**, *96*, 2625-2657.
 - (9) Valentine, A. M.; Lippard, S. J. *Dalton Trans.* **1997**, *21*, 3925-3931.
 - (10) Solomon, E. I.; Brunold, T. C.; Davis, M. I.; Kemsley, J. N.; Lee, S.-K.; Lehnert, N.; Neese, F.; Skulan, A. J.; Yang, Y.-S.; Zhou, J. *Chem. Rev.* **2000**, *100*, 235-349.
 - (11) Merckx, M.; Kopp, D. A.; Sazinsky, M. H.; Blazyk, J. L.; Müller, J.; Lippard, S. J. *Angew. Chem. Int. Ed.* **2001**, *40*, 2782-2807.
 - (12) Colby, J.; Dalton, H. *Biochem. J.* **1978**, *171*, 461-468.
 - (13) Fox, B. G.; Froland, W. A.; Dege, J. E.; Lipscomb, J. D. *J. Biol. Chem.* **1989**, *264*, 10023-10033.
 - (14) Gassner, G. T.; Lippard, S. J. *Biochemistry* **1999**, *38*, 12768-12785.
 - (15) Lund, J.; Dalton, H. *Eur. J. Biochem.* **1985**, *147*, 291-296.

- (16) Lund, J.; Woodland, M. P.; Dalton, H. *Eur. J. Biochem.* **1985**, *147*, 297-305.
- (17) Kopp, D. A.; Gassner, G. T.; Blazyk, J. L.; Lippard, S. J. *Biochemistry* **2001**, *40*, 14932-14941.
- (18) Fox, B. G.; Liu, Y.; Dege, J. E.; Lipscomb, J. D. *J. Biol. Chem.* **1991**, *266*, 540-550.
- (19) Froland, W. A.; Andersson, K. K.; Lee, S.-K.; Liu, Y.; Lipscomb, J. D. *J. Biol. Chem.* **1992**, *267*, 17588-17597.
- (20) Fox, B. G.; Hendrich, M. P.; Surerus, K. K.; Andersson, K. K.; Froland, W. A.; Lipscomb, J. D.; Münck, E. *J. Am. Chem. Soc.* **1993**, *115*, 3688-3701.
- (21) Liu, K. E.; Valentine, A. M.; Wang, D.; Huynh, B. H.; Edmondson, D. E.; Salifoglou, A.; Lippard, S. J. *J. Am. Chem. Soc.* **1995**, *117*, 10175-10185.
- (22) Liu, K. E.; Lippard, S. J. *J. Biol. Chem.* **1991**, *266*, 12836-12839; 24859.
- (23) Paulsen, K. E.; Liu, Y.; Fox, B. G.; Lipscomb, J. D.; Münck, E.; Stankovich, M. T. *Biochemistry* **1994**, *33*, 713-722.
- (24) Liu, Y.; Nesheim, J. C.; Lee, S.-K.; Lipscomb, J. D. *J. Biol. Chem.* **1995**, *270*, 24662-24665.
- (25) Merckx, M.; Lippard, S. J. *J. Biol. Chem.* **2002**, *277*, 5858-5865.
- (26) Stainthorpe, A. C.; Murrell, J. C.; Salmond, G. P. C.; Dalton, H.; Lees, V. *Arch. Microbiol.* **1989**, *152*, 154-159.
- (27) Stainthorpe, A. C.; Lees, V.; Salmond, G. P. C.; Dalton, H.; Murrell, J. C. *Gene* **1990**, *91*, 27-34.
- (28) Coufal, D. E.; Blazyk, J. L.; Whittington, D. A.; Wu, W. W.; Rosenzweig, A. C.; Lippard, S. J. *Eur. J. Biochem.* **2000**, *267*, 2174-2185.
- (29) Cardy, D. L. N.; Laidler, V.; Salmond, G. P. C.; Murrell, J. C. *Mol. Microbiol.* **1991**, *5*, 335-342.

- (30) Cardy, D. L. N.; Laidler, V.; Salmond, G. P. C.; Murrell, J. C. *Arch. Microbiol.* **1991**, *156*, 477-483.
- (31) McDonald, I. R.; Uchiyama, H.; Kambe, S.; Yagi, O.; Murrell, J. C. *Appl. Environ. Microbiol.* **1997**, *63*, 1898-1904.
- (32) Grosse, S.; Laramée, L.; Wendlandt, K.-D.; McDonald, I. R.; Miguez, C. B.; Kleber, H.-P. *Appl. Environ. Microbiol.* **1999**, *65*, 3929-3935.
- (33) Shigematsu, T.; Hanada, S.; Eguchi, M.; Kamagata, Y.; Kanagawa, T.; Kurane, R. *Appl. Environ. Microbiol.* **1999**, *65*, 5198-5206.
- (34) Nielsen, A. K.; Gerdes, K.; Degn, H.; Murrell, J. C. *Microbiology* **1996**, *142*, 1289-1296.
- (35) Nielsen, A. K.; Gerdes, K.; Murrell, J. C. *Mol. Microbiol.* **1997**, *25*, 399-409.
- (36) West, C. A.; Salmond, G. P. C.; Dalton, H.; Murrell, J. C. *J. Gen. Microbiol.* **1992**, *138*, 1301-1307.
- (37) Chang, S.-L.; Wallar, B. J.; Lipscomb, J. D.; Mayo, K. H. *Biochemistry* **1999**, *38*, 3799-3812.
- (38) Brandstetter, H.; Whittington, D. A.; Lippard, S. J.; Frederick, C. A. *Chem. & Biol.* **1999**, *6*, 441-449.
- (39) Smith, T. J.; Slade, S. E.; Burton, N. P.; Murrell, J. C.; Dalton, H. *Appl. Environ. Microbiol.* **2002**, *68*, 5265-5273.
- (40) Murrell, J. C.; Gilbert, B.; McDonald, I. R. *Arch. Microbiol.* **2000**, *173*, 325-332.
- (41) Coufal, D. E. Ph.D. Thesis, Massachusetts Institute of Technology: Cambridge, MA, 1998.
- (42) Merckx, M.; Cadieux, E.; Lippard, S. J., unpublished results.
- (43) Pikus, J. D.; Studts, J. M.; Achim, C.; Kauffmann, K. E.; Münck, E.; Steffan, R. J.; McClay, K.; Fox, B. G. *Biochemistry* **1996**, *35*, 9106-9119.

- (44) Pikus, J. D.; Studts, J. M.; McClay, K.; Steffan, R. J.; Fox, B. G. *Biochemistry* **1997**, *36*, 9283-9289.
- (45) Ryoo, D.; Shim, H.; Canada, K.; Barbieri, P.; Wood, T. K. *Nat. Biotechnol.* **2000**, *18*, 775-778.
- (46) Powlowski, J.; Sealy, J.; Shingler, V.; Cadieux, E. J. *Biol. Chem.* **1997**, *272*, 945-951.
- (47) Jahng, D.; Wood, T. K. *Appl. Environ. Microbiol.* **1994**, *60*, 2473-2482.
- (48) Jahng, D.; Kim, C. S.; Hanson, R. S.; Wood, T. K. *Biotechnol. Bioeng.* **1996**, *51*, 349-359.
- (49) Lloyd, J. S.; De Marco, P.; Dalton, H.; Murrell, J. C. *Arch. Microbiol.* **1999**, *171*, 364-370.
- (50) Lloyd, J. S.; Finch, R.; Dalton, H.; Murrell, J. C. *Microbiology* **1999**, *145*, 461-470.
- (51) Murrell, J. C. *Biodegradation* **1994**, *5*, 145-159.
- (52) Massey, V. J. *Biol. Chem.* **1957**, *229*, 763-770.
- (53) Stookey, L. L. *Anal. Chem.* **1970**, *42*, 779-781.
- (54) Sambrook, J.; Fritsch, E. F.; Maniatis, T. *Molecular Cloning: A Laboratory Manual*; 2nd ed.; Cold Spring Harbor Laboratory Press: Cold Spring Harbor, NY, 1989.
- (55) Morales, V. M.; Bäckman, A.; Bagdasarian, M. *Gene* **1991**, *97*, 39-47.
- (56) Salifoglou, A.; Coufal, D. E.; Lippard, S. J., unpublished results.
- (57) Whittington, D. A.; Lippard, S. J., unpublished results.
- (58) Brusseau, G. A.; Tsien, H.-C.; Hanson, R. S.; Wackett, L. P. *Biodegradation* **1990**, *1*, 19-29.
- (59) Phelps, P. A.; Agarwal, S. K.; Speitel, G. E., Jr.; Georgiou, G. *Appl. Environ. Microbiol.* **1992**, *58*, 3701-3708.
- (60) Green, J.; Prior, S. D.; Dalton, H. *Eur. J. Biochem.* **1985**, *153*, 137-144.
- (61) Gassner, G. T.; Lippard, S. J., unpublished results.

- (62) Rosenzweig, A. C.; Frederick, C. A.; Lippard, S. J.; Nordlund, P. *Nature* **1993**, *366*, 537-543.
- (63) Rosenzweig, A. C.; Nordlund, P.; Takahara, P. M.; Frederick, C. A.; Lippard, S. J. *Chem. & Biol.* **1995**, *2*, 409-418.
- (64) Lloyd, J. S.; Bhambra, A.; Murrell, J. C.; Dalton, H. *Eur. J. Biochem.* **1997**, *248*, 72-79.
- (65) Stafford, G. P.; Scanlan, J.; McDonald, I. R.; Murrell, J. C. *Microbiology* **2003**, *149*, 1771-1784.
- (66) Sigler, P. B.; Xu, Z.; Rye, H. S.; Burston, S. G.; Fenton, W. A.; Horwich, A. L. *Annu. Rev. Biochem.* **1998**, *67*, 581-608.
- (67) Buzy, A.; Millar, A. L.; Legros, V.; Wilkins, P. C.; Dalton, H.; Jennings, K. R. *Eur. J. Biochem.* **1998**, *254*, 602-609.
- (68) Murrell, J. C. *Microbiology* **2002**, *148*, 3329-3330.

Table 6.1: Descriptions of Plasmids Used for Constructing sMMO Expression Vectors

Plasmid	Characteristics ^a
pMMB190	IncQ <i>lacI</i> ^q <i>bla</i> (Ap ^R) <i>Ptaclac lacZ</i> \square <i>rrnB</i>
pMMB206	pMMB190 \square <i>bla</i> \square <i>cat</i> from pUC8CM
pMMB207	pMMB206 \square (<i>Ptaclac</i> , polylinker, and <i>lacZ</i> \square) \square (<i>Ptac</i> and polylinker from pMMB66EH)
pMMB277	pMMB206 \square <i>Plac</i> UV5
pCR2.1	Ap ^R , Km ^R , multi-copy insertion vector for PCR products (Invitrogen)
pTrc99A	Ap ^R , <i>lacI</i> ^q / <i>Ptrc</i> -based multi-copy expression plasmid, MCS (Amersham Pharmacia)
pKK223-3	Ap ^R , <i>lacI</i> ^q / <i>Ptac</i> -based multi-copy expression plasmid, MCS (Amersham Pharmacia)
pJLB001	pCR2.1 \square <i>mmo</i> operon PCR product
pJLB001-C	pJLB001, base inversion in <i>mmoZ</i> “corrected” by SDM
pJLB100	pMMB190 \square <i>mmo</i> operon PCR product
pJLB200	pMMB206 \square <i>mmo</i> operon from pJLB100
pJLB201	pMMB277 \square <i>mmo</i> operon from pJLB100
pJLB201-C	pMMB277 \square <i>mmo</i> operon from pJLB001-C
pJLB207	pMMB207 \square <i>mmo</i> operon from pJLB001-C; no <i>lacZ</i> \square
pJLB300	pMMB277 \square (<i>mmoX</i> , <i>mmoY</i> , <i>mmoZ</i> from pTXYZ)
pJLB400	pMMB277 \square <i>mmo</i> operon from pTX-C; no T ₂ transcription termination site
pTXY	pTrc99A \square <i>mmoX</i> – <i>mmoY</i> PCR product
pTXYZ	pTXY \square <i>mmoZ</i> PCR product
pTX-Z	pTrc99A \square <i>mmoX</i> – <i>mmoZ</i> PCR product
pTX-C	pTX-Z \square <i>orfY</i> – <i>mmoC</i> PCR product
pRED	pKK223-3 \square <i>mmoC</i> PCR product

^a Abbreviations: Ap, ampicillin; *bla*, gene encoding \square -lactamase; *cat*, gene encoding Cm acetyltransferase; Cm, chloramphenicol; \square , deletion; *lacZ* \square , sequence coding for the \square -peptide of \square -galactosidase; Km, kanamycin; MCS, multiple cloning site (polylinker); \square , insertion; PCR, polymerase chain reaction; *Plac* UV5, promoter; *Ptac*, *trp-lac* hybrid promoter; *Ptaclac*, *Ptac* and *Plac* UV5 in tandem; ^R, resistance; SDM, site-directed mutagenesis.

Table 6.2: Open Reading Frames Located Near the *M. capsulatus* (Bath) *mmo* Operon

Gene	Length (nt)	Strand ^a	MW (kDa)	Putative function/homology
<i>mmoG</i>	1680	+	59.5	chaperonin with homology to GroEL/Hsp60
<i>regB</i>	1836	-	67.4	response regulator (sensory transduction system)
<i>regA</i>	3534	-	128.6	response regulator/hybrid sensory histidine kinase
<i>mmoR</i>	1746	+	63.4	transcriptional regulator, σ^{54} -dependent activator
<i>fdoI</i>	636	-	24.3	formate dehydrogenase, α subunit
<i>fdoH</i>	873	-	31.6	formate dehydrogenase, β subunit
<i>fdoG</i>	3201	-	118.7	formate dehydrogenase, γ subunit
<i>pcm</i>	678	+	24.5	protein-L-isoaspartate carboxymethyltransferase
<i>rtcA</i>	1086	+	37.8	RNA 3'-terminal phosphate cyclase

^a DNA strand containing *mmo* genes defined as + strand.

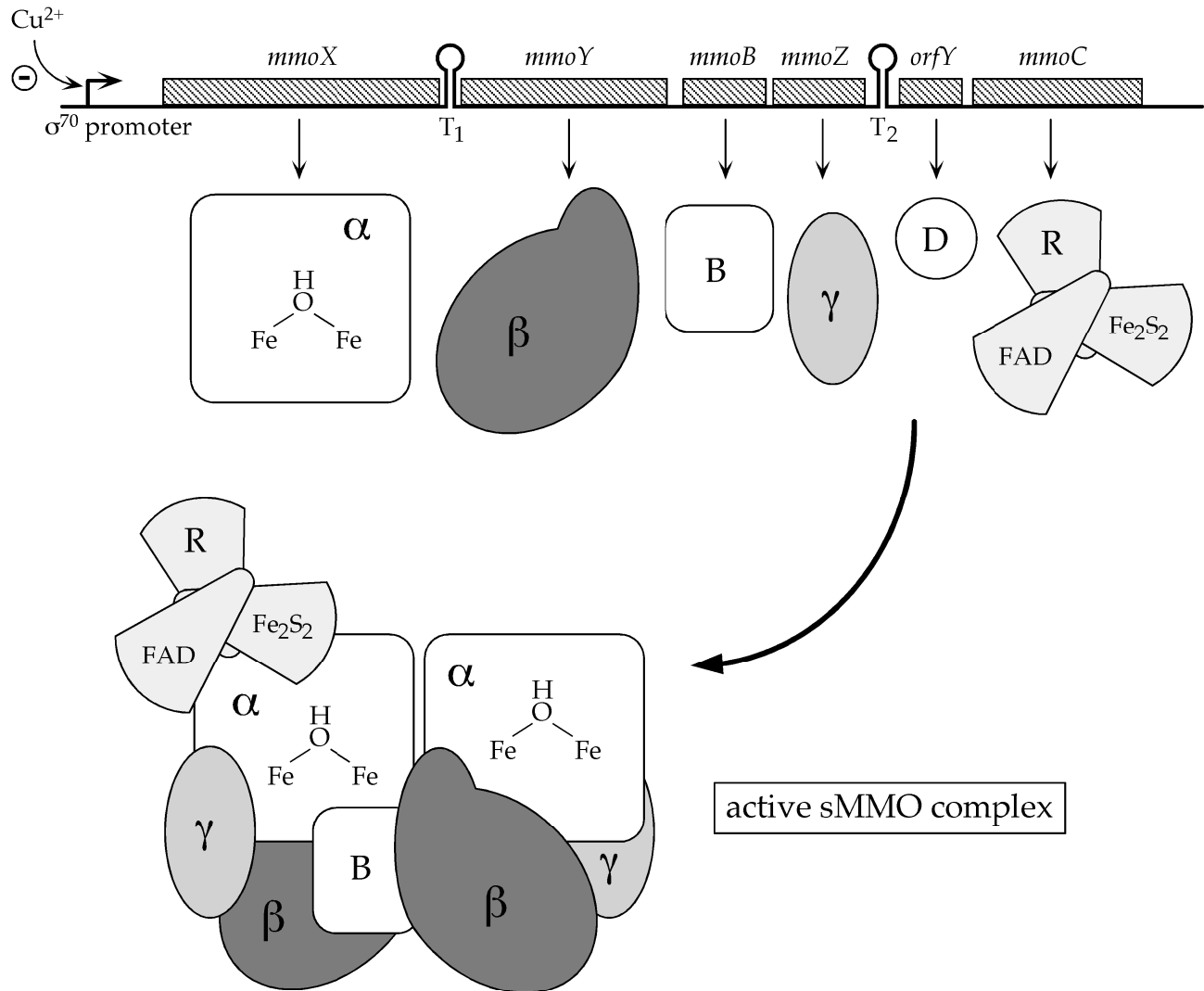


Figure 6.1. Schematic of the *mmo* operon of *M. capsulatus* (Bath). The six ORFs are clustered on a 5.5-kb section of DNA under the control of a single σ^{70} -dependent copper-controlled promoter located upstream of *mmoX*. The two σ -independent transcription termination sites are labeled T_1 and T_2 .

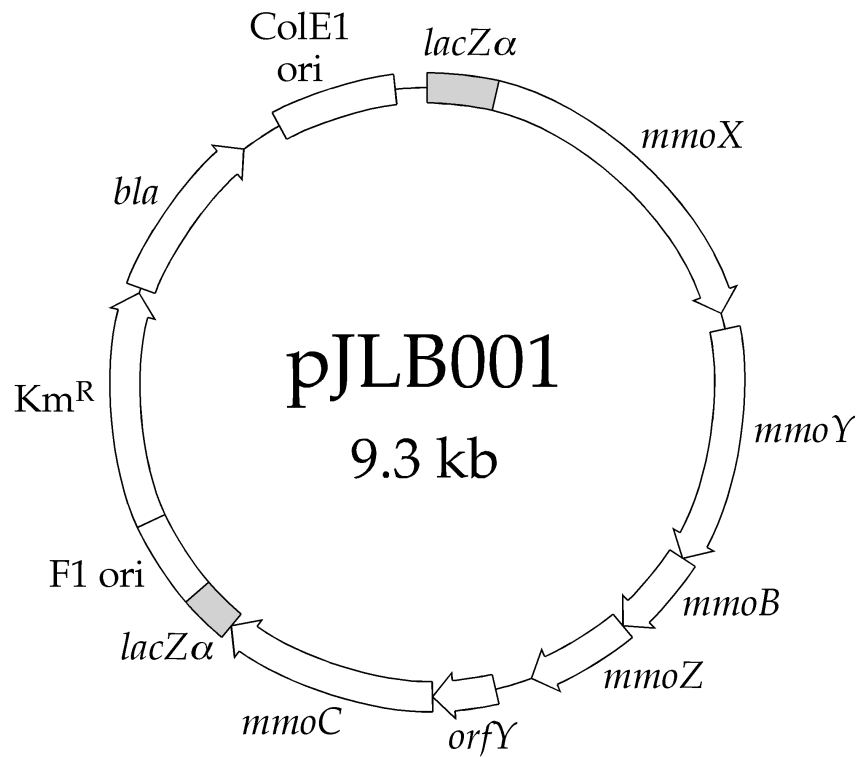


Figure 6.2. Plasmid map for the pJLB001 sequencing plasmid, which was constructed by ligating the *mmo* operon PCR product directly into the pCR2.1 vector.

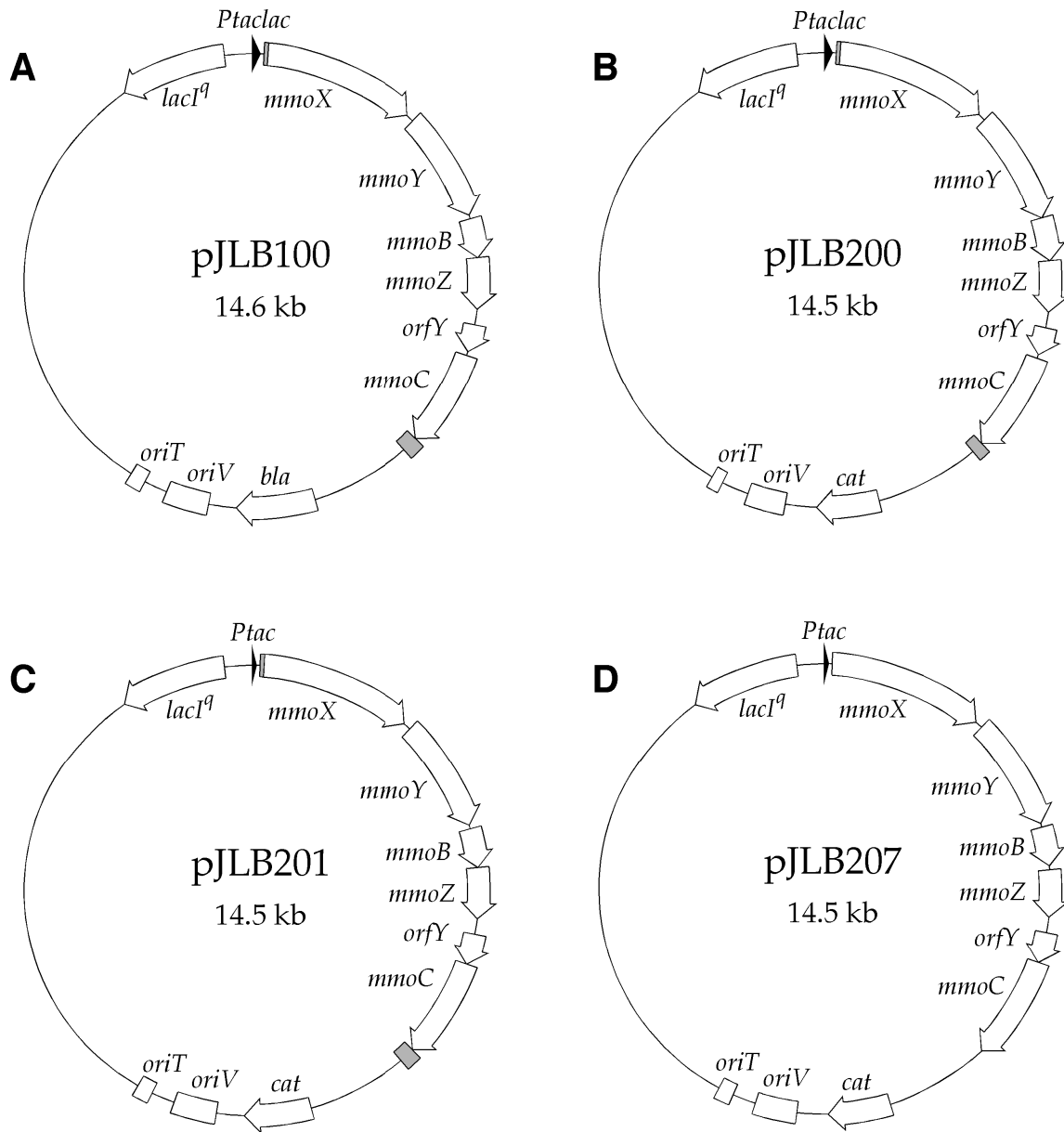


Figure 6.3. Series I expression vectors. Plasmid maps for (A) pJLB100 (*taclac* promoter, Ap^R), (B) pJLB200 (*taclac* promoter, Cm^R), (C) pJLB201 (*tac* promoter, Cm^R), and (D) pJLB207 (*tac* promoter, Cm^R, no *lacZ* gene; two-base inversion in *mmoZ* introduced by site-directed mutagenesis). The disrupted *lacZ* gene in pJLB100, pJLB200, and pJLB201 is shaded gray. Abbreviations: *bla*, gene encoding β -lactamase; *cat*, gene encoding Cm acetyltransferase; Ap^R, ampicillin resistance; Cm^R, chloramphenicol resistance.

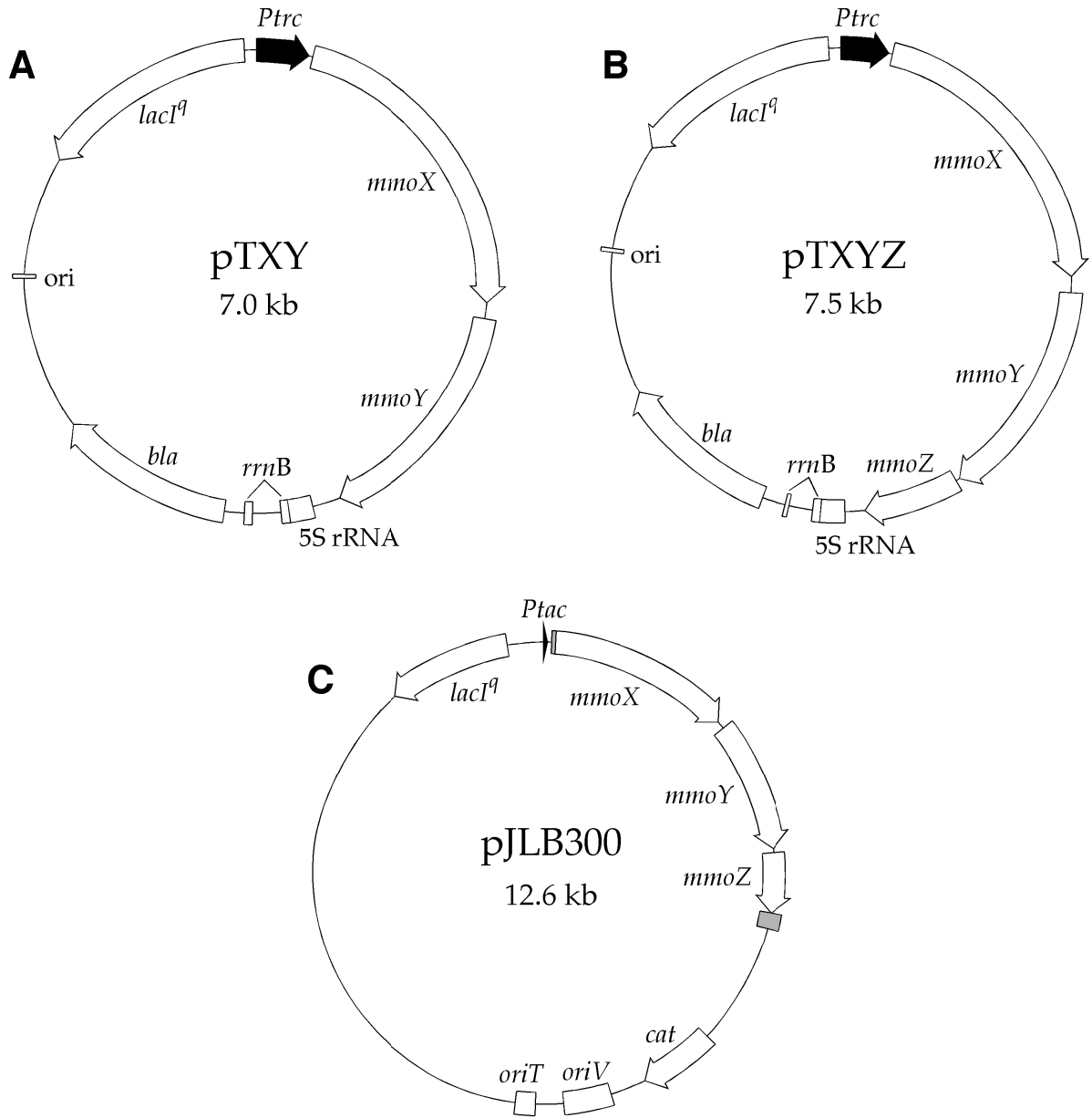


Figure 6.4. Construction of pJLB300. The *M. capsulatus* (Bath) *mmoX*–*mmoY* genes were ligated into pTrc99A to produce pTXY (A). Insertion of *mmoZ* into pTXY yielded pTXYZ (B). To make pJLB300 (C), the *mmoX*–*mmoY*–*mmoZ* fragment of pTXYZ was transferred into the MCS of pMMB277. Abbreviations: *bla*, gene encoding β -lactamase; *cat*, gene encoding chloramphenicol acetyltransferase.

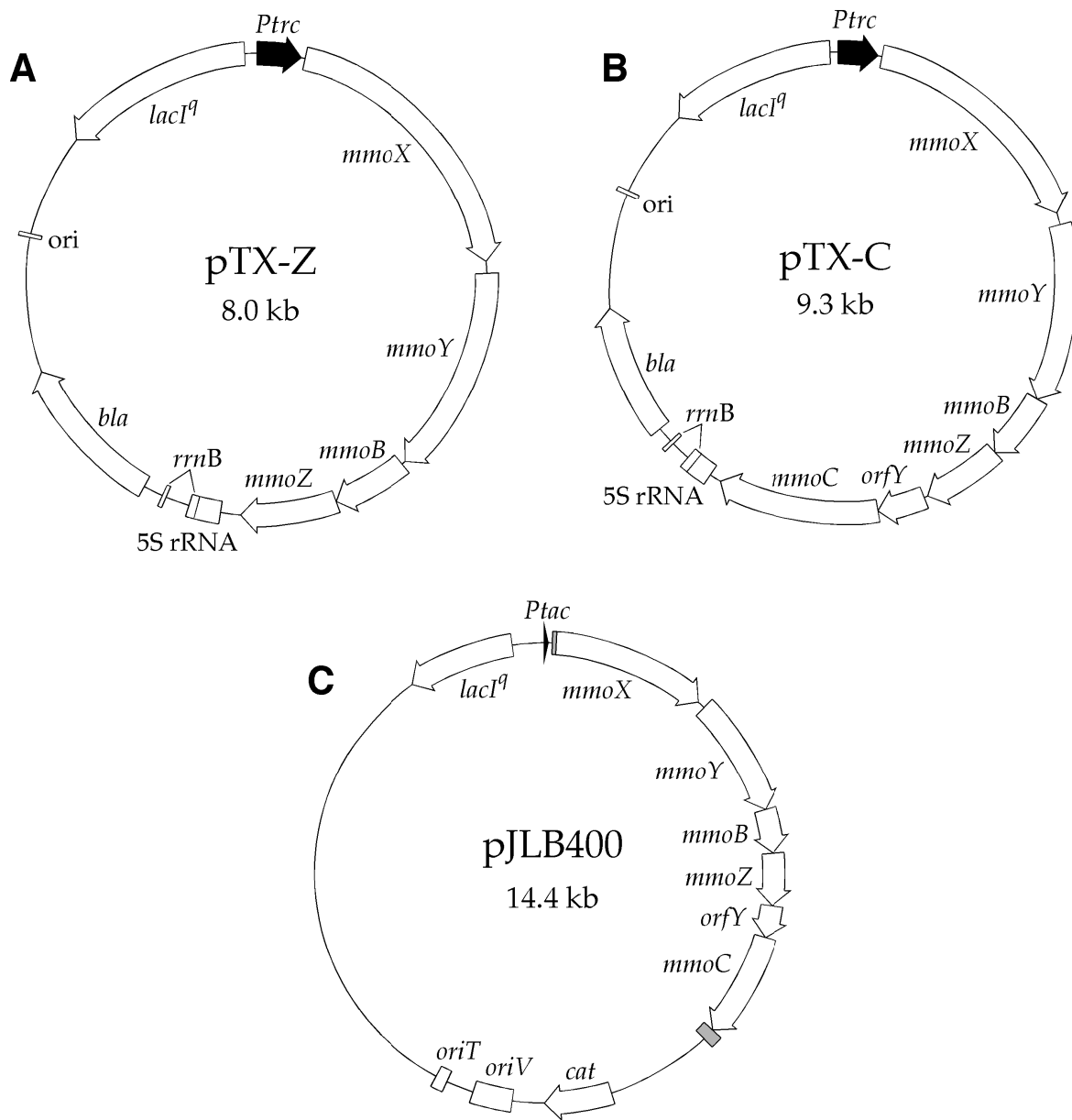


Figure 6.5. Construction of pJLB400. The *M. capsulatus* (Bath) *mmoX*–*mmoZ* genes were ligated into pTrc99A to produce pTX-Z (A). Insertion of the *orfY*–*mmoC* fragment into pTX-Z yielded pTX-C (B). To make pJLB400 (C), the *mmoX*–*mmoC* operon of pTX-C was transferred into the MCS of pMMB277. Abbreviations: *bla*, gene encoding β -lactamase; *cat*, gene encoding chloramphenicol acetyltransferase.

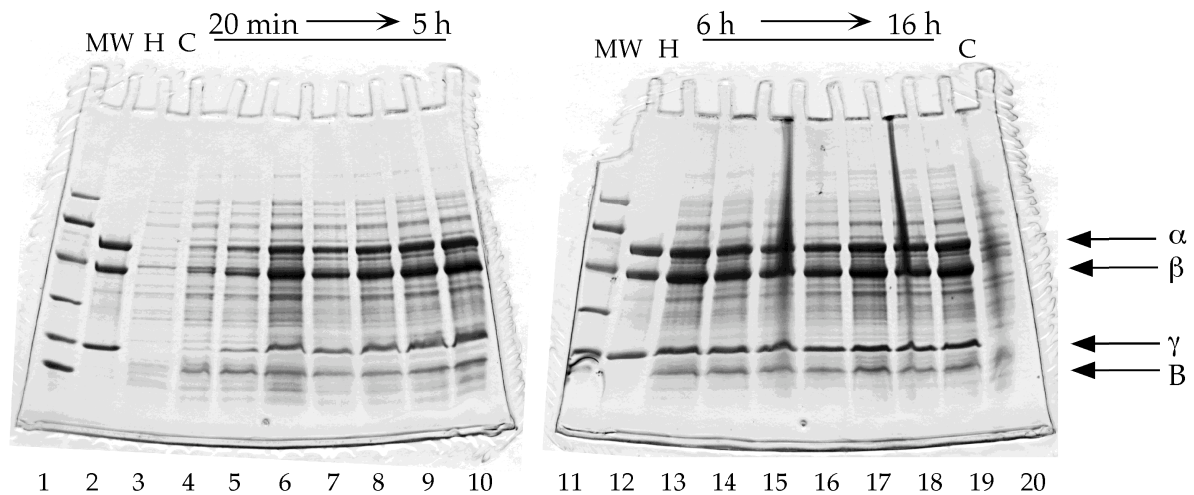


Figure 6.6. Denaturing polyacrylamide gel electrophoretic analysis of proteins produced by the JM105/pJLB100 system. Lanes 1 and 11, molecular weight standards; lanes 2 and 12, MMOH from *M. capsulatus* (Bath); lane 3, control pMMB190 system without *mmo* operon insert, 20 min after induction; lanes 4-10, time points collected 20 min to 5 h after induction with 0.4 mM IPTG; lanes 13-19, continued time points collected 6 to 16 h after induction; lane 20, control pMMB190 system 16 h after induction. The protein molecular weight markers (Bio-Rad) used for SDS-PAGE were (protein, kDa): phosphorylase B, 97.4; serum albumin, 66.2; ovalbumin, 45.0; carbonic anhydrase, 31.0; trypsin inhibitor, 21.5; and lysozyme, 14.4.

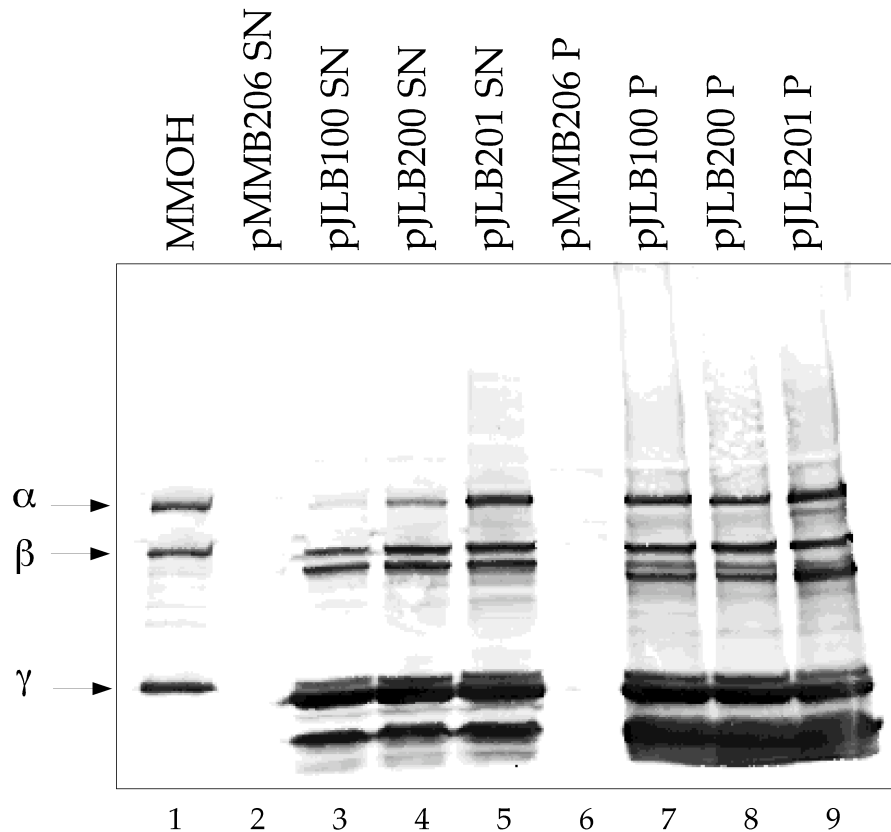


Figure 6.7. Western blot analysis of MMO hydroxylase produced by three series I expression plasmids. Lane 1, MMOH from *M. capsulatus* (Bath); lanes 2-5, soluble protein isolated from *E. coli* JM105 cells containing pMMB206, pJLB100, pJLB200, and pJLB201, respectively. Lanes 6-9, denatured insoluble protein expressed from plasmids pMMB206, pJLB100, pJLB200, and pJLB201, respectively. MMOH expression was induced with 0.05 mM IPTG, and cells were collected 5 h after induction.

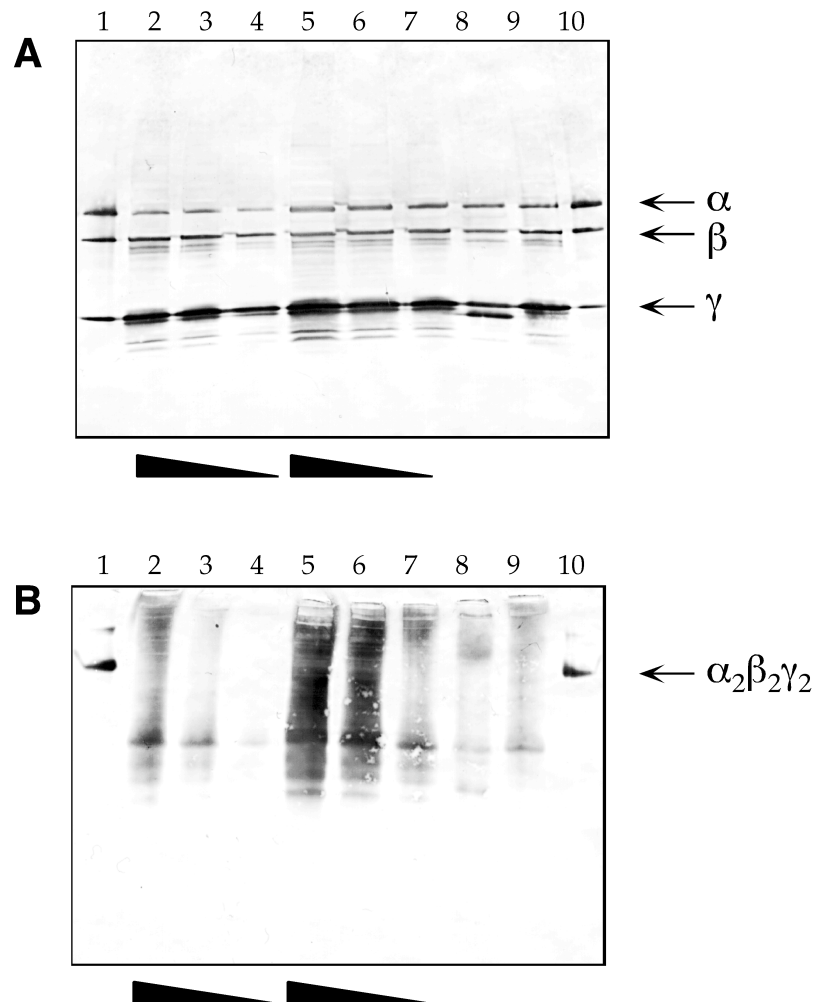


Figure 6.8. SDS-PAGE (A) and native PAGE (B) Western blot analyses of MMOH expressed from pJLB201 with 0.05 mM IPTG in either *E. coli* BL21(DE3) or JM105 cells. Lanes 1 and 10, MMOH from *M. capsulatus* (Bath); lanes 2-4, decreasing amounts of soluble protein from BL21(DE3)/pJLB201 expression cells, collected 3 h after induction; lanes 5-7, decreasing amounts of soluble protein isolated from BL21(DE3)/pJLB201 expression cells, collected 8 h after induction; lane 8, soluble protein from JM105/pJLB201 cells induced for 5 h; lane 9, soluble protein from BL21(DE3)/pJLB201 cells induced for 5 h.

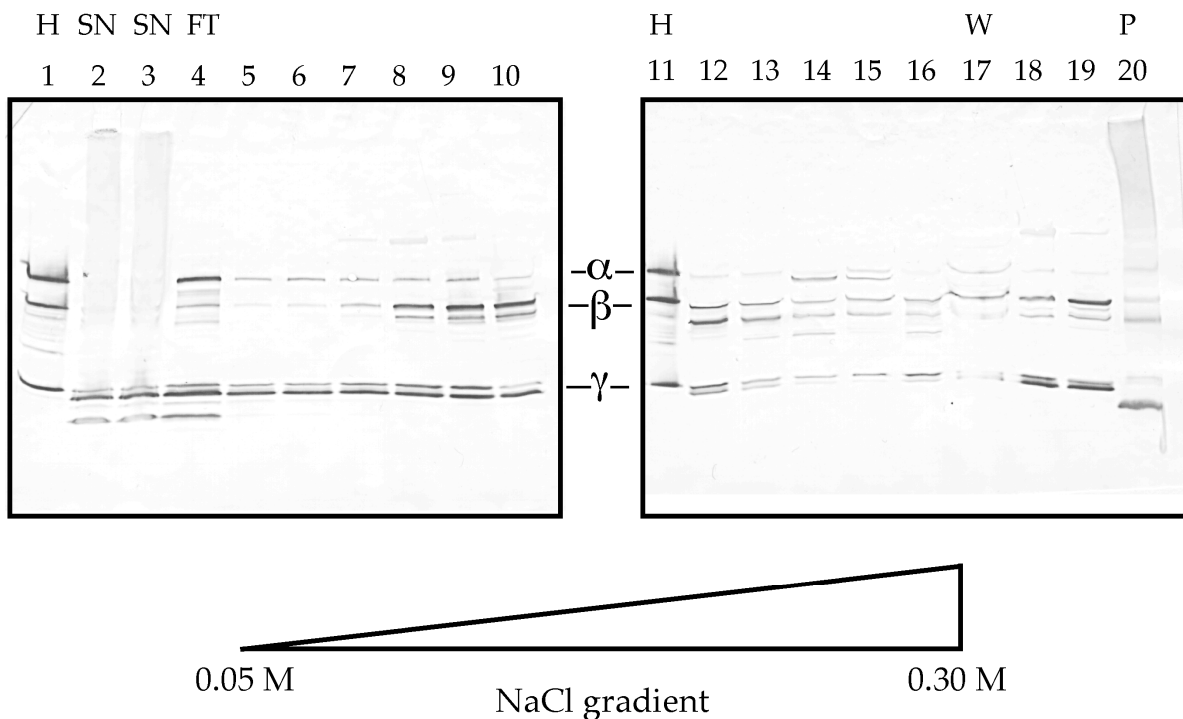


Figure 6.9. Western blot analysis of MMO hydroxylase in fractions of soluble protein expressed by *E. coli* JM105/pJLB201 resolved on a Q-Sepharose Fast Flow column. Lanes 1 and 11, MMOH from *M. capsulatus* (Bath); lanes 2 and 3, unfiltered and filtered samples, respectively, before column separation; lane 4, flowthrough and wash fractions; lanes 5-16, fraction pools for NaCl gradient (0.05 to 0.30 M); lane 17, final column wash (2 M NaCl); lanes 18 and 19, fraction pools for the 115-150 mM NaCl region where native MMOH elutes under similar conditions; lane 20, insoluble proteins denatured in urea.

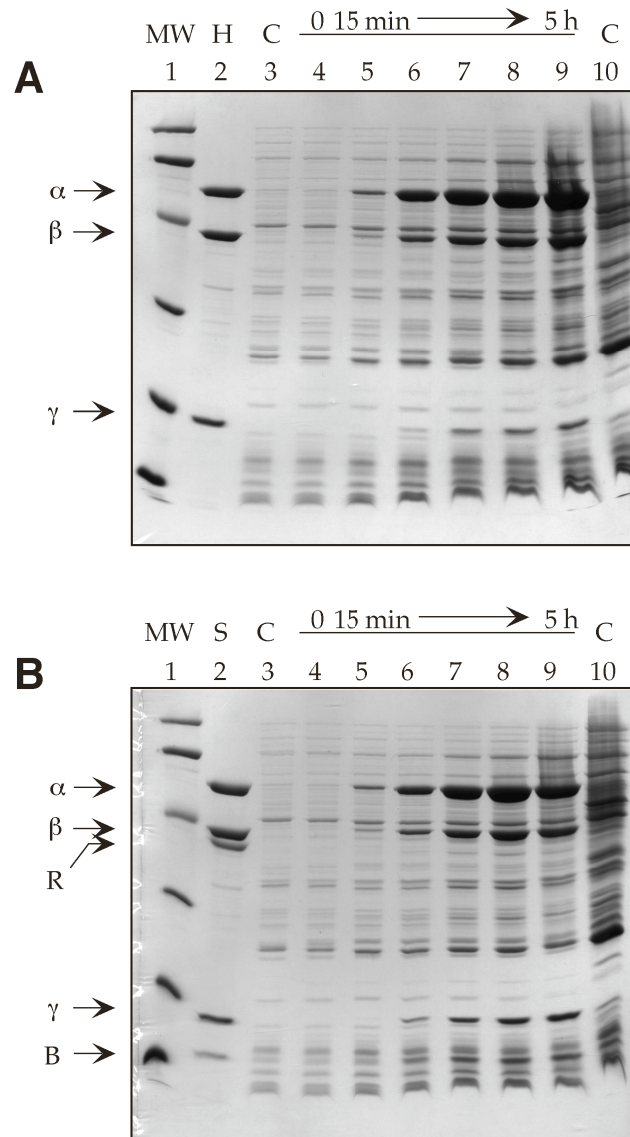


Figure 6.10. SDS-PAGE analysis of proteins produced in *E. coli* JM105/pJLB300 (A) or JM105/pJLB400 (B) induced with 0.5 mM IPTG over a period of 5 h at 37 °C. (A) Lane 1, molecular weight standards; lane 2, MMOH from *M. capsulatus* (Bath); lane 3, JM105/pMMB277 before induction; lane 4, JM105/pJLB300 before induction; lanes 5-9, JM105/pJLB300 expression time points between 15 min and 5 h after induction; lane 10, JM105/pMMB277 5 h after induction. (B) JM105/pJLB400 time-point samples identical to those in (A) except for the inclusion of MMOB and MMOR in lane 2.

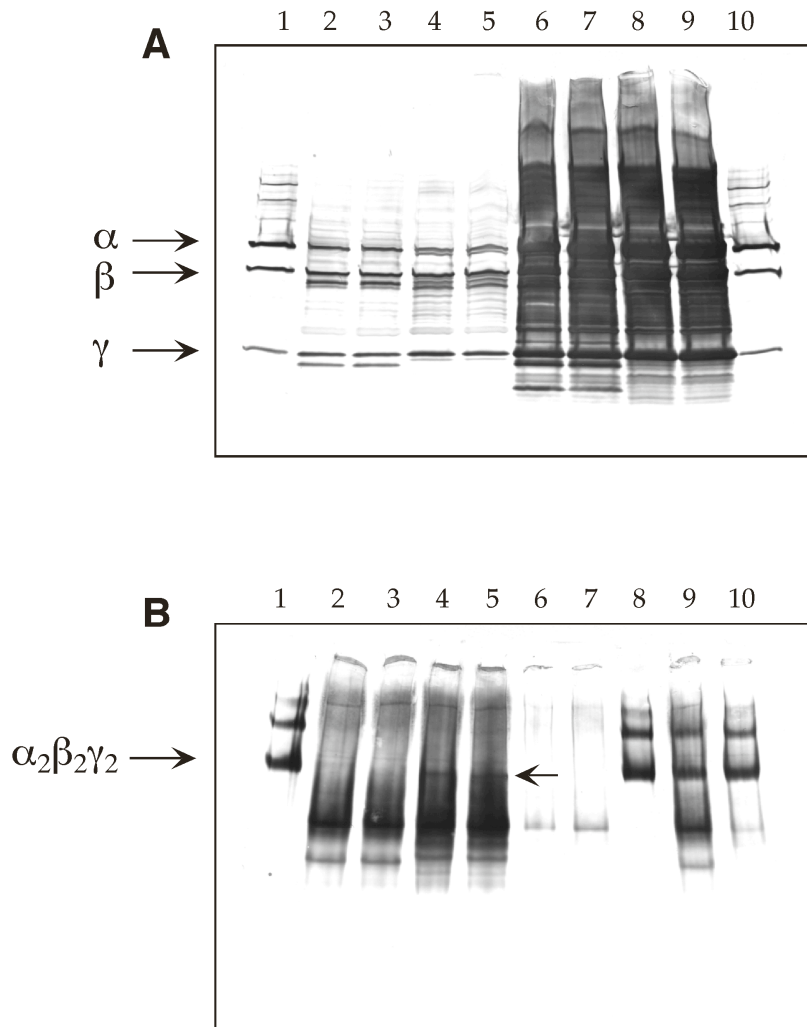


Figure 6.11. SDS-PAGE (A) and native PAGE (B) Western blot analyses of MMOH expressed from pJLB300 with 0.05 mM IPTG in either *E. coli* JM105 or BL21(DE3) cells. (A) Lanes 1 and 10, MMOH from *M. capsulatus* (Bath); lanes 2 and 3, soluble protein from JM105/pJLB300 cells; lanes 4 and 5, soluble protein from BL21(DE3)/pJLB300 cells; lanes 6-9, denatured insoluble protein expressed from JM105 (lanes 6 and 7) or BL21(DE3) (lanes 8 and 9). (B) Lanes 1 and 8, MMOH; lanes 2-5, as in (A); lanes 6 and 7, soluble protein from JM105/pJLB300+pRED-K2 and JM105/pJLB400+pRED-K2 expressions, respectively; lane 9, soluble protein from JM105/pJLB300 (lane 2) spiked with native MMOH; lane 10, soluble protein from JM105/pJLB300+pRED-K2 (lane 6) spiked with native MMOH. The arrow is pointing to the faint band of assembled MMOH in the BL21(DE3)/pJLB300 samples. The high molecular weight band in the standards is a degradation product of the native MMOH protein.

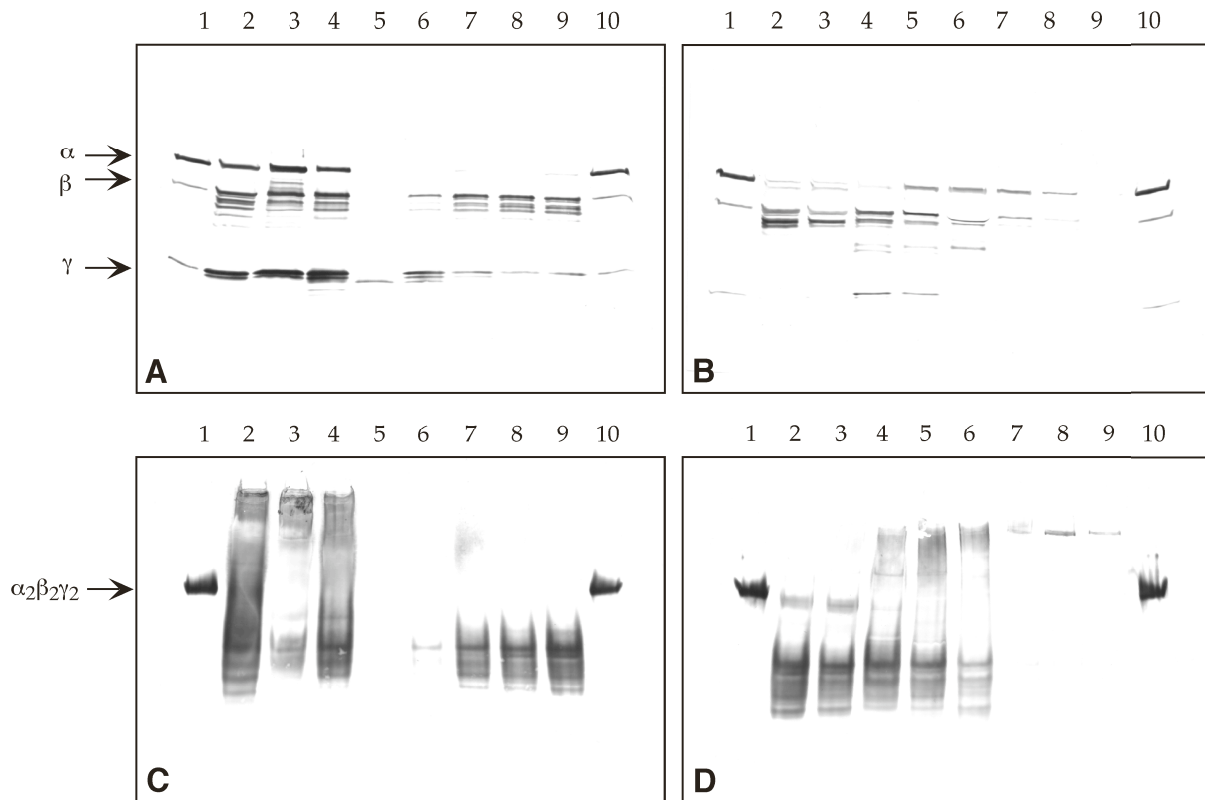


Figure 6.12. (A) and (B), SDS-PAGE Western blots of MMOH in fractions of soluble protein expressed by *E. coli* BL21(DE3)/pJLB300 resolved on a Sepharose CL-6B column. Lanes 1 and 10, MMOH from *M. capsulatus* (Bath). (A) Lane 2, soluble cell extract; lane 3, column flowthrough; lanes 4-9, column fractions containing increasing NaCl concentrations. (B) Lanes 2-9, continuation of NaCl gradient in Western blot A. (C) and (D), native Western blots exactly as corresponding blots A and B, respectively.

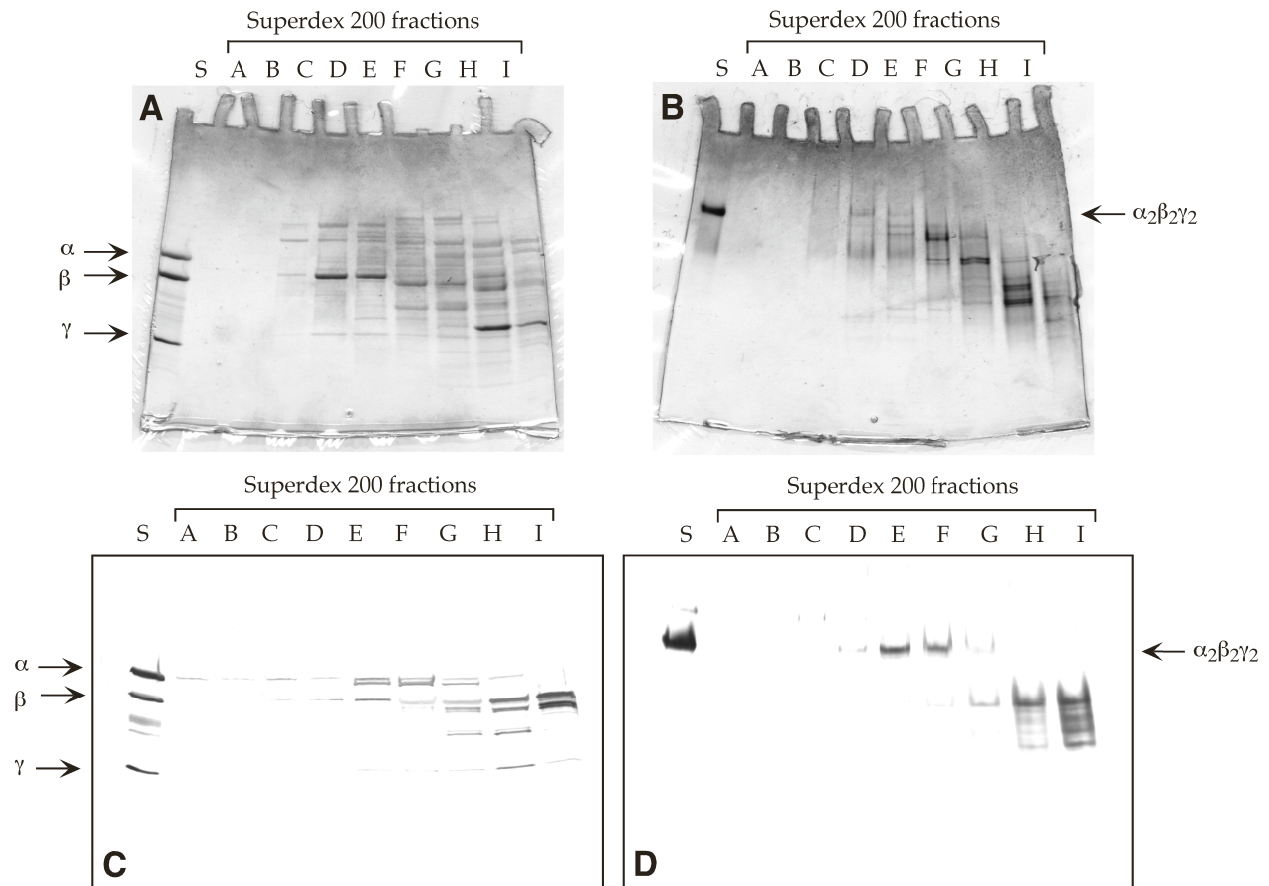


Figure 6.13. SDS-PAGE gel (A), native PAGE gel (B), SDS-PAGE Western blot (C), and native PAGE Western blot (D) of MMOH in fractions of soluble protein expressed by *E. coli* BL21(DE3)/pJLB300 resolved on a Superdex 200 size-exclusion column. Lane S, MMOH from *M. capsulatus* (Bath); lanes A-I, pools of column fractions.

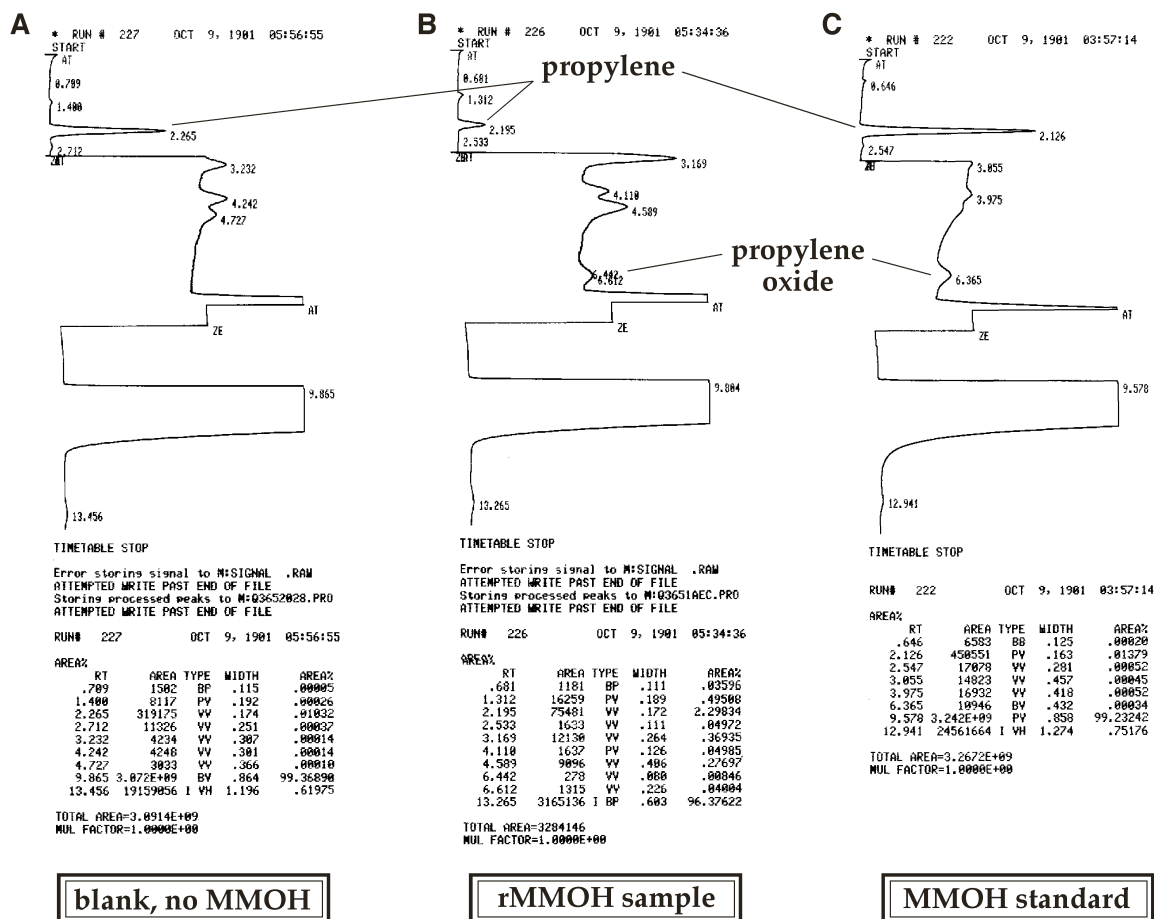


Figure 6.14. Gas chromatography (GC) traces for detection of propylene oxide in steady-state sMMO propylene assays. Each assay was performed in a 400- μ L volume containing 100 nM MMOB, 100 nM MMOR, 0.8 mM propylene, 0.16 mM NADH, and buffer [25 mM MOPS (pH 7.0) and 1 mM DTT]. After incubation at ambient temperature for 5-20 min, samples were extracted with chloroform, and 5- μ L aliquots of the organic material were analyzed by GC. Traces are shown for (A) a blank containing no MMOH, (B) the partially purified rMMOH sample, and (C) a standard containing 100 nM MMOH. The sensitivity between 3.0 and 7.4 min was increased for trials A and B compared to trial C.

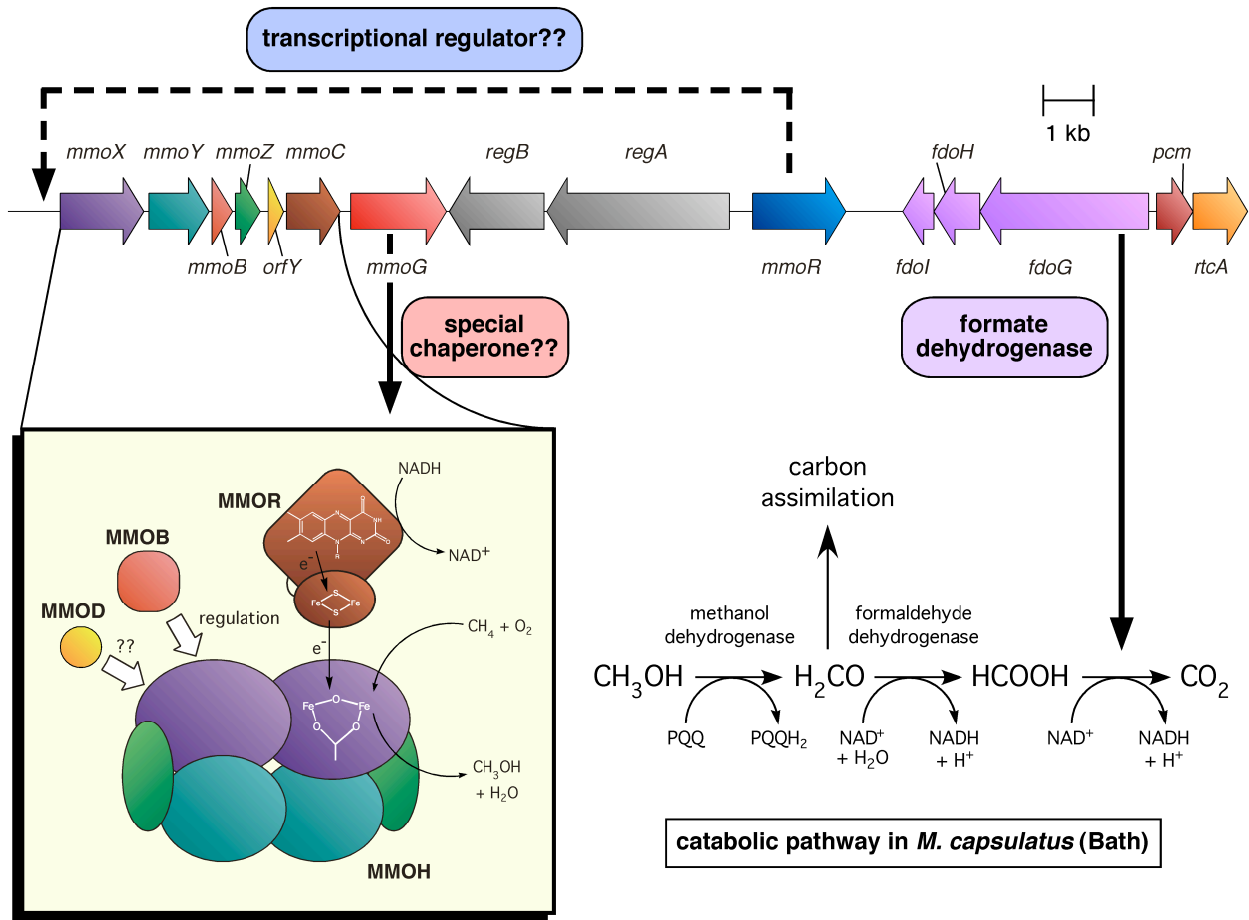


Figure 6.15. Open reading frames located downstream of the *M. capsulatus* (Bath) *mmo* operon. Possible functions, based on sequence homology to other proteins, are indicated for some of the putative gene products.

Mcapsulatus	1	-----MAKEV	VYR	---	GSARQR	MMQ	IEI	LARAAI	PTLGAT	GPSVMI
Mtrichosporium	1	MTNPRKRERRRPAFDV	TREKF	VARNIR	FGD	VVR	RDLLAG	VVDALAD	AVAVTL	GPGRNVVI
consensus	1		*	*	*	*	..	*..	**	* * *
Mcapsulatus	40	QHRADGLPPISTR	DGVTVANSIVL	KDRVANL	GARL	LRD	VAGTMS	REAGDG	TTT	AIIVLARH
Mtrichosporium	61	EHRAAGLPPVATK	DGVTVAQAVEL	LAGRTQS	VGVSL	VROMA	TAVAKE	EAGDG	TTT	SVVLARR
consensus	61	***	*****	.	*	*	*	*	*	*****
Mcapsulatus	100	IAREMFKSLAVG	ADPIALKRGID	RAVARVSE	DIGARAWR	GDK	ESVILG	VAAVAT	KGEPGV	
Mtrichosporium	121	LAAETRKALAA	GMNPRDIVL	GMEKAARI	VDRDLA	ARARR	CD	TRALAH	VATLA	AGGDESI
consensus	121	.	*	*	*	*	*	*	*	*
Mcapsulatus	160	GRLLEALDAVG	VHGAVSIELG	ORREDLL	DVVD	GYRWE	KGYL	SPYFV	TDRARE	LAELEDV
Mtrichosporium	181	GAIVADALTRAGE	GGVVDVLE	GAAALC	DEMDI	VEGMR	WEQGYR	SPYF	M	TDSARKIAE
consensus	181	*	..	**	*	*	*	*	*	*
Mcapsulatus	220	YLLMTDREVVDF	IDLVPLEAV	TEAGSLL	IAADRV	HEKAL	GLLLNH	VR	GVFKAV	AVTA
Mtrichosporium	241	YILLYDRVINQF	SELVPALEL	VRRQR	GSLI	V	ENI	VE	EALP	GLLLNHIR
consensus	241	*	*	*	*	*	*	*	*	*
Mcapsulatus	280	PGFGDKRPNRLL	DLAALTGGRA	VLEA	QGDR	LDR	VTLAD	LGRV	RR	AVVS
Mtrichosporium	301	PGVGD	SRVYEF	LHDLAALT	GGRAIME	EAC	GEE	LSN	V	MAHL
consensus	301	**	**	*	*	*	*	*	*	*
Mcapsulatus	339	TEASRARLEGLR	LEAEQYRAL	KPGOG	SATGR	LHELE	EIE	EARI	VGL	SGKSA
Mtrichosporium	361	GAAITERLAAAR	QO	ADWIT	DGDP	SKG	SPSG	KR	H	LENL
consensus	361	*	**	.	*	*	*	*	*	*
Mcapsulatus	399	EMKERMVRIEN	AYRSVVS	ALEEG	VLP	GGGV	GFLG	SMPV	LA	E
Mtrichosporium	421	LIKERMORIEN	ALASARA	ARSD	GVV	AGGG	VGLY	RARA	AL	T
consensus	421	.	****	****	*	*	..	****	*	*
Mcapsulatus	459	TEPLRIIGENS	GLS	GEAV	VAKVMD	HANP	GWGY	DOE	SGS	F
Mtrichosporium	481	DEPIRRIIAAN	ACRDA	HEFL	FELKRS	NDD	FW	CM	M	R
consensus	481	**	*	*	*	.	.	*	*	*
Mcapsulatus	518	KAASVAGTFL	TTEAVVLE	IPD	TDAFAG	FSAEW	AAAT	RED	PRV	
Mtrichosporium	540	NAVATASSL	MTVECAV	THIP	PSD	PTYG	FD	PH	AAAT	RED
consensus	541	*	*	.	*	*	*	*	*	*

Figure 6.16. Sequence alignment of GroEL homologs from *M. capsulatus* (Bath) (Mcapsulatus) and *M. trichosporium* OB3b (Mtrichosporium). Identical residues are depicted in reverse, and conservative substitutions are shown with a gray background. The proteins are 43% identical and 26% dissimilar.

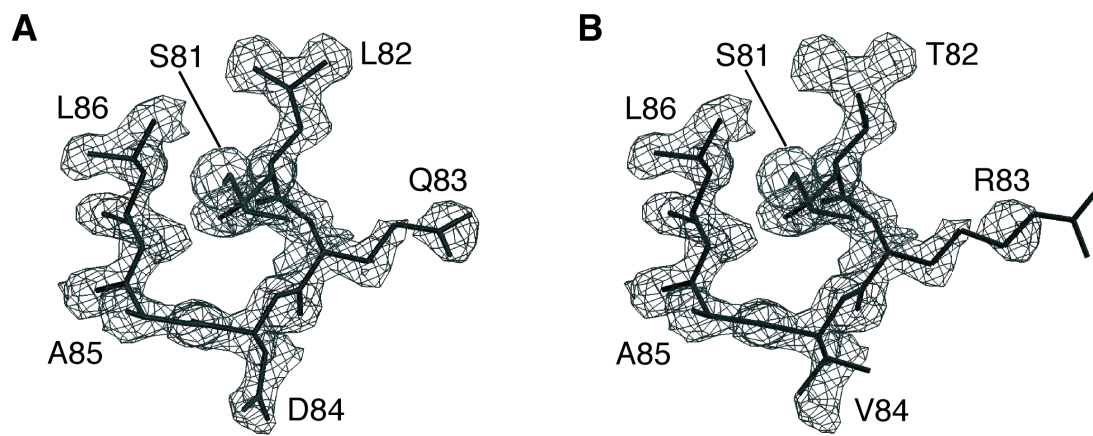


Figure 6.18. Comparison of α -subunit protein sequences with the *M. capsulatus* (Bath) MMO hydroxylase X-ray crystal structure electron density. Comparison of fits for the α -subunit sequences (A) S⁸¹LQDAL reported in this work and (B) S⁸¹TRVAL reported in ref 67 with the electron density map for the *M. capsulatus* (Bath) MMOH crystal structure.

Biographical Note

The author was born on July 9, 1974 in Providence, Rhode Island to Janet and Jack Blazyk. Following a brief spell in Columbia, South Carolina, she was raised in Athens, Ohio with two younger sisters, Laura and Katherine. She graduated from Athens High School in 1992 and entered the Honors Tutorial College at Ohio University. She earned a Bachelor of Science degree in Chemistry in 1996. During her undergraduate studies, she worked in the laboratories of Professor Malcolm C. Modrzakowski and her father at Ohio University and Professor James E. Penner-Hahn at the University of Michigan in Ann Arbor, Michigan. In 1996 the author began graduate work in biological chemistry at the Massachusetts Institute of Technology with a predoctoral fellowship from the Howard Hughes Medical Institute.

Jessica L. Blazyk**Education**

Ph.D., Biological Chemistry
1996-2003

Massachusetts Institute of Technology, Cambridge, MA
Advisor: Professor Stephen J. Lippard

B.S., Chemistry
1992-1996

Ohio University, Athens, OH
Honors Tutorial College

Publications

Blazyk, J. L.; Gassner, G. T.; Lippard, S. J. Intermolecular Electron Transfer Reactions in Soluble Methane Monooxygenase from *Methylococcus capsulatus* (Bath): A Role for Hysteresis in Protein Function. To be submitted for publication in *J. Am. Chem. Soc.*

Blazyk, J. L.; Lippard, S. J. Domain Engineering of the Reductase Component of Soluble Methane Monooxygenase from *Methylococcus capsulatus* (Bath). Submitted for publication in *J. Biol. Chem.*

Blazyk, J. L.; Lippard, S. J. Expression and Characterization of Ferredoxin and Flavin Adenine Dinucleotide-Binding Domains of the Reductase Component of Soluble Methane Monooxygenase from *Methylococcus capsulatus* (Bath). *Biochemistry* **2002**, *41*, 15780-15794.

Kopp, D. A.; Gassner, G. T.; Blazyk, J. L.; Lippard, S. J. Electron-Transfer Reactions of the Reductase Component of Soluble Methane Monooxygenase from *Methylococcus capsulatus* (Bath). *Biochemistry* **2001**, *40*, 14932-14941.

Merkx, M.; Kopp, D. A.; Sazinsky, M. H.; Blazyk, J. L.; Müller, J.; Lippard, S. J. Dioxygen Activation and Methane Hydroxylation by Soluble Methane Monooxygenase: A Tale of Two Irons and Three Proteins. *Angew. Chem. Int. Ed.* **2001**, *40*, 2782-2807.

Coufal, D. E.; Blazyk, J. L.; Whittington, D. A.; Wu, W. W.; Rosenzweig, A. C.; Lippard, S. J. Sequencing and Analysis of the *Methylococcus capsulatus* (Bath) Soluble Methane Monooxygenase Genes. *Eur. J. Biochem.* **2000**, *267*, 2174-2185.

Presentations

J. L. Blazyk, G. T. Gassner, S. J. Lippard. Expression and Characterization of Domains of the Reductase Component of the Soluble Methane Monooxygenase from *Methylococcus capsulatus* (Bath). ASBMB/ASPET 2000 Joint Meeting (Boston, MA: June 2000).

J. L. Blazyk, H. Brandstetter, S. J. Lippard. Expression and Site-Directed Mutagenesis of Protein Components of the Soluble Methane Monooxygenase System from *Methylococcus capsulatus* (Bath). 216th American Chemical Society National Meeting and Exposition (Boston, MA: August, 1998).

J. L. Blazyk, S. J. Lippard. Expression and Site-Directed Mutagenesis of sMMO Proteins from *Methylococcus capsulatus* (Bath). Methane Monooxygenase Symposium, Massachusetts Institute of Technology (Cambridge, MA: November 1997).

J. L. Blazyk, T. L. Stemmler, G. Wong, J. E. Penner-Hahn. Preparation and Characterization of Isotopically Labeled Derivatives of *L. plantarum* Mn Catalase. 1995 Great Lakes Area REU Poster Session, Michigan State University (East Lansing, MI: July 1995).

J. L. Blazyk, T. L. Stemmler, Y. K. Sharma, J. E. Penner-Hahn. Kinetic Characterization of Fluoride Inhibition of *L. plantarum* Mn Catalase. 1994 Summer Undergraduate Research Symposium, Bowling Green State University (Bowling Green, OH: July 1994).